Morphology and topology of cosmological fields during the Epoch of Reionization

A Thesis

Submitted for the Degree of

Doctor of Philosophy

in the Faculty of Science

by

Akanksha Kapahtia

Joint Astronomy Programme
Department of Physics
Indian Institute of Science
Bangalore – 560 012, INDIA

June 21, 2020

Declaration

I hereby declare that the work presented in this thesis titled, "Morphology and topology of cosmological fields during the Epoch of Reionization" is the result of research work carried out by me, under the supervision of Dr. Pravabati Chingangbam at Indian Institute of Astrophysics, Bengaluru and Dr. Tarundeep Saini at Department of Physics, Indian Institute of Science, Bengaluru under the Joint Astronomy Programme (JAP) hosted by the Department of Physics, Indian Institute of Science, Bengaluru.

I further declare that this thesis has not been submitted for the award of any degree, diploma, associateship, fellowship etc. of any university or institute. In accordance to the general practice, due acknowledgements have been made wherever the work described is based on other investigations.

Akanksha Kapahtia
Date: 21^{st} June, 2020
S. R. Number: 01-07-00-10-11-14-1-11437

Department of physics,
Indian Institute of Science,
Bengaluru - 560 012
India

Dedicated to the frontline workers
and healthcare providers
during the COVID-19 pandemic.

Acknowledgements

The journey of PhD is the beginning of the road to being an independent researcher. Like any other journey, the ride has been full of ups and down, both leading to a deeper realization of my potential and limits, amounting to academic and personal growth. Having aspired to become an astronomer since the age of 13, this has been like living a dream which could not have been successful without the support of some important people. Firstly, I thank my mother for believing in me and my ambitions, no matter how unrealistic they were at times and my father who inspired a deep sense of integrity and hardwork. They always encouraged me to do my best and motivated me to justify what I do. I thank my brother for encouraging me to be bold and fearless in pursuit of my goals. I thank my grandparents who have blessed me and inspired me in their own ways since childhood.

I deeply acknowledge my PhD supervisor, Dr. Pravabati Chingangbam for her constant support and guidance. She has taught me to have a simple outlook towards problems at hand and organize them. She greatly helped me improve my communication skills and express my thoughts clearly. The sincere efforts that she has put into training me, starting from my coursework days has helped me transition towards being a confident researcher. With her impeccable patience she provided me with both time and space to learn and progress at my own rythm. She has inspired me to be grounded and confident.

I thank Dr. Stephen Appleby at Korea Institute of Advanced studies, Seoul for providing our group with the codes for calculating Minkowski tensors. He helped me learn the intricacies of Minkowski tensors and its numerical aspects. I thank him for his valuable feedback on my papers and for funding my trip to KIAS, Seoul which was a great learning exposure. I thank Prof. Tirthankar Roy Choudhury of NCRA, Pune for being a great teacher at the 21cm schools that I attended. His immense knowledge of the subject has greatly helped me enhance my thought process. His valuable suggestions and feedback on my research has gone a long way to provide me with a definitive direction. I thank Dr. Raghunath Ghara at Technion for discussing various aspects of radio interferometry which enabled me to develop mock simulations in my final project. I would like to give my heartfelt thanks to Prof. T.R. Seshadri of Delhi University, for the numerous discussions and lectures on cosmology. I thank him for being a great source of motivation and encouragement. I thank Dr. Girish Kulkarni at TIFR, Mumbai for some useful suggestions and advices on how to improve my research and other skills. I thank Prof. Tarundeep Saini and Prof. Shiv Sethi for their help and valuable advices during my first year at IISc. A special thanks to Prof Annapurni Subramaniam, Prof Jayant Murthy and Prof. P. Sreekumar for providing a conducive environment for research at IIA during their directorship. I thank the Dean, Prof. G.C. Anupama and the faculty and staff of the Board of Graduate Studies at IIA for providing us with oppurtunities and facilities for academic growth. I thank all the teachers and organizers of the various cosmology schools that I attended so far. I would also like to thank the JAP coursework teachers at IIA, RRI and IISc for their efforts to build our foundations.

I thank Anish, Fayaz and Ashok at IIA computer center for the smooth working of IIA computer clusters and being available whenever I needed help. Special thanks to the library staff at IIA, who ensured a peaceful and stimulating environment in the library. A very special thanks to Manjunath and Chandrashekhar at Bhaskara, who help in the smooth functioning of the guest house, thereby making our stay comfortable and cherishable. A heartfelt gratitude to all the cooks and domestic staff at IIA, especially to the cooks who stayed back at Bhaskara for us during pandemic lockdown days. I would also like to extend my gratitude to the administration and domestic staff at IISc, for making my stay in the first year comfortable.

I would like to extend my thanks to my groupmates Fazlu, Priya and Joby. On that note, I would like to give a very special thanks to my senior and friend Vidhya. Her in depth and creative thought process lead to several stimulating discussions during my first few years at IIA. I thank my JAP senior and friend Janakee for helping me gain exposure to important literature on EoR during my early years in PhD. I also thank her for spending time to give feedback on my thesis. I thank all my other seniors at IIA and IISc who have helped me in one or the other way. I thank my batchmates for all the fun and discussions we had during coursework days. A special thanks to Avinash and Sandeep for being supportive friends and readily available for help, whenever I needed them.

A very special thanks to my dearest friends Shweta at IISc, Pavana, Maya and Pruthvi at IIA and Bidisha for being my pillars of love and strength during this time. I thank Ramya for being a patient listener and a fun roommate. Thanks to Sioree, for her care and all the interesting Physics discussions. A heartfelt gratitude to Parinita, Krishna and adorable little Ameya for being like a family away from home and a great emotional support. A special thanks to all my family, friends and mentors who have been there with me throughout this journey.

List of Publications

- *A novel probe of ionized bubble shape and size statistics of the epoch of reionization using the contour Minkowski Tensor*,
  Akanksha Kapahtia, Pravabati Chingangbam, Stephen Appleby, and Changbom Park,
  J. Cosmol. Astropart. Phys. **10** 011 (2018).

- *Morphology of 21cm brightness temperature during the Epoch of Reionization using Contour Minkowski Tensor*,
  Akanksha Kapahtia, Pravabati Chingangbam and Stephen Appleby,
  J. Cosmol. Astropart. Phys. **09** 053 (2019).

- *Prospects of Constraining models of EoR using morphological descriptors*,
  Akanksha Kapahtia, Pravabati Chingangbam, Raghunath Ghara, Tirthankar Roy Choudhury and Stephen Appleby,
  (2020) Manuscript under preparation

Table of contents

List of figures

List of tables

1

Introduction

According to the hot Big bang model, the universe started in a hot dense early phase and is expanding adiabatically (Gamow, 1946; Alpher et al., 1948; Peebles, 1993; Hubble, 1934). Further, the Cosmological Principle (Weinberg, 1972; Dodelson, 2003) states that the universe is statistically homogenous and isotropic on large scales (greater than 250 million light years (Yadav et al., 2010)). However, at small scales observations show gravitationally bound structures such as stars, galaxies and clusters of galaxies interwoven into a web of sheets, voids and filaments. Understanding the origins and evolution of structures in the universe is one of the foremost goals in cosmology. This chapter summarizes the various important epochs which lead to the formation of the first luminous objects and their subsequent effects on the intergalactic medium (IGM).

The chapter begins with a description of the homogenous isotropic universe in section 1.1. This is followed by section 1.2 which describes the evolution of the inhomogenous universe, setting the stage for a description of the Epoch of Reionization (EoR), which is the central goal of study in this thesis. This is followed by a brief description of various observational probes and statistical tools to study EoR in section 1.3. The chapter concludes with an outline of the aim of study and the overall structure of the thesis.

1.1 Brief account of homogenous and isotropic universe

The evolution of the homogenous and isotropic universe can be described by the Friedman Lematre Robertson Walker metric (Friedmann, 1924; Lemaître, 1931; Robertson, 1935; Walker, 1937), with the following line element [1]:

$$ds^2 = c^2\,dt^2 - a^2(t)\left(\frac{dr^2}{1-kr^2} + r^2 d\theta^2 + r^2 sin^2\theta d\phi^2\right), \tag{1.1}$$

where r, θ, ϕ are the usual spatial spherical coordinates, t is the temporal coordinate and c is the speed of light. The scale factor $a(t)$ describes the expansion of the universe and k is the curvature parameter. The universe is spatially flat if $k = 0$, negatively curved if $k = -1$ and positively curved if $k = +1$. The expansion of the universe can be described by the Friedmann equations :

$$\dot{a} + kc^2 = \frac{8\,\pi\,G}{3}\rho a^2. \tag{1.2}$$

$$\ddot{a} = -\frac{4\pi G}{3}\left(\rho + \frac{3p}{c^2}\right). \tag{1.3}$$

For a perfect fluid in a spatially flat universe with an equation of state $p = w\rho c^2$, the scale factor varies with cosmic time as $a(t) = a_0\,t^{\frac{2}{3(w+1)}}$. The value of w is zero for pressureless matter and $1/3$ for radiation. The expansion rate is described by the Hubble parameter, $H(t) = \dot{a}/a$. As the universe expands the wavelength λ_e of a light signal emitted at time t_e, will be redshifted to λ_o at the time of observation t_o. This redshifting is described by the cosmological redshift z :

$$\frac{1+z}{1+z_0} = \frac{\lambda_o}{\lambda_e} = \frac{a(t_0)}{a(t_e)},$$

where z_0 is the redshift in the observer's frame today and will be taken to be zero for the rest of the thesis. Observations indicate that the universe can be described by a parameterization of the hot big bang model, called the ΛCDM model. According to this model, the current universe has three main components, dark energy (described by the cosmological constant Λ), cold dark matter and Baryonic matter. From the first Friedmann's equation (eq. 1.2) the expansion rate

[1] A line element is the distance between two points in a given coordinate system. In this case, the coordinate sytem is four dimensional, with 3 spatial dimensions and one temporal dimension. The metric describes this distance by encapsulating the information of the geometry of the underlying space

can be written as:

$$\frac{H}{H_0} = \sqrt{\Omega_r a^{-4} + \Omega_m a^{-3} + \Omega_k a^{-2} + \Omega_\Lambda}, \tag{1.4}$$

where $\Omega_x = \rho_{x0}/\rho_c$ is the density parameter for a particular species of current average energy density ρ_{x0} and ρ_c is the critical density which is the density of a spatially flat universe (see appendix E). The era of precision cosmology has established that the smallest number of parameters required to fit the available observational data to the Λ CDM model is six (Dodelson, 2003). Small fluctuations in the energy density of the universe set during the first fraction of a second after the big bang has lead to the universe as we observe today which comprises of objects such as stars, galaxies and clusters of galaxies. The dominance of cold dark matter in the universe lead to the universe evolving in a bottom up fashion, with the smallest collapsed objects forming first (Peebles, 1980).

1.2 Evolution of the Inhomogenous Universe

The current observable universe consists of collapsed luminous structures on a web of overdense and underdense regions. While the universe is homogenous on large scales, it is inhomogenous at smaller scales with the highest density regions harbouring collapsed luminous objects. The starting stage for the evolution of these initial inhomogenities to the first collapsed luminous structures is set by the following important epochs, in chronological order since the big bang:

1. ***Inflation***: The phase of the evolving universe characterized by an exponential expansion of the underlying space, with the volume of the universe expanding to about 10^{78} times it's original volume in a tiny fraction of a second (Guth, 1981; Starobinsky, 1980; Linde, 1982). This epoch is thought to have occurred at about $\sim 10^{-32}$ seconds after the big bang. During this epoch the initial fluctuations are generated, which later grew into the large scale structures of the universe. Most inflationary theories predict that these initial tiny fluctuations were very close to Gaussian in nature with almost scale invariant power spectrum, $P(k) \propto k^{n_s}$ with n_s close to one. This is in agreement with the current observations of the Cosmic Microwave Background radiation (Planck Collaboration et al., 2018).

2. ***Nucleosynthesis***: This is the epoch when the first nuclei began to form and occurred at about $\sim 10^{-6}$ seconds after the big bang. Before this epoch the high number density of photons coupled with the hot environment destroyed any nuclei or atoms that could

form [2]. The universe was largely radiation dominated during this time and the baryonic component comprised of neutrons, protons (^{1}H), electrons (e^-) and neutrinos. The expansion and cooling of the universe during this time led to the formation of the first light nuclei – Helium-3 (^{3}He), Helium-4 (^{4}He) , deuterium (^{2}H) and trace amounts of Lithium isotope, (^7Li) (Kolb & Turner, 1990).

3. ***Epoch of recombination***: This is the epoch when the universe had cooled in order for protons and electrons to combine and form the first neutral hydrogen atoms. This occurred about 380,000 years after the big bang and at a redshift of $z \sim 1100$ (Peebles, 1968; Zeldovich et al., 1968). Thereafter, the photons decouple from the rest of the ionized plasma and free stream. These photons are seen today as a background of radiation redshifted to the microwave region of the black body spectra and cooled to a temperature of 2.72548 ± 0.00057 K (Penzias & Wilson, 1965; Dicke et al., 1965; Fixsen, 2009). This radiation is called the Cosmic Microwave Background (CMB). From the point of view of the growth of initial inhomogenities into the first luminous objects, the residual free electrons after recombination plays an important role. Relic electrons (with a number density n_e) must be present and the ionized fraction must be varying very slowly with redshift after recombination, because the rate of expansion of the universe will begin to exceed the rate of recombination .
The ionized fraction, $x_e = n_e/n_H$ [3] can be derived using the Saha's equation, as a function of the CMB temperature, T_{CMB} [4]. However, the assumption of equilibrium does not hold at $z \lesssim 1000$ and one has to solve for the variation of x_e with time (or redshift) . Post recombination, the relic electrons and the CMB photons are constantly interacting through inverse Compton scattering process. But, these electrons also interact with neutral hydrogen atoms. This, combined with the fact that the photon number density is much higher than the baryon number density (thus radiation has higher heat capacity compared to baryons) the kinetic temperature of gas, $T_K = T_\gamma$. Therefore, the gas and the photons remain thermally coupled and the gas temperature T_K, follows the evolution of

[2]For a stable nucleus or atom to form, the temperature of the universe should be less than the binding energy of the nucleus or atom.

[3]For clarity of notation used in this thesis, n_{HI} is the number density of neutral hydrogen atoms and n_H is the number density of hydrogen in both ionized and neutral state i.e., the number density of hydrogen nuclei is $n_H = n_{HI} + n_p$, where n_p is the number density of protons.

[4]The Saha equation describes the ratio of number densities for the ionized and neutral state of an atom in ionization equilibrium. For hydrogen in the ground state, it is written as:

$$\frac{n_e n_p}{n_{HI}} = \frac{g_e\, g_p}{g_H} \frac{(2\pi m_e k_b T)^{3/2}}{(2\pi\hbar)^3} e^{-(13.6eV)/k_b T},$$

where $g_e = g_p = 2$ and $g_H = 4$.

$T_{CMB} \propto 1/(1+z)$. Thus, the evolution of x_e and evolution of T_K form a coupled set of equations (Seager et al., 1999). This will be elaborated in section 2.2.3. The interaction rate of CMB photons with relic electrons eventually decreases below the rate at which the universe is expanding. Thereafter, the gas thermally decouples from the CMB and follows the usual adiabatic cooling with redshift i.e. $T_K \propto (1+z)^{-2}$. The redshift of thermal decoupling z_{td}, can therefore be calculated by comparing the rate of interaction of CMB with the gas to the rate of expansion of the universe. The rate of interaction via the inverse compton scattering is given by:

$$t_{IC} = \frac{3m_e c}{8\sigma_T a_R T_\gamma^4}\left(\frac{1+x_e+f_{He}}{x_e}\right), \tag{1.5}$$

where f_{He} is the fraction of helium and other constants are defined in Appendix E. The expansion timescale is $1/H(z)$, which is to be substituted from eq. 1.4 and assuming a matter dominated universe, one obtains the redshift of thermal decoupling to be, $z_{td} \sim 136$ for $x_e \sim 10^{-4}$. This point will be re-visited in section 2.2.3.

4. ***Cosmic Dark ages***: Subsequent to the epoch of recombination the baryonic content of the universe is dominated by neutral hydrogen atom ($\sim 75\%$) and Helium ($\sim 25\%$) while the non baryonic content is dominated by cold dark matter . The fluctuations in the energy density of the matter content follow the mild inhomogenities set during inflation which grow as the universe evolves. This epoch, until the appearance of the first luminous sources at about 1 billion years after the big bang, is called the Cosmic dark ages. The name is derived from the fact that there is no direct observational probe of this epoch other than the neutral hydrogen spin flip transition at 21cm wavelength (Furlanetto et al., 2006).

1.2.1 Cosmic Dawn - Formation of the first structures:

The initial perturbations set by inflation, grow under gravity as the universe evolves. It is these slight inhomogenties that grow into the first luminous sources that we see in today's universe (Peebles, 1980; Mo et al., 2010). In order to study the growth of these inhomogenities in matter relative to the average background density $\bar{\rho}$, the following quantity is defined:

$$\delta(\mathbf{x},t) = \rho(\mathbf{x},t)/\bar{\rho}(t)$$

- Linear growth of perturbations: The initial growth of density perturbations can be described by linear perturbation theory, because $\delta(\mathbf{x},t) \ll 1$. The evolution of these perturbations can be obtained in the Newtonian regime if they are well within the horizon[5] and described by the following equations for a matter dominated universe[6] (Peebles, 1980):

$$\ddot{\delta}(\mathbf{x},t)+2H(t)\dot{\delta}(\mathbf{x},t) = \frac{c_s^2}{a(t)^2}\nabla^2\delta(\mathbf{x},t)+4\pi G\bar{\rho}(t)\delta(\mathbf{x},t) \quad (1.6)$$

$$\ddot{\delta}_k+2H(t)\dot{\delta}_k = \delta_k\left(4\pi G\bar{\rho}-k^2c_s^2\right), \quad (1.7)$$

Eq. 1.7 is obtained when $\delta(\mathbf{x},t)$ in eq. 1.6 is written as a Fourier series, i.e. $\delta((\mathbf{x},t)) = \sum_k \delta_k(t)e^{i\mathbf{ak}.\mathbf{x}}$. Here, k is the physical wave number and $c_s = \partial p/\partial\rho$ is the speed of sound. Thus, eq. 1.7 describes the evolution of a perturbation at a physical scale $\lambda = 1/|\mathbf{k}|$.

- Jean's scale: The Jean's scale is defined as the scale $\lambda = \lambda_J$ corresponding to a $k = k_J$ where the right hand side of eq. 1.7 is zero when $\dot{a} = 0$ or $H(t) = 0$ (i.e. in a non expanding universe). Therefore one can define the Jean's scale to be $\lambda_J = 2\pi/k_J = c_s\left(\frac{\pi}{G\bar{\rho}}\right)^{1/2}$.
The solutions to eq. 1.7 would be oscillatory if the right hand side is negative, i.e. $\lambda < \lambda_J$ and the solution would be growing exponentially, if $\lambda > \lambda_J$. Thus, physically the Jean's scale λ_J defines the scale beyond which an overdense regions will collapse under gravity and would no longer be supported by pressure. The mass enclosed inside $\lambda = \lambda_J/2$ is called the Jean's mass $M_J = \frac{4\pi}{3}\rho\left(\frac{\lambda_J}{2}\right)^3$.
If the expansion of the universe is taken into account then one obtains power law solutions of the form where $\delta \propto t^n$, where $n = -1$ (*decaying mode*) or $n = 2/3$ (*growing mode*), for the case $\lambda \gg \lambda_J$ in a flat Einstein de-Sitter universe. Thus the effect of the expansion of the universe is to prevent the collapse of structures, changing exponential growth to a power law growth. The overdensity at time t relative to that at time t_0 changes as:

$$\delta(a(t)) = \frac{D(a(t_0))}{D(a(t))}\delta(a(t_0)),$$

[5]Note that the horizon here refers to the *Hubble horizon*, $c\,H(t)^{-1}$ and the same terminology is used throughout the thesis unless mentioned otherwise. In order to study the events which are within the particle horizon at time t, but now outside of the Hubble horizon, one needs full general relativistic treatment. See Appendix (E.1) for the detailed definition of horizons.

[6]It is to be noted that during the regime of cosmic dawn to the Epoch of Reionization, ($6 \lesssim z \lesssim 100$), the density of the universe is mostly dominated by matter. The universe behaves like a flat Einstein de-Sitter universe (a matter only universe in which $k = 0$ and $\Lambda = 0$ and $a(t) \propto t^{2/3}$) and thus one can safely assume, $H = H_0\sqrt{\Omega_M}a^{-3/2}$.

where D is called the growth factor and $D(a(t)) \propto a(t)$ in a matter dominated universe.

- Non-linear Collapse: Once the perturbations become non linear, i.e. $\delta \sim 1$, the above theory of linear perturbations does not hold. In order to study the non-linear evolution, one has to either resort to N-body simulations or model it using symmetries such as collapse of a spherical overdensity (Peebles, 1980; Padmanabhan, 1993; Mo et al., 2010). In the latter case, the collapse is modelled as a competition between gravity and the underlying expansion of the universe. The spherical overdensity would grow to a maximum size r_{max} and turn around to collapse. At the time of turnaround $\delta \simeq 5.55$ and at the time of total collapse, $\delta_c \simeq 178$. Note that these values correspond to a situation where there is no pressure support to stop the perturbation from collapsing on itself.

- Virialization: In an actual collapse in the absence of pressure support, the spherically collapsing region would virialize before completely collapsing on itself i.e. when $E_k = -1/2U$ [7]. One can then infer the radius at which this virialization takes place for a given overdensity. It turns out that under spherical collapse model this occurs when the overdensity has collapsed to an $r = r_{max}/2$. In that case for a virialized structure, $\delta_c \simeq 145$. If the evolution of a spherically collapsing overdensity is modelled using an extrapolation of the linear perturbation theory, then at the point of virialization $\delta_c \simeq 1.686$. The collapse of dark matter into virialized structures (also called as dark matter halos) occurs before baryons can collapse. This is because, before matter domination the universe is dominated by radiation which exerts a radiation pressure on baryons, thereby preventing the growth of baryonic perturbations. As stated before, smaller halos would eventually merge into bigger halos which become the sites of formation of galaxies and clusters of galaxies.

- Collapse into luminous structures: Subsequent to the collapse and virialization of dark matter to form dark matter haloes, the baryons start falling into these dark matter potential wells and get shock heated to the virial temperature of the halos. To form stable structures the gas must cool radiatively in order for gravitational collapse to dominate over radiation pressure. One of the major cooling processes that takes place during the formation of the first structures is that through collisional excitation by electrons between levels of

[7] From the virial theorem one can define the virial mass, M_{vir} and virial temperature, T_{vir}. Equating kinetic energy per particle to potential energy per particle inside a virialized halo of mass M_{vir}:

$$\frac{GM_{vir}}{R_{vir}} \simeq v^2 \simeq \frac{3}{2}\frac{k_B T_{vir}}{m_p}.$$

Therefore, for a constant density $M_{vir} \propto T_{vir}^{3/2}$.

molecular (H_2) or atomic (H) hydrogen (between 1s-2s level i.e. the Ly-alpha transition). If the collisional excitation is followed by a radiative de-excitation and the photon escapes the halo, the gas cools. For collisional excitation the electrons are expected to have a certain amount of kinetic energy such that the collisions can excite to the particular level. For Ly-alpha to collisionally excite, the virial temperature of the halo must be $T_{vir} \gtrsim 10^4\ K$. On the other hand for H_2 cooling, $T_{vir} \lesssim 10^4$. Initially only atomic and molecular hydrogen is present and hence the cooling is not as efficient as for other heavier elements. Therefore the first stars were massive and short-lived (Barkana & Loeb, 2001; Ciardi & Ferrara, 2005; Bromm et al., 2002; Glover, 2005). As the first stars end up in supernovae, they enrich the medium inside the halos with metals which are more efficient coolants than atomic or molecular hydrogen. This decreases the Jean's length causing the big gas clouds fragment into smaller objects.

1.2.2 Epoch of Reionization:

As the first stars form, they radiate Lyman continuum photons, which escape their respective halos and ionize the neutral hydrogen in the Inter galactic Medium (Arons & Wingert, 1972). These photons lie in the ultraviolet regime of the spectrum. This epoch when the first luminous sources radiate ionizing photons and gradually ionize the universe marks the commencement of the EoR (Zaroubi, 2012; Barkana & Loeb, 2001). Our current understanding indicates that the EoR started at around redshift of $z \simeq 30$, when the first luminous objects formed (Tegmark et al., 1997; Bromm et al., 2002; Glover, 2005) and observational evidence suggests that it ended at a redshift of $z \simeq 6$ (Fan et al., 2006; Becker et al., 2001). A recent study by (Kulkarni et al., 2019) points towards an end of reionization at a redshift of $z \lesssim 5.5$.

In this subsection the basic physics of ionization is described. Ionization of neutral hydrogen in the ground state takes place when there are ionizing photons of energy $\mathbf{E \geq 13.6\ eV}$ which lies in the ultraviolet part of the black body spectrum. The process is reversible with recombination taking place in the reverse direction:

$$H + h\nu \leftrightarrows p + e^-.$$

Thus, there are two competing processes (Dyson & Williams, 1997):

- <u>Recombination</u>: The recombination rate per unit volume depends upon the number density of recombining species and is therefore directly proportional to $n_e n_p$. It should also depend upon the rate at which an electron encounters a proton. This rate of encounter depends upon the velocity distribution of the electrons which will further depend upon the temperature of the gas, T_e . Recombination can take place to any level n of the atom, which depends upon the energy of the electron. Thus the rate of recombination for hydrogen (for which $n_e = n_p$) to a level n is given by:

$$\dot{\mathcal{N}}_{rec} = n_e n_p \alpha_n(T_e) \equiv n_e^2 \alpha_n(T_e)\ (m^{-3}s^{-1}), \tag{1.8}$$

where $\alpha_n(T_e)$ is the recombination coefficient to the n^{th} level [8].

- Ionization: The ionization of an atom can in principle happen at any level of that atom. However, for hydrogen in the IGM one can safely assume it to take place only at $n = 1$, since the lifetimes of other excited states is small and the hydrogen atom quickly de-excites to the ground state. The ionization rate per unit volume for a region that receives ionizing photons at a rate N_{ph} per unit area per unit time is given by:

$$\dot{\mathcal{N}}_{ion} = \alpha_0 n_{HI}\, N_{ph}\ (m^{-3}s^{-1}), \tag{1.9}$$

where α_0 is the ionization cross-section[9] for a hydrogen atom in its ground state and n_{HI} is the number density of neutral hydrogen atoms.

If there is a luminous source emitting ionizing photons at a rate $S_* = N_{ph} \times 4\pi r^2$, then the volume of region that it can ionize is not indefinitely large. This is because at some $r = R_S$, the rate at which the source emits ionizing photons is equal to the rate at which recombinations occur:

$$\frac{4}{3}\pi R_S^3 (x\, n_H)^2 \alpha_A = S_*, \tag{1.10}$$

where x is the ionized fraction and therefore, $n_e = x \times n_H$.

The sphere of maximum volume that a source emitting ionizing radiation can ionize is called a **Stromgren Sphere** (Strömgren, 1939) and the radius of that sphere, $R_S = \frac{S_*}{\alpha_A} \frac{3}{4\,\pi} \frac{1}{(x\,n_H)^2}$ is called the **Stromgren Radius**. In an expanding universe if a source turns on at a redshift z_i, then analogous to eq. 1.10 and using $n_H = n_H(z_i) \times \left(\frac{1+z}{1+z_i}\right)^3$, one obtains (Shapiro & Giroux,

[8] Recombinations to $n = 1$ level are usually balanced by an immediate reionization, hence these recombinations are usually not considred. If the recombinations to all states ($n \geq 2$) of hydrogen are taken into account it is called the *Case-A recombination* and denoted by α_A. If only the recombinations to $n = 2$ is taken into account it is called the *Case-B* recombination and denoted by α_B.

[9] Effective area for ionization presented to a photon by an atom and can be taken to be a constant ($\alpha_0 = 6.8 \times 10^{-22}\ m^2$). In actual it depends upon the energy of the incident photon and decreases with increasing energy.

1987):

$$R_s(z) = \left(\frac{3\,N_{ph}}{4\pi\, x\, \alpha_A\, C\, n_H^2} \right)^{1/3} \frac{(1+z_i)}{(1+z)} \equiv R_s(z_i) \frac{(1+z_i)}{(1+z)}, \tag{1.11}$$

where C is the clumping factor which describes the local inhomogenity in the IGM and is given by $C = \langle n_H^2 \rangle / \langle n_H \rangle^2$. This is included to take into account the higher rate of recombination in regions where the number density is higher.

The progress of reionization takes place in three different stages (Gnedin, 2000; Choudhury, 2009):

1. Pre-mergers : This is the scenario where individual sources host bubbles which grow in size.

2. Mergers: This is the stage where the bubbles begin to overlap and percolate.

3. Post-mergers: This stage marks the end of bubble mergers or the progress of reionization, thereby ionizing the entire universe.

Since, the progress of ionization depends upon the growth and morphology of ionized regions which in turn depend upon the properties of individual sources, any indirect or direct observations of the EoR can provide an insight into the evolution of the first luminous sources and their properties. The sources responsible for reionization is still a debatable topic, due to the uncertainity in the modelling parameters that describe them. However, it is understood that the first sources were metal free stars which evolved to metal poor and metal enriched galaxies later on. Quasars can also contribute to reionization through ionization by secondary electrons (Madau & Haardt, 2015). Quasars would contribute significantly at high redshifts ($z \gtrsim 8$), while galaxies contribute more at lower redshifts ($z \lesssim 6$) (Volonteri & Gnedin, 2009).

1.3 Observational probes of the EoR

1.3.1 Cosmic Microwave Background

There are two observational signatures of the EoR on the CMB which are described below (Reichardt, 2016):

- ***Large scale polarization of the CMB*** (Rees, 1968): As the universe begins to ionize, the free electrons scatter CMB photons. Due to this, photons that appear along a given line of sight would have actually originated in a direction other than the line of sight of the observer. The optical depth to scattering of a CMB photon along the line of sight up till a given redshift is given by:

$$\tau_{CMB} = \int n_e(z)\sigma_T(cdt/dz)dz = n_H(0)c\ \sigma_T \int_0^{z_{max}} dz\, x_e(z)\,\frac{(1+z)^2}{H(z)}, \tag{1.12}$$

where σ_T is the Thomson's scattering cross-section and $x_e = n_e(z)/n_H(z)$. Therefore, $e^{-\tau_{CMB}}$ of the total CMB photons received along a line of sight originate from a different direction. This damps the temperature anisotropies by the same amount. At a given redshift, the electrons would scatter photons from within the horizon at that time. Thus the total angular power in the temperature fluctuations of the CMB damps by a factor of $e^{-2\tau_{CMB}}$ at angular scales smaller than the horizon scale at the time of scattering. Scattering of CMB photons would also induce a finite linear polarization of the CMB photons. Only a quadrupolar distribution of CMB intensity would produce a finite polarization of the photons (Hu & White, 1997). This appears as a bump at scales larger than the horizon scale in the angular power spectrum of the E-mode polarization of CMB. The induced power is proportional to τ_{CMB}^2. Therefore the amplitude of the polarization power spectrum will provide a measure of τ_{CMB}. From eq. 1.12, one can see that τ_{CMB} will only give an integrated measure of ionized gas along the line of sight but not a detailed evolution of the ionization state of the universe over cosmic time. The current constraints on $\tau_{CMB} = 0.054$ from the Planck satellite mission (Planck Collaboration et al., 2018).

- ***Kinetic Sunyaev-Zel'dovich Effect (kSZ) effect*** (Sunyaev & Zeldovich, 1972; Birkinshaw, 1999): The Doppler shift due to the relative motion between ionized bubbles and the CMB photons causes a temperature shift in the CMB along a given line of sight. Therefore the kSZ power depends upon the fluctuations in ionized regions along the line of sight which further depends upon the sources of ionization and hence the duration of EoR. Since this effect is due to the inhomogenities in the baryonic density, ionized fraction and velocity field during EoR it is a small scale effect (Knox et al., 1998; Phillips, 1995).

1.3.2 Ly-alpha line

The Ly-alpha line corresponds to a rest frame wavelength of 1216 Å and is the energy difference between the principle quantum numbers, $n = 2$ and $n = 1$ of atomic hydrogen. The importance of using Ly-alpha as an observational probe is described below:

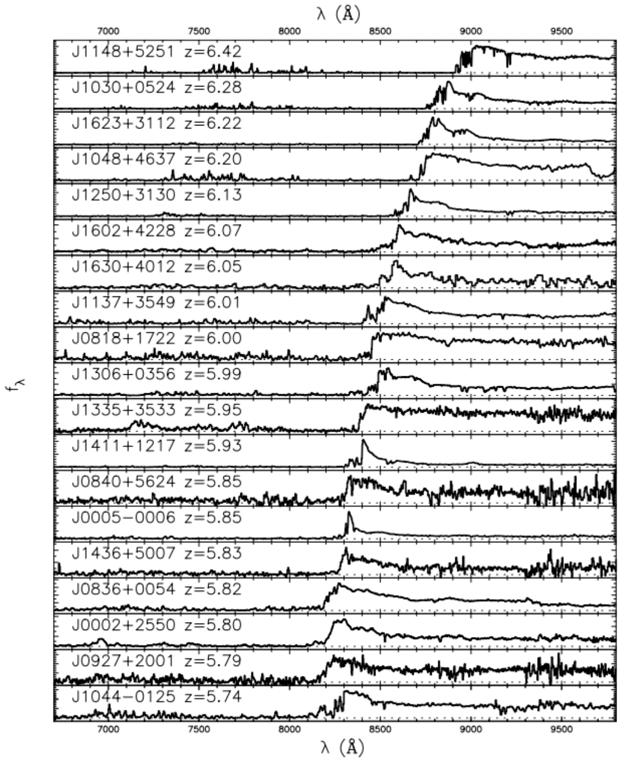

Fig. 1.1 The figure shows the spectra of quasars in the redshift range of $z \sim 5.7$ to $z \sim 6.46$ from (Fan et al., 2006). There is almost zero intensity between $z \sim 6.42$ to $z \sim 6$ for wavelengths below $1216(1+z)$ Å. At redshifts below 6, the intensity begins to rise at these wavelengths because the universe has ionized and there is no neutral hydrogen to absorb Ly-alpha.

- ***Gunn-Peterson Effect*** (Scheuer, 1965; Gunn & Peterson, 1965; Field, 1962): The continuum photons bluewards of the Lyα resonance that are emitted by luminous quasars and galaxies are redshifted into the Lyα wavelengths as they traverse through the IGM. If these photons happen to pass through a neutral hydrogen cloud, these photons are absorbed. Therefore, on observing the spectra of distant quasars one obtains a series of absorption lines bluewards of the wavelength corresponding to the redshifted Lyα as shown in Fig. 1.1 (Fan et al., 2003, 2006; Becker et al., 2001). At low resolution one would simply see an absoprtion trough. Assuming a narrow line profile, the optical depth to Ly-alpha, i.e. the Gunn-Peterson optical depth along a line of sight is given by:

$$\tau_{GP} \simeq 1.6 \times 10^5 \, x_{HI}(1+\delta) \left(\frac{1+z}{4}\right)^{3/2}, \tag{1.13}$$

where x_{HI} is the neutral hydrogen fraction and δ is the overdensity in matter. The above expression shows that even a tiny neutral hydrogen fraction of $x_{HI} \sim 10^{-5}$ would lead to an optical depth $\tau_{GP} > 1$ at any redshift, $z \geq 3$. In reality, x_{HI} increases at $z > 6$, which means an even higher optical depth. Therefore photons which redshift through Ly-alpha resonance during the EoR would be completely absorbed, thereby forming the absorption trough. If there is no neutral hydrogen cloud at the point where the photon is redshifted to Ly-alpha, it would redshift further without getting absorbed by any hydrogen along the line of sight after that point. Thus, the forest of absorption lines blueward of the Ly-alpha in the rest frame spectra of quasars along different lines of sight will tell about the distribution of neutral hydrogen. This varying forest of absorption lines along different lines of sight is called the ***Ly-alpha forest***. The transition of the universe from being neutral to ionized is captured by the variation in the spectra blueward of Ly-alpha as shown in Fig. 1.1. However, due to high optical depth of Ly-alpha to neutral hydrogen, it is not possible to obtain a detailed ionization history of the universe as even a small neutral fraction would turn the IGM opaque.

- ***Ly-alpha emitters (LAEs)*** (Malhotra & Rhoads, 2004; Jensen et al., 2013): These are young star forming galaxies. The stars in these galaxies emit ionizing radiation which ionizes the hydrogen in the interstellar medium (ISM). The electrons and protons thus produced, recombine and de-excite to emit Ly-alpha photons. This can happen either within the interstellar medium of the galaxy and a fraction of Ly-alpha photons escape into the IGM, or it can happen when ionizing photons escape the galaxy to ionize the surrounding IGM from where the Ly-alpha is emitted on recombination. As mentioned above, Ly-alpha is strongly absorbed by neutral hydrogen. Therefore, the hydrogen in the IGM will strongly suppress the Ly-alpha flux from such galaxies which would make it difficult to observe them. However, during reionization such galaxies will be surrounded by large ionized bubbles which would allow these line photons to pass through. If the selection bias due to redshift evolution of halo mass function is taken into account [10], the decreasing number of LAEs at high redshift would indicate towards an evolving neutral hydrogen fraction. Therefore, the luminosity function of LAEs during EoR has a smaller amplitude compared to the luminosity function[11] post EoR . However, the complex radiative transfer of Ly-alpha through the ISM of these galaxies make it difficult to interpret the observations as solely due to the evolving ionization state of the IGM.

[10] Halo mass function is the number density of halos per unit mass interval. The halo mass function evolves with redshift, with decreasing number density of halos at higher redshift.

[11] Luminosity function is the number of galaxies per unit luminosity interval.

Future galaxy surveys will be able to give a more detailed description of these galaxies during EoR.

1.3.3 21 cm line

In the context of astrophysics, the theoretical prediction of the 21cm line was made by Hendrik van de Hulst in 1944 (Van de Hulst, 1982). He proposed it as a technique to study the interstellar medium of the Milky Way. The first observation of this line was made by Ewen and Ed Purcell in 1951 (Ewen & Purcell, 1951). The observational probes described in the previous subsections, provide indirect constraints on the duration of EoR, but they do not provide a description of the detailed evolution of the ionized state of neutral hydrogen. The hyperfine transition of the ground state of neutral hydrogen provides for a way to directly infer the IGM properties during EoR (Field, 1958; Hogan & Rees, 1979; Scott & Rees, 1990). The 21cm line is a weaker transition as compared to the Ly-alpha transition, but it has the following advantages (Chapter 12 of (Loeb & Furlanetto, 2013)):

1. The optical depth to 21cm emission is much less as compared to Ly-alpha and hence one can obtain a tomography of the IGM during EoR.

2. It can probe regions of low IGM temperatures as it can be easily excited through collisions due to it's lower excitation energy.

The 21cm line corresponds to a frequency of 1420.4 MHz. It will be redshifted and observed at radio frequencies for redshifts corresponding to the duration of EoR. The major observational challenge of detecting 21cm from the EoR is the foreground contamination due to the diffuse galactic synchrotron and extragalactic point sources which are almost five orders of magnitude higher than the expected signal (Furlanetto et al., 2006; Shaver et al., 1999; Peng Oh & Mack, 2003; Bowman et al., 2009).

1.4 Statistical measures for 21cm Cosmology

The 21cm signal is described by the contrast of it's brightness temperature (Appendix (A)) against the CMB temperature . Therefore, for a particular observation frequency ν_o and at a spatial point $\mathbf{x}$:

$$\delta T_b(\mathbf{x}, \nu_\mathbf{o}) \equiv T_b(\mathbf{x}, \nu_\mathbf{o}) - T_{CMB} \tag{1.14}$$

The evolution of δT_b with redshift is the same as observing at a range of frequencies, thereby enabling one to obtain a tomography of the neutral hydrogen content with cosmic time. The major methods to study the 21cm signal are (Greig, 2019):

1. Monopole or global signal: The global signal is the sky average of the brightness temperature as a function of frequency. This does not contain the spatial information of the signal but it does describe the evolution of the IGM in terms of global astrophysical properties (Furlanetto, 2006; Pritchard & Loeb, 2010). It requires simpler and cheaper instrumentation (Shaver et al., 1999). The global signal has been claimed to have been detected by the EDGES (Experiment to Detect the Global Epoch of Reionization Signature) experiment (Bowman et al., 2018) and there is an ongoing effort by experiments such as SARAS (Shaped Antenna measurement of the background RAdio Spectrum) (Singh et al., 2017, 2018), LEDA (Large Aperture Experiment to Detect the Dark Ages) (Price et al., 2018) and the BIGHORNS (Sokolowski et al., 2015) . The detailed physics and the expected evolution of the global signal is described in chapter 2.

2. Fourier space measures: In Fourier space, the commonly used method for studying fluctuations is the fourier transform of the two-point correlation function called power spectrum (see Appendix B). It is advantageous from the observational point of view, as radio interferometers directly measure the power spectrum of the 21cm brightness temperature (Zaldarriaga et al., 2004; Furlanetto et al., 2004b; Bharadwaj & Ali, 2004). Redefining the brightness temperature in eq. 1.14 in terms of the fractional fluctuations about the mean, $\delta_{21}(\mathbf{x}) = (T_b(\mathbf{x}) - \overline{T}_b)$ the power spectrum P_{21} is defined as:

$$\langle \overline{\delta}_{21}(\mathbf{k}_1)\overline{\delta}_{21}(\mathbf{k}_2)\rangle \equiv (2\pi)^3 \delta_D(k_1 - k_2) P_{21}(\mathbf{k}_1), \tag{1.15}$$

where δ_D is the Dirac delta function. Usually the 21cm power spectrum is also defined as the dimensionless power spectrum as:

$$\Delta^2_{21}(\mathbf{k}) = \frac{k^3}{2\pi^2} P_{21}(\mathbf{k}). \tag{1.16}$$

The power spectrum can then either be a spherically averaged power spectrum, $P(k)$ (Morales & Hewitt, 2004) or the cylindrically averaged power spectrum, $P(k_{||}, k_\perp)$. The modes parallel to the line of sight are $k_{||}$ i.e. in the frequency direction while $k_\perp$ are the modes perpendicular to the line of sight obtained in the sky plane (Wang et al., 2006). The advantage of using the cylindrically averaged power spectrum is that the effect of foreground get contained in a wedge-like region while the clean signal can be recovered from the remaining modes (Liu et al., 2014). The radio interferometers measure a quantity called visibility (Thompson et al., 1986) (see Appendix C) which is related to the power spectrum. Some of the ongoing and future radio interferometers aimed at making a statistical detection of the 21cm signal are the 21 CentiMeter Array (21CMA, (Huang et al., 2016)), Giant Meterwave Radio Telescope (GMRT) (Paciga et al., 2013), Low Frequency Array (LOFAR) (van Haarlem et al., 2013), Murchison Widefield Array (MWA) (Tingay et al., 2013), Precision Array to Probe the Epoch of Reionization (PAPER) (Parsons et al., 2010), Hydrogen Epoch of Reionization (HERA) (DeBoer et al., 2017) and Square Kilometre Array (SKA) (Braun et al., 2015; Koopmans et al., 2014; Ahn et al., 2015). The limitation of using the power spectrum for 21 cm studies is that the field is highly non-Gaussian in nature (Cooray, 2005; Bharadwaj & Pandey, 2005). For a Gaussian field the power spectrum contains all the spatial information while no new information is obtained from higher order correlations. Therefore, one needs to resort to higher order fourier statistics, such as the bispectrum (Watkinson et al., 2017; Majumdar et al., 2018; Hutter et al., 2020) trispectrum (Cooray et al., 2008) or the phase space statistics (Gorce & Pritchard, 2019) to infer non-gaussian features of the 21cm signal. However, the challenge of going to higher and higher order is the decreased signal to noise ratio from future observational probes.

3. Topological measures : A topological measure of statistics describes patterns and shapes in the data. From the point of view of the 21cm obervations, the Square Kilometer array would be able to provide us with two dimensional images of the brightness temperature in real space. In real space, both the phase and amplitude information of a field is retained. On the other hand, power spectrum does not contain the phase information of the field (Watts et al., 2003; Matsubara, 2007) [12]. In order to obtain statistical properties of the 21cm images one can eiether study the usual one point statistics (Wyithe & Morales, 2007; Harker et al., 2009; Watkinson & Pritchard, 2014) or study the topology of real space field. The advantage of using topology based methods is that they would enable one to obtain information of all orders of correlation which is advantageous owing to the highly non-Gaussian nature of the 21cm brightness temperature field. Therefore, these tools would be complementary to the Fourier space measures described before. Some of

[12] A real valued field $f(r)$ can be expanded as a Fourier series:

$$f(r) = \sum \tilde{f}(k) e^{\iota k.r},$$

where $\tilde{f}(k) = |\tilde{f}(k)| e^{\iota \phi_k}$ is a complex number. The power spectrum of the field (appendix B.1) depends upon $|\tilde{f}(k)|^2$ i.e. the phase information is lost when we take the power spectrum.

the methods which have been employed so far for studying real space topology of 21cm brightness temperature are:

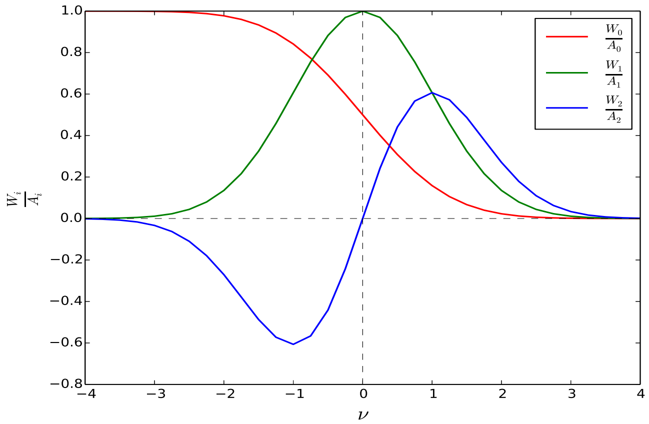

Fig. 1.2 The figure shows the variation of the scalar Minkowski functionals for a 2D Gaussian random field. Here W_0 is the area (*red*), W_1 is the contour length (*green*) and W_2 is the genus (*blue*). The SMFs in the plot have been scaled by the total area, A_0. The variation of SMFs with threshold for a Gaussian random field of a given mean and variance is the same while the amplitude depends upon the variance of the field (Schmalzing & Górski, 1998).

- Scalar Minkowski Functionals (SMFs): The scalar Minkowski functionals are defined for the excursion set [13] of a field. In n dimensions there are $n+1$ SMFs. The analytical forms for SMFs for a Gaussian random field are known (Fig. 1.2), therefore they can be used to quantify non-Gaussian deviations in a given field. They have been extensively used in cosmology to study the CMB and large scale structure topology (Gott III et al., 1990; Mecke et al., 1993; Schmalzing & Buchert, 1997; Schmalzing & Górski, 1998; Ganesan et al., 2015; Buchert et al., 2017). In two dimensions the SMFs are the contour length, area fraction and the genus of the excursion set. In the context of 21cm and EoR they have been widely explored. In (Lee et al., 2008) only the genus statistics for neutral regions was explored during the pre-overlap, overlap and post overlap phase of EoR. In (Hong et al., 2010; Wang et al., 2015), SMFs in 2D were studied by taking into account instrumental noise. In three dimensions there are four SMFs, the volume fraction, area, mean curvature

[13] Set of all points greater than or equal to the chosen value of field threshold.

and the Euler characteristic. In (Gleser et al., 2006) they studied the SMF for gas and neutral regions to study the progress of ionization. The deviation between the SMF for gas and neutral regions implies ionization. The effect of different fields on the brightness temperature fields was explored in (Yoshiura et al., 2017). They also explored pre-heating epoch and the effect of various models for EoR on the evolution of morphology. In (Chen et al., 2019) the various topological phases of the ionized field as reionization progresses were studied.

- Shapefinders : The shapefinders are derived from the SMFs described above and had been introduced to study the large scale structure topology (Sahni et al., 1998). Shapefinders give a measure of the filamentarity and planarity of structures. In the context of EoR they were used to study the topology of ionized regions in conjunction with largest cluster statistics (Bag et al., 2018, 2019) , where it was found that the largest ionized region around the time the ionized bubbles percolate is filamentary in shape.
- Persistent Homology : This deals with the study of Betti numbers (section 3.1.2) in terms of tunnels, cavities or connected components and their persistance (birth and death rates) (Pranav et al., 2019). In the context of EoR they have been used to study the various topological stages of ionized bubbles and identified two new stages post overlap of ionized bubbles (Elbers & Weygaert, 2019).

Some other methods are based on percolation theory (Furlanetto & Oh, 2016) and fractal dimension (Bandyopadhyay et al., 2017).

1.5 Aim of the thesis

A given topology based method should be able to condense maximum information in limited number of statistical measures while describing the physical processes which they encapsulate. In this thesis we explore one such measure, called the **Tensor Minkowski Functionals** (TMFs) which are a family of tensors and a generalization of the SMFs described above. Minkowski tensors provide anisotropy information over and above the size and shape information encoded in SMFs (Schröder-Turk et al., 2013; G E Schröder-Turk et al., 2010). The TMFs have been used to study the morphology of galaxies in (Rahman & Shandarin, 2003). For cosmological studies TMFs have been recently introduced to study the anisotropy in CMB data from Planck (Ganesan & Chingangbam, 2017; Joby et al., 2019) and CMB weak lensing (Goyal et al., 2020). They have also been used to study mock galaxy catalogues (Appleby et al., 2018a). For Gaussian random field the analytical forms for TMFs have been explored in (Chingangbam et al., 2017) and (Appleby et al., 2018b, 2019). We also use topological quantities called the *Betti numbers* which give information in terms of counts of structures. The 21cm maps are generated from the publicly available code 21cmFAST (Mesinger et al., 2011). We develop a statistical method using one of the Minkowski tensors called Contour Minkowski Tensor (CMT) and Betti numbers to infer the observable effect of various physical parameters of the EoR. We then analyse the capability of our statistics to predict constraints on model parameters and ionization history using SKA like interferometers. We find that CMT in combination with *Betti numbers* is complementary to the topological and Fourier space methods described in the previous section.

The thesis is organized as follows. A detailed description of 21cm cosmology and an overview of 21cmFAST is given in chapter 2. The definition and mathematical formulation of CMT and Betti numbers is given in chapter 3. As a first step towards our study, in chapter 4 a proof of concept of using our statistics to infer the sizes and shapes of ionized bubbles is explored on idealized 21cm simulations generated from 21cmFAST. We show how the ionization history can be inferred from the 21cm brightness temperature morphology in terms of ionized bubble sizes, shapes and counts. In chapter 5 we give a qualitative description of the morphology of the ionization field, density and spin temperature field under different ionization and heating scenarios. Therafter, we study the overall effect of varying the models on the 21cm brightness temperature morphology and show that one model can be distinguished from another. In chapter 6 we construct a mock 21cm map from SKA and explore the possibility of using our statistics to constrain model parameters of EoR and the ionization history of the universe. Chapter 7 describes some preliminary results obtained for TMFs in 3D as a starting stage for future work. All useful definitions, constants and formulae used in this thesis are described in Appendices at the end of this thesis and are referred wherever required.

2

21cm as a probe of the Epoch of Reionization

This chapter describes the physics of the radiative transfer of 21cm through the IGM from the Cosmic dawn to the Epoch of Reionization. The chapter begins with a description of 21cm transition in section 2.1. The transfer of radiation due to the 21cm transition, through the expanding universe is described in section 2.2. Section 2.3 describes 21cmFAST, the publicly available semi-numerical code (Mesinger et al., 2011) used for simulating the cosmological 21cm signal in this thesis. The basic definitions and fundamentals of radiative transfer physics is described in appendix A.

2.1 21cm transition of the neutral hydrogen atom

The electron and the proton possess intrinsic spin angular momentum **S** and **I** respectively. In the ground state (n=1) of neutral hydrogen atom the orbital angular momentum of the electron, **L** is zero. Therefore the total angular momentum of the hydrogen atom is **F**= **S**+**I**. The electron and proton spins can be either parallel or antiparallel to each other. The magnitude of both **S** and **I** is equal to $\frac{h}{2\pi}$. Therefore, **F** can take values 0 (antiparallel) or 1 (parallel). The anti parallel configuration has lower energy as compared to the parallel configuration. The energy difference between the $1_1S_{1/2}$ ($\mathbf{F}=1$) and $1_0S_{1/2}$ ($\mathbf{F}=0$)[1] states is given by 5.9×10^{-6} eV which corresponds to a wavelength of 21.1061 cm or a frequency of $\nu_{21}=1420.4057$ MHz (Bradt, 2008).

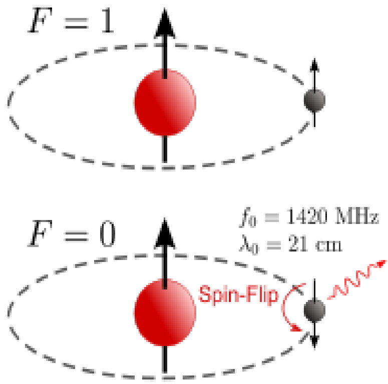

Fig. 2.1 The 21cm spin flip transition of the neutral hydrogen atom. The arrows denote the directions of the spins of nucleus and electron. (*Image credit*: Wikipedia.org)

The energy splitting arises due to the interaction between the electron and proton magnetic dipole moments. In the presence of a magnetic field, the $F=1$ state is further split into three components and is therefore called a triplet while the $F=0$ state is called a singlet.

2.2 The 21cm radiation in an expanding universe

If we have a two level system in thermodynamic equilibrium at a temperature T, then the ratio of the population between the two levels is given by the Boltzmann's law:

$$\frac{g_0n_1}{g_1n_0}=exp(-h\nu_{21}/k_BT), \tag{2.1}$$

where $n_{(1,0)}$ is the population of the respective levels and $g_{(1,0)}$ is the degeneracy of the states. If the system is not in equilibrium, then one can define a temperature called spin temperature T_S, which describes the relative population in the two levels. It is the temperature of the equilibrium

[1]The notation used is $_FL_J$, where L is the orbital angular momentum of the electron, J is the total angular momentum of the electron and F is the total angular momentum of the atom. Note that as described in section 2.1 $J=S$ for electron in the ground state of neutral hydrogen.

system with the same population ratio and is defined as follows:

$$\frac{g_0 n_1}{g_1 n_0} = exp(-h\nu_{21}/k_B T_S), \tag{2.2}$$

where n_0 and n_1 are the number densities in the upper and lower energy states respectively. If we consider that $T_s \sim T_K$, the gas kinetic temperature (which is of the order of 1000 mK or higher), then since $g_1/g_0 = 3$ for neutral hydrogen and $T_* = h\nu_{21}/k_b = 68\ mK$, the right hand side of eq. 2.2 would almost be unity and $n_1 \simeq 3/4\ n_{HI}$, where n_{HI} is the total number density of neutral hydrogen. Therefore a measure of the 21 *cm emission* gives an approximate measure of n_{HI} because a considerable fraction is in the n_1 level.

The absorption coefficient can be written using eq. A.26:

$$\alpha_\nu = \frac{c^2}{8\pi\nu_{21}^2}\frac{g_1}{g_0} n_0 A_{21}(1 - exp^{-h\nu_{21}/k_B T_S})\phi(\nu). \tag{2.3}$$

For the 21cm transition, $h\nu_{21}/k_B \ll T_S$, even when the gas is cooler than the CMB temperature and the transition is observed in absorption. Therefore, $exp^{-h\nu_{21}/k_B T_S} \sim 1 - h\nu_{21}/k_B T_S$. Since $g_1/g_0 = 3$, using this approximation on eq. 2.2 gives $n_0 \simeq n_{HI}/4$. Using the same approximation on eq. 2.3 the absorption coefficient for the 21cm transition can be written as (Field, 1958):

$$\alpha_\nu \sim \frac{3c^2}{32\pi\nu_{21}^2} n_{HI} A_{21} \frac{h\nu_{21}}{kT_S}\phi(\nu). \tag{2.4}$$

2.2.1 The optical depth of 21cm line

The optical depth of the 21cm line is confined to a very specific redshift because the transition is a very narrow transition. Therefore, $\phi(\nu) = \delta_D[\nu_{21} - (1+z')\nu]$, where ν is the observed frequency and z' is the redshift of the emitter which is very near the redshift z of observation. In the argument of the delta function above, ν_{21} is the central frequency of the broadened profile in the emitter frame and ν is the observed frequency which is fixed. Therefore, $\nu_{21} = \nu(1+z)$ and $\phi(\nu) = (1+z')/\nu_{21}\ \delta_D(z-z')$. In order to calculate the optical depth for 21cm transition through a path length spanning across a redshift range, substitute eq. 2.4 in eq. A.7 and the above form of the line profile function, $\phi(\nu)$ to obtain:

$$\tau_\nu = \int \frac{3c^2}{32\pi\nu_{21}^2} n_{HI} A_{21} \frac{h\nu_{21}}{kT_S} \frac{(1+z')}{\nu_{21}} \delta(z-z') \frac{ds}{dz'} dz' \tag{2.5}$$

$$= \frac{3c^2}{32\pi\nu_{21}^2} n_{HI} A_{21} \frac{h\nu_{21}}{kT_S} \frac{(1+z)}{\nu_{21}} \frac{ds}{dz}. \tag{2.6}$$

Since the primordial abundance of hydrogen is ~ 0.75 of the total baryonic abundance in terms of mass, the neutral hydrogen number density is given by $n_{HI} \sim 0.75 \times x_{HI} n_B$, where n_b is the total baryon number density, such that $n_b = \rho_b / m_H$. Assuming that baryon overdensity follows the total matter overdensity, $\rho_b = (1+\delta)\overline{\rho}_b$ where δ is the matter over density given by $\delta = (\rho - \overline{\rho})/\overline{\rho}$. Therefore, in terms of Ω_b the neutral hydrogen number density can be written as:

$$n_{HI} = 0.75 \times x_{HI}(1+\delta)\frac{\Omega_b}{m_H}\rho_c(1+z)^3 \tag{2.7}$$

$$= 0.75 \times x_{HI}(1+\delta)\frac{\Omega_b}{m_H}\frac{3H_0^2}{8\pi G}(1+z)^3, \tag{2.8}$$

and the proper length per redshift:

$$\frac{ds}{dz} = \frac{c}{H_0(1+z)\left[\Omega_m(1+z)^3 + \Omega_k(1+z)^2 + \Omega_\Lambda\right]^{1/2}}. \tag{2.9}$$

In a matter dominated universe, the proper length per redshift is:

$$\frac{ds}{dz} = \frac{c}{H_0 \Omega_m^{1/2}}(1+z)^{-5/2}. \tag{2.10}$$

Therefore the optical depth after substituting eq. 2.8 and 2.9 in eq. 2.10 is:

$$\tau_\nu = \frac{3c^3}{32\pi\nu_{21}^3}\frac{0.75}{m_H}\frac{3}{8\pi G}A_{21}\frac{h\nu_{21}}{k_b}\left(\frac{H_0\Omega_b}{\Omega_m^{1/2}}\right)\frac{x_{HI}(1+\delta)}{T_S}(1+z)^{3/2}. \tag{2.11}$$

2.2.2 The 21cm brightness temperature

The radiative transfer equation can be written in terms of the brightness temperature for the case of a neutral hydrogen cloud capable of a 21cm transition, over a background of cosmic microwave background radiation of temperature T_{CMB}, using the radiative transfer equation, eq. A.17, as:

$$T_b(\nu_o) = T_{CMB}e^{-\tau_\nu} + T_S(1 - e^{-\tau_\nu}), \tag{2.12}$$

where ν_o is the observed frequency. Therefore, the differential brightness temperature, obtained by subtracting the CMB in the background, for 21cm transition is obtained as:

$$\delta T_b(\nu_o) \simeq (T_S - T_{CMB})\tau_\nu. \tag{2.13}$$

In an expanding universe, the brightness is conserved as:

$$I_\nu(0) = \frac{I_\nu(z)}{(1+z)^3}.$$

$$\implies T_b(\nu_{21})\nu_{21}^2 = \frac{T_b(\nu_o)\nu_o^2}{(1+z)^3} = \frac{T_b(\nu_o)\nu_{21}^2}{(1+z)}$$

$$\implies T_b(\nu_{21}) \times (1+z) = T_b(\nu_o),$$

where the definition of the brightness temperature in terms of intensity is used from eq. A.15

Here, $T_b(\nu_o)$ is the brightness temperature in the observer's frame at $z = 0$. Therefore, one can recast eq. 2.13 in terms of brightness temperature values in the emitter frame on the right hand side and observed brightness temperature value on the left hand side by dividing right hand side of the equation by $(1+z)$. Thus the differential 21cm brightness temperature at an observed frequency ν_o, corresponding to a redshift z in a matter dominated universe is given by (Zaroubi, 2012; Pritchard & Loeb, 2012):

$$\delta T_b(\nu_o) \sim 26.7\ mK(1+z)^{1/2} x_{HI}(1+\delta)\left(1 - \frac{T_{CMB}}{T_S}\right). \tag{2.14}$$

The cosmological parameters used in this equation are defined in appendix (E.1).

2.2.3 The spin temperature evolution

The value of T_S describes the relative populations in the two hyperfine levels of neutral hydrogen. Any physical processes in the evolving IGM in the early universe will determine this relative population and therefore the value of T_S. The value of the Einstein's coefficient A_{21} for the 21cm transition is $2.85 \times 10^{-15}\ s^{-1}$. This corresponds to a lifetime of 1.1×10^7 years for the triplet ($n = 1$) state. The small value of A_{21} coupled with the small energy difference between the two levels of the transition ($h\nu_{21}/k \equiv T_* = 68.1\ mK$) makes collisional excitation and de-excitation important processes, besides radiative processes, to establish the population of the two levels. So essentially there are two mechanisms for establishing the population, low energy collisions and radiation. If a hydrogen cloud was isolated and in equilibrium, then the value of T_S would be the physical temperature of the cloud, as inferred from the usual Boltzmann distribution. However, the hydrogen clouds in the IGM would not be in equilibrium but would reside in an environment where they would receive radiation from their surroundings and re-radiate into the IGM. Then, using the rates of transition per atom, due to the various processes one can use the principle of detailed balance to obtain the steady state population of the two levels.

The only known radio backgound corresponding to the observed frequencies for the 21cm radiation from the early universe, would be the cosmic microwave background (CMB) with a brightness temperature, T_{CMB}. There are three different processes which establish the value of the spin temperature, T_S as the IGM evolves in the early universe (Field, 1958; Pritchard & Loeb, 2012):

1. Absorption and simulated emission of CMB photons: This is the same as the radiative transfer for a 2-level system described in section A.5, with the background radiation, I_γ being the CMB. Therefore, the rate of upward transition is $B_{01}\, I_\gamma = 3\frac{T_{CMB}}{T_*}$ and the rate of total downward transition is $B_{10}\, I_\gamma + A_{10} = \left(1 + \frac{T_{CMB}}{T_*}\right) A_{10}$, (using eq. A.24 and A.15). Therefore the ratio of the rate of upward (P^R_{01}) to downward (P^R_{10}) transition due to CMB can be written as:

$$\frac{P^R_{01}}{P^R_{10}} \simeq 3\left(1 - \frac{T_*}{T_{CMB}}\right), \tag{2.15}$$

   because $T_{CMB} \gg T_*$.

2. Collisions with other hydrogen atoms, electrons and protons: This process will dominate when the density of the gas is high. The rate of collisional transitions denoted by P^C depends upon the number density n_i of the colliding species i and some function of the kinetic temperature T_K, of the system. Therefore, the ratio of rates of upward to downward transition due to collisions is the same as in thermal equilibrium:

$$\frac{P^C_{01}}{P^C_{10}} = 3\, exp(-T_*/T_K) \simeq 3\left(1 - \frac{T_*}{T_K}\right). \tag{2.16}$$

3. Scattering of UV photons: This takes place when a Ly-α photon excites a hydrogen atom in the ground state $(n = 1)$ from a triplet/singlet state, to an $n = 2$ state and the atom relaxes back to a spin flipped state which is different from the starting hyperfine level. This process is called the Wouthuysen-Field (WF) effect (Wouthuysen, 1952; Field, 1959). The mechanism is briefly described in Fig. 2.2.

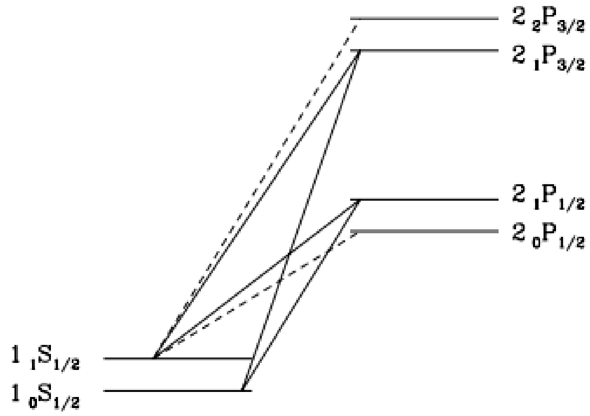

Fig. 2.2 The figure describes the WF-effect between the 1S (n=1, L=1) and 2P (n=2, L=2) levels of the neutral hydrogen atom. From the electric dipole selection rules the only allowed transitions are $\Delta F = 0, 1$ except $F = 0 \rightarrow 0$. Therefore of the six allowed transitions, only four contribute to mixing the ground state hyperfine levels. These shown in solid lines in the figure. (*Image credit: (Loeb & Furlanetto, 2013)*)

The ratio of upward to downward transition due to the WF-effect is given by:

$$\frac{P_{01}^{L}}{P_{10}^{L}} = 3\left(1 - \frac{T_C}{T_K}\right) \tag{2.17}$$

Here T_C is the color temperature of the Ly-α profile radiation field. Repeated scatterings of the Ly-α photons by HI atoms leads to, $T_C \simeq T_K$.

Since the time scales of the above processes to establish thermal equilibrium are much shorter than the age of the universe, one can assume that the rate of upward transition is the same as the rate of downward transition:

$$n_1(P_{10}^{R} + P_{10}^{C} + P_{10}^{L}) = n_0(P_{01}^{R} + P_{01}^{C} + P_{01}^{L}). \tag{2.18}$$

Writing $P_{10}^{R} = \left(1 + \frac{T_{CMB}}{T_*}\right) A_{10}$ and using the fact that $T_{CMB} \gg T_*$ one can rewrite the above equation as:

$$\frac{n_1}{n_0} \approx 3\left(1 - \frac{T_*}{T_S}\right) = 3\frac{\frac{T_{CMB}}{T_*}A_{10} + \left(1 - \frac{T_*}{T_K}\right)P_{10}^{C} + \left(1 - \frac{T_*}{T_C}\right)P_{10}^{L}}{A_{10}\left(1 + \frac{T_{CMB}}{T_*}\right) + P_{10}^{C} + P_{10}^{L}}. \tag{2.19}$$

The above form is obtained by using eq. 2.15, 2.16 and (2.17). Again using the fact that $T_{CMB} \gg T_*$, the above equation becomes:

$$\begin{aligned}\frac{n_1}{n_0} &\approx 3\left(1 - \frac{T_*}{T_{CMB}}\right)\left[\frac{1 + \left(1 - \frac{T_*}{T_K}\right)\frac{P_{10}^{C}T_*}{A_{10}T_{CMB}} + \left(1 - \frac{T_*}{T_C}\right)\frac{P_{10}^{L}T_*}{A_{10}T_{CMB}}}{1 + \frac{P_{10}^{C}T_*}{A_{10}T_{CMB}}\left(1 - \frac{T_*}{T_{CMB}}\right) + \frac{P_{10}^{L}T_*}{A_{10}T_{CMB}}\left(1 - \frac{T_*}{T_{CMB}}\right)}\right] \\ &= 3\left[\frac{\left(1 - \frac{T_*}{T_{CMB}}\right) + \left(1 - \frac{T_*}{T_K}\right)\frac{P_{10}^{C}T_*}{A_{10}T_{CMB}} + \left(1 - \frac{T_*}{T_C}\right)\frac{P_{10}^{L}T_*}{A_{10}T_{CMB}}}{1 + \frac{P_{10}^{C}T_*}{A_{10}T_{CMB}} + \frac{P_{10}^{L}T_*}{A_{10}T_{CMB}}}\right].\end{aligned} \tag{2.20}$$

The coupling constant for collisions is defined as, $x_c \equiv \frac{P_{10}^{C}T_*}{A_{10}T_{CMB}}$ and the coupling constant for Ly-α via the WF-effect is, $x_\alpha \equiv \frac{P_{10}^{L}T_*}{A_{10}T_{CMB}}$. The expression for T_S after rearranging the above equation, is obtained to be (Field, 1958; Pritchard & Loeb, 2012):

$$T_S^{-1} = \frac{T_{CMB}^{-1} + x_c T_K^{-1} + x_\alpha T_c^{-1}}{1 + x_c + x_\alpha}. \tag{2.21}$$

Therefore the evolution of the spin temperature in an expanding universe will be determined by the evolution of the CMB temperature, T_{CMB} the kinetic temperature, T_K (considering that $T_C \rightarrow T_K$) and the two coupling constants, x_C and x_α. Below, I briefly describe the physics affecting these parameters before I elaborate upon how they affect the overall evolution of the brightness temperature in an expanding universe:

- **Collisional Coupling Constant x_c:** For a particular species i, the collisional constant is given by

$$x_C^i = \frac{P_{10}^C T_*}{A_{10} T_{CMB}} \equiv \frac{n_i \kappa_{10}^i T_*}{A_{10} T_{CMB}}, \tag{2.22}$$

where κ_{10}^i is the rate coefficient for spin de-excitation in collisions with that particular species. The species i present during those epochs are protons, electrons and other hydrogen atoms. From the quantum mechanical cross-sections of these collisions, the H-H collisions have lower cross sections, but still they dominate over collisions because the abundance of hydrogen atoms is much higher than other species and the ionized fractions are lower at high redshifts . The e-H collisions can become important in ionized gas (Furlanetto & Furlanetto, 2006). Overall the collisional coupling is weak unless the gas is very dense.

- **Ly-α Coupling Constant x_α:** This coupling mechanism occurs due to the *Wouthuysen-Field Mechanism*, as described before. The value of x_α will depend upon the rate of scattering of Ly-α photons within the gas and is given by (Madau et al., 1997):

$$P_\alpha = 4\,\pi \sigma_0 \int d\nu J_\nu(\nu) \phi_\alpha(\nu). \tag{2.23}$$

In the above equation, σ_0 is the absorption cross section of Ly-α photon and $\phi_\alpha(\nu)$ is the line profile of this absorption and J_ν is the specific intensity I_ν averaged over the total solid angle. The total scattering rate , P_α is related to the de-excitation rate for the hyperfine ground state levels, P_{10}^L as (Loeb & Furlanetto, 2013) :

$$P_{10}^L = \frac{4}{27} P_\alpha. \tag{2.24}$$

Therefore the Ly-α coupling constant can be written as (Pritchard & Furlanetto, 2006):

$$x_\alpha = \frac{4\,P_\alpha\,T_*}{27\,A_{10}\,T_{CMB}}. \tag{2.25}$$

The only required, unkown quantity to estimate x_α is the Ly-α background. It is an astrophysical quantity and modelled by semi-analytical and numerical techniques. In future sections I will describe one such semi- analytical technique used in the publicly available simulation code used to obtain results in this thesis.

- **The effective color temperature of UV radiation field T_c:** This is the temperature of the black body having the same gradient as the gradient of the line about a central frequency ν (see appendix (A.3) for details). It is expected that Ly-α coupling will depend upon the gradient of the background about the Ly-α resonance because of the spread in energy across the hyperfine levels. In an extremely optically thick medium ($\tau \gg 1$), repeated scatterings cause atomic recoils making the profile same as the profile of a black body. Since this condition is always met in the IGM we have $T_c \simeq T_K$ (Wouthuysen, 1952; Field, 1959).

- **The gas kinetic temperature T_K:** The evolution of T_K can be inferred from the first law of thermodynamics:

$$dU = dW + dQ = -PdV + dQ \tag{2.26}$$

Effect of adiabatic expansion : Since the universe expands adiabatically, in a post recombination regime and in the absence of any direct heat exchange between the CMB and the neutral hydrogen atoms, $dQ = 0$. The primordial neutral hydrogen atoms behave like an ideal gas at a temperature T_K. Therefore the internal energy is $dU = \frac{3}{2} N_{HI} k_B dT_K$ and $dW = -PdV = -n_{HI} k_B T_K dV$ (using $PV = Nk_bT$). Thus, for a constant number of hydrogen atoms, eq. 2.26 gives:

$$\frac{3}{2}\frac{dT_K}{T_K} = \frac{dn_{HI}}{n_{HI}}. \tag{2.27}$$

This implies, $T_K^3 \propto n_{HI}^2$. Due to expansion of the universe, $n_{HI} \propto (1+z)^3$. Therefore, due to adiabatic expansion of the universe the variation of the kinetic temperature is given by, $T_K \propto (1+z)^2$. Other than the effect of expansion of the universe there will be other mechanisms which will influence the evolution of the kinetic temperature of the neutral hydrogen in the IGM.

As mentioned in section 1.2, the IGM after recombination is not fullly ionized, but has a residual fractional ionization, $x_e = n_e/n_H$. The evolution of x_e in a comoving frame is given by:

$$\frac{dx_e(\mathbf{x}, z')}{dz'} = \frac{dt}{dz'}[\Lambda_{ion} - \alpha_A C x_e^2 n_b f_H]. \tag{2.28}$$

The above equation describes the two competing processes of ionization (first term) and recombination (second term) which determine the evolution of x_e. The ionization rate per baryon is described by Λ_{ion}, α_A is the case A recombination coefficient (see footnote 8), $C \equiv \langle n^2 \rangle / \langle n \rangle^2$ is the clumping factor and f_H is the fraction of hydrogen (both in ionized and neutral form). Note that n_b is the number density of baryons which is not in comoving coordinates. The total number of baryons for a gas containing both neutral and ionized hydrogen is given by $N_b = N_{HI} + N_p + N_e = (1 + x_e)N_H$. Therefore,

$$U = \frac{3}{2}(1 + x_e)N_H k_B T_K,$$

which implies:

$$dU = \frac{3}{2}N_H(1 + x_e)k_B dT_K + \frac{3}{2}N_H k_B T_K dx_e.$$

Similarly,

$$dW = -PdV = \frac{N_H(1 + x_e)}{V}k_B T_K dV = \frac{N_H(1 + x_e)}{n_b}k_B T_K dn_b.$$

There will be different heating processes which will determine dQ.

The full equation of evolution for T_K after substituting in eq. 2.26 is written as:

$$\frac{dT_K(\mathbf{x}, z')}{dz'} = \frac{2}{3k_B(1 + x_e)}\frac{dt'}{dz'}\sum_p \varepsilon_p + \frac{2T_K}{3n_b}\frac{dn_b}{dz'} - \frac{T_K}{1 + x_e}\frac{dx_e}{dz'}. \tag{2.29}$$

In the above equation, the first term describes the heat input encoded in, $\varepsilon_p(\mathbf{x}, z')$ which is the heating rate per baryon for a process p. The second term describes the evolution of T_k due to the expansion of the universe and the third term describes the change in the number of gas particles when it is ionized. There are two major heating processes which determine ε_p before and after the cosmic dawn:

1. *Before Cosmic dawn*: Before the first luminous sources begin to form, the neutral hydrogen atoms interact with the CMB photons via the relic electrons. The Compton scattering between CMB photons and the residual electrons sets $T_K = T_{CMB}$. The

Compton heating rate is given by (Seager et al., 1999):

$$\frac{2}{3k_b(1+x_e)}\varepsilon_{comp} = \frac{x_e}{1+f_{He}+x_e}\frac{8\sigma_T u_\gamma}{3m_e c}(T_\gamma - T_K). \tag{2.30}$$

The thermal temperature, T_K remains coupled with the T_{CMB}, until x_e becomes very small. It finally decouples at a redshift of $z_{dec} \simeq 137(\Omega_b h^2/0.022)^{0.4} - 1$ (Peebles, 1993). Once the gas thermally decouples from the CMB, the first term in eq. 2.29 is almost negligible as there is no other source for heating the IGM. In the absence of any ionizing source, the evolution of x_e in eq. 2.29 is also small. Therefore after decoupling T_K evolves adiabatically as $T_K \propto (1+z)^2$.

2. *After Cosmic dawn*: Once the first luminous objects form, they emit radiation which ionizes and heats the IGM. The most important mechanism of heating of the IGM during these epochs is via secondary ionizations due to X-ray emission from the first sources of light (Shull, 1979). The evolution of T_K due to X-rays requires one to model these first sources (Furlanetto & Stoever, 2010; Venkatesan et al., 2001). One requires semi-analytical or numerical simulations to model these sources. In section 2.3, I will describe the modelling of X-ray sources as incorporated in the publicly available code, 21cmFAST.

2.2.4 Expected evolution of the 21cm brightness temperature

As mentioned earlier, from eq. 2.14, the evolution of the brightness temperature with redshift, z depends upon the evolution of the neutral hydrogen fraction, x_{HI} , the matter overdensity δ and the relative evolution of T_{CMB} and T_S. Further, the evolution of T_S depends upon the evolution of T_K, T_{CMB} and the coupling constants x_c and x_α. Therefore, the timeline for expected evolution of δT_b with redshift can be described as follows (Mesinger et al., 2011; Furlanetto, 2006):

1. Dominance of Collisions: $\mathbf{T_S \simeq T_K \leq T_{CMB}}$

   At very high redshifts due to absence of any ionizing sources, hydrogen is almost neutral and therefore $x_{HI} \simeq 1$. Moreover, the matter overdensities are still linear , $\delta \ll 1$. Since the first luminous sources have not yet appeared, there are no Ly-α photons and therefore $x_\alpha = 0$.

   Thus until the epoch of thermal decoupling at $z \simeq z_{dec}$, $T_K \simeq T_{CMB}$ and from eq. 2.21, $T_S \simeq T_K \simeq T_{CMB}$. As a consequence, from eq. 2.14, $\delta T_b \simeq 0$, ie. there is no signal in emission or absorption from these epochs.

   After thermal decoupling T_K evolves adiabatically, but because the universe is very dense, the probability of collisions is very high and therefore x_C is large. So, while T_K decouples from T_{CMB}, T_S remains coupled to T_K and follows the adiabatic cooling of the gas. Since, T_K cools faster than CMB post thermal decoupling, $T_S < T_{CMB}$. Therefore, $\delta T_b < 0$ and is seen in absorption. Since collisional coupling is very efficient during these epochs, the fluctuations in δT_b would be dominated by those in the density field, δ.

2. Collisional Decoupling: $\mathbf{T_S \simeq T_{CMB} > T_K}$

   The universe is still in the regime before the formation of the first luminous sources. As the universe expands the probability of collisions decreases until x_C becomes less effective in coupling T_S to T_k. Therefore from eq. 2.21 T_S begins to approach the T_{CMB}. If the first luminous sources appear before collisions become ineffective, this transition may not appear.

3. Ly-α Coupling : $\mathbf{T_S \simeq T_K < T_{CMB}}$

   As the first sources begin to appear the WF-coupling becomes efficient. The WF effect couples T_S to T_K. Since it is easier for Ly-α coupling to occur than heating of the gas, T_S begins to follow T_K, which is cooling adiabatically. This makes δT_b even more negative. Higher density regions are more strongly coupled than lower density voids where the coupling is still weak.

4. X-ray Heating : $\mathbf{T_S \leq T_{CMB} \rightarrow T_S > T_{CMB}}$

   As Ly-α coupling begins to saturate and T_S becomes comparable to T_K in most of the IGM, T_S reaches a minimum value and then begins to increase. The highest density regions now host the X-ray sources which heat up the IGM surrounsing them, while regions far away are still cold and uniformly cooling.

   Soon the X-rays permeate most of the IGM and raise the temperature of regions near the sources to $T_S = T_K > T_{CMB}$, while regions away from the sources still have $T_S = T_K < T_{CMB}$. Slowly the entire IGM is heated above T_{CMB}. Therefore, δT_b becomes positive and is seen in emission.

5. Reionization: As X-rays have mean free path higher than the ionizing UV-radiation, the effect of ionization follows X-ray heating. As X-rays have heated the IGM much above the CMB temperature, $T_{CMB} \ll T_S$ makes δT_b insensitive to T_s and δT_b reaches the peak of emission. The further evolution of δT_b depends upon the evolution of $x_{HI}(1+\delta)$. As the universe begins to ionize, x_{HI} decreases and the δT_b signal starts decreasing until the entire universe is ionized and there is no further 21cm signal, i.e. $\delta T_b = 0$.

2.3 An overview of the semi-numerical public code 21cm-FAST

As described in the previous subsection, a complete picture of the evolution of the 21cm brightness temperature, would require one to model astrophysical sources over a range of redshifts for a given cosmology. In order to model the EoR, one would require modelling astrophysical objects and their detailed radiative transfer through the IGM. Such a modelling would require a huge parameter space, most of which is unknown due to the lack of any direct observations of the luminous objects during EoR. An accurate way to model EoR would be to perform N-body and full radiative transfer simulations over a range of redshifts. However, such simulations are computationally expensive owing to the large dynamic range. Therefore, most cosmological studies resort to less extensive semi-numerical simulations. Most upcoming and current interferometers capable of detecting the 21cm would have an effective resolution much lower than the resolution of a typical radiative transfer simulation. Due to this reason, semi-numerical techniques provide a good compromise between computational speed and resolution that is within the reach of upcoming radio experiments to detect the 21cm fluctuations.
For the purpose of this thesis, the brightness temperature has been simulated using the publicly available code 21cmFAST (Mesinger et al., 2011). The code generates the density, ionization and spin temperature at every pixel, using semi numerical techniques. I briefly describe below, the various techniques that the code uses to generate the brightness temperature in a comoving box (see appendix (E) for definition of comoving coordinate system) of volume $L^3 = V$ divided into N^3 regular grid points.

1. **Density field**:

   (a) *The initial conditions*: The initial conditions for the density field of the universe, $\delta(\mathbf{x})$ is represented as a Gaussian random field and can therefore be completely described by the power spectrum, $P(\mathbf{k})$ (defined in appendix(B)), where $\delta(\mathbf{k})$ is the fourier transform of $\delta(\mathbf{x})$. The initial conditions are generated by populating the grid in k-space with the fourier transform of the density field, as:

   $$\delta(\mathbf{k}) = \sqrt{\frac{V\ P(\mathbf{k})}{2}}(a_k + ib_k),$$

   where a_k and b_k are Gaussian random numbers.

   (b) *Evolved Density and velocity field:* The evolved density field is generated using the standard Zel'dovich approximation (Zel'Dovich, 1970) which is an extrapolation of the linear Lagrangian perturbation theory (LPT) to the non-linear regime (see Appendix B.5). The particle position is described by $x = x_1 + \psi(x_1)$, where x_1 is the initial, x is the updated coordinate and ψ is the displacement from it's initial position. On differentiating with respect to time, one can obtain the velocity $v = d\psi/dt$. In LPT the motion of the particle is described in terms of the dynamical variable ψ, which is related to the density as $\delta(\mathbf{x_1}) = -\nabla\psi(\mathbf{x_1})$. Therefore the code calculates $\psi(\mathbf{x_1})$, to obtain the density field at x_1. After generating the initial conditions as above, the velocity field at a redshift z is generated in k-space:

$$\mathbf{v}(k,z) = \frac{i\mathbf{k}}{k^2}\dot{D}(z)\delta(\mathbf{k}),$$

where $D(z)$ is the growth factor. It's inverse Fourier transform is $v(\mathbf{x_1}, z) = \dot{D}(z)v_x(\mathbf{x})$ (where v_x is the inverse Fourier transform of $\frac{i\mathbf{k}}{k^2}$). Therefore the LPT provides ease of separation of temporal and spatial variables and hence saves computational cost. An integration of the velocity v over time will allow one to calculate the dynamical variable as, $\psi(\mathbf{x_1}) = D(z)v_x(\mathbf{x_1})$. This is then used to evaluate the value of the evolved density δ at a given point $\mathbf{x_1}$ and redshift z. For the redshifts under study, the densities are mildly non-linear and still in a regime where Zel'dovich approximation suffices to describe the density field of the universe.

2. **Ionization field**: The ionization field is based on the excursion set formalism for modelling reionization, pioneered by (Furlanetto et al., 2004a). The semi-analytic model is based on the ansatz that a collapsed halo of mass M_h can ionize a region of mass $M(R)$:

$$M(R) = \zeta M_h \tag{2.31}$$

Here, ζ is an efficiency factor which describes the number of ionizing photons per unit baryon that escape the halo. It depends upon uncertain source properties [2]. The advantage of using such an ansatz is that since the size of an ionized region depends only upon the halo mass, one can obtain a fair representation of EoR using the global parameter ζ, rather than any detailed radiative transfer simulations. However, if one has clustering or sub-structure in halos then it is difficult to model ionized regions in this way around

[2]The factor can be described in terms of other globally defined parameters and is usually written as:

$$\zeta = f_{esc} f_* N_\gamma m_p,$$

where N_γ is the number of ionizing photons per unit mass in stars, f_* is the fraction of total mass inside the halo which is converted into stars and f_{esc} is the fraction of photons that escape the halo.

individual sources. Therefore, one considers *self ionized regions*, which is essentially a region of size R, within which all of the hydrogen is ionized. For such a region, the number of photons produced by all haloes within this region must be greater then the number of neutral hydrogen atoms inside this region (which may or may not be inside collapsed halos). Therefore,

$$N_\gamma \geq N_{HI}, \tag{2.32}$$

One can write $N_\gamma = \zeta N_{HI}^{coll}$, where N_{HI}^{coll} is the number of neutral hydrogen atoms inside collapsed objects. Therefore, the above condition becomes:

$$f_{coll}(\mathbf{x}, z, R) \geq \zeta^{-1}, \tag{2.33}$$

where f_{coll} is the collapsed fraction and can be written as:

$$f_{coll}(\mathbf{x}, z, R) = \frac{1}{\bar{\rho}_m} \int_{M_{min}}^{\infty} dM\, M\, \frac{dn}{dM}. \tag{2.34}$$

Not all halos would be capable of hosting an ionizing source and hence there is a minimum cut-off mass of the halos which we denote by M_{min}. It is usually taken to be the mass corresponding to the M_{vir} for which the corresponding T_{vir} is the temperature above which atomic or molecular hydrogen cooling can occur. This is by assuming that T_{vir} is the same as the temperature of baryonic gas inside that halo, because initially the gas will follow the dark matter and get shock heated to the virial temperature of the halo. Therefore, using the Press-Schecter ansatz and the extended Press-Schecter model (Press & Schechter, 1974), the collapse fraction f_{coll} can be written in terms of the overdensities (see appendix B for details). Since, the collapsed fraction here is being calculated within the region of size R instead of the entire cosmological volume, the problem reduces to that of conditional Press-Schecter model (Bond et al., 1991a; Lacey & Cole, 1993) where only the trajectories which pass through (σ_R^2, δ_R) in the $\delta - \sigma^2$ plane are considered (Appendix B.4). Thus, using eq. B.11 and B.15, one can write the collapsed fraction in eq. 2.34 as:

$$f_{coll}(\mathbf{x}, z, R) = erfc\left[\frac{\delta_{crit}(z) - \delta_R(\mathbf{x}, z)}{\sqrt{2\left[\sigma_{M_{min}}^2 - \sigma_R^2\right]}}\right]. \tag{2.35}$$

Thus the condition in eq. 2.33 reduces to a condition on the overdensity at a scale R:

$$\delta_R \geq \delta_{crit}(z) - \sqrt{2}\, erf^{-1}(1-\zeta)\ \left[\sigma^2_{M_{min}} - \sigma^2_R\right]^{1/2}. \tag{2.36}$$

In 21cmFAST, an ionization field is constructed by smoothing the evolved density field around a central pixel, at some initial scale $R = R_{mfp}$ [3]. The scale is then progressively decreased to smaller values. At every step, the f_{coll} corresponding to that scale is calculated and the condition in eq. 2.33 is checked. If the condition is satisfied at a certain R step, then the central pixel is marked as fully ionized (i.e. $x_{HI} = 0$) and it performs the same steps at the next pixel. If the condition is not satified then the smoothing is carried out at the next smoothing scale around the central pixel, until the condition is met. If the condition is not satisfied till the last smoothing step, the pixel is given a neutral fraction value $x_{HI} = \zeta f_{coll}$, which is a partially ionized pixel.

So far this formalism assumed that ionization would win over recombination within a region where the number of photons is greater than or equal to the number of neutral hydrogen atoms irrespective of the clumpiness of the region. However, in actual the rate of recombination is not homogenous but depends upon the density of the region, with higher density regions undergoing more number of recombinations. The effect of recombinations is to slow down reionization (Miralda-Escudé et al., 2000). If the effect of inhomogenous recombination is included then the condition in eq. 2.33 becomes:

$$f_{coll}(\mathbf{x}, z, R) \geq \zeta^{-1}(1 + n_{rec}(\mathbf{x}, z, R)). \tag{2.37}$$

The additional second term is the number of recombinations and accounts for the extra photons required per recombination. In 21cmFAST, it is modelled according to the cell's ionization history and density (Sobacchi & Mesinger, 2014).

3. **Spin temperature**: The code incorporates spin temperature using semi-analytical models similar to (Furlanetto & Stoever, 2010). As described in section 2.2.3, the code must model x_C, x_α and T_K. This is briefly described below:

   (a) x_C : the collisional coupling constant is written as:

$$x_C = \frac{0.0628}{A_{10} T_{CMB}} \left[n_{HI} \kappa^{HH}_{1-0}(T_K) + n_e \kappa^{eH}_{1-0}(T_K) + n_p \kappa^{pH}_{1-0}(T_K) \right],$$

[3] Usually the largest scale is chosen to be the mean free path of photons towards the end of reionization.

where κ is taken from (Zygelman, 2005).

(b) T_K: In order to model T_K, the code solves the coupled set of equations, eq. 2.28 and eq. 2.29. For the purpose of this thesis we will focus on the regime post cosmic dawn, where sources capable of producing X-rays would have started to appear. Therefore, the code models the X-ray heating rate per baryon, ε_X which is to be substituted in eq. 2.29. When an X-ray photon knocks out an electron from neutral hydrogen atom, this fast moving primary electron further transfers it's energy in the following three ways (Shull, 1979):

- Heating - due to collisions with other slow moving electrons.
- Secondary ionization of neutral hydrogen atoms.
- Excitation of ground state hydrogen.

The fraction of energy that goes into the respective processes is determined by the energy of the primary electron and the ionization state of the medium (Shull, 1979; Furlanetto & Stoever, 2010). The code computes the X-ray heating rate per baryon by taking into account the total contributions from sources inside concentric sperical shells around $(\mathbf{x}, z')$. The X-ray emission rate per redshift interval from luminous sources between $z\prime\prime$ and $z'' + dz''$ corresponding to a volume element dV , such that $z'' \geq z'$ is:

$$\frac{d\dot{N}_X}{dz} = \zeta_X f_* \rho_b (1 + \delta_{nl}^{R''}) \frac{dV}{dz''} \frac{df_{coll}}{dt}, \tag{2.38}$$

where ζ_X is the number of photons per solar mass in stars. It has been assumed that the number of photons emitted is proportional to the fraction of collapsed mass inside dark matter halos and f_* is the fraction of baryons converted to stars. One can think of, $f_* \rho_b (1 + \delta_{nl}^{R''}) \frac{dV}{dz''}$ as the star formation rate ζ_*, in units of solar mass per second, in the shell. It is assumed that the X-ray luminosity of sources can be written as, $L \propto (\nu/\nu_0)^{-\alpha}$, where ν_0 is the lowest X-ray frequency that can escape into the IGM and α is the X-ray spectral index. Thus, the number of photons of frequency ν arriving per second, per unit frequency, at $(\mathbf{x}, z')$ is :

$$\frac{d\phi_X(\mathbf{x}, \nu, z', z'')}{dz'} = \frac{d\dot{N}_X dz''}{\alpha} \nu_0^{-1} \left(\frac{\nu}{\nu_0}\right)^{-\alpha-1} \left(\frac{1+z''}{1+z'}\right)^{-\alpha-1} e^{-\tau_X}, \tag{2.39}$$

where τ_X is the optical depth and accounts for attenuation due to photoionization of various species by X-rays in reaching the point of observation from the point of emmission. In order to gain speed, 21cmFAST assumes that all photons for which

$\tau_X \leq 1$ are absorbed. Thus the expression for ε_X:

$$\varepsilon_X(\mathbf{x}, z') = \int_{\nu_0}^{\infty} d\nu \sum_i (h\nu - E_i^{th}) f_{heat} f_i x_i \sigma_i \int_{z'}^{\infty} dz'' \frac{d\phi_X/dz''}{4\pi r_p^2}, \tag{2.40}$$

where r_p is the proper distance between the point at redshift $z = z'$ and $z = z''$. All existing species at that epoch are included in the above integral through their cross-section for photoionization and their fraction, f_i where $i = HI,\ HeI\ or\ HeII$. The fraction of the secondary electron's energy that goes into heat is given by $f_{heat}(h\nu - E_i^{th})$.

(c) x_α: The WF-coupling factor is given by :

$$x_\alpha = 1.7 \times 10^{11} (1+z)^{-1} S_\alpha J_\alpha, \tag{2.41}$$

where S_α is a corrective factor for atomic physics and J_α is the Ly-α background flux. J_α is a result of two processes:

i. Stellar emission of photons which can get redshifted in the Ly-α resonance, i.e. between Ly-α and the Lyman limit[4]. Therefore, the Ly-α flux received at a given redshift z is given by (Pritchard & Furlanetto, 2006):

$$J_{\alpha,*} = \frac{f_* n_{b,0} c}{4\pi} \int_z^{\infty} \left[dz' (1+z')^3 (1+\bar{\delta}_{nl}^{R''}) \frac{df_{coll}}{dz'} \sum_{n=2}^{n(z')} f_{recycle}(n)\ \varepsilon(\nu_n') \right].$$

ii. Contribution from X-rays ($J_{\alpha,X}$): Is calculated similar to eq. 2.41 above by replacing f_{heat} by $f_{Ly-\alpha}$.

Then, the total Ly-α background is given by:

$$J_{\alpha,tot}(\mathbf{x}, z) = J_{\alpha,X}(\mathbf{x}, z) + J_{\alpha,*}(\mathbf{x}, z). \tag{2.42}$$

4. **Brightness temperature**: After modelling all the astrophysical processes [5], the 21cm brightness temperature is calculated in 21cmFAST, as follows:

$$\delta T_b(\nu) = 27 x_{HI} (1+\delta_{nl}) \left(1 - \frac{T_\gamma}{T_S}\right) \times \left(\frac{1+z}{10}\frac{0.15}{\Omega_m h^2}\right)^{1/2} \left(\frac{\Omega_b h^2}{0.023}\right) mK. \tag{2.43}$$

[4]This range is chosen in order to account for photons which can also cascade to the $n = 2$ level and thereby cause a Ly-α transition.

[5]The effect of peculiar velocities has been ignored in the thesis.

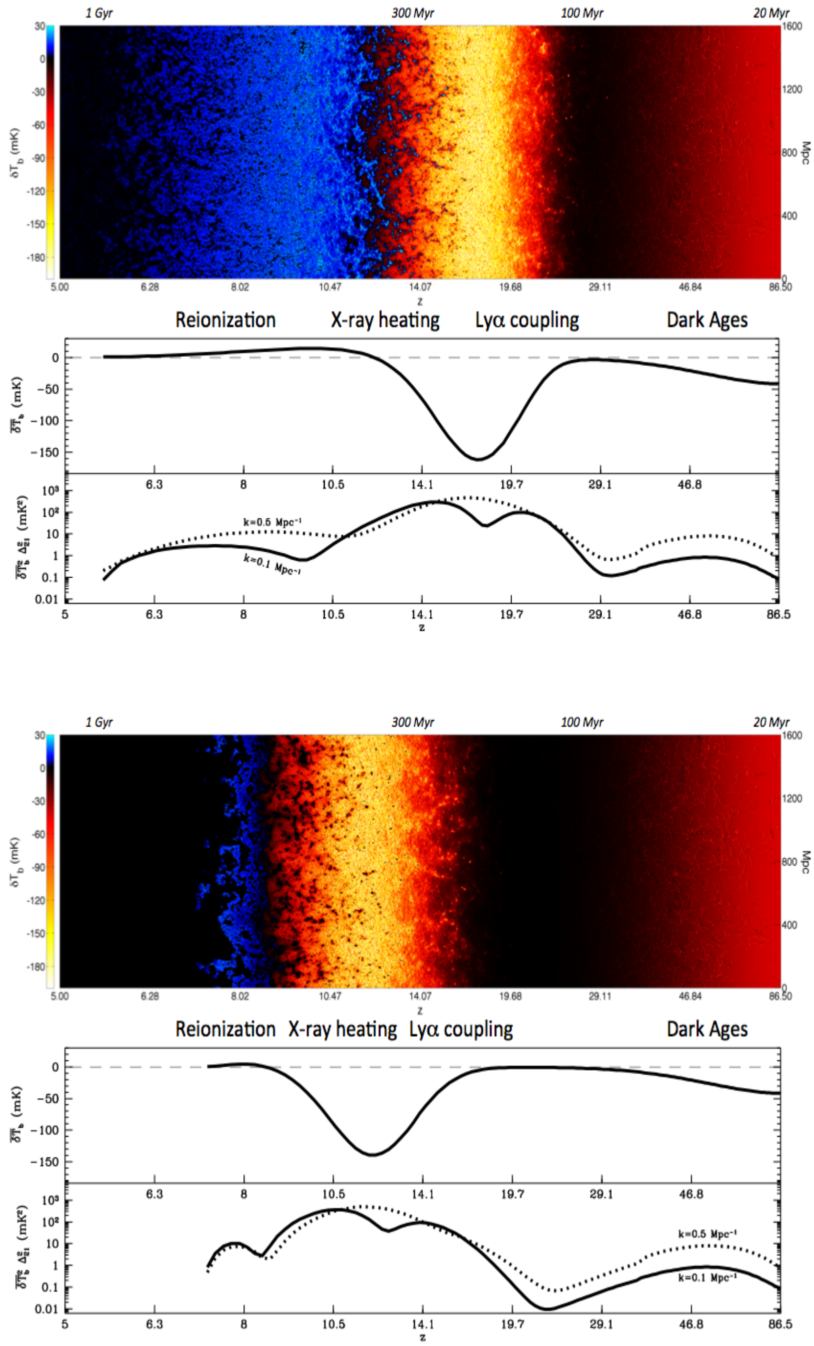

Fig. 2.3 The top panel shows the fluctuations of δT_b for a scenario where reionization is driven by faint galaxies while the bottom panel shows a scenario with bright galaxies. The color map plots δT_b while the plots below it show the mean value of δT_b (top) and power spectrum (bottom) of the 21cm brightness temperature [*Courtsey: (Mesinger et al., 2016)*].

Fig. 2.3 shows the fluctuation history in real space and in terms of power spectrum and global evolution of δT_b, based on different sets of astrophysical scenarios generated with 21cmFAST from (Mesinger et al., 2016). One can see from the figures that heating and reionization begins later for brighter galaxies (i.e. higher M_{vir} and ζ). This is expected because a higher M_{vir} implies lower collapse fraction as compared to fainter galaxies at a given epoch. The heating epoch is wider in case of brighter galaxies and reionization is fast (due to higher value of ζ).

2.3.1 Comments on the usefulness of semi-numerical techniques for topological studies of EoR

In this subsection we will briefly review 21cmFAST in comparison to more exact simulations of EoR . As described in the previous sections of this chapter, the theoretical progress of reionization depends upon the detailed physics of formation and evolution of the first stars and galaxies and their subsequent feedback effects on the IGM. Therefore analytical methods which can predict the mean and other first or even second order statistics of EoR would not be able to predict the detailed evolution which imprints several higher order effects on the evolution of the IGM. Thus, another way could be to resort to fully numerical simulations. Such a simulation would encompass modelling dark matter (using N-body simulations), gas (using hydrodynamic simulation techniques) and transfer of ionizing radiation (using radiative transfer simulations). In order to study EoR, one would therefore require modelling a range of scales and a huge parameter space. This implies that a complete modelling of EoR would require simulations with very high resolutions and large box sizes. Given these requirements and the low computational efficiency of fully numerical simulations, it becomes necessary to use simulations that are a compromise between fully numerical and fully analytical techniques for modelling EoR. In that direction, 21cmFAST provides a good tool for studying EoR. The following points summarize the difference between using 21cmFAST and exact numerical simulations of (Trac & Gnedin, 2011) for two major field components underlying EoR modelling based on (Mesinger et al., 2011):

- Matter field: In 21cmFAST there is no separate treatment of baryonic physics and dark matter. The authors found that the matter power spectrum obtained from 21cmFAST follows the gas and dark matter from full N-body+hydrodynamic matter simulations of (Trac & Gnedin, 2011) on scales $\gtrsim$ 2Mpc for all $z \gtrsim 7$. Therefore, if sufficiently smoothed, the two simulations are in agreement with each other for the redshifts spanning EoR. In this thesis we will work with smoothing scales which are $\gtrsim$ 2.5Mpc.

- Ionization Field: The semi-numerical excursion set based technique used in 21cmFAST has been compared with full N-body+radiative transfer simulations in (Zahn et al., 2011).

Computation of f_{coll} in 21cmFAST is carried out using Fast Fourier Radiative Transfer (FFRT) algorithm which as described before, computes f_{coll} directly on evolved density fields. The authors found that the technique leads to more connected bubbles because exact locations of ionized regions are not identified unlike the case of radiative transfer simulations. They also found that at earlier times FFRT produces more number of bubbles at small scales as compared to the full numerical simulations. At later stages there are slightly larger bubbles in semi numerical techniques due to their higher connectivity. Moreover the ionized field in case of 21cmFAST is more correlated with the underlying density field than the fully numerical simulations. The authors found that the differences between the simulations are smaller than other modelling uncertainities related to the sources and sinks of reionization. They conclude that both the methods agree with each other to 10s of percent level. Therefore, for parameter estimation studies, the use of semi-numerical simulations is justified and is fairly accurate.

The above comparisons were performed in k-space using power spectrum. A detailed study comparing the topology from these simulations, quantified using topology based statistics as described in Section 1.4 would be carried out in near future. It remains to see whether the topological differences lie within the precision of the images obtained using future interferometers such as the Square Kilometre Array (SKA).

3

Morphology of 2- dimensional random fields

Cosmological fields can be viewed as random fields that are defined on two or three dimensions. Examples of such fields are the CMB temperature and polarization, galaxy surveys and 21cm brightness temperature. The 21cm brightness temperature and matter density fields are 3-dimensional fields which would be observed at different redshift slices in 2D. The random nature of these fields can be traced back to the physical mechanism of generation of fluctuations of the gravitational potential in the very early universe. Currently, it is widely accepted that quantum fluctuations of the inflaton field during inflation gave rise to these fluctuations. Each type of cosmological field then gets modulated by the physical processes that affect them in their subsequent time evolution. Therefore, we can expect that analyzing the statistical properties of cosmological fields will yield vital information of the generation of the fluctuations and the physical processes that took place in the history of the universe.

This chapter introduces morphological descriptors called Minkowski tensors (MTs) and Betti numbers, mathematically and their numerical calculation for a random field in two dimensions. Section 3.1 gives an introduction and describes the properties of the morphological descriptors used in this thesis. Section 3.2 describes the numerical calculation of these descriptors. In section 3.3 we show how one can construct useful statistics from these morphological descriptors to condense maximum information in limited number of descriptors. Finally, in section 3.4 we describe Gaussian random fields in terms of these statistical descriptors.

3.1 Geometrical and topological properties of random fields

A set of objects are said to possess the same morphology if one object of the set can be superimposed on to the other under some rigid transformations (such as translation, rotation or reflection in Euclidean space). On the other hand, two objects are said to possess the same topology if one can be moulded into another through a continous deformation (i.e. without disconnecting what was connected or connecting which was disconnected). Therefore, the connectedness and the continuity of the points within the structure are maintained during the deformation (Barr, 1989). For a random field, its spatial description can be given in terms of the change in the topological or morphological properties of it's excursion sets. As will be elaborated in future subsections these properties change sytematically as the threshold of the field is varied.

The advantage of using real space techniques for cosmological data sets in image plane is to associate a quantative measure to the images instead of analysing the data pixel by pixel. Morphological properties are typically integrals over the Fourier quantities. So far in the literature their use in cosmological applications have mostly been restricted to constraining primordial non-Gaussianity. Hence, their full power has not been exploited yet. The major limitation has been the difficulty in getting data which are both high precision and high resolution, and that cover sufficiently large volumes. With the rapid improvement of observationing techniques and upcoming observations which will provide such data it becomes a worthwhile exercise to devise morphological statistics to extract cosmological information and to forecast the extent of their usefulness on future observed data.

3.1.1 Excursion Set

For a smooth (differentiable everywhere) 2D scalar field $u(x)$ on a Euclidean plane ($\mathbb{E}^2$), the set of all points with field values greater than or equal to a threshold $u(x) = \nu$ is called an excursion set:

$$Q_\nu = \{x \in \mathbb{E}^2 | u(x) \geq \nu\} \tag{3.1}$$

For any given random field the boundary of the excursion set at a given threshold consists of a random distribution of smooth curves. The curves are essentially the contours at which the field has value ν. These contours would enclose one or more simply connected or multiply connected regions. [1]

3.1.2 Betti Numbers

Betti numbers are topological quantities that deal with the counting of holes. It is the number of ways in which a cut from one edge to the other of a structure can be made without separating it into two disjoint structures. Clearly this is possible only for mutiply connected regions (Flegg, 1974). In two dimensions one can have simply connected regions (will be referred to as *connected regions* from here onwards) which is essentially a 0-dimensional hole or a 1-dimensional hole which is a hole in the usual sense. For the excursion set of a random field, the contours at the field threshold ν would either enclose a connected region or a hole. There is a systematic variation in the number of holes (β_1) and connected regions (β_0)as the threshold of the field is varied. This behaviour can be used to infer the statistical and topological properties of the field (Pranav et al., 2019). Figure 3.1 shows a random density field with zero mean and standard deviation 1 along with it's excursion set for the field threshold at $\nu = 0$.

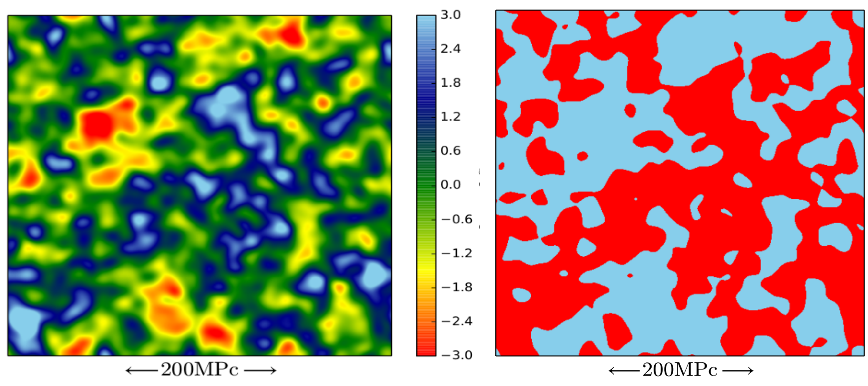

Fig. 3.1 The left panel shows an evolved density field at a redshift of $z \simeq 18$ generated from 21cmFAST. The field is almost Gaussian in nature and has been redefined to have a mean value 0 and standard deviation 1. The right panel is the excursion set of the field at $\nu = 0$. The red regions are the connected regions, while the sky blue regions surrounded by connected regions are holes.

[1]A region is simply connected if any closed curve on it can be contracted to a point without leaving the surface, otherwise it is called mutiply connected. An example of former is a disc while that of latter is a disc with one or more holes in it.

3.1.3 Tensor Minkowski Functionals

For a closed convex curve[2] C let $\vec{r}$ be the position vector of any point on the curve, $\hat{n}$ denote the unit vector normal to the tangent vector, κ is the local curvature of the curve at the point (see appendix E.2.0.1 for the mathematical definitions). The tensor Minkowski functionals in 2D are defined as (Mecke & Arns, 2005; McMullen, 1997; Hug et al., 2008; Alesker, 1999):

$$W_0^{m,0}(C) = \int_C \vec{r}^m da \tag{3.2}$$

$$W_1^{m,n}(C) = \frac{1}{2}\int_C \vec{r}^m \otimes \hat{n}^n ds \tag{3.3}$$

$$W_2^{m,n}(C) = \frac{1}{2}\int_C \vec{r}^m \otimes \hat{n}^n \ \kappa \, ds, \tag{3.4}$$

where ds is the infinitisimal arc length of the curve (eq. E.4) and da is the area that the curve encloses. The tensor product is given by, $\vec{A} \otimes \vec{B} = \frac{1}{2}(A_i B_j + A_j B_i)$. Also $\vec{r}^m$ means m times tensor product of $\vec{r}$ and $\hat{n}^n$ is the n times tensor product of $\hat{n}$. These powers are the rank of the tensor obtained after taking this tensor product. Therefore the rank of the above tensors is given by $m+n \leq 2$ (for our case). For $m+n=0$ the above three equations reduce to the following three scalar Minkowski functionals (SMFs) (G E Schröder-Turk et al., 2010; Chingangbam et al., 2017):

$$W_0(C) = \int_C da \tag{3.5}$$

$$W_1(C) = \frac{1}{2}\int_C ds \tag{3.6}$$

$$W_2(C) = \frac{1}{2}\int_C \kappa ds, \tag{3.7}$$

where W_0 is the area, W_1 is the contour length and W_2 is called the genus of the structure (see 1.4 for cosmological applications). If $m+n=1$, then they are the vectorial Minkowski functionals. For $m+n=2$, it is straightforward to see from eqs. (3.2-3.4) that there are seven Minkowski tensors. These rank 2 MTs can be further divided into:

- Translational Invariant: $W_1^{1,1}$,$W_2^{1,1}$, $W_2^{0,2}$ and $W_1^{0,2}$
- Translational Covariant: $W_0^{2,0}$, $W_1^{2,0}$ and $W_2^{2,0}$

[2] A closed curve in Euclidean space is called *convex* if the straight line joining any two arbitrary points in the region enclosed by the curve also lies within the same region. It is called *non-convex* if there is at least one pair of points such that some part of the line joining them lies outside the region.

For the purpose of cosmological studies we would require a translational invariant measure as there is no preferred coordinate frame. However, of the four translational invariant tensors only $W_1^{1,1}$,$W_2^{1,1}$& $W_2^{0,2}$ are linearly independent. It has been shown in (Chingangbam et al., 2017; G E Schröder-Turk et al., 2010) that $W_1^{1,1}$ & $W_2^{0,2}$ do not provide any new information over their scalar counterparts:

$$\begin{aligned} W_0\mathbf{E} &= W_1^{1,1} && (3.8)\\ W_1\mathbf{E} &= W_1^{0,2} + W_2^{1,1} && (3.9)\\ W_2\mathbf{E} &= 2W_2^{0,2} && (3.10) \end{aligned}$$

Therefore, we restrict our attention to $W_2^{1,1}$, by performing integration by parts and using the definitions from appendix (E.2.0.1):

$$\begin{aligned} W_2^{1,1}(C) &= \frac{1}{2}\int_C \vec{r}\otimes\hat{n}\ \kappa ds && (3.11)\\ &= \frac{1}{2}\int_C \hat{T}\otimes\hat{T} ds, && (3.12) \end{aligned}$$

We define the ***Contour Minkowski Tensor*** (CMT) with the following symbol:

$$\mathscr{W}_1 = \int_C \hat{T}\otimes\hat{T}\ \mathrm{d}s. \tag{3.13}$$

Note that the numerical factor on the r.h.s. of eq. 3.13 is different from that in eq. 3.12. The reason for choosing the notation in this way is described below. Expanding the tensor product and taking the trace of eq. 3.13 :

$$\begin{aligned} \mathrm{Tr}(\mathscr{W}_1) &= \frac{1}{2}\mathrm{Tr}\int (\hat{\mathrm{T}}_\mathrm{i}\hat{\mathrm{T}}_\mathrm{j} + \hat{\mathrm{T}}_\mathrm{j}\hat{\mathrm{T}}_\mathrm{i})\ \mathrm{ds}\\ &= \frac{1}{2}\int (2\,\hat{T}_1^2 + 2\,\hat{T}_2^2)\ ds\\ &= \int ds && (3.14) \end{aligned}$$

where the last step follows because $\hat{T}$ is a unit vector . The final result is simply the second scalar MF, the total contour length or perimeter of the curve denoted by W_1.

Another important morphological information that CMT provides is that of intrinsic shape and alignment. $\mathscr{W}_1$ is translation invariant and transforms as a rank-2 tensor under rotations. It has dimension of length. Since it is symmetric and defined for a closed curve, it has two eigenvalues denoted by λ_1 and λ_2 which are real and positive. For convenience of notation we choose $\lambda_1 < \lambda_2$. When the eigenvalues are different they pick out two orthogonal directions and we can effectively approximate the arbitrary curve as an ellipse whose semi-minor axis is aligned with the eigenvector of λ_1 while the semi-major is aligned with that of λ_2. This intrinsic shape is captured by the *shape anisotropy parameter*:

$$\beta \equiv \frac{\lambda_1}{\lambda_2}. \tag{3.15}$$

By definition $0 < \beta \leq 1$. If $\beta = 1$ we refer to the curve as isotropic. Isotropic curves are those that have m-fold, $m \geq 3$, rotational symmetry. Note that circular shape is just one of the possible isotropic shapes, given by the limit $m \to \infty$. For a generic curve, β will have value between zero and one.

If we have many curves and we average over each element of $\mathscr{W}_1$ and obtain the eigenvalues of this average matrix as Λ_1 and Λ_2 with $\Lambda_1 \leq \Lambda_2$, then we define the ratio:

$$\alpha \equiv \frac{\Lambda_1}{\Lambda_2}. \tag{3.16}$$

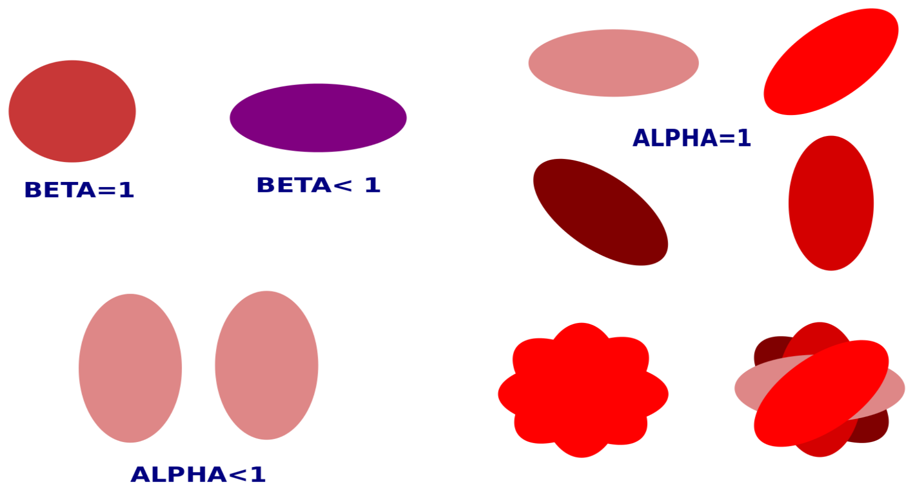

(a) (b)

Fig. 3.2 The figure shows an example of β and α for curves. A circle has $\beta = 1$ since it is isotropic while an ellipse has $\beta < 1$ [fig. (a) (*top*)]. For many curves, if the curves are aligned along the same direction as in fig. (a) (*bottom*) , then there is an overal anisotropy i.e. $\alpha < 1$. On the other hand $\alpha = 1$ for randomly oriented ellipses as shown in fig. (b). When superposed on each other, the randomly oriented ellipse would have a boundary which is isotropic.

This parameter α gives a measure of the net alignment or relative orientation of the curves. It is the β of the curve obtained by superimposing all curves over each other. Therefore, for a single curve $\alpha = \beta$. An example of β and α is shown in fig. 3.2.

So far eq. 3.13 has been used to define $\mathscr{W}_1$ for a single curve. We next shift attention to smooth random fields. As mentioned earlier, at each given threshold value of a random field the boundaries of the excursion or level set enclose either connected regions or holes. We therefore obtain sets of these two types of curves for every threshold. The morphological properties of the excursion sets, and as a consequence that of these boundaries, change smoothly as the threshold value is varied.

In order to express the gemetric form of $\mathscr{W}_\infty$ in terms of the field, we first need to specify the parameteric forms, $x(t)$ of the curves which describe the contours at a fixed threshold of the field, $u(x) = \nu$. Pick a point x_0 on the contour, where $\nu = u(x_0)$. Then in a sufficiently small neighbourhood of that point a parameterization $x(t)$ of the contour can be found. Therefore, one can define the contour implicitly as (Schmalzing & Górski, 1998):

$$u(\mathbf{x}(t)) = \nu. \tag{3.17}$$

Differentiating both sides of this equation, with respect to the parameter t gives (sum over repeated indices):

$$\frac{\partial u}{\partial x_i}\frac{dx_i}{dt} = 0, \tag{3.18}$$

Since $d\mathbf{x}/dt$ is the unit tangent vector, $\hat{T}$ (appendix (E.2.0.1)) and there is freedom of choosing the parameterization, the components of the unit tangent vector is chosen in the following way:

$$\hat{T}_i = \varepsilon_{ij}\frac{\partial u/\partial x_j}{|\nabla u|}, \tag{3.19}$$

where ε_{ij} is the anti-symmetric Levi-Civita tensor in two dimensions (appendix E.2.0.1). This choice satisfies eq. 3.18.

Therefore, using this form of $\hat{T}$ in eq. 3.13, $\mathscr{W}_1$ for a particular curve C can be expressed as:

$$\mathscr{W}_1 = \int_C \mathrm{d}s\, \frac{1}{|\nabla u|^2}\, \mathscr{M}, \tag{3.20}$$

where the matrix $\mathscr{M}$ to be evaluated at the points along the curve is given by,

$$\mathscr{M} = \begin{pmatrix} \left(\dfrac{\partial u}{\partial x_2}\right)^2 & \dfrac{\partial u}{\partial x_1}\dfrac{\partial u}{\partial x_2} \\ \\ \dfrac{\partial u}{\partial x_1}\dfrac{\partial u}{\partial x_2} & \left(\dfrac{\partial u}{\partial x_1}\right)^2 \end{pmatrix} \tag{3.21}$$

It is again easy to see in this form that the trace of $\mathscr{W}_1$, which is $\int \frac{Tr(\mathscr{M})}{|\nabla u|^2}\, ds$ gives W_1. The analytical forms of α for a Gaussian isotropic field has been derived in (Chingangbam et al., 2017). The analytical form of β is not yet known. For a Gaussian random field , $\partial u/\partial x_1$ and $\partial u/\partial x_2$ are always uncorrelated and hence the off-diagonal terms of $\langle \overline{\mathscr{W}}_1 \rangle$ are always 0 for such a field. Here, the overbar represents the averaging over each contour of the excursion set. Therefore if a Gaussian field is not isotropic then $\beta < 1$ with zero off diagnol components, while if the field is non-Gaussian then the off-diagonal elements are non-zero. Thus, while α encodes the global properties of the field, β is a measure of morphology of individual structures in the excursion set.

3.2 Numerical Calculation of Contour Minkowski Tensor

In this thesis we utilize β in conjunction with W_1 and Betti numbers to study the morphology of the fields during EoR. Due to the highly non-Gaussian nature of the fields and the absence of any analytical form for β and Betti numbers even for a Gaussian random fields, we need to resort to numerical calculation of the eigenvalues of $\mathscr{W}_1$ for each structure in the excursion set. The numerical calculation of CMT and Betti numbers in this thesis is based on the method used in (Appleby et al., 2018a; Ganesan & Chingangbam, 2017) which is summarized below:

- A discrete field in 2D would lie on a regular grid, $1 \leq i, j \leq N_{pix}$ and have a value u_{ij} on a given grid point. Once a threshold ν is chosen, then the field at everyy i,j pixel can either be within the excursion set ($\delta_{ij} \geq \nu$) or outside ($\delta_{ij} < \nu$) .

- In order to form a boundary that separates regions which are in or out of the excursion set, we follow the *marching square algorithm* (Mantz et al., 2008; G E Schröder-Turk et al., 2010). In this method one sweeps through the entire grid. At each grid point (i, j), a square is generated from the adjacent pixels $(i+1, j)$,$(i, j+1)$,$(i+1, j+1)$ which can either be in or out of the excursion set. Therefore, there are 2^4 possibilities .

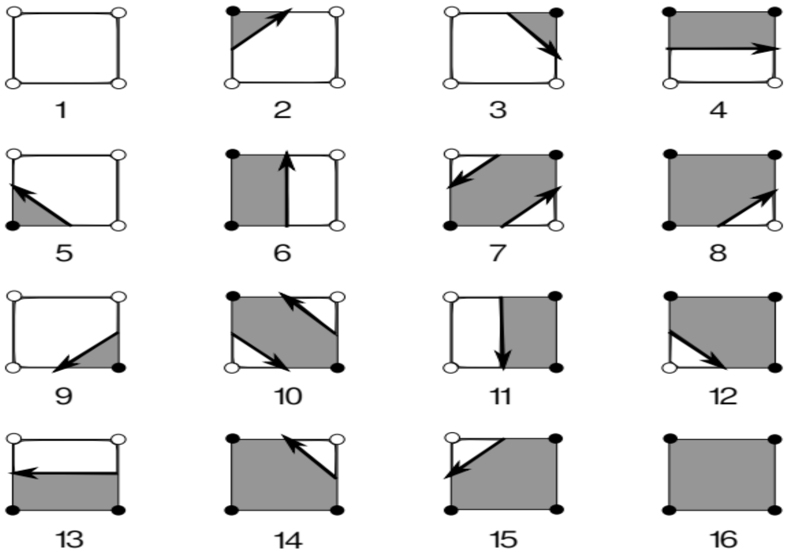

Fig. 3.3 The figure shows sixteen possible types of squares for a given pixel, which can be constructed from the adjacent pixels depending upon whether a pixel is *in* (black dots) or *out* (white dots) of the excursion set. By performing a linear interpolation of field values betwen each *in* and *out* state of a given square, the point where the field has value ν is identified. These points are identified as vertices and joined by means of lines directed in such a way that they run anticlockwise about an *in* state. *Image credit: (Appleby et al., 2018a)*

- Thereafter, a closed perimeter is created by linearly interpolating along the edges of the square by using the values of δ_{ij} at the corners, to find the point where $\delta = \nu$ [3]. This is described in fig. 3.3.

- The points where the interpolated point meets the edges of the squares is called the vertex and the vector that defines the boundary is an edge $'\mathrm{e}'_{\mathrm{ab}}$, where *a* and *b* are the two vertices within which this edge is present.

- In order to identify a hole or a connected region, the algorithm applies the Friends of friends (FoF) algorithm. For every grid point having a value δ_{ij} which is inside a connected (included in the excursion set) region, the surrounding 4 values $\delta_{i\pm1,j\pm1}$ are assigned to the same connected region, if they are also within the excursion set. The operation is repeated iteratively on these points. The same procedure is repeated for holes. This enables us to calculate the Betti numbers.

[3]Remember that the boundaries of the excursion set are essentially the contours of the field where it has the value equal to the threshold ν

- In order to calculate $\mathscr{W}_1$, it is sufficient to note that the edges $'\mathrm{e}'_{\mathrm{ab}}$ identified as boundary between two vertices is actually the tangent vector and therefore the unit tangent vector is given by $\vec{e}_{ab}/|e_{ab}|$. Also the path length element ds is the same as the edge length e_{ab} since the curve is actually a polygon. Therefore the final output of the code is,

$$(\mathscr{W}_1)_{ab} = \sum_{a,b} \frac{1}{|e_{ab}|} (\vec{e}_{ab} \otimes \vec{e}_{ab}), \tag{3.22}$$

which is given separately for each connected region or hole at a given threshold. This output is then used for constructing the quantities of interest for the analysis of our random field. In the next section I will elaborate upon the statistical quantities that we finally use for studying the physical properties of cosmological fields during EoR.

3.3 Statistics of interest

Before elaborating upon the different statistical quantities used for the analysis of the EoR fields it is important to understand how the fields should be defined so as to extract maximum information. For any field, subtracting its mean values merely shifts the field values and does not change its geometrical and topological properties. A rescaling $u \to \tilde{u} \equiv u/a$, where a is some constant, at every spatial point also does not alter the topology and the geometry of the excursion sets even though field values get remapped. This is obvious from the right hand side of eq. 3.20 and (3.21) where the integrand is clearly independent of field rescalings by constant factors. Hence, we shoose to work with fields rescaled to zero mean and standard deviation one by redefining our field to $\tilde{u} = (u - \mu)/\sigma_u$, where μ is the mean and σ_u is the standard deviation of the field.

The CMT can also give an estimate of the size of the area enclosed by the curve. Let $\lambda \equiv \lambda_1 + \lambda_2$ denote the perimeter of the closed curve. Then, using this perimeter to define a circle by equating λ to $2\pi r$, we determine r to be

$$r \equiv \lambda/2\pi. \tag{3.23}$$

For an arbitrary closed curve the isoperimetric inequality relates the area, A, enclosed by the curve, to its perimeter λ as

$$A \leq \frac{\lambda^2}{4\pi}. \tag{3.24}$$

This implies that r will in general result in an overestimation of the size of the area enclosed by the curve. The overestimation will be more for non-convex curves. Therefore, r actually gives an upper bound of the size. We emphasize that the perimeter of the structure can be calculated exactly, *it is only the interpretation of the idealized circle that r over-estimates.* For determining the radius for a single structure knowledge of contour length (or W_1) is sufficient and we do not require the CMT. However, when we have an ensemble of structures, in addition to W_1, the number of curves (or Betti numbers), is required to obtain the estimate of the mean size of structures. The truly new information that we obtain from the CMT is that of the shape of the curve. Nevertheless, it neatly unifies the size and shape information in a single tensor quantity, and we employ it to obtain estimates of the size of structures in conjunction with the Betti numbers. In this work the fields are simulated with periodic boundary conditions and hence we do not need to consider the effect of boundary cuts. However, actual data (for example the brightness temperature field or galaxy surveys) will be measured only over a limited region of the sky. In that case connected regions and holes that coincide with survey boundaries should be disregarded and the effect of the mask must be assessed by applying it to Gaussian random fields and also on simulated fields.

Note that we could calculate the area of each structure directly and also roughly estimate its shape anisotropy by finding its centre of mass and taking the ratio of the smallest and largest distances of the boundary from the centre. The computational advantage of the CMT over such ad hoc methods becomes clear when we apply to a large collection of curves, such as those given by the boundaries of excursion sets. The CMT is superior to simplistic approaches because they are based on very general mathematical framework with well defined transformation properties. This makes them unambiguous and easy to apply to any distribution of structures.

We reserve the symbols λ_i, r and β to denote the eigenvalues, approximate radius and the ratio of the eigenvalues for a single curve. Let

$$\overline{\lambda}_{i,\mathrm{x}}(\nu) \equiv \frac{\sum_{j=1}^{n_\mathrm{x}(\nu)} \lambda_{i,\mathrm{x}}(j)}{n_\mathrm{x}(\nu)}, \tag{3.25}$$

$$\overline{r}_\mathrm{x}(\nu) \equiv \frac{\sum_{j=1}^{n_\mathrm{x}(\nu)} r_\mathrm{x}(j)}{n_\mathrm{x}(\nu)}, \tag{3.26}$$

$$\overline{\beta}_\mathrm{x}(\nu) \equiv \frac{\sum_{j=1}^{n_\mathrm{x}(\nu)} \beta_\mathrm{x}(j)}{n_\mathrm{x}(\nu)}, \tag{3.27}$$

denote their averages over all curves at a given ν. Note that the usual scalar Minkowski Functionals are traditionally presented in this form as functions of the threshold.

3.4 Overview of morphology of Gaussian random fields

Before we proceed to interpret the morphology of excursion sets for any given field we first provide a general description of how the excursion set changes when the threshold is varied and then discuss the special case of Gaussian random fields. In principle one can identify three different regimes as the threshold is varied from the highest value and progressively lowered. Initially, there exists isolated small connected regions around the highest peaks of the field and their number would gradually increase as more peaks enter the excursion set when lowering the threshold. In the second regime as we further lower the threshold, some of these small connected regions merge thereby decreasing their number. Finally in the third regime, as the threshold is decreased further these connected regions all merge to form a single connected region with holes puncturing it. These holes eventually shrink in size and disappear as we go lower in threshold and finally a single connected region remains which spans the entire region over which the field is defined.

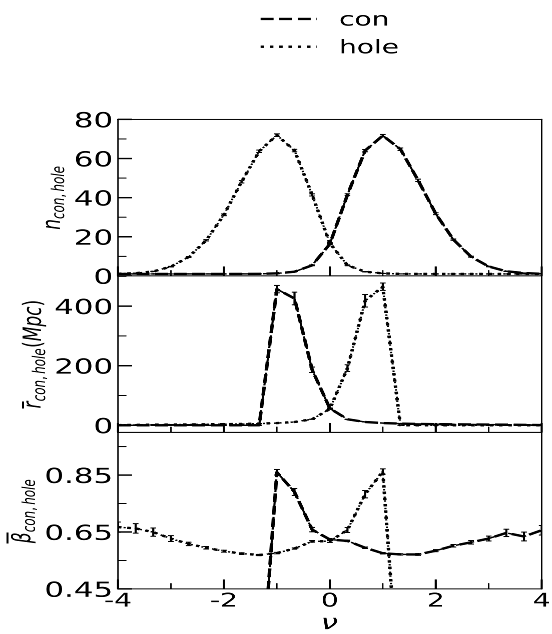

Fig. 3.4 Variation of $n_{con,hole}$, $\bar{r}_{con,hole}$ and $\overline{\beta}_{con,hole}$ with field threshold ν for a Gaussian random field constructed from 100 realizations of the density field on a 512 $\times$ 512 grid drawn from a flat power spectrum. The error bars denote the error in mean over 100 realizations of the field.

Gaussian random fields are special since one can obtain analytic expressions for many morphological properties. They are useful ideal cases whose knowledge helps to study the departure of fields from Gaussian behaviour. For Gaussian random fields the analytic expression for the total contour length of all boundary contours (connected regions and holes) is known and has a simple closed form expression given by $W_1 = Ae^{-\nu^2/2}$ (Tomita, 1986), where the amplitude A depends on the ratio of the variance of the gradient of the field to the variance of the field per unit area. However, closed form expressions for $n_{con,hole}$, $\bar{r}_{con,hole}$ and $\bar{\beta}_{con,hole}$, are not known. $n_{con,hole}$ has been calculated numerically in (Park et al., 2013), while $\bar{\beta}_{con,hole}$ has been studied extensively using numerical computation in (Appleby et al., 2018a), $\bar{r}_{con,hole}$ has not been studied before.

We can infer their behaviour at very high and positive and very low and negative thresholds. Since $n_{tot} \sim n_{con}$ for large positive thresholds, $\nu \gg 0$ we expect that in this regime $\bar{r}_{con} \propto e^{-\nu^2/2}/n_{con}(\nu)$. Similarly, $n_{tot} \sim n_{hole}$ for large negative thresholds, $\nu \ll 0$. We expect that in that regime $\bar{r}_{hole} \propto e^{-\nu^2/2}/n_{hole}(\nu)$. Since $W_2 = n_{con} - n_{hole}$ and $n_{hole} \to 0$ as $\nu \to \infty$, at $\nu \gg 0$, we have $n_{con} \sim W_2$, where W_2 is the genus of the excursion set which is $\propto \nu e^{\nu^{-2}}$ (Tomita, 1986). Therefore $n_{con}(\nu) \propto \nu e^{-\nu^2}$. Similarly $n_{hole}(\nu) \propto \nu e^{-\nu^2}$ at $\nu \ll 0$ (note that ν is negative here). Therefore $\bar{r}_{con,hole} \propto \nu^{-1}$ at these thresholds. The units of scale will enter through the amplitude, which will be proportional to the ratio of the variance of the field to the variance of the gradient of the field.

As an initial test we quantify the morphology of Gaussian random fields, as encapsulated in $n_{con,hole}$, $\bar{r}_{con,hole}$ and $\bar{\beta}_{con,hole}$. We simulate 100 realizations with input flat power spectrum on a 512×512 square pixel grid. Then we smooth the fields over 12 pixels and compute the morphological quantities using these simulations. Fig. (3.4) show the plots of $n_{con,hole}$ (top), $\bar{r}_{con,hole}$ (middle) and $\bar{\beta}_{con,hole}$ (bottom). All plots are averaged over 100 realizations. n_{con} peaks at $\nu = 1$, while n_{hole} peaks at $\nu = -1$. We can see from the plots for $\bar{r}_{con,hole}$ at threshold values where $n_{con,hole}$ are large, that the average size of the structures are small, and vice versa. Further, $\bar{r}_{con,hole}$ have an artificial sharp drop at $|\nu| > 1$. This is because we use periodic boundary condition on our simulation box which generates large unphysical structures that do not have a boundary. In order to avoid this we have excluded regions having area > 0.9 times the area of the simulation box. The plots for $\bar{\beta}_{con,hole}$ show that the average shape of the structures do not vary much across the threshold range (i.e., remains within a small range of around 0.65), except the few large connected regions at very high negative threshold values, and the few large holes at high positive threshold values which exhibit higher β values. We find that all plots are symmetric about the threshold corresponding to the mean, $\nu = 0$.

The results obtained in this chapter for a Gaussian random field will be useful as a benchmark for analyzing the behaviour of the morpology of the fields of the EoR at different redshifts in the subsequent chapters.

3.5 Random fields in Cosmology

As described in Chapter 1 cosmological evolution is a result of non-linear gravitational collapse of highest density regions seeded during inflation. The perturbations of the density field is therefore a three-dimensional random field with well defined extremas. This implies that the field is smooth and differentiable. The highest density peaks (or maximas) are sites of formation of collapsed objects like clusters of galaxies or galaxies. Depending upon the type of structures we want to probe one can smooth the field (say with a scale determined by mass M) and choose a threshold to study the statistics of these peaks both as a function of their height or their spatial distributions (for clustering (Bardeen et al., 1986)). The connected regions described in this chapter, will form around points of maxima, while holes will form around points of minima. As the threshold of the field is varied, in going from maximum (or minimum) to minimum (or maximum) field threshold, one is expected to encounter a connected region around a peak (or hole around a valley), which will connect at saddle points (or fragment if it is a hole) (Pranav et al., 2019). Thus the study of maxima and minima of the field are closely related to the topology of the density profiles around these peaks, however density profiles start becoming uncorrelated with that of the underlying peak as one goes away from the peak. For example it was found in (Bardeen et al., 1986) that spheroidal density profiles around peaks are very improbable and can occur only around rare peaks and the profiles are generally triaxially assymetric. Using these insights, the behaviour of β at the high threshold limit have been calculated in (Appleby et al., 2018a) , for a Gaussian random field where the authors found that the numerically calculated value of β approaches the theoretical prediction of β at high field thresholds for a Gaussian random field. Cosmological fields such as the ionization field are different from ideal Gaussian fields as will be shown in Chapter 4 and Appendix D. While ionization fields essentially consist of only extremas (in the form of fully neutral or completly ionized regions and also since the thickness of ionization fronts is very small (Chapter 3)), the field does not have localized peaks as in the case of density field and hence it cannot be interpretted as directly related to the shape of peaks.

4

Bubble size and shape statistics using CMT : A proof of concept

4.1 Motivation

In section 1.2.2 the growth of ionized regions and it's dependence on source properties during the EoR was described. It was also shown in section 2.2.4 that fully ionized regions correspond to regions where δT_b is zero. Therefore, characterizing the shapes and sizes of ionized regions would give the following two important insights on the EoR:

1. The properties of the first sources of light: The shape and number of these ionized regions would enable us to study the formation and evolution of the very first luminous objects in the universe.

2. The ionization history of the universe: If sources of reionization are modelled effectively one can obtain a detailed evolution of the mean ionization fraction with redshift. This can in turn help us obtain stringent constraints on cosmological parameters.

An important quantity to infer reionization morphology is the distribution of bubbles of different sizes. There have been several studies on studying the size distribution of bubbles (see (Lin et al., 2016; Friedrich et al., 2011; Giri et al., 2018) for a comparison of different methods). Any analysis that focusses on studying the size distribution relies upon the definition of a "bubble". In most of these studies, the bubbles are assumed to be spherical (or circular in 2D). In actual, during the EoR the morphology of ionized regions is complex and one needs measures which can quantify this complex morphology. There have been analytical techniques based on excursion set approach to infer the bubble size statistics ((Furlanetto et al., 2004a)) as described in section 2.3 [1]. An improved model of the excursion set based approach was introduced in (Paranjape & Choudhury, 2014). The authors did away with the simplifying assumptions of uncorrelated steps and random appearance of collapsed halos in the underlying density field as was used in (Furlanetto et al., 2004a). In (Iliev et al., 2006) the authors used the friends-of-friends algorithm to identify connected ionized regions and plotted a distribution of volumes. In (Zahn et al., 2007), the bubble size distribution was calculated using radiative transfer simulations. The authors used what is called as the spherical average method (SPA) which identifies the largest sized ionized spheres around each pixel in the simulation. Another method known as the mean free path method is based on Monte Carlo inference ((Mesinger & Furlanetto, 2007)). This method measures the distribution of photon path length from a randomly selected ionized pixel traced until a stopping criteria for the ray is met (usually set by the point where the ray meets a fully neutral pixel). The method based on watershed algorithm ((Lin et al., 2016)) based on identifying contours of same field value as boundaries and points of minima as centers of ionized regions. Lastly there is a technique based on granulometry ((Kakiichi et al., 2017)) which relies on seiving a binary field through successively larger sized holes. Other than the real space methods described above, (Gorce & Pritchard, 2019) used bispectrum phases to infer a characteristic size for the bubbles.

Other than the size distribution there are topological descriptors which are based on Minkowski functionals, shapefinders, persistent homology and percolation theory. These have been described briefly in section 1.4.

As a first step towards our goal to understand the morphological properties of the 21cm brightness temperature and the kind of physical information that can be inferred, in this chapter we present a proof-of-concept of how the reionization history is encoded in the characteristic shape and size of the ionized and neutral hydrogen regions. For this purpose we employ the statistical descriptors constructed from *Contour Minkowski Tensor* (CMT) described in chapter 3. The advantage of using CMT over other topology based methods is that it encapsulates both size and shape information in a single quantity. Since, for the purpose of this thesis we have focussed on 2D morphology of 21cm images, this step only provides for an understanding of the bubble sizes encoded by the statistics in order to serve as a starting point to generalize to the

[1] This terminology of excursion set in this context is different from the definition in section 3.1.

bubble sizes in 3D. In order to do that we would need to develop methods, which would utilize the information available from 2D images of 21cm maps (chapter 7). A fair comparison with other methods in literature can only be made when generalized to 3D Minkowski tensors while utilizing the information which would be available to us in 2D images of δT_b. We focus mainly on the ionization field, and its effect on the differential brightness temperature. A full analysis of all the fields of the EoR and comparison of different models of reionization will be discussed in chapter 5. It is important to note that our analysis is carried out using idealized simulations using the publicly available code 21cmFAST (section 2.3). We have not considered the impact of foreground contamination and instrument noise on our results. The effect of instrumental noise will be explored in chapter 6.

4.2 Contour Minkowski Tensor for reionization fields

We begin by describing a toy model of growth and mergers of ionized bubbles as EoR progresses. The left panel of Fig. 4.1 shows a simplistic example of two isolated bubbles of identical shape at some initial time (top, left). As described in chapter 3, the ratio $\beta \equiv \lambda_1/\lambda_2$ measures the *shape anisotropy* of the curve. As EoR progresses, these bubbles would grow in size and merge. The right panel of the figure shows the corresponding evolution of β. At the time the bubbles are still apart the value of β will be lower than one since they are elliptical. As the bubbles grow in time, β remains the same until they merge to form one single region (left, middle) at time $t = t_{\rm m}$. At this time β will drop to its minimum, since the resultant shape is highly anisotropic. Thereafter, as the big region grows further β will again start rising towards one (left, bottom). This simplified scenario will be relevant when we apply CMT to the EoR.

We now focus on the fields relevant to the EoR, $x_{\rm HI}$ and δT_b. As described in chapter 2 when EoR begins, the evolution of δT_b is dominated by the x_{HI} field. Therefore, we simulated our brightness temperature field using 21cmFAST (v1.2) on a 200 Mpc box with 512^3 pixels at 10 different redshifts for $\zeta = 50$, $T_{vir} = 3\times10^4$ K and $\zeta_X = 2\times10^{56}$. We generate the x_{HI} and δT_b fields at several redshift values and smooth them with a Gaussian smoothing kernel using different values of the smoothing scale R_s. Our field u is redefined to the standard normal form, $u \to \tilde{u} \equiv (u-\mu)/\sigma$, where μ is the mean and σ is the standard deviation of u. This redefinition does not alter its geometrical and topological properties, but allows for a uniform choice of threshold values to compare fields at different redshifts. Thereafter, we divide the field into two dimensional slices. We use 32 slices of thickness 6.4 Mpc each. Our results are robust against reasonable variation of the slice thickness (not smaller than smoothing scale). In Fig. 4.2 we show the redshift evolution of a slice of the $x_{\rm HI}$ field plotted as function of spatial coordinates x, y. The figure shows how the *shape* of the field changes with redshift. At very high and very

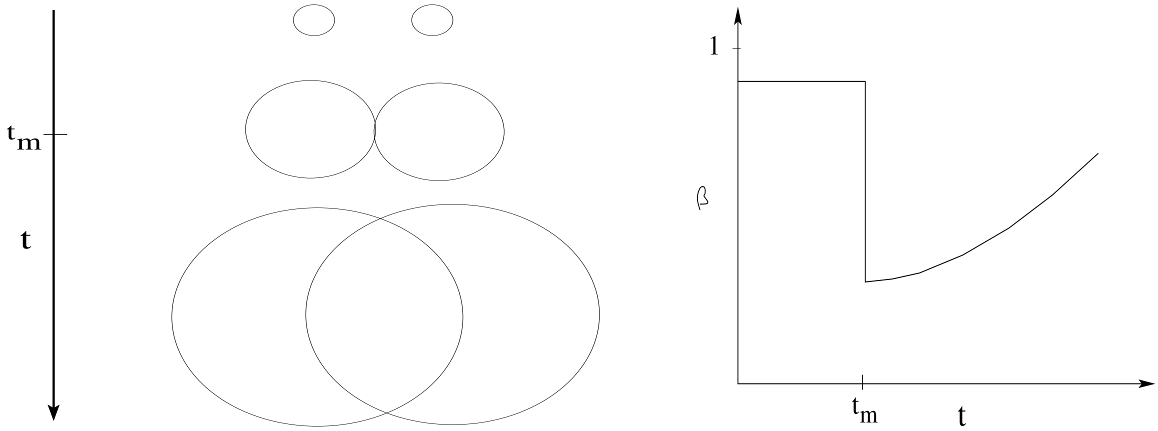

Fig. 4.1 *Left:* A simplistic depiction of two elliptic regions that grow, merge to become a single region at time $t = t_{\rm m}$, and then grow further (top to bottom). *Right*: The average value of β will be constant till the two ellipses merge at $t_{\rm m}$, at which time β will drop sharply, and then increase again as the combined region grows further. This depiction captures the essence of the time evolution of the shapes of ionized regions that grow, merge and grow further.

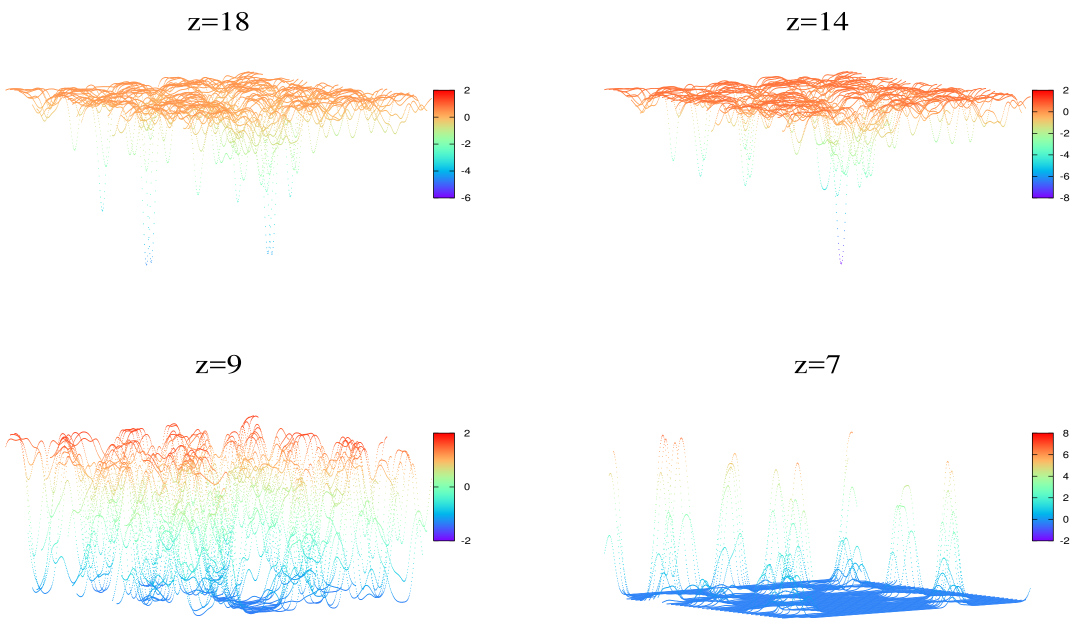

Fig. 4.2 Redshift evolution of a slice of the $x_{\rm HI}$ field. These figures carry the same information as Fig. 4.3, but presented in a form that makes the visualization of the field levels easy.

low redshifts, $x_{\rm HI}$ is highly skewed as is evident from the panels showing $z = 18, 14$ and 7. Note that the $z-$axis scales are not the same in different panels. From the figure, we can see that at relatively early redshifts, $z = 18$ and 14 when $x_{HI} \simeq 1$ at almost all threshold values there are numerous holes but only one connected region. At $z = 9$ there are roughly the same number of holes and connected regions, and at $z = 7$, there are mostly connected regions.

We now define our notation for various quantities of interest. We choose threshold values ν, of the standard normal field $\tilde{u}$. ν will be in units of the standard deviation of $\tilde{u}$, which is one. At each ν we denote the numbers of curves enclosing connected regions and holes by $n_{\rm con}(\nu)$ and $n_{\rm hole}(\nu)$, respectively. The suffix 'con' and 'hole' refer to boundaries of connected regions and holes, respectively. $n_{\rm con}(\nu)$ and $n_{\rm hole}(\nu)$ are the Betti numbers for a random field. Then, at each redshift z we define,

$$N_{\rm x}(z) \equiv \int_{\nu_{\rm low}}^{\nu_{\rm high}} {\rm d}\nu \, n_{\rm x}(\nu, z), \tag{4.1}$$

where the suffix 'x' stands for either 'con' or 'hole'. The lower and upper threshold cutoffs, $\nu_{\rm low}$ and $\nu_{\rm high}$, can be chosen depending on the threshold range of interest. For well behaved smooth random fields, n_ν goes to zero as $\nu \pm \infty$. Therefore, the integral on the r.h.s of the above equation converges, and $N_{\rm x}$ is always finite even when the cutoff thresholds are taken to infinity. $N_{\rm x}(z)$ represents the ensemble of all curves within the chosen threshold range in the simulation box at a fixed redshift. Since for our practical purpose ν is sampled at a finite number of values, the integral is carried out as a Riemann sum. Then, we define:

$$\lambda_{i,{\rm x}}^{\rm ch}(z) \equiv \frac{\int_{\nu_{\rm low}}^{\nu_{\rm high}} {\rm d}\nu \, n_{\rm x}(\nu, z) \bar{\lambda}_{i,{\rm x}}(\nu)}{N_{\rm x}(z)}, \tag{4.2}$$

$$r_{\rm x}^{\rm ch}(z) \equiv \frac{\int_{\nu_{\rm low}}^{\nu_{\rm high}} {\rm d}\nu \, n_{\rm x}(\nu, z) \bar{r}_{\rm x}(\nu)}{N_{\rm x}(z)}, \tag{4.3}$$

$$\beta_{\rm x}^{\rm ch}(z) \equiv \frac{\int_{\nu_{\rm low}}^{\nu_{\rm high}} {\rm d}\nu \, n_{\rm x}(\nu, z) \bar{\beta}_{\rm x}(\nu)}{N_{\rm x}(z)}. \tag{4.4}$$

These integrals are convergent for the same reason as explained for $N_{\rm x}(z)$.

Physical interpretation of $r_{\rm x}^{\rm ch}$ and $\beta_{\rm x}^{\rm ch}$: The physical information encoded in $r_{\rm x}^{\rm ch}(z)$ and $\beta_{\rm x}^{\rm ch}(z)$ are essentially derived from λ_i. In the subsequent part of the chapter we will present physical interpretation only for $r_{\rm x}^{\rm ch}(z)$ and $\beta_{\rm x}^{\rm ch}(z)$. $r_{\rm x}^{\rm ch}(z)$ condenses the size information for each type of structure from the entire field into one number, at each redshift. This number gives the largest possible average radius of the structure. It is well defined and independent of the observer measuring it. We interpret $r_{\rm x}^{\rm ch}(z)$ to be the *characteristic radius* for each type of structure, with the superscript 'ch' referring to 'characteristic'. In particular, $r_{\rm hole}^{\rm ch}$ for the $x_{\rm HI}$ field give the characteristic size of the ionized bubbles at each redshift. Likewise, we interpret

$\beta_{\mathrm{x}}^{\mathrm{ch}}(z)$ to be the *characteristic shape anisotropy* of the corresponding structures at each redshift. Note that the results for the characteristic radius and shape will depend on the choice of the values of the threshold cutoffs ν_{high} and ν_{low}. The choice also determines our definition of connected regions as neutral regions and holes as ionized bubbles. We will comment on this when we present our results in section 4.2.2.

4.2.1 Progress of reionization and length and time scales

The focus of this work is to track the redshift evolution of the numbers, sizes and shapes of neutral (connected) regions and ionized regions (or holes). Before we carry out quantitative analysis, it is instructive to use physical reasoning and anticipate their redshift evolution. In fig (4.3) we show the progress of reionization for a two dimensional slice of $x_{\mathrm{HI}}(\vec{x})$ at four different redshifts. In all the panels the pale yellow regions are the neutral regions while the black are the ionized regions. At the relatively high redshift (see the panel for $z = 16$) the ionized regions are all small and isolated on a big connected neutral region. They are anisotropic and as EoR progresses (see the panel for z=12), the number of ionized bubbles increases with time because new ionizing sources are getting formed. On the other hand, the size of the ionized regions which appeared earlier grows. Their anisotropy will also evolve. As the bubble sizes grow, two or more bubbles can merge. As bubble mergers take place the shape of the bubbles will become more anisotropic and the rate at which anisotropy evolves, increases (see the panel at z=9). Towards the end of EoR the ionized regions would all have merged into a big connected region with isolated neutral regions on it (see the panel for z=7).

Therefore, the average number, size and shape of ionized regions at any redshift will be governed by three factors:

1. The rate of formation of ionizing sources.
2. The rate at which the ionized regions grow.
3. The rate of bubble mergers.

These factors will in turn depend on physical parameters such as ζ and T_{vir} (eqs.(2.31) and (2.33)). We expect that at early redshifts the rate of formation of ionizing sources will be greater than the rate of bubble mergers, and vice versa at later redshifts. We refer to the redshift at which they are equal as z_{frag}. Around this redshift we also expect that the single connected (neutral hydrogen) region will begin to fragment into multiple smaller connected regions. Therefore, at z_{frag} the number of ionized bubbles will turn over and start decreasing, while the number of connected regions will start increasing. The anisotropy of the shapes of the ionized bubbles within the neutral regions will also show an increase.

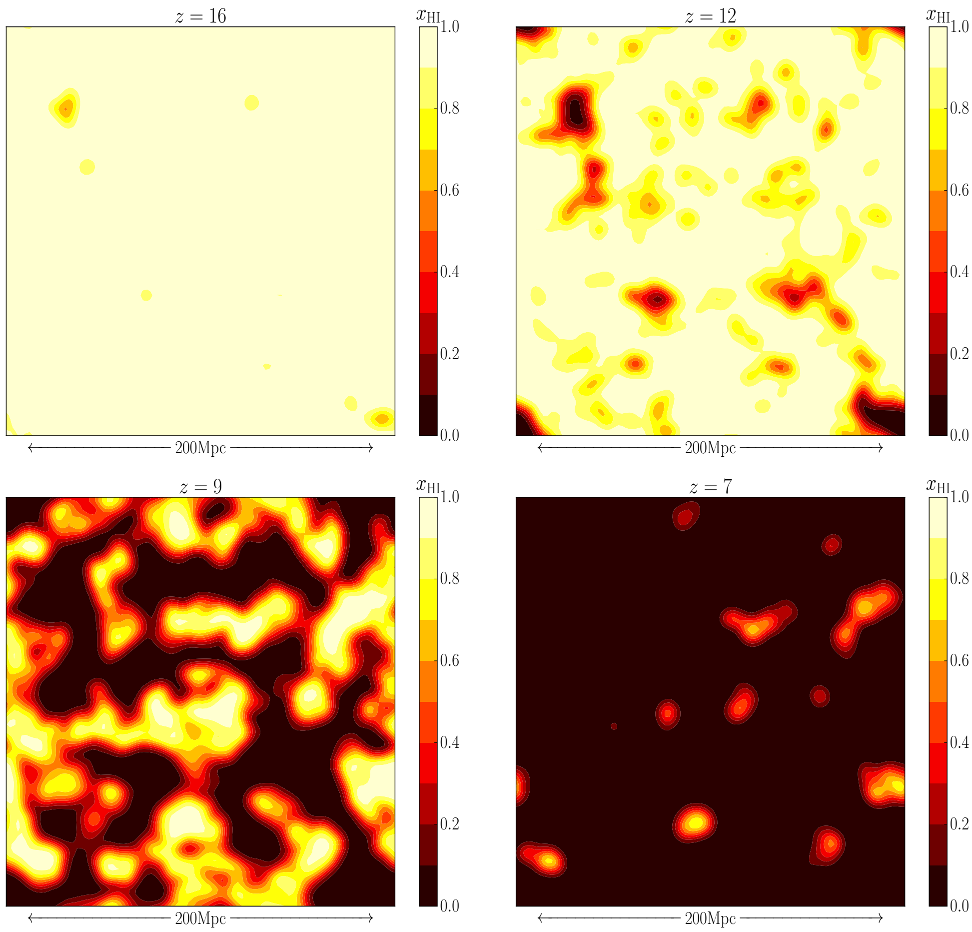

Fig. 4.3 The four images show a two dimensional slice of $x_{\mathrm{HI}}(\vec{x})$ at four different redshifts for the model of interest here. These images highlight the redshift evolution of the numbers, shapes and sizes of the connected regions (pale yellow) corresponding to neutral regions, and hole regions (varying from dark yellow to black) corresponding to ionized regions.

Let $z_{0.5}$ denote the redshift when $\bar{x}_{\rm HI} = 0.5$. As reionization progresses there must be an epoch when the number of connected regions and holes cross each other and become equal. We will show in the next section, that the equality happens at $z_{0.5}$. Then, even further as z decreases beyond $z_{0.5}$, the merged bubbles will still grow in size with a corresponding decrease of anisotropy. At the same time, the number of connected regions will increase as more and more fragmentation occurs, with a corresponding decrease in size. This process will continue up to a redshift $z = z_{\rm e}$, after which the number of connected regions will drop due to ionization of the entire region reaching completion and the number of holes will go to zero.

The different transition redshifts are as summarized below:

- z_{frag}: Redshift at which N_{hole} turns over to decrease from an initial stage of growth. It marks the value of z where the bubble merger rate begins to dominate over rate of appearance of new collapsed sources.
- $z_{0.5}$: Redshift at which $\bar{x}_{HI} = 0.5$.
- z_e: Redshift at which N_{con} turns over to decrease from an initial duration of increase marking the point where mergers approach end.

We will determine $z_{\rm frag}$, $z_{0.5}$ and $z_{\rm e}$ by using the contour Minkowski Tensor. We will then quantify the anticipated evolution described above for the numbers of ionized bubbles and connected regions, their sizes and anisotropy in the following section.

4.2.2 Results for $x_{\rm HI}$

Let $y_{\rm HI} \equiv (x_{\rm HI} - \bar{x}_{\rm HI})/\sigma_{\rm HI}$, where $\sigma_{\rm HI}$ is the rms of $x_{\rm HI}$. In Fig. 4.4 we show plots of $n_{\rm x}, \bar{r}_{\rm x}$ and $\overline{\beta}_{\rm x}$ versus ν, (defined in eqs. 3.26 and 3.27) calculated using $y_{\rm HI}$. The smoothing scale is $R_s = 2$ Mpc. The left column corresponds to holes, while the right corresponds to connected regions. All panels show a shift of the plots towards higher positive threshold range as the redshift decreases. This is due to decrease of $\bar{x}_{\rm HI}$. We see that at $z = 11.99$ the number of holes (top, left panel) is large, spans a wide range of threshold values, and peaks at roughly the field mean value (correponding to $\nu = 0$). The number of holes drops rapidly as the redshift decreases. The sizes of holes (middle, left panel) are small for most values of ν at $z = 11.99$. They are large at threshold values that correspond to field values close to $\nu = 1$. This simply means that, for level sets at such thresholds, holes enclose large inter-connected regions which are highly non-convex. This correlates with the fact that the number of holes are few at such thresholds. As the redshift decreases, the size of holes show rapid increase. The shape of

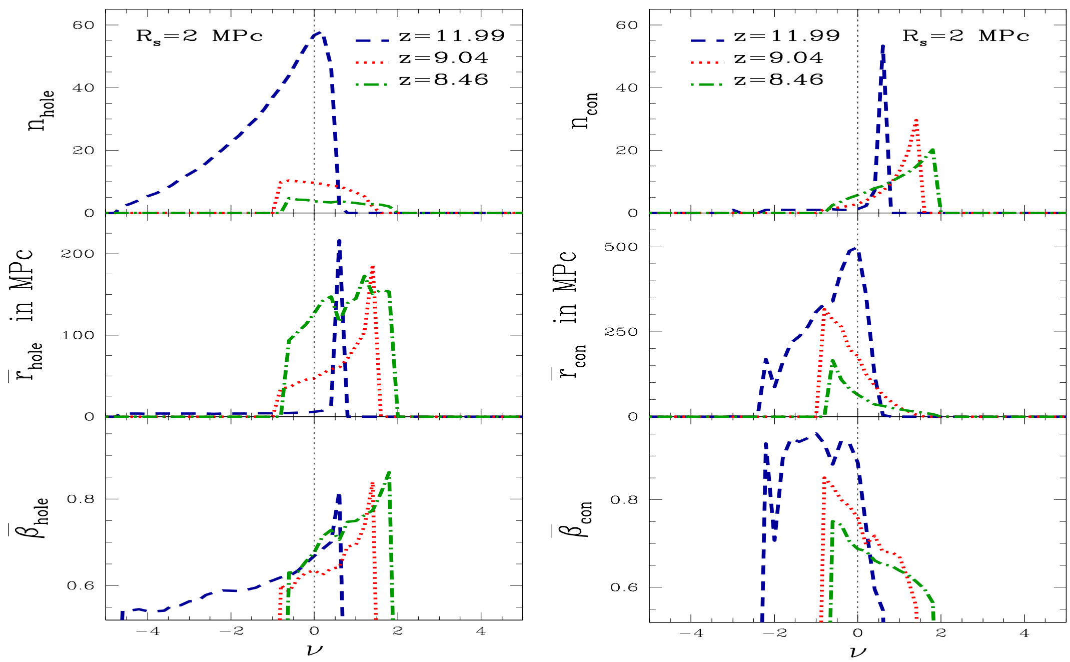

Fig. 4.4 Plots for n_x (top), $\bar{r}_x$ (middle) and $\overline{\beta}_x$ (bottom) versus ν (see Eqs. 3.26 and 3.27), for smoothing scale $R_s = 2$ Mpc for different redshift values. Left column shows holes while right column shows connected regions.

of holes (bottom, left panel) are more anisotropic at highly negative values and less so near threshold corresponding to $\nu = 1$ for $z = 11.99$. This implies that the shape of the random and highly non-convex level set boundary contours tend to be more isotropic, in comparison to that of the typically convex holes that are obtained for large negative threshold values. In general, ionized regions correspond to holes for negative threhold values. A precise identification of the ionized region, and its size and shape, will be threshold dependent.

Connected regions have quite different redshift evolution in comparison to holes, as can be seen in the right column of Fig. 4.4. They are more numerous at higher positive threshold values at all redshifts (top, right panel). They exhibit overall decrease of size with decreasing redshift (middle, right panel). We can also see that they are more anisotropic at higher thresholds (bottom, right panel). Complementary to holes, neutral regions correspond to connected regions for positive threhold values. A precise identification of the neutral region, and its size and shape, will again be threshold dependent.

Note that we have chosen to show plots for $z = 11.99,\ 9.04$, and 8.46 just so that the evolution trend for all quantities is easy to compare visually. It is straightforward to extrapolate the trend to higher and lower redshift values. Also these three redshifts capture the changing morphology of the ionization field as described in Fig. 4.2. They capture the changing shape of the field in flipping of peaks at high redshifts to valleys, at low redshifts, via the flipping of the threshold dependence of n_{hole} about $\nu = 0$, in going from $z = 11.99$ to $z = 8$.

Although we do not focus on analyzing the non-Gaussian nature of the fields in this thesis, we point out that the shapes of all the plots in Fig. 4.4 reveal the highly non-Gaussian nature of the $x_{\rm HI}$ field as compared to Fig. 3.4.

As mentioned above, the interpretation of the size and shape of ionized and neutral regions depends on the threshold of interest. In what follows, we choose to interpret them by computing the integrated quantities defined in Eqs. 4.3 and 4.4 so as to condense the information in the entire threshold range for each variable into a single number. For holes, $\nu_{\rm low}$ is taken to be the minimum value of $y_{\rm HI}$, and $\nu_{\rm high} = \nu_{\rm cut}$, where $\nu_{\rm cut}$ is chosen to be some appropriate value. For connected regions, $\nu_{\rm high}$ is taken to be the maximum value of $y_{\rm HI}$, and $\nu_{\rm low} = \nu_{\rm cut}$. We choose the value of $\nu_{\rm cut}$ to be around the mean value of $y_{\rm HI}$, which is zero. In order to show how the choice of $\nu_{\rm cut}$ affects the interpretation of number, shape and size of holes and connected regions we present calculations using $\nu_{\rm cut} = 0, \pm 0.5$, at each redshift. These choices are made such that holes can be interpreted as ionized regions and connected regions as neutral regions.

In the top panels of Fig. 4.5 we show the redshift evolutions of $\bar{x}_{\rm HI}$ (top left) and $\sigma_{\rm HI}$ (top right) for the smoothing scales $R_s = 2$ and 4.5 Mpc, for the model of reionization that we are considering here. $z_{0.5} \simeq 9.3$ is marked by a vertical dotted line. The other two lines mark $z_{\rm frag}$ and $z_{\rm e}$, which were defined earlier in Section (4.2.1). We can see that $\sigma_{\rm HI}$ is larger for smaller

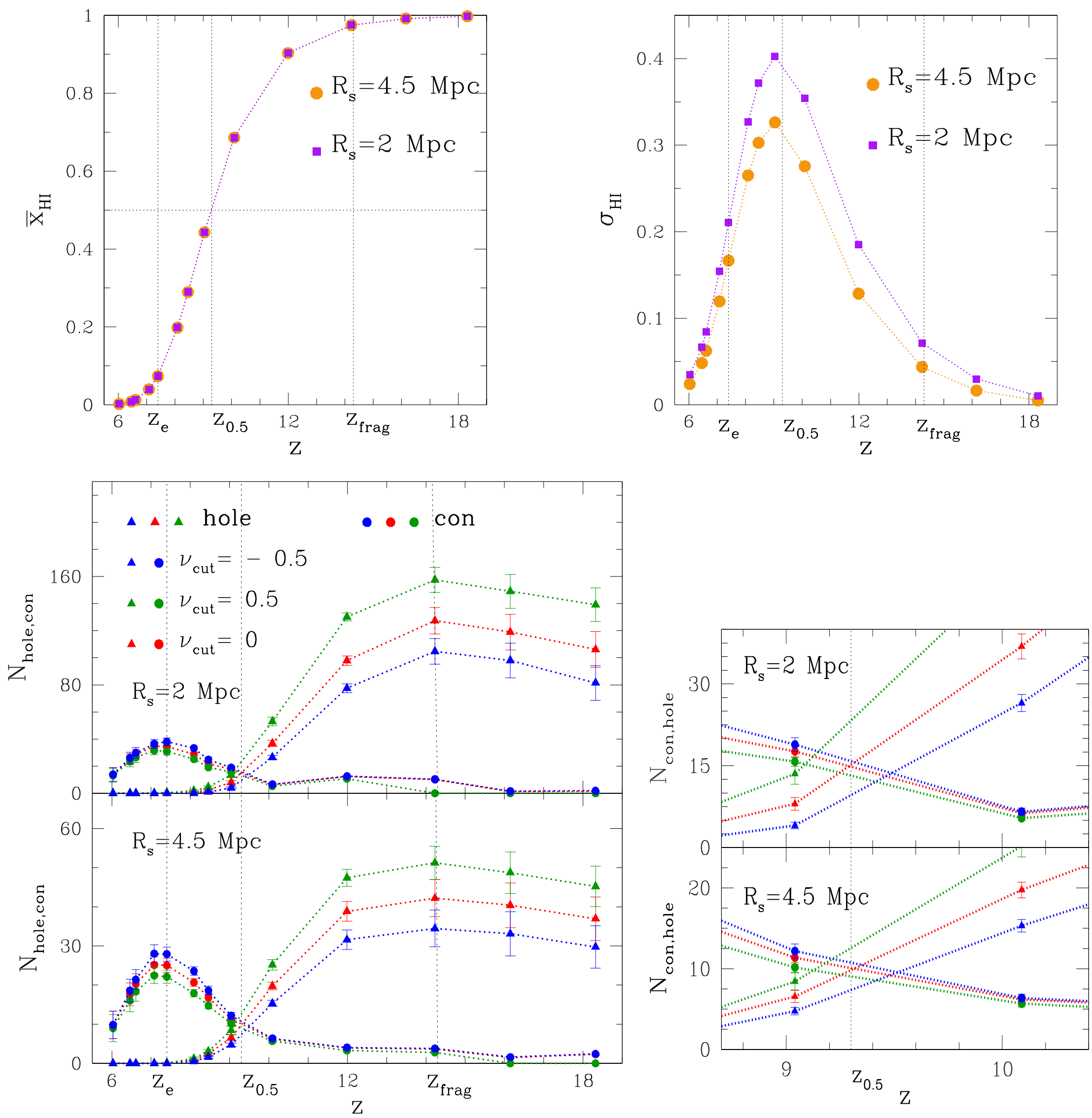

Fig. 4.5 *Top left:* Redshift evolution of the mean of the ionization field, $\bar{x}_{\rm HI}$. *Top right:* Redshift evolution of the standard deviation of $x_{\rm HI}$, denoted by $\sigma_{\rm HI}$. *Bottom left:* $N_{\rm x}$ defined in Eq. 4.1 for $x_{\rm HI}$ for two smoothing scales $R_s = 4.5$ and 2 Mpc, and three different choices of $\nu_{\rm cut}$. Dots represent connected regions while triangles represent holes. The three dotted vertical lines mark $z_{\rm frag} \sim 14.3$, $z_{0.5} \sim 9.3$ and $z_{\rm e} \sim 7.4$. Note that the $y-$axis ranges are different for the two values of R_s. *Bottom right:* Same as bottom left, but with the region of cross over between $N_{\rm con}$ and $N_{\rm hole}$ zoomed in to highlight that $N_{\rm hole}$ and $N_{\rm con}$ cross over at $z = z_{0.5}$ for $\nu_{\rm cut} = 0$. Error bars are the standard deviation from the 16 field slices.

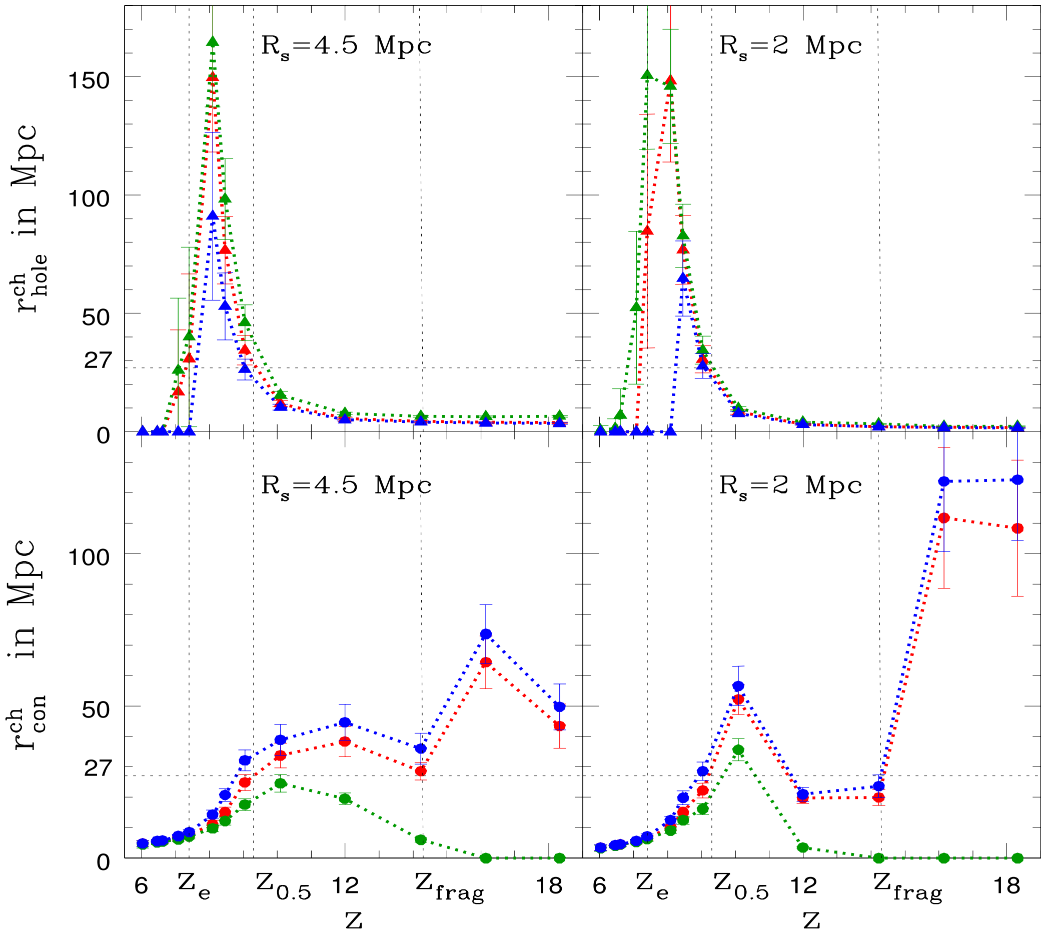

Fig. 4.6 $r^{\rm ch}_{\rm hole}$ and $r^{\rm ch}_{\rm con}$ (defined in Eq. 4.3), for $x_{\rm HI}$ for two smoothing scales $R_s = 4.5$ and 2 Mpc. Green, red and blue plots correspond to $\nu = 0.5, 0$ and -0.5, respectively. $z_{\rm frag}$, $z_{0.5}$ and $z_{\rm e}$ are marked. The horizontal dotted line marks the value of $r^{\rm ch}_{\rm hole}$ at $z_{\rm e}$ for the case of $\nu_{\rm cut} = 0$. Error bars are the standard deviation from the 32 field slices.

smoothing scale. It has a maximum at roughly $z_{0.5}$, and the peak location is not affected by smoothing scale.

$N_{\rm hole,con}$ are shown in the bottom left panel of Fig. 4.5. The bottom right panel shows a zoomed in version. Different colours correspond to different values of $\nu_{\rm cut}$: red for 0, blue for -0.5 and green for $+0.5$. Triangles represent holes, while circles represent connected regions. $N_{\rm hole}$ exhibits two stages of evolution, namely, a slow increase at early redshifts which is then followed by a rapid decrease. The turnover takes place at around $z = z_{\rm frag} \simeq 14.3$. $N_{\rm hole}$ shows a decrease as $\nu_{\rm cut}$ is decreased, which is as expected from its definition. In contrast, $N_{\rm con}$ first exhibits an increasing phase, followed by a decreasing phase. The turnover takes place at redshift $z = z_{\rm e} \simeq 7.3$. $N_{\rm con}$ shows an increase as $\nu_{\rm cut}$ is decreased, which is again as expected. $N_{\rm hole}$ and $N_{\rm con}$ cross over at $z = z_{0.5}$, for $\nu_{\rm cut} = 0$. As is clear from the plots, $z_{\rm frag}$ and $z_{\rm e}$ are independent of the smoothing scale and $\nu_{\rm cut}$. $z_{\rm frag}$ corresponds to $\bar{x}_{\rm HI} = 0.97$ and $z_{\rm e}$ to $\bar{x}_{\rm HI} = 0.04$. We note that the values of $z_{\rm frag}$, $z_{0.5}$ and $z_{\rm e}$ that we have quoted are approximate and not based on accurate determination.

Based on the evolution of $N_{\rm hole}$ and $N_{\rm con}$, we can divide the epoch of reionization into three time regimes, namely, $z \gtrsim z_{\rm frag}$, $z_{\rm frag} \gtrsim z \gtrsim z_{\rm e}$, and $z \lesssim z_{\rm e}$. In the following we describe the behaviour of $N_{\rm x}$, $r^{\rm ch}_{\rm x}$ and $\beta^{\rm ch}_{\rm x}$ in these three time regimes:

1. $z \gtrsim z_{\rm frag}$: During this epoch, ionized bubbles are being formed. The typical size of an ionizing source, when it emerges, is much smaller than the smoothing scales we choose. Smoothing has the effect of smearing out the ionized field values. Hence the smoothed field is only partially ionized at every pixel. The value of $\bar{x}_{\rm HI}$ is close to one. The number of holes increases as more sources get formed, and as a consequence $N_{\rm hole}$ increases with decreasing redshift till $z_{\rm frag}$. The increase in $N_{\rm hole}$ indicates that the rate of formation of new ionizing sources happens faster than the rate of mergers of ionized regions. $N_{\rm con}(z)$ counts the isolated neutral regions. Since at this time the entire region is essentially one connected (neutral) regions with holes (ionized regions) puncturing it, the information in $N_{\rm con}(z)$ is not statistically significant.

   $r^{\rm ch}_{\rm hole,con}$ are shown in Fig. 4.6. Redshifts where $r^{\rm ch}_{\rm hole,con} = 0$ means there are no structures. Different colors correspond to different values of $\nu_{\rm cut}$, as in Fig. 4.5. $r^{\rm ch}_{\rm hole}$ is roughly constant during this epoch and is determined by the smoothing scale. During this time $r^{\rm ch}_{\rm hole}$ gives a good estimate of the size of ionized bubbles because most ionized regions have convex boundaries. In Fig. 4.2 we notice that for early and late redshifts, level sets near the mean value of the field tend to have larger boundaries compared to other threshold values. As a consequence, larger $\nu_{\rm cut}$ results in larger $r^{\rm ch}_{\rm hole}$.

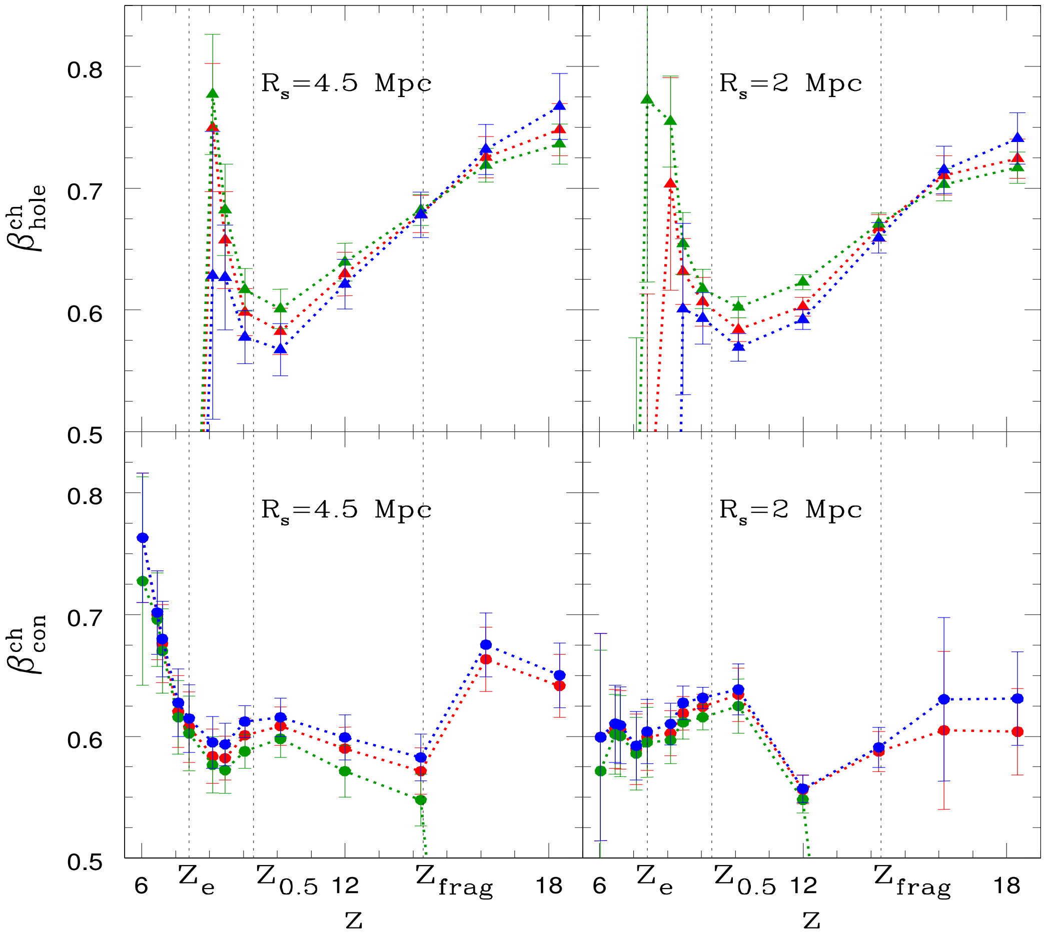

Fig. 4.7 β^{ch}_{hole} and β^{ch}_{con} defined in Eq. 4.3 for x_{HI} for two smoothing scales $R_s = 4.5$ and 2 Mpc. Green, red and blue plots again correspond to $\nu = 0.5, 0$ and -0.5, respectively. Note that $\beta^{ch}_x = 0$ means there are no structures. Error bars are the standard deviation from the 32 field slices.

As mentioned earlier there is essentially just one connected region during this regime. Depending on the value of $\nu_{\rm cut}$ we can obtain more than one connected region due to the uneven nature of the field near its mean value. $r^{\rm ch}_{\rm con} = 0$ for large redshifts for $\nu_{\rm cut} = 0.5$ because the maximum value of the field $y_{\rm HI}$ is lower than this value. At $z_{\rm frag}$, as the neutral region begins fragmenting $r^{\rm ch}_{\rm con}$ becomes useful to probe.

$\beta^{\rm ch}_{\rm hole,con}$ are shown in Fig. 4.7. At $z \simeq 18$ we find that $\beta^{\rm ch}_{\rm hole}$ is less than one, and larger for smaller $\nu_{\rm cut}$. This is because the ionized regions tend to be more isotropic close to the ionizing centres. Moreover, smaller smoothing scale gives smaller values of $\beta^{\rm ch}_{\rm hole}$. Therefore, even at such early redshifts ionized regions are not isotropic. They become more anisotropic as the redshift decreases. The increase of anisotropy implies that the rate of merger of ionized regions is nonzero and increasing (as depicted in Fig. 4.1), even though in this time regime the rate of formation of new ionizing sources is greater than the merger rate. We find that the plots of $\beta^{\rm ch}_{\rm hole}$ for the three values of $\nu_{\rm cut}$ cross just before $z_{\rm frag}$ when the merger rate overtakes the source formation rate. $\beta^{\rm ch}_{\rm con}$ also exhibits anisotropy during this regime. The average anisotropy is more than that of holes (lower value of β).

2. $z_{\rm frag} \gtrsim z \gtrsim z_{\rm e}$: $N_{\rm hole}$ drops sharply after $z_{\rm frag}$, as seen in Fig. 4.5 due to rate of mergers becoming larger than the rate of formation of sources. Fragmentation of the connected region results in increase of $N_{\rm con}$. At roughly $z_{0.5}$, $N_{\rm con} \sim N_{\rm hole}$. After $z_{0.5}$, $N_{\rm con}$ continues increasing as the fragmentation process carries on, while $N_{\rm hole}$ continues to decrease.

   From $z_{\rm frag}$ onwards $r^{\rm ch}_{\rm hole}$ grows, while $r^{\rm ch}_{\rm con}$ decreases, as seen in Fig. 4.6. They eventually cross over, which means the average sizes of ionized and neutral regions are the same. Both $r^{\rm ch}_{\rm hole}$ and $r^{\rm ch}_{\rm con}$ depend on $\nu_{\rm cut}$, as expected. For the case of $\nu_{\rm cut} = 0$ we find that their cross over happens at $z = z_{0.5}$. $r^{\rm ch}_{\rm hole}$ provides a fair estimate of the ionized bubble size until the bubble boundaries become highly non-convex due to multiple mergers. As mentioned in Section 3.2, the area enclosed within the ionized regions is actually smaller than the area of the circle whose radius is given by $r^{\rm ch}_{\rm hole}$. We find that $r^{\rm ch}_{\rm hole}$ grows to a value of ~ 27 Mpc at $z_{0.5}$ for $\nu_{\rm cut} = 0$ (horizontal dotted line). This number is independent of the smoothing scale, as can be expected since the smoothing scale is much smaller than this derived characteristic size.

   We see in Fig. 4.6 that $r^{\rm ch}_{\rm hole}$ continues to grow well beyond $z = z_{0.5}$. By this time the number of holes is very few, and consists of small ionized regions enclosed within neutral regions and others that are very large and highly non-convex. The large non-convex ones result in the growth of $r^{\rm ch}_{\rm hole}$ that we find. Due to the high non-convexity of the holes it is possible that some holes have boundary perimeters that are larger than the perimeter of the simulation box. As mentioned earlier, the high non-convexity of the holes during this time also implies that though the perimeter is obtained from exact calculation, the interpretation of $r^{\rm ch}_{\rm hole}$ as the radius of an idealized circle over-estimates the actual size of the ionized regions to a large extent. Therefore, it is not a useful interpretation during this time regime. Meanwhile, $r^{\rm ch}_{\rm con}$ continues to drop as neutral regions fragment further.

We find that $\beta^{\rm ch}_{\rm hole}$ continues to decrease further after $z_{\rm frag}$, and then exhibits a turn around at around $z \simeq 10$, just before $z_{0.5}$. The turn around redshift is independent of smoothing scale. This indicates that most bubbles have merged and the few holes contributing to the value β are the highly non-convex ones close to the field mean value which tend to be more isotropic. In contrast, $\beta^{\rm ch}_{\rm con}$ exhibits increasing anisotropy after $z \simeq 10$, has a minimum a around $z \simeq 8.5$ and then tends to become isotropic after, for $Rs = 4.5$ Mpc. The behaviour prior to $z \simeq 10$ is dominated by statistical fluctuation and is statistically insignificant. For $Rs = 2$ Mpc we do not see any rise in isotropy, which can be explained by the fact that larger Gaussian smoothing tends to isotropize small scale regions.

3. $z \lesssim z_{\rm e}$: As the ionization process takes over most of the region, $N_{\rm con}$ will turn over and decrease, and we find that this happens at around $z_{\rm e} \simeq 7.4$. By this time the EoR is getting complete and both $N_{\rm con}$ and $N_{\rm hole}$ drop towards zero. $r^{\rm ch}_{\rm hole}$ peaks at before $z_{\rm e}$, depending on $\nu_{\rm cut}$. Thereafter it drops sharply as only a few holes are left within neutral regions. $r^{\rm ch}_{\rm con}$ continues to fall towards zero as the entire region becomes fully ionized.

As was the case for connected regions in regime 1, in this regime all physical quantities associated with holes regions during this epoch are not statistically significant since the number of hole regions enclosed within neutral regions is practically zero.

4.2.3 Results for $\delta T_{\rm b}$

In Fig. 4.8 we show the redshift evolutions of $N_{\rm x}$, $r^{\rm ch}_{\rm x}$ and $\beta^{\rm ch}_{\rm x}$ for $\delta T_{\rm b}$ for two smoothing scales $R_s = 4.5$ (left panels) and 2 Mpc (right panels). Orange dots show connected regions and purple triangles show holes. We can see that the redshift evolutions for all quantities trace that of $x_{\rm HI}$ at later redshifts from roughly $z \sim 10$ onwards. The physical reason for this behaviour is that at these relatively low redshifts the factor that depends on T_γ/T_s in the expression for δT_b given in Eq. (2.43) becomes negligible due to T_s becoming much larger than T_γ.

For redshifts higher than $z > 10$ the behaviour of δT_b will be primarily controlled by that of T_s. We postpone analysis of T_s and $\delta_{\rm NL}$ to Chapter (5) since our main interest here is to understand the ionization field.

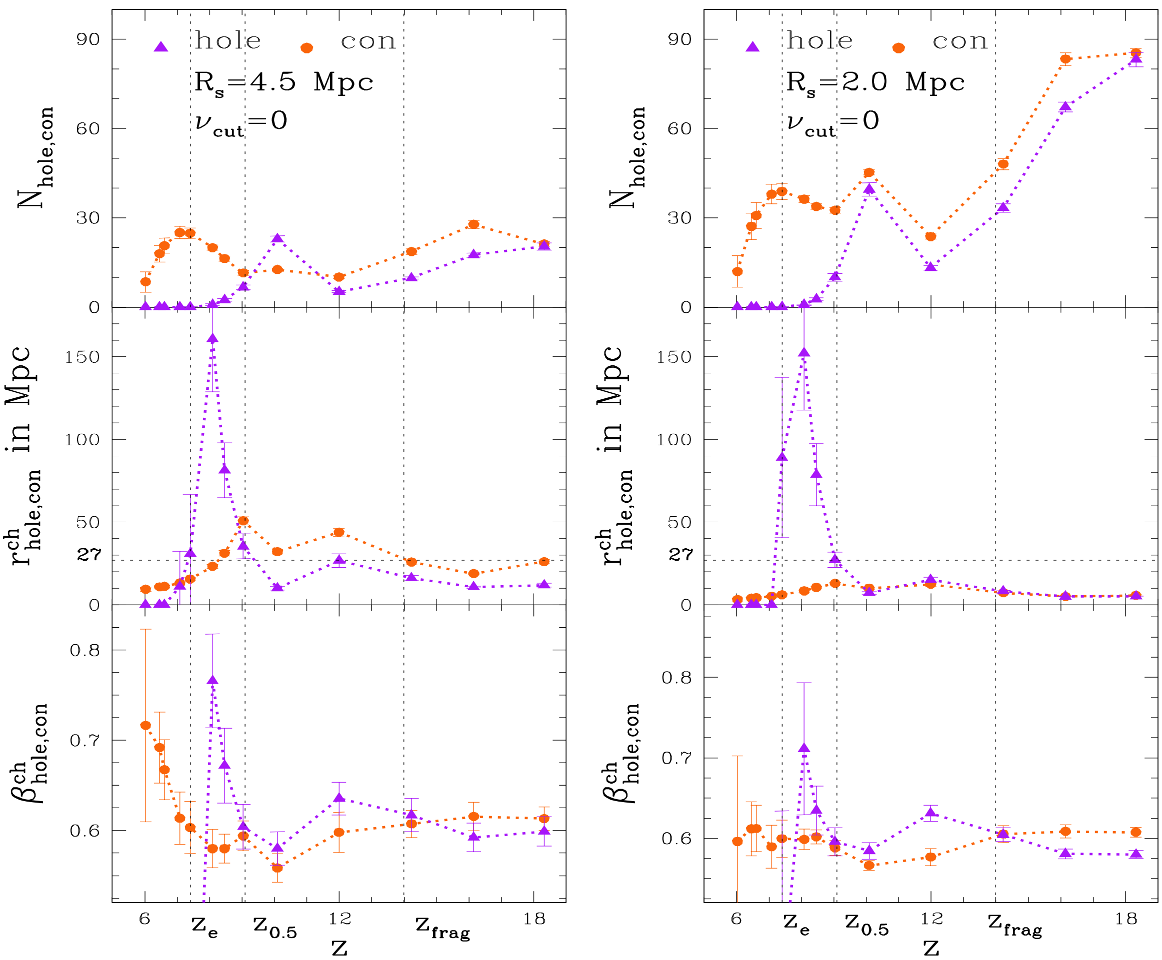

Fig. 4.8 N_x, r_x^{ch} and β_x^{ch} for δT_b, for the same smoothing scales as for x_{HI}, for $\nu_{cut} = 0$. Purple triangles denote holes while orange dots denote connected regions. The three dotted vertical lines again mark $z_{frag} \sim 14.3$, $z_{0.5} \sim 9.3$ and $z_e \sim 7.4$ for comparison with figs. 4.5, 4.6 and 4.7. Error bars are the standard deviation from the 16 field slices.

4.2.4 Probability distributions of r and β for $x_{\rm HI}$ and δT_b

We now estimate the probability distribution functions (PDF) of r and β. The correct way to analyze the PDF would be to calculate it for all structures at each threshold. However, our simulation box is not big enough to provide sufficiently large $n_{\rm x}(\nu)$ to obtain good statistical result. Hence, we use the ensemble of *all curves* at *all threshold values* sampled. As a result the sizes and shapes of the curves are not all independent, but those corresponding to one peak or trough of the field are correlated. Nevertheless, using the full ensemble of curves will reflect the true PDF.

In Fig. (4.9) we show the PDFs of r for $x_{\rm HI}$ (left panel) and δT_b (right panel) for $R_s = 4.5$ Mpc. We find that the PDFs are highly skewed, as can be expected. We have chosen to show x range upto 40 Mpc so as to highlight the redshift evolution for lower values of r where the probabilities are high. The tails extend well beyond 40 Mpc, particularly at intermediate redshifts around $z_{0.5}$. For $x_{\rm HI}$, we see that the PDFs in the upper panel become flatter as the redshift decreases from high values to the intermediate value of 9.04, indicating that the mean value is becoming larger. The structures are predominantly holes during this time and the increase of the mean reflects the growing size of the ionized regions. In the lower panel, we see that the probabilities again increase towards smaller values of r as the redshift drops below 9.04. This is due to the structures during this time being predominantly fragmented connected regions which are becoming smaller as ionization progresses. In the right panels showing δT_b we can see that the plots in the lower panel trace the corresponding plots for $x_{\rm HI}$, while those in the upper panels differ. This is again due to δT_b tracing $x_{\rm HI}$ during the later redshifts.

In Fig. (4.10) we show the PDFs of β for $x_{\rm HI}$ (left) and δT_b (right), for the same redshifts and smoothing scale as in Fig. (4.9). All the PDFs tend to zero as $\beta \to 1$, implying that exactly isotropic structures are improbable. In the top left panel for $x_{\rm HI}$ we can see that the peaks of the PDFs shift towards lower values of β as the redshift decreases. This reflects the fact that the mean shape of ionized bubbles becomes more anisotropic as explained earlier. Then in the bottom left panel we see that the peaks of the PDFs again shift back to higher values of β as the redshift decreases, and the turn over takes place around $z \sim z_{0.5}$. The PDFs of δT_b on the right again trace those of $x_{\rm HI}$ for lower redshifts and differ for higher redshifts.

4.3 Conclusion and discussion

So far we have proposed a new method based on the contour Minkowski Tensor to probe the shape and size statistics of ionized bubbles. These statistics reveal important time scales associated with the EoR. Our first result is that ionized bubbles are not isotropic in shape, as can be expected from visual inspection of simulations of the ionization fraction field, and

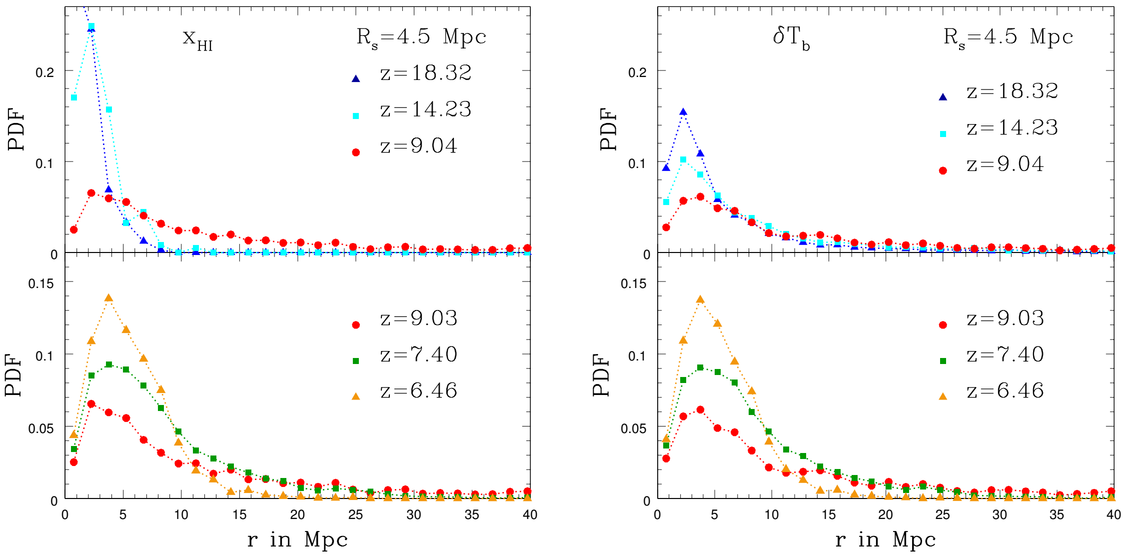

Fig. 4.9 PDFs of the size parameter r obtained from the ensemble of all curves, including both holes and connected regions, from all sampled threshold values, at different redshift for $x_{\rm HI}$ (left) and δT_b (right).

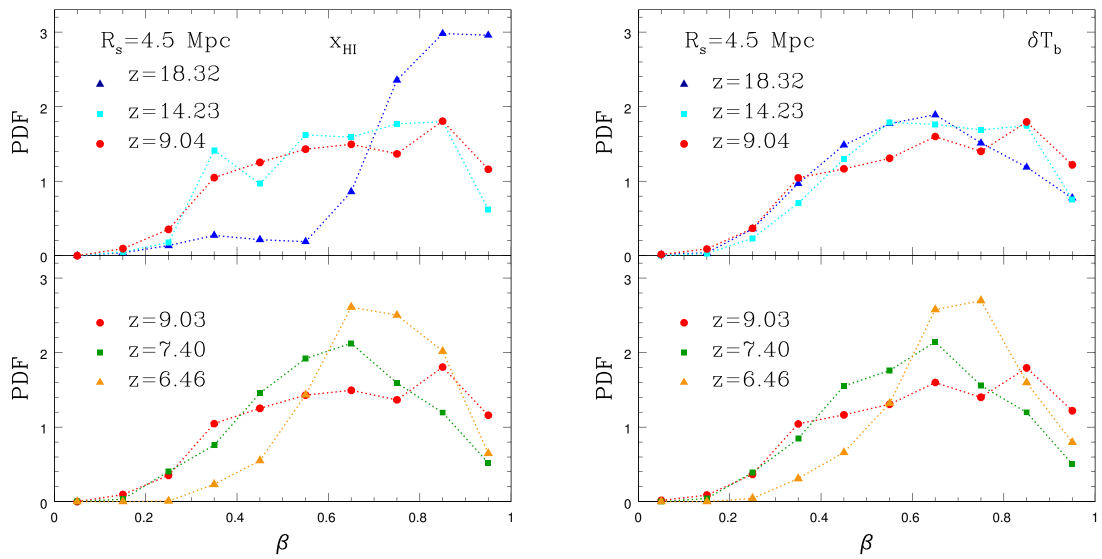

Fig. 4.10 Redshift evolution of the PDF of the shape parameter β obtained from the ensemble of all curves of our threshold sampling. The shift of the peak to lower β values implies that as the redshift decreases to roughly $z \simeq z_{0.5}$ the shape of ionized bubbles become more anisotropic. This is due to merger of bubbles becoming numerous. Then, as z decreases further below $z_{0.5}$, most mergers are over, and the PDF reflects the shape of connected (neutral) hydrogen regions, and their overall shape tends is less anisotropic.

our method gives a precise quantification of their complex morphology. Our second result is the quantification of the mean size of ionized bubbles and their redshift evolution. For the model of reionization considered in this chapter, we find that the characteristic radius of ionized bubbles grow to the value ~ 27 Mpc at $z_{0.5}$, independent of smoothing scales. We show that the variation of the size and shape parameter as a function of redshift reveal the time epochs when mergers of ionized bubbles become dominant over the creation of new ionizing sources, when maximum mergers happen, and when mergers end due to the entire region becoming ionized.

As shown in section 4.2.2, the value of the bubble size varies with the choice of the limits of integration over the standard normal field threshold. However, we emphasize that upon fixing the integration limits the result is unambiguous and can be compared meaningfully across different simulations (and observed data in the future) so as to understand the impact of variation of physical parameters of different models of the EoR. For the model that we have used in this work, our result is exact, upto the numerical inaccuracies of the Riemann sum that approximate the integrations. Further we have presented our result in the form of a radius of an idealized circle, in keeping with the usual discussions found in the literature. However, given the highly complicated shapes of the ionized regions it makes better sense to use the perimeter of the regions directly as a physical observable rather than an idealized radius. By defining an idealized radius, it makes it easier to compare our method with other methods in literature. As mentioned before, a comparison of the measure of scales with other methods in literature would only be feasible when extended to Minkowski tensors in 3D which we intend to carry out in the future.

The calculations shown in this chapter represent the first step showing the usefulness of the CMT in probing the EoR. We have focussed on developing the technique and applied it mainly to the ionization field. In Fig. 2.3, we saw how different models can lead to entirely different topology of δT_b at a given redshift. We have demonstrated our results for only one history of reionization or model. The details of the redshift evolution - the precise shape of $r_{\mathrm{x}}^{\mathrm{ch}}$ and $\beta_{\mathrm{x}}^{\mathrm{ch}}$ versus z, and the location of the transition time scales are expected to vary depending on the details of the reionization process. Thus, we expect that our method will be useful to test different models of reionization which is elaborated in chapter 5. We reiterate that our analysis is based on idealized simulations. The reliability and usefulness of our method in realistic observational scenarios where foreground contamination and instrument noise dominate the signal, needs to be investigated further. Moreover, the error bars that we have shown are obtained using two-dimensional slices from the three-dimensional simulations. The correlation that is inherent due to the slicing implies that our error bars are underestimated.

Given that the signal at the frequencies of interest are dominated by foreground signals by several orders of magnitude we can foresee that a sound understanding of the properties of the foregrounds themselves, as well as instrumental effects, will be necessary in order to reliably use our method on real data. We would also like to state that in general observed or simulated data is always discrete whereas theoretical fields are continous. Hence, recovery of theoretically expected topological statistics will be affected by errors arising as a result of field discretization. The errors mainly arise as result of shot noise at the level of pixel resolution. But this is taken care of by smoothing the discretefields. Ideally the fields must be smoothed at a minimum scale, which is equivalent to about four to five pixels, so as to avoid both shot noise and structures which are very small (for which identifying contours in marching square algorithm would introduce errors due to discretization (Appleby et al., 2018a)). In our current and future analysis, this smoothing scale is chosen by considering this point. Moreover, we ensure that it is not below the scale corresponding to the resolution of the instrument whose data we intend to use in future. Another point worth mentioning is that one can expect degeneracies that will arise between a choice of the threshold of interest and the physical quantities that have cosmological and astrophysical variations. Any change in the model would also cause a variation in the overall statistics of the field. Our method of choosing a mean subtracted and normalized field threshold, therefore takes care of such degeneracies. Even if we do not normalize the field, our method of taking an average over thresholds will do away with such degeneracies, since the overall area under the curve is independent of the way the field threshold is defined.

5

Morphology of the 21cm Brightness temperature: Model Comparison

5.1 Motivation

It was described in chapter 2 that the brightness temperature field is actually dependent upon the evolution of the large scale structure via density fields δ, evolution of heating via spin temperature T_S and the ionization history via the neutral hydrogen fraction x_{HI}. The goal of this chapter is to trace the history of the IGM during EoR for different astrophysical scenarios and to demonstrate how they can be discriminated by using the methods developed in chapter 4. We track the morphological properties encoded in the Betti numbers and CMT of the fluctuations in the density, ionization and spin temperature fields. We qualitatively analyse the redshift evolution of the morphology of these fields and show how their evolution is traced by the brightness temperature field as different signatures in the redshift evolution of it's CMT and Betti numbers. We identify three regimes in the redshift evolution of Betti numbers and CMT of the brightness temperature field which encode the underlying evolution of the IGM in terms of it's heating and ionization history. We also show how different astrophysical scenarios leading to different IGM histories result in a shift of these regimes. Our analysis uses simulations of the EoR, obtained using the publicly available code `21cmFAST` (section 2.3).

The chapter is organized as follows. In section 5.1.1 we describe the different astrophysical models we consider. In sections 5.2 to 5.4 we analyse the simulated density, ionization and spin temperature fields. In section 5.5 we describe how the morphology of brightness temperature encodes the morphological evolution of all other fields during EoR and hence the heating and ionization history of the IGM. We end with discussion of our results in section 5.6.

5.1.1 Description of models of reionization

In order to study the morphology of the cosmological fields during epoch of reionization we have generated δ_{nl}, x_{HI}, T_S and δT_b fields on a 512^3 grid of a $(200\ \mathrm{Mpc})^3$ box using 21cmFAST(v1.3). This gives a pixel resolution of ~ 0.4 Mpc. The initial conditions are generated on a 1024^3 grid at a redshift of $z = 300$. Different parameter sets describe different ionization and heating scenarios which affect the fluctuations and global evolution of x_{HI} and T_S fields. It is to be noted that the evolution of the δ_{nl} field is only affected by the initial conditions and the cosmology adopted in 21cmFAST (section 2.3).

We choose a *fiducial model* described by a fixed set of parameter values for the ionization efficiency ζ (eq. 2.31), minimum value of T_{vir} (eq. 2.31) for a halo to collapse and x-ray heating efficiency ζ_X (eq. 2.38). We do not include inhomogenous recombination (eq. 2.37) for the brightness temperature calculation of our *fiducial model* and choose a fixed X-ray spectral index of $\alpha = 1.2$.

In order to compare different models, we change one or more of the parameters while keeping the others fixed, such that they describe a different astrophysical setting affecting one or more of the fields which determine the brightness temperature. This has been done to conveniently compare with the *fiducial model* and easily extend to any complicated history. Our choice of models is as follows:

- *Fiducial model*: $\zeta = 17.5$, $\zeta_X = 2 \times 10^{56}$, $T_{vir} = 3 \times 10^4$ K and $\alpha = 1.2$.
- *Recombination*: Model with the effect of inhomogenous recombination taken into account with the same set of parameters as the fiducial model.
- *Model with less massive sources*: $\zeta = 10.9$, $\zeta_X = 2 \times 10^{56}$, $T_{vir} = 1 \times 10^4$ K and $\alpha = 1.2$.
- *Model with more massive sources*: $\zeta = 23.3$, $\zeta_X = 2 \times 10^{56}$, $T_{vir} = 5 \times 10^3$ K and $\alpha = 1.2$.
- *Model with increased X-ray efficiency*: $\zeta = 17.5$, $\zeta_X = 1 \times 10^{57}$, $T_{vir} = 3 \times 10^4$ K and $\alpha = 1.2$.

The models have been chosen to yield the end of reionization roughly at $z_e \sim 6$ and optical depth to CMB $\tau_{re} \sim 0.05$ (Planck Collaboration et al., 2018). We choose population 2 stars as the stellar population responsible for early heating. The models adopted in this work represent simplified, parameterized ionization histories. In actuality the efficiency of heating and ionization would depend upon finer details and evolution of the astrophysical objects during the epoch of reionization. However the parameterized models considered here do give a general picture of IGM history in terms of globally defined parameters.

The *fiducial model* corresponds to $\tau_{re} \sim 0.054$. Including inhomogenous recombination delays the redshift at which reionization ends. Recombinations slow down the growth of ionized regions by depleting the number of photons available for ionizing. This depletion of photons is accounted for by $\bar{n}_{rec}$ in the criterion in Eq. (2.37) . The ζ values corresponding to $T_{vir} = 1 \times 10^4\ K$ and $T_{vir} = 5 \times 10^4\ K$ give optical depth values of $\tau_{re} \sim 0.058$ and $\tau_{re} \sim 0.052$ respectively. The value $\zeta_X = 2 \times 10^{56}$ for the *fiducial model* and $\zeta_X = 10^{57}$ correspond to 0.3 and one X-ray photon per baryon, respectively. For our analysis we choose the ΛCDM parameters as given in (Planck Collaboration et al., 2018).

The choice of T_{vir} determines the collapse fraction and hence it would affect the evolution of x_{HI} and T_S. ζ affects only the evolution of x_{HI} field while ζ_X affects T_S evolution and has very small effect on x_{HI} which decreases at lower z values relevant to the EoR as X-rays contribute more to heating than to ionization there (Shull, 1979; Furlanetto & Stoever, 2010). The effect of inhomogenous recombination on x_{HI} becomes prominent during late stages of reionization (Sobacchi & Mesinger, 2014; Choudhury et al., 2009).

5.2 Morphology of Density field: δ_{nl}

As discussed in section (2.3), `21cmFAST` simulates δ_{nl} using the Zel'dovich approximation (Appendix B.5). In this section we follow the redshift evolution of the field as manifested in its morphological properties. Holes at negative threshold values correspond to voids while connected regions at positive thresholds correspond to peaks.

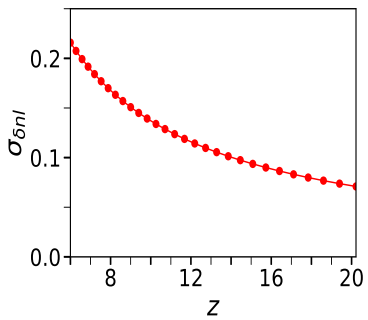

Fig. 5.1 Redshift evolution of the standard deviation, $\sigma_{\delta_{nl}}$, of the density field.

The increase in the amplitude of fluctuations of δ_{nl} is captured by the redshift evolution of the variance of the field, denoted by $\sigma^2_{\delta_{nl}}$. Fig. 5.1 shows $\sigma_{\delta_{nl}}$ versus redshift. As the density perturbations grow, the high density peaks increase in height at the cost of low density regions which become more under dense. In the linear regime, this growth is described as $\delta(z) = \delta_o/(1+z)$, where δ_o is the initial density contrast. This leads to the increase in $\sigma_{\delta_{nl}}$ that we observe in the plot. The relatively large smoothing scale of 4.5 Mpc adopted for our analysis ensures δ_{nl} remains approximately linear for the redshift range that is under consideration.

In Fig. 5.2 we show the variation of the morphology of δ_{nl} with the field threshold ν. The quantities are plotted as the mean over the 32 slices for a given ν value. Due to low statistics at very high and very low ν values we plot the variation up over the range $-2 < \nu < 2$. As done in section 3.2 we remove structures which have an area > 0.9 times the area of the slice. In Fig. 5.2a we plot n_{con}, n_{hole} (top), r^{ch}_{con}, r^{ch}_{hole} (middle) and β^{ch}_{con}, β^{ch}_{hole} (bottom) as functions of threshold, at three redshift values $z = 16.41, 13.28$ and 10.26. Notice the shift in positions of error bars. This is due to the choice of our ν range between the maximum and minimum value of the field which changes with redshift. On visual comparison of n_{con} and n_{hole} with Fig. 3.4 we find that all three redshifts roughly have the shape expected from a Gaussian random field (see section 3.2). This is a consequence of the approximately linear evolution of density perturbations at the smoothing scale that we have chosen. Further, we find that the variation of both n_{con} and n_{hole} with redshift is small. For a decreasing redshift, we can discern a small increase in n_{con} for high positive thresholds $\nu \gtrsim 1$, while for n_{hole} we find a small decrease towards high negative thresholds, $\nu \lesssim -1$. This implies that in the high density regions that correspond to large positive ν, more sub-structure is forming as the redshift decreases. This is a consequences of peaks growing in height and hence a corresponding increase in n_{con} at these high ν values relative to those at higher z values. Peaks grow at the cost of low density voids making the density field positively skewed with decreasing redshift. At a given ν for a particular z value we observe that $n_{con} \neq n_{hole}$ .The differences become more pronounced with decreasing redshift. It is visually discernible at $\nu \sim |2|$. This assmmetry is indicative of non-gaussianity introduced by gravity. For a Gaussian field the values are expected to be symmetric about $\nu = 0$ (See Fig. 3.4).

The middle panel of Fig. 5.2a shows the variation of the sizes $\bar{r}_{con}$ and $\bar{r}_{hole}$ with threshold ν. We find that the size (perimeter) of connected regions around $\nu \sim -1$ is statistically larger than that of holes around $\nu \sim +1$. This is an interesting feature in tracking the non-Gaussianity of perturbations induced by gravitational collapse, since for a Gaussian field the two statistics should be symmetric about 0 (Fig. 3.4).

The bottom panel of Fig. 5.2a shows the variation of $\bar{\beta}_{con}$ and $\bar{\beta}_{hole}$ versus ν. Again these plots are close to the expected shape for Gaussian fields (Fig. 3.4). We can see very mild variation of the shape with redshift at intermediate ν values but differences at high and low ν values. The asymmetry between β_{con} and β_{hole} is not as pronounced as for $n_{con,hole}$ and $r_{con,hole}$.

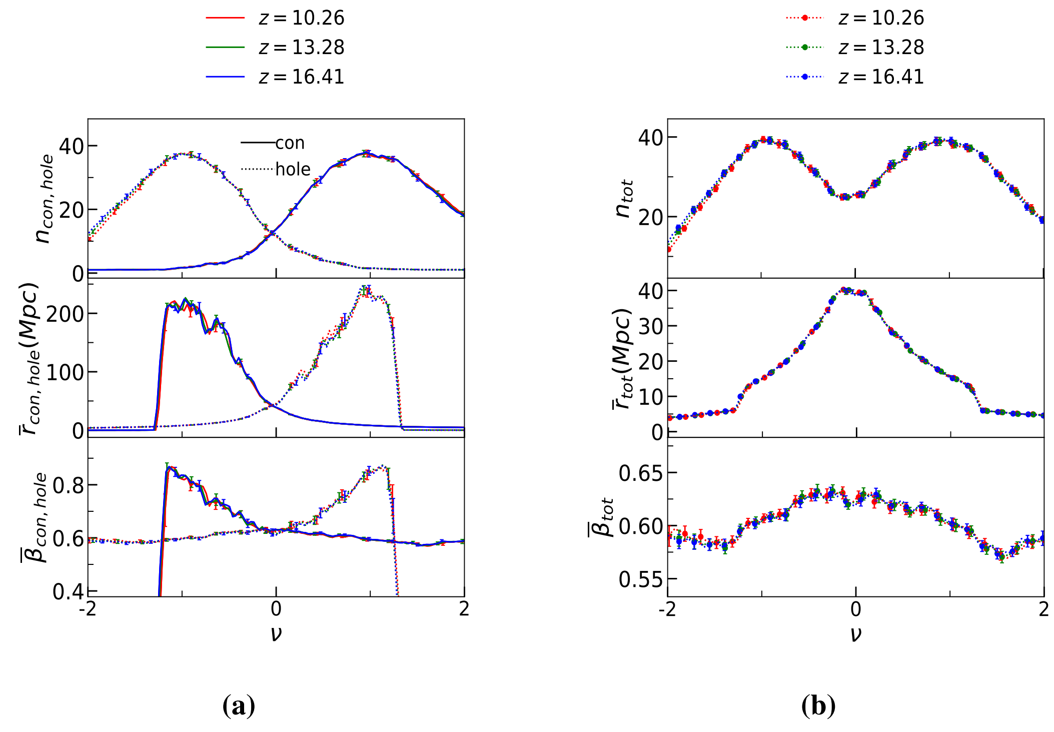

Fig. 5.2 (a) $n_{con,hole}$ (top), $\bar{r}_{con,hole}$ (middle) and $\bar{\beta}_{con,hole}$ (bottom) versus ν at redshifts 10.26 (red), 13.26 (green), and 16.41 (blue). (b) n_{tot} (top), $\bar{r}_{tot}$ (middle) and $\bar{\beta}_{tot}$ (bottom) with ν, for the three redshift values as above. The error bars denote the error in mean over 32 slices.

In Fig. 5.2b we plot the variation of n_{tot}, $\bar{r}_{tot}$ and $\bar{\beta}_{tot}$. These plots combine the information contained in 5.2a in such a way that most of the contribution for positive threshold values comes from connected regions, while for negative threshold values the contribution comes from holes. This is seen in the top panel of the figure for n_{tot}. At lower ν values $n_{hole} > n_{con}$ while $\bar{\beta}_{hole} < \bar{\beta}_{con}$. At these ν values the total morphology is a result of the morphology of the single large connected region punctured by numerous holes. Note that we have excluded the single large connected region at low thresholds and so the morphology is purely due to holes at $\nu \lesssim -1.5$. Opposite trend is expected for high ν values. The effect of the single large connected region and hole is very pronounced in the statistic r_{tot} as it is a dimensional quantity unlike $\bar{\beta}_{tot}$. We see a tilt in $\bar{r}_{tot}$ and $\bar{\beta}_{tot}$ towards higher ν values. Since $\bar{\beta}_{con}$ and $\bar{\beta}_{hole}$ are almost symmetric about $\nu = 0$, the tilt in $\bar{\beta}_{tot}$ can be attributed to the asymmetry between n_{con} and n_{hole} at these thresholds. The tilt is more pronounced at lower z values as the difference between n_{con} and n_{hole} is more for lower redshifts.

In Fig. 5.3 we plot the redshift evolution of N_x, r_x^{ch} and β_x^{ch}, plotted as a mean of the integrals defined in Eqs. 4.1, 4.3 and 4.4 respectively over the 32 slices under consideration.

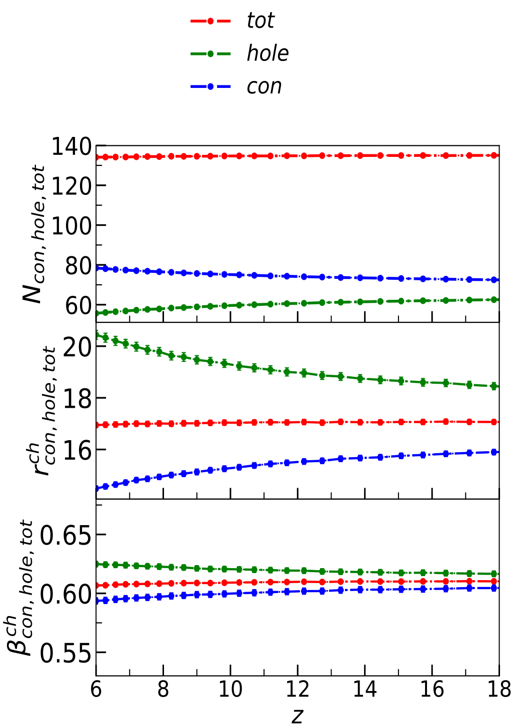

Fig. 5.3 Redshift evolution for sum over all thresholds for connected regions (*blue*), holes (*green*) and for all structures (both connected regions (*red*)) described by $N_{con,hole,tot}$ (*top*), $r^{ch}_{con,hole,tot}$ (*middle*) and $\beta^{ch}_{con,hole,tot}$ (*bottom*). The error bars denote the error in mean of the integrals in eq. 4.2, 4.3 and 4.4 over the 32 slices.

The error bars are calculated as an error in mean over these 32 slices. Note that we follow the same methodology for calculation of the redshift evolution for all other fields in the subsequent sections. These plots contain the physical information encoded in Fig. 5.2 condensed into a single number at each redshift value. The limits of the ν integration, $\nu_{\rm high}$ and $\nu_{\rm low}$, are set to be the maximum and minimum values of the field.

The top panel indicates that the numbers of connected regions and holes integrated over all threshold values decreases as a function of redshift. The middle panels shows that the size of high density regions, integrated over all thresholds, shrink in size as the redshift decreases. In contrast the size of holes (voids) grow with decreasing redshift. This is due to the attractive nature of gravitational collapse. In the bottom panel we find that β_x^{ch} does not show much variation with redshift z and that the connected regions are more anisotropic than holes. This can be attributed to the fact that a higher density anisotropic region would become more anisotropic due to formation of *Zel'dovich Pancakes* (Appendix B.5).

5.3 Morphology of neutral hydrogen fraction field: x_{HI}

The morphology of the neutral hydrogen field was studied in Chapter 4 for different smoothing scales and different values of ν_{cut}. ν_{cut} refers to the value of threshold above (below) which a connected region (hole) is interpreted as a neutral (ionized) region. In this work we choose to work with $\nu_{cut} = 0$, which is the mean value of the x_{HI} field. The choice of ν_{cut} allows for the inclusion of extremely small peaks or shallow valleys at lower and higher z values where the variance ($\sigma_{x_{HI}}$) of the x_{HI} field is very small (Fig. 5.4).

It was found that for this choice of ν_{cut}, $N_{con} \sim N_{hole}$ at $x_{HI} = 0.5$. For the x_{HI} field, a connected region corresponds to a neutral region and a hole corresponds to an ionized region. Ionized bubbles grow in size and merge. The rate of formation and growth of ionized bubbles, their sizes and the rate at which they merge depend upon the astrophysical properties of the collapsed objects and mean free path of ionizing photons. Statistically, mergers of ionized bubbles lead to an increase in anisotropy of the bubbles as expected and demonstrated in Chapter (4). One would expect that locally apart from mergers, the anisotropy in the growth of a bubble could also depend upon the clumpiness of the density field around it. Therefore for two objects with the same astrophysical properties the bubble around one could be more anisotropic than the other because of more clumpiness in the distribution of neutral hydrogen around it. However for a given matter power spectrum the *average* anisotropy of structures (as measured by $\overline{\beta}$) in our excursion set of ionized field can be attributed to mergers alone. The number of mergers depend upon the astrophysical properties of sources.

The different transition redshifts describing the evolution of morphology of the neutral hydrogen field as defined in Chapter 4 are z_{frag}, $z_{0.5}$ and z_e. We define z_{re} as the redshift at which EoR ends, i.e. $\bar{x}_{HI} \sim 0$. The values of these transition redshifts will depend upon the different physical processes of reionization, and hence on the model of EoR. Therefore, their values can be important characteristic features that can discriminate different models. Note that in Chapter 4 it was found that at $z_{0.5}$, $N_{con} = N_{hole}$. We will show this to be true for all models we have considered in our study.

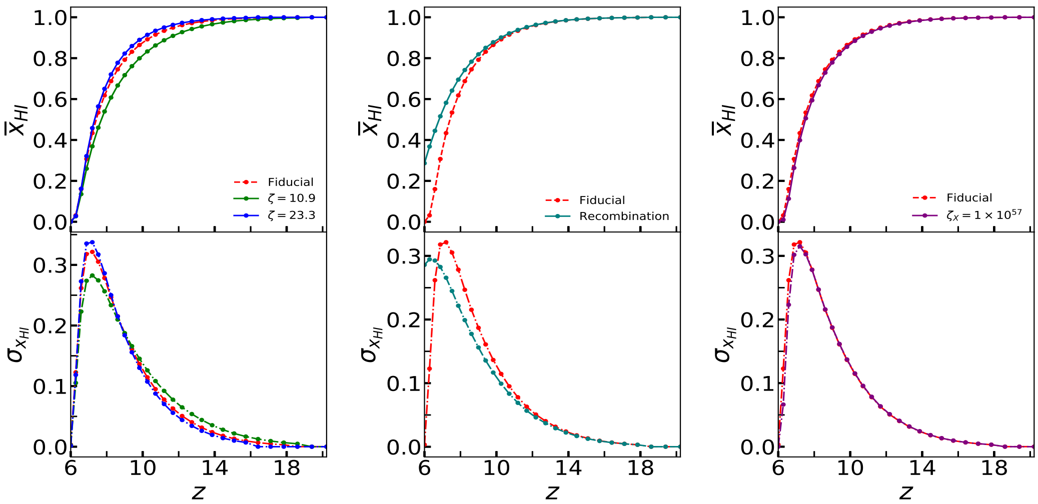

Fig. 5.4 Evolution of mean and standard deviation for neutral hydrogen field, x_{HI} for different models, relative to the *fiducial model* in red.

In Fig. 5.4, we show the evolution of $\bar{x}_{HI}$ and the rms fluctuation of x_{HI} denoted by $\sigma_{x_{HI}}$ for all models under consideration. In order to obtain an ionization history of the IGM it would suffice to obtain the various transition redshifts of the evolution of morphology as described summarized in Table 5.1 and observe how they shift relative to the *fiducial model*. However, for a detailed astrophysical modelling, one would have to compare at redshift values corresponding to the same epoch in the ionization history as described by Table 5.1. Therefore in addition to comparing the general shift in the values of z_{frag}, $z_{0.5}$ and z_e, we also compare the morphological descriptions specifically at these transition redshifts. The values of redshifts obtained for these transition are not exact because the simulations generate fields at discrete z values (logarithmic interval of 1.0404 in $(1+z)$ for our case).

In the following subsections, we interpret and describe the morphology of the x_{HI} field for our choice of models.

Model	z_{frag}	$z_{0.5}$	z_e	z_{re}	τ_{re}
Fiducial	~ 11.69	~ 7.407	~ 6.58	~ 6.28	~ 0.054
$T_{vir} = 1 \times 10^4 K$	~ 13.857	~ 7.698	~ 6.58	~ 6.00	~ 0.058
$T_{vir} = 5 \times 10^4 K$	~ 11.194	~ 7.32	~ 6.58	~ 6.00	~ 0.052
$\zeta_X = 1 \times 10^{57}$	~ 12.73	~ 7.5	~ 6.58	~ 6.28	~ 0.034
Recombination	~ 12.2	~ 6.8	–	< 6.00	

Table 5.1 Model histories chosen for our analysis. The table shows the redshift $z_{0.5}$ at which $\bar{x}_{HI} = 0.5$, z_{frag} at which fragmentation starts, z_e where mergers complete and z_{re} where reionization ends. The last column is the optical depth to the last scattering surface.

5.3.1 Models with different T_{vir} values

As noted in section 5.1.1, different combinations of T_{vir} and ζ can give similar ionization histories. However the fluctuations in x_{HI} field are expected to differ. This is because a lower T_{vir} value corresponds to less efficient sources as compared to higher T_{vir} values. This is reflected in the respective ζ values required for reionization to end at the same z_{re}. The sources with lower T_{vir} values would lead to a higher collapse fraction at a given redshift as compared to higher T_{vir} and hence would be more numerous. Therefore reionization will start earlier for a lower T_{vir} value. Such sources would lead to bubbles which are more numerous and smaller in size at a given redshift as compared to sources with higher T_{vir} values. Fig. 5.5 shows the redshift evolution of the morphology of the neutral hydrogen fraction field for different combinations of T_{vir} and ζ, as described by $N_{con,hole}$, $r^{ch}_{con,hole}$ and $\beta^{ch}_{con,hole}$.

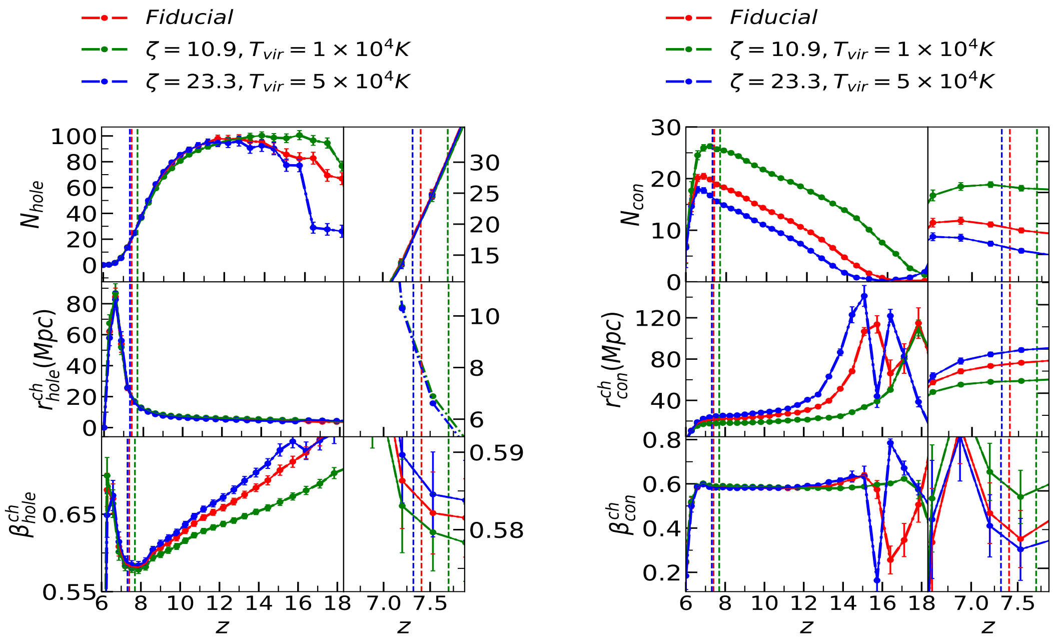

Fig. 5.5 The morphology of neutral hydrogen fraction for different values of T_{vir} and ζ for holes (*left panel*) and connected regions (*right panel*), relative to the *fiducial model*. The vertical lines show $z_{0.5}$ where $\bar{x}_{HI} = 0.5$ and $N_{con} = N_{hole}$ for $\nu_{cut} = 0$. The smaller panels on the right show a zoomed in version of the same plots to capture the variations around $z_{0.5}$.

The left panel of Fig. 5.5 reflects our qualitative reasoning. More numerous bubbles are reflected in the higher value of N_{hole} for the lowest T_{vir} value of 1×10^4 K until $z \sim z_{frag}$. We note that z_{frag} is highest for the model with the lowest T_{vir} value, i.e. mergers begin to dominate earlier. This leads to a shift of $z_{0.5}$ and z_e to higher z values for lower T_{vir} values. This occurs because even though the sources are less efficient, they are more numerous. This leads to a correspondingly higher number of bubbles and hence merging begins to dominate at a z value earlier than cases where T_{vir} is greater. The differences in N_{hole} for different models is less pronounced once mergers dominate the morphology as seen in the zoomed panel at $z = z_{0.5}$ for N_{hole}. However they differ in morphology. The plot of r^{ch}_{hole} and the zoomed panel, show that the size of bubbles at $z_{0.5}$ is smallest for the lowest value of T_{vir}. Bubbles for lower T_{vir} values are more anisotropic at $z_{0.5}$ as is seen for their β^{ch}_{hole} values. The large bubbles formed as a result of mergers for the case of smaller T_{vir} values is a consequence of more numerous and faster rates of merging as compared to larger T_{vir} values. More mergers statistically increases anisotropy by $z = z_{0.5}$ as seen in the relatively smaller values of β^{ch}_{hole} for smaller T_{vir} values.

The right panel of Fig. 5.5 shows the variation of N_{con}, r^{ch}_{con} and β^{ch}_{con}. We notice that the connected regions are more numerous for smaller T_{vir} values across the redshift range of interest.

This is because they are less efficient sources and even if there are more mergers the number of efficient photons available to ionize the regions with same density is less than for the *fiducial model* for which the sources are more efficient. The large neutral region that fragments will fragment into smaller sized neutral regions in the case of more mergers. Therefore an opposite trend is seen for r^{ch}_{con}. If a single large connected region is fragmented, then the model in which there are more fragments, the size of the fragments will be smaller. However we observe that the connected regions for lower T_{vir} are less anisotropic as seen in the zoomed in panel at $z = z_{0.5}$. This is opposite to the trend for holes. It is not straightforward to anticipate this trend but it indicates that more mergers are leading to fragmentation of connected neutral regions into less anisotropic peices.

5.3.2 Model with inhomogenous recombination

The morphology of ionized fields when inhomogenous recombination is included in the excursion set formalism has been studied in ((Sobacchi & Mesinger, 2014; Choudhury et al., 2009)) using the power spectrum of the 21cm brightness temperature, δT_b. Here we carry out a complementary study in real space. The prescription for incorporating inhomeogenous recombination is described in eq. (2.37). The rate of recombination in a region with number density of electrons n_e is $\propto \langle n_e^2 \rangle$. The effect of recombination manifests some time after reionization begins ($z \lesssim 12$ from visual inspection of Fig. 5.4) and becomes more pronounced with decreasing redshift. At early stages the number of photons is insufficient to ionize hydrogen in high density regions. Therefore only the lower density regions are ionized, where ionization dominates over recombinations. Therefore at this stage, recombination is unimportant in both high and low density regions. At later times as the collapsed fraction increases, the photons are able to permeate higher density neutral regions and ionize. But in those regions the rate at which recombination occurs is faster than the rate at which the photons are ionizing. The increased number of recombinations lead to decreased efficiency of ionization when compared with the *fiducial model* due to a paucity of ionizing photons in high density regions. Therefore at these late redshifts some higher density regions which would have otherwise been ionized in case of the *fiducial model* remain neutral.

The important salient point is that when comparing with the *fiducial model*, the rate of appearance of newer ionized regions is the same but the rate of growth and merger of ionized regions is different in the two cases. Inhomogenous recombinations slow down the entire process of growth and mergers. The inhomogenity in the density distribution introduces an additional anisotropy in the excursion set morphology beyond the anisotropy due to mergers alone. The redshift at which the EoR ends for the model with recombination is $z_e < 6$. But here we shall only analyse recombination until $z = 6$ so that we can compare with the *fiducial* *model*. In Fig. 5.6 we show the effect of inhomogenous recombination relative to the *fiducial model* and from Table 5.1 we see that the different transition redshifts in the evolution of x_{HI} morphology are shifted to lower z values relative to the *fiducial model*.

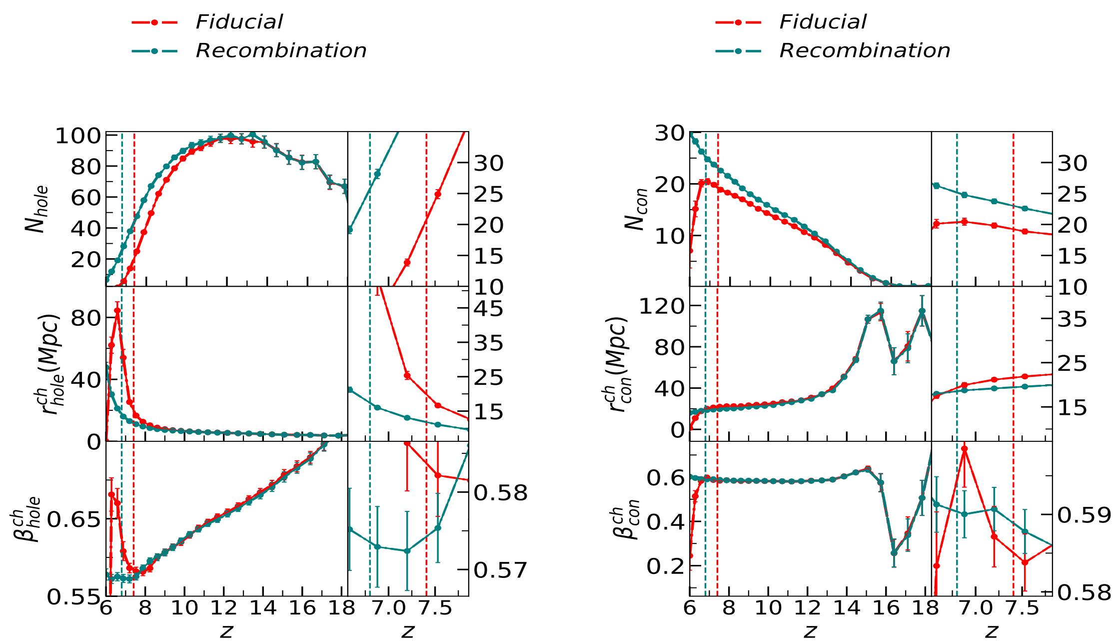

Fig. 5.6 The morphology of neutral hydrogen fraction with inhomogenous recombination relative to the *fiducial model* without recombination. The vertical lines show $z_{0.5}$. The smaller panels on the right show a zoomed in version of the same plots to capture the variations around $z_{0.5}$ which is midway through ionization history and $N_{con} = N_{hole}$

The left panel of Fig. 5.6 shows the redshift evolution of N_{hole}, β^{ch}_{hole} and r^{ch}_{hole}. We observe that the number of holes for the model with recombination is nearly the same as that of *fiducial model* at very early redshifts until z_{frag}. At $z \sim 12$ they start diverging i.e. number of holes for the model with inhomogenous recombination is more than that for the *fiducial model*. This confirms that recombination has suppressed the number of mergers as compared to the *fiducial model* .

The variation of r^{ch}_{hole} with redshift shows that there is no substantial difference in bubble sizes as a result of recombination until $z \sim z_{0.5}$. At $z = z_{0.5}$, the model with recombination has bubble sizes smaller than the *fiducial model* with a difference in size ~ 3 Mpc. This is again a result of a smaller number of mergers relative to the *fiducial model*.

The variation of β^{ch}_{hole} with redshift shows that the value is nearly equal to the *fiducial model* until $z \gtrsim z_{0.5}$ where β^{ch}_{hole} is lower for the model with recombination by 1%. Moreover the turnover is more gradual in the case of the model with recombination due to the slowing down of the entire process of reionization as discussed above. At $z_{0.5}$ the value of β^{ch}_{hole} is less compared to that for the *fiducial model*. The higher anisotropy seen for the model with recombination is because of the inhomogenity in the density field.

The right panel of Fig. 5.6 shows the variation of the morphology for connected regions. The number of connected regions N_{con} is more for the model with recombination at $z < z_{frag}$. This is because the neutral regions in high density regions which could get ionized in the case of *fiducial model* remain neutral when inhomogenous recombination is included. Moreover the mergers in the case of inhomogenous recombination lead to merged ionized regions which are smaller due to suppresion at high density regions. This leads to fragmentation of the neutral region into correspondingly higher number of fragments. A higher number of smaller fragments generates a smaller value of r^{ch}_{con} compared to the *fiducial model*. We do not observe much difference between the two models for β^{ch}_{con} at $z = z_{0.5}$. At this z value the connected regions of the *fiducial model* are high density neutral regions which cannot be ionized due to insufficient photons to ionize them. For the model with recombination the connected regions are either the ones where ionization never occured like in case of *fiducial model* or where ionization occured but recombination took over. The former regions are the same regions as in the case of the *fiducial model* while the latter regions would be holes in the *fiducial model* at the same z values because the efficiency of ionizing sources is the same in both the cases. Since N_{con} is different in the two cases at $z = z_{0.5}$, the β values show that the the connected regions in the case of the model with recombination are dominated by regions which did not ionize and are the same regions as the high density neutral regions at $z = z_{0.5}$ for the *fiducial model*.

We emphasise that the effect of including inhomogenous recombinations to our *fiducial model* leads to a shift in the redshifts of transitions, towards lower z values.

Model	$r^{ch}_{z_{0.5}}$ (Mpc)
Fiducial	$\sim 20.5 \pm 0.78$
$T_{vir} = 1 \times 10^4 K$	$\sim 15 \pm 0.424$
$T_{vir} = 5 \times 10^4 K$	$\sim 22.5 \pm 0.96$
$\zeta_X = 1 \times 10^{57}$	$\sim 20 \pm 0.689$
Recombination	$\sim 17.5 \pm 0.548$

Table 5.2 The characteristic size of ionized regions at $z = z_{0.5}$ for the different EoR models under consideration. The errors are the error on mean over the 32 slices.

In Table 5.2 we summarize the characteristic bubble sizes for the different models at $z = z_{0.5}$. The characteristic bubble size at $z_{0.5}$ for our *fiducial model* is ~ 20.5 Mpc. For a linear increase in T_{vir}, the bubble sizes show a somewhat linear increase. This point will be revisited in chapter 6. The size of bubbles is reduced to ~ 17.5 Mpc once the effect of recombinations is accounted for.

5.4 Morphology of Spin Temperature field: T_S

In this section we analyse the morphology of the T_S field. As described in section 2.2.3, the evolution of T_S is a result of the evolution of T_{CMB}, T_K, x_c and x_α. For the redshift range under study the collisional coupling constant x_c satisfies $x_c \ll x_\alpha$ where x_α is the Ly-α coupling constant. This is because as the universe expands, the probability of collisions between e^-e^-, e^-H and $H-H$ decreases. The Ly-α coupling constant x_α depends upon the emissivity of sources capable of producing Ly-α transitions. Ly-α excitations occur due to emission from the first collapsed objects. Since Ly-α is a lower energy transition, excitation is possible by low emissivity sources, unlike X-rays which requires more efficient sources. Therefore, Ly-α coupling will precede X-ray heating of the IGM (See section 2.2.3). Ly-α does not contribute much to the heating of the IGM but couples T_S to T_K (Furlanetto & Stoever, 2010). Therefore, prior to X-ray heating while T_K is still following adiabatic cooling due to the expansion of the universe, regions with higher matter density will have higher value of x_α. Due to this reason the $x_\alpha T_K$ term dominates in the expression for T_S in eq. 2.21. In the redshift range under study $T_K < T_{CMB}$. Therefore $T_K \leq T_S \leq T_{CMB}$. Higher the value of x_α lower is the value of T_S and it approaches T_K. Otherwise it approaches T_{CMB}. If $x_\alpha \gg 1$ and $T_{CMB}^{-1} \ll x_\alpha T_K^{-1}$ then Ly-α coupling saturates which means $T_S \sim T_K$. In regions where coupling due to Ly-α is still inefficient, T_s will be higher than T_K but less than T_{CMB}, as can be seen from eq. 2.21. Therefore prior to X-ray heating, any fluctuation in the matter density field will lead to fluctuations in f_{coll} and hence x_α (see eq. 2.41 and the paragraph following it) which further leads to fluctuations in T_S. Note that in this regime, T_K is not fluctuating but follows adiabatic cooling due to the expansion of the universe. Eventually Ly-α coupling saturates in most of the IGM, where T_K is coupled to T_S. Meanwhile, X-ray heating starts in very high density regions and T_K begins to rise. In these regions the fluctuations in T_S are a result of the fluctuations in T_K. Since X-rays have large mean free path compared to ionizing ultraviolet, the effect of X-ray heating is not as localized as ionizing radiation around high density regions and soon permeates the entire IGM, until all of the IGM is under the influence of X-ray heating. Thereafter, the fluctuations in T_S are completely determined by the fluctuations in heating due to X-rays. Further, 21cmFAST assumes a power law spectra for X-rays, due to which most of the X-rays are soft X-rays and are immediately absorbed in their surrounding medium (hard X-rays would have larger mean free path and heating would not be as efficient as for soft X-rays (Fialkov et al., 2014).

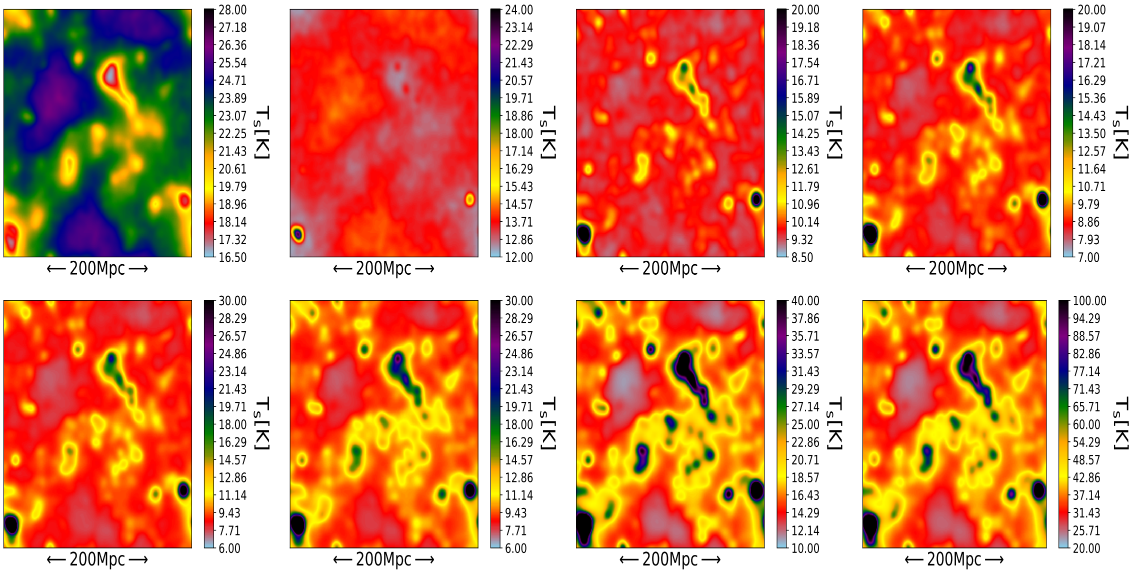

Fig. 5.7 Evolution of spin temperature with redshift at different redshifts for our *Fiducial Model*. *Top row: (Left to Right)* z=20.22, 18.60, 17.11 and 16.41. *Bottom row: (Left to Right)* z= 15.73, 15.08, 13.28 and 11.68. Note that since the range of field values vary with redshift, the color coding in the colorbar changes accordingly.

In Fig. 5.7, we exhibit the maps of T_S for our *fiducial model*. Note that the colour bars have different range for every map as the temperature ranges change with redshift. We describe the evolution from $z = 20.22$ to $z = 11.68$ and largely focus on interpreting the morphology at these redshift values. At lower redshifts, fluctuations in T_S are not reliable from 21cmFAST as the code does not take into account the effect of fluctuations in the ionization fields on the evolution of heating fluctuations (ionized regions cause difference in X-ray optical depth along different lines of sight), which will change the topology of heated regions and can be captured by radiative transfer codes such as (Ghara et al., 2015). We shall explore such more exact topologies as a part of our future work. Therefore, we shall not intereprett the T_S field below redshift values where $x_{HI} \lesssim 0.8$. Starting from the top left map at z=20.22 we find that the high density regions are cooler regions, surrounded by lower density warmer regions where Ly-α coupling is inefficient. Heating due to X-rays has not begun at this redshift. In the next panel at $z = 18.60$, some X-ray heated regions appear in places which correspond to the coolest regions in the maps at $z = 20.22$ (c.f. violet regions in the map). These are regions of highest density where emissivity of sources is sufficient for X-ray heating to start. The rest of the regions are still dominated by fluctuations in Ly-α coupling alone. Also notice that there is less scatter in the value of T_S at these redshifts and all of the IGM has temperature less than that at the previous redshift of $z = 20.22$, except for places where X-ray heating has started. The sky blue regions are the coolest, yet high density regions. In the next panel at $z = 17.11$ we see that in some of the coolest regions at $z = 18.60$, some new X-ray sources appear while the rest of the IGM decreases further in temperature (note the lower limit of the colour bar). On the other hand in regions where X-ray sources appeared at earlier redshifts, those heated regions have increased in size as the effect of X-rays starts permeating outwards. This same trend of newer X-ray sources appearing, the increase in size of older X-ray heated regions and the rest of the IGM decreasing in temperature, is seen until the map for $z = 15.08$. Thereafter we see that even the lowest temperature regions are increasing in temperature. Therefore fluctuations in T_S maps at $z \sim 13.28$ and $z \sim 11.68$ are dominated by fluctuations in X-ray heating. Now the cooler regions are regions which are far away from the X-ray sources where only a few X-ray photons have reached. At higher redshifts the number of X-ray photons is less, therefore the X-ray heated regions are more localized and outside IGM is following the fluctuations due to Ly-α coupling. At lower redshifts we see that heated regions grow in size and merge with nearby X-ray heated regions. At these redshifts the effect of X-rays is more pronounced as number of objects capable of X-ray emission have increased. Therefore they heat the over all IGM temperature. In actual it is the hard X-rays which are responsible for uniform heating, while soft X-rays heat up the immediate vicinity of the sources (Fialkov et al., 2014; Raste & Sethi, 2018). However, in this work we will stick to the basic treatment in 21cmFAST and would postpone other topologies of T_S to future work.

The evolution of $\overline{T}_s$ with z is shown in Fig. 5.8.

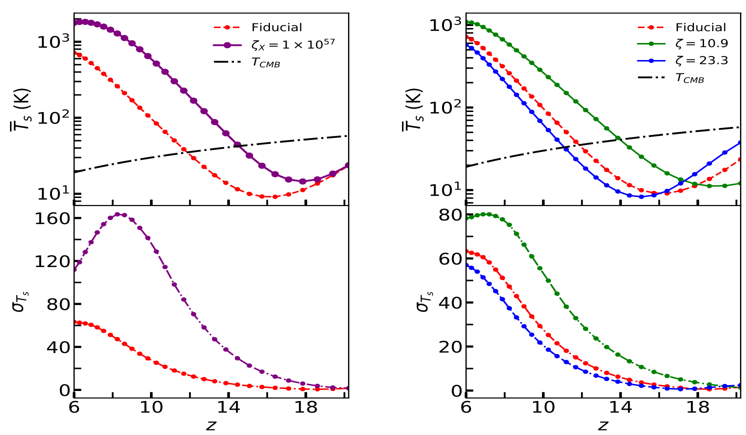

Fig. 5.8 Evolution of the mean and standard deviation for spin temperature with redshift, relative to the *fiducial model* for an enhanced X-ray heating efficiency in the (*left*) and different values of T_{vir} (*right*). The black dashed line marks the evolution of the temperature of the CMB.

As X-ray heating starts to dominate over adiabatic cooling due to the expansion of the universe, the evolution of T_S shows a turnover from an initial period of decrease (at $z \lesssim 16.4$ in the case of our *fiducial model*). This appears as an absorption peak in the $\overline{\delta T_b}$ evolution (**?**). Now T_K is also a fluctuating component as heating starts around high density regions. It is the fluctuations in T_K that dominate the fluctuations in T_S at the redshifts where X-ray heating dominates. In Fig. 5.9, we show the morphology of T_S for models with a different X-ray heating efficiency, while Fig. 5.10 shows models with different values of T_{vir} in comparison to the *fiducial model*. The connected regions correspond to hotter regions while holes correspond to low temperature valleys. We shall first focus on interpreting the T_S morphology for our *fiducial model* (plotted in red in Fig. 5.9 and Fig. 5.10).

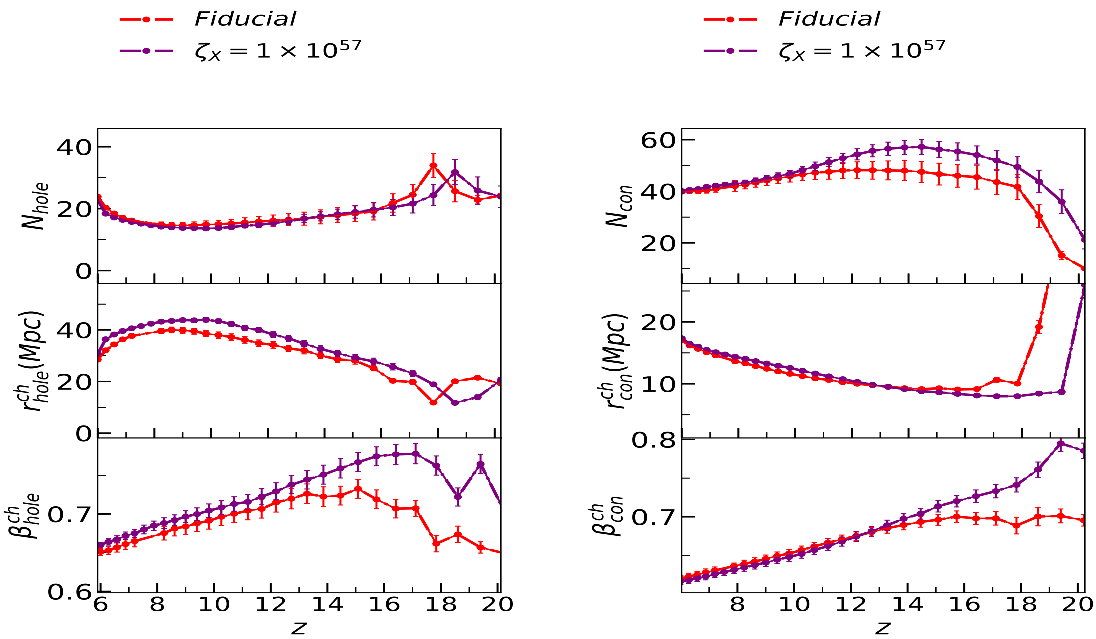

Fig. 5.9 The morphology of spin temperature T_S for the *fiducial model* relative to the model with an increased X-ray heating.

We see from the plot in the top panel of fig. (5.9) that initially until $z \gtrsim 18$, N_{hole} does not vary significantly while N_{con} is increasing with decreasing redshift. We find $N_{hole} > N_{con}$. This shows that initially when Ly-α coupling dominates the field, the morphology is dominated by holes. These holes are the cooler regions where Ly-αcoupling is more efficient, surrounded by higher temperature regions where the coupling is inefficient. These surrounding relatively higher temperature regions (which would be a single large connected region punctured by holes) and one or two scattered X-ray heated regions correspond to connected regions (which would be isolated small connected regions inside holes which are lying inside the single big connected region described above). As described in the maps above, the coolest regions at an early redshift become sites where X-ray sources appear at later redshifts. Therefore regions which correspond to holes switch over to connected regions later on. This leads to a decrease in the number of holes and an increase in the number of connected regions with redshift as more X-ray sources begin to appear.

The evolution of r^{ch}_{con} and r^{ch}_{hole} in the middle panel shows an initial drop in r^{ch}_{con} until $z \sim 18$. At these high redshifts (c.f. map for $z = 20.22$ in Fig. 5.7), connected regions correspond to larger hotter regions adiabatically cooling in the low density voids. Later very small X-ray heated regions start appearing around sources. As more X-ray sources appear, the average of the sizes starts to be dominated by the connected regions corresponding to X-ray heated regions (isolated small connected regions inside holes). Therefore we observe a drop in r^{ch}_{con}. After $z \sim 17$ the morphological properties of connected regions are morphologies of X-ray heated regions. These X-ray heated regions grow and merge with nearby X-ray heated regions. Therefore there is an increase in r^{ch}_{con} with redshift.

As X-ray heating dominates, connected regions correspond to higher temperature regions concentrated around high density regions and holes are coooler regions far away from the X-ray sources. As heating proceeds, these X-ray heated regions grow in size. Therefore we get a mild increase in r^{ch}_{con} . The evolution of r^{ch}_{hole} also shows an increase with redshift. This is because initially the holes are those concentrated around Ly-α efficient sources. Inside these holes X-ray heating starts taking place and the inner regions of the holes now host connected regions. Since, r^{ch}_{hole} is an average over the thresholds for holes, it would have contribution from the outer bigger contours of the holes and as the inner ones are now occupied by connected regions, they also have an inner boundary (the holes would be like a ring around connected regions due to X-ray heated regions on the inner boundary and inefficiently coupled relatively hotter regions on the outer boundary (c.f. the skyblue regions around X-ray heated sources in the panel for $z = 18.60$) in Fig. 5.7). Therefore the overall size of the holes increases as X-ray heated regions concentrate in the inner regions of holes and expand. At later redshifts the holes are the coolest regions which are far away from X-ray sources and are influenced by few X-ray photons reaching them (c.f. the map for $z = 13.28$ and 11.68 in Fig. 5.7). Therefore the evolution is not as rapidly changing at these later redshifts.

The bottom panels of figures 5.9 and 5.10 describe the evolution of β^{ch}_{hole} and β^{ch}_{con}. The variation of β^{ch}_{con} shows constant evolution for early redshifts and a steady decrease thereafter. The initial constant evolution is because initially the connected regions do not evolve much as these are in low density voids where Ly-α coupling is inefficient and the effect is that of uniform adiabatic cooling. The shape of these regions is not affected until the effect of X-ray heating reaches them. They may also correspond to scattered but few X-ray heated regions where X-ray heating has just started. These regions would be localized peaks around X-ray sources and would be isolated. Therefore other than a change in size there is no change in the shape of these regions. As X-ray heating proceeds to uniformity, these regions merge with nearby X-ray heated regions which leads to an increase in anisotropy. On the other hand β^{ch}_{hole} shows a decrease in anisotropy initially, followed by an increase around $z \sim 18$. The gradual transition from this initial increase to a decrease around $z \sim 15$ is due to a flip in the interpretation of holes as regions in low density voids where the effect of X-ray heating has not reached. These are not localized regions, unlike the cooler regions at earlier redshifts.

In Fig. 5.9 we show the redshift evolution of $N_{hole,con}$, $r^{ch}_{con,hole}$ and $\beta^{ch}_{con,hole}$ for the model with increased X-ray heating efficiency ($\zeta_X = 1 \times 10^{57}$). We find that the overall shape of the plots is the same while there is a general shift towards higher redshifts. This is because an increased X-ray emissivity leads to an early heating of the IGM. Note that the collapsed fraction is the same at a given redshift in both the cases, only the X-ray emissivity is higher for a greater value of ζ_X.

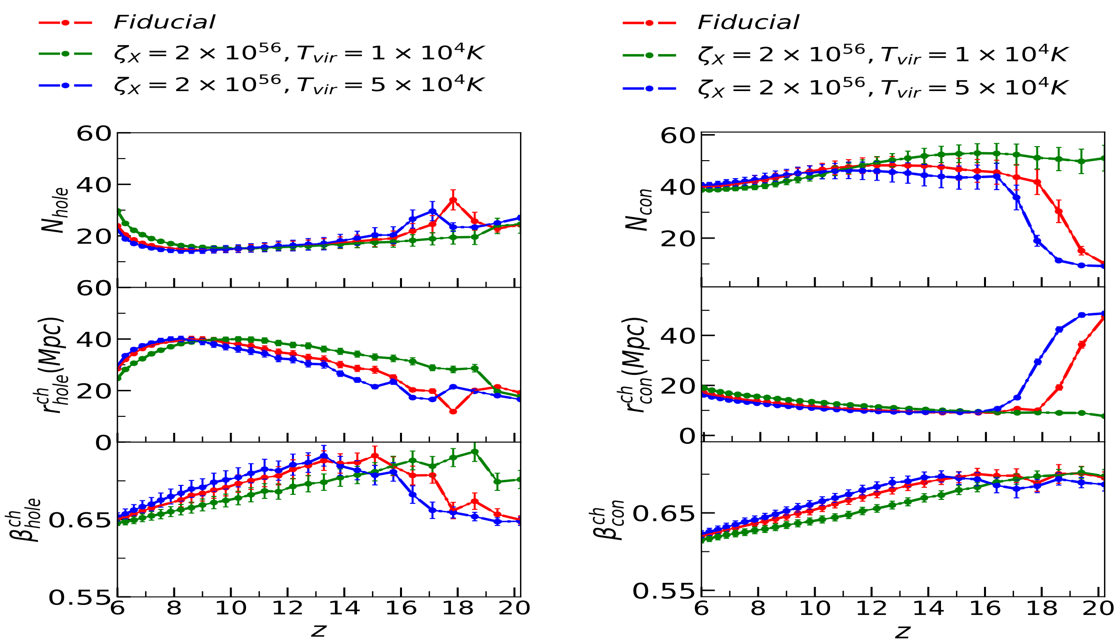

Fig. 5.10 The morphology of spin temperature T_S for the *fiducial model* relative to the models with different T_{vir} values.

In Fig. 5.10 we show the redshift evolution of $N_{hole,con}$, $r^{ch}_{con,hole}$ and $\beta^{ch}_{con,hole}$ for the models with different T_{vir} values. The error bars denote the error in mean over 32 slices. Note that here the X-ray heating efficiency is the same for all the three cases (i.e. $\zeta_X = 2\times10^{56}$). We observe that the shape of the plots is the same apart from a shift towards higher z values for lower T_{vir} (less massive) sources. Lower T_{vir} leads to a higher collapse fraction at a given redshift relative to higher T_{vir} values. Therefore there are more numerous sources which leads to this shift towards higher z. However the overall X-ray emissivity would be lower. Therefore the redshift evolution is more gradual for the lowest T_{vir} values. This trend can be seen in both Fig. 5.8 and Fig. 5.10.

5.5 Morphology of the Brightness Temperature field: δT_b

The evolution of the brightness temperature δT_b is determined by the evolution of x_{HI}, T_S and δ_{nl} fields. The fluctuation in δT_b is sourced by those in δ_{nl} until the growing non linearities become important. However as the first objects form, which is a highly non linear process and reionization and X-ray heating progresses, the fluctuations are not directly sourced by the underlying density fluctuations but by the processes of heating and ionization. In Fig. 5.11 we

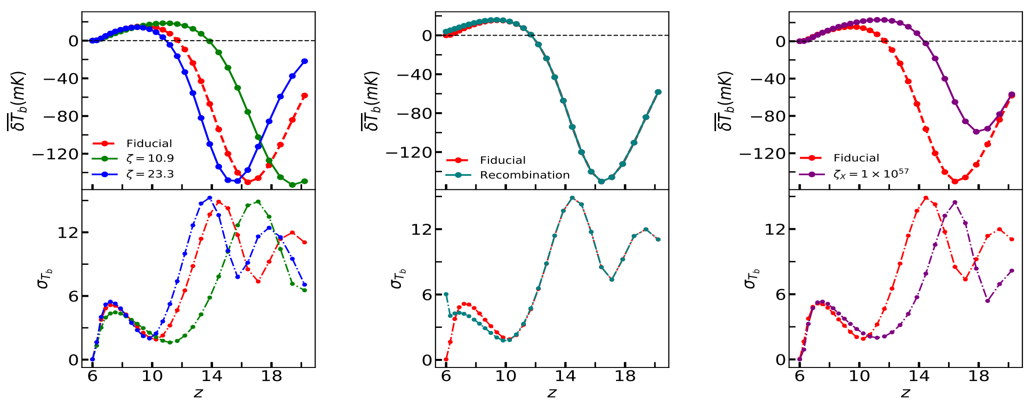

Fig. 5.11 The evolution of the mean 21cm brightness temperature δT_b for the different models, relative to the *fiducial model* (in Red).

show the redshift evolution of the average brightness temperature $\delta\overline{T}_b$ and its standard deviation σ_{T_b} for the various models under consideration. Transitions or turnovers are as expected for different models (Furlanetto, 2006). The main transition points are the dip where X-ray heating dominates over Ly-α coupling, followed by the transition point where the fluctuations due to ionization dominates (i.e. where the plot crosses the horizontal dashed line to a positive δT_b value). The evolution of σ_{T_b} shows three peaks. The first peak at the highest z values corresponds to the regime where the fluctuations in Ly-α coupling dominates and saturate. This is followed by the second peak which describes the regime where fluctuations due to X-ray heating take over and saturate. The third peak is due to the fluctuations in x_{HI} field which dominate in this regime as reionization progresses.

In 5.12 we show the redshift evolution of the morphology of the brightness temperature field for the range of redshifts from $z = 20.22$ to $z = 6$ for our *fiducial model*. We also mark the redshifts where the transition epochs were observed for the evolution of x_{HI} morphology. We observe two more transition points and name them as z_{EoR} and z_{tr}.

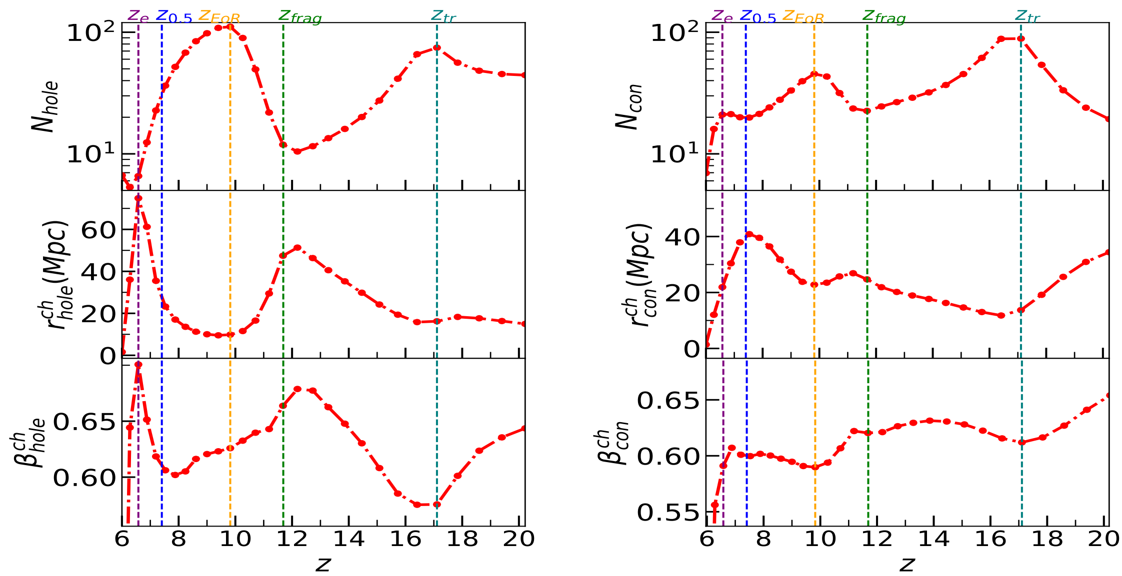

Fig. 5.12 The morphology of brightness temperature field δT_b, for *fiducial model* with $\nu_{cut} = 0$. The vertical lines (*purple, blue and teal*) mark the transitions observed for the x_{HI} field i.e. z_e, $z_{0.5}$ and z_{frag}. The redshift z_{EoR} (*orange*) marks the redshift below which the morphology of holes in the δT_b field directly trace the morphology of holes in x_{HI} field. The redshift z_{tr} marks the epoch before which the δT_b morphology is similar to T_S morphology and is dominated by fluctuations in the Ly-α coupling.

The redshift z_{EoR}, is where the redshift evolution of the morphology of holes in the brightness temperature field is similar to those in the x_{HI} field to 10% (elaborated further in the later part of the section). The redshift, z_{tr} is where the morphology of the brightness temperature field transitions from being similar to the morphology of T_S field to a regime where the morphology is an interplay between the morphology of T_S and x_{HI} fields. In Fig. 5.12 we focus on interpreting the evolution of δT_b morphology for the *fiducial model* to identify the transition redshifts mentioned above. Comparison of different models will be carried out later in the section. The fluctuations in δT_b arise from a product of fluctuations in x_{HI}, $(1+\delta_{nl})$, and $(1-T_{CMB}/T_S)$ It is not straightforward to interpret the individual contributions. We can identify roughly three regimes from Fig. 5.12.

- **Regime 1**: High redshift $z \gtrsim z_{tr}$

  As described in section 5.4 this is the regime where the fluctuations in T_S is dominated by fluctuations in Ly-α coupling described by x_α. The regions where coupling is more efficient correspond to valleys in T_S and are high density peaks in the density field. However the density fluctuations are smaller scale fluctuations (see $r^{ch}_{con,hole}$ in Fig. 5.3) compared to the fluctuations in T_S (see $r^{ch}_{con,hole}$ in Fig. 5.10) and do not evolve much with redshift. In this regime one can ignore x_{HI} in the product $x_{HI}(1+\delta_{nl})(1-T_{CMB}/T_S)$ because nearly all of the IGM is neutral and $\bar{x}_{HI} \sim 1$. Therefore the morphology of the fluctuations of δT_b is an interplay between the fluctuations of $(1+\delta_{nl})$ and $(1-T_{CMB}/T_S)$. Since fluctuations of δ_{nl} and hence that of $(1+\delta_{nl})$, do not show much variation with redshift, any evolution in the fluctuations of $(1-T_{CMB}/T_S)$ will determine the evolution of δT_b fluctuations, however the morphology will be affected by both. The difference in the scales of fluctuations and the fact that the x_α fluctuations are anti-correlated with those in the δ_{nl} field will reduce the overall value of $N_{con,hole}$ below that of δ_{nl} but more than that for T_S (also notice that the fluctuations in T_S in this regime have small variance as seen in Fig. 5.8). The numbers are however closer to the values for the T_S field. The increase in both N_{con} and N_{hole} with redshift is due to the corresponding evolution in the values for T_S field and has been described in section 5.4. Therefore the morphology of δT_b in this regime is dominated by that of T_S field, more specifically by the Ly-α fluctuations. This is further corroborated by the plots for $r^{ch}_{con,hole}$ in Fig. 5.12, where the values are similar to those for the T_S field. The shape of $\beta_{con,hole}$, shows an initial decrease which is not straightforward to understand as both δ and T_S field dominate in this regime. It is interesting to note that the dip in $\beta_{con,hole}$ corresponds to the peak in the $N_{con,hole}$ plots.

- **Regime 2**: Intermediate redshift $z \lesssim z_{tr}$ and $z \gtrsim z_{EoR}$

  This is the regime where no single field is expected to dominate the morphology. This is a phase where the δT_b morphology will transition from that which is determined completely by T_S to the one which is determined completely by x_{HI}. Therefore, within this transition period one would expect that the morphology of δT_b would go from a period where T_S dominates more than x_{HI} to a period where x_{HI} dominates more than T_S. Initially, for $z \gtrsim z_{frag}$ the morphology is dominated by T_S but determined by a combination of fluctuations in X-ray heating and Ly-α. In this regime Ly-α coupling is approaching saturation while several X-ray efficient sources start to appear. These correspond to highest peaks in the T_S field and positively correlate with the density field. This erases the smaller scale fluctuations in the field caused by the density field because X-rays have high mean free path and X-ray heated peaks in T_S are much higher than the very slowly evolving δ_{nl} peaks. Therefore we see a decrease in the number of structures $N_{con,hole}$ and a corresponding decrease in the size of holes and connected regions, $r^{ch}_{con,hole}$. Scattered ionized regions also start appearing at these z values. These would correspond to holes in the δT_b field. Therefore the morphology of holes in this regime is expected to be a combination of that of T_S and x_{HI} field. The number of holes, N_{hole} for x_{HI} is more than that for T_S. However the redshift evolution is closer to that for T_S than that of x_{HI} because the holes corresponding to the x_{HI} field correspond to very small regions in the T_b field and are fewer in number at these redshifts. Both $\beta_{con,hole}$ show an increase till z_{frag}. This increase is a trend observed in the T_S field at these redshifts. Since most of the region is a single connected neutral region, the morphology of connected regions for δT_b is dominated by the T_s field in such regions. Thus in this regime both T_S and x_{HI} affect the morphology but it is the evolution of T_S morphology that is marginally dominant. At lower z values, i.e. $z_{EoR} \lesssim z \lesssim z_{frag}$ the morphology is dominated by the morphology of the x_{HI} and $1 - T_{CMB}/T_S$ field, but the evolution is dominated more by the morphology of x_{HI} field. The increase in the number of small ionized regions and the fact that X-ray heating is saturated in most of the IGM leads to an increase in N_{hole}. Since the ultra violet radiation capable of ionizing neutral hydrogen has lower mean free path than X-rays, such numerous regions are smaller in size and would appear in hottest regions of the IGM. This is reflected in the decrease in the average size of holes, r^{ch}_{hole}. Post z_{frag} there is an increase in the number of connected regions N_{con} and a corresponding decrease in r^{ch}_{con}. Post z_{frag} the trend in the variation of $\beta_{con,hole}$ begins to transition to that towards x_{HI} dominating over T_S as described above. Note that this entire regime is a regime of transition.

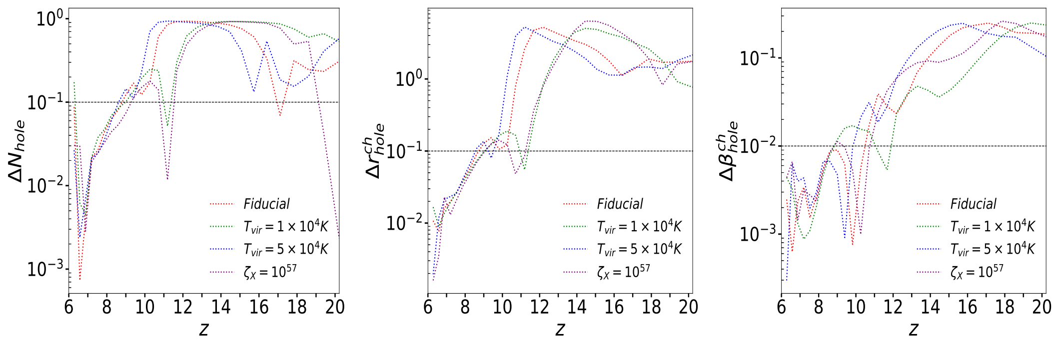

Fig. 5.13 The fractional difference for N_{hole}, r_h^{ch} and β^{ch}_{hole} between δT_b and x_{HI} relative to x_{HI} for all the models under consideration. The horizontal line in the left and middle panel marks the point where the differences ΔN_{hole} and Δr^{ch}_{hole} are 10% respectively, while the horizontal line on the right panel marks the point where $\Delta\beta^{ch}_{hole}$ is 1%.

- **Regime 3**: Low redshift $z < z_{EoR}$

  This is the regime where the morphology of ionized regions is directly manifested in the morphology of the brightness temperature field δT_b. In Fig. 5.13 we plot the fractional differences between the two fields as a function of redshift. The fractional difference $\Delta F = \frac{F_{\delta T_b} - F_{x_{HI}}}{F_{x_{HI}}}$, where F is the quantity of interest for holes, i.e. N_{hole}, r^{ch}_{hole} and β^{ch}_{hole}. The reason why we compare only for holes is because once ionization begins, holes give a more physical picture as ionized regions in the morphology of brightness temperature field. Any fully ionized region would appear as a hole in the brightness temperature field excursion set. We define z_{EoR} to be the lowest redshift where Δr_h^{ch} is 10%. We observe that thereafter the difference decreases with decreasing z. For this choice of z_{EoR}, $\Delta\beta^{ch}_{hole}$ is always below 1%. Therefore one can infer $z_{0.5}$ and z_e to good accuracy from the δT_b morphology. We also find that at $z = z_{0.5}$, $N_{con} \simeq N_{hole}$ for δT_b.

The evolution of brightness temperature morphology for the different models relative to the *fiducial model* is shown in Fig. 5.14. The shape of the redshift evolution of the δT_b morphology as encoded in $N_{con,hole}$, $r^{ch}_{con,hole}$ and $\beta^{ch}_{con,hole}$ is similar for all models under consideration except for the shifts in the various transitions described above. The results are summarized in Table 5.3.

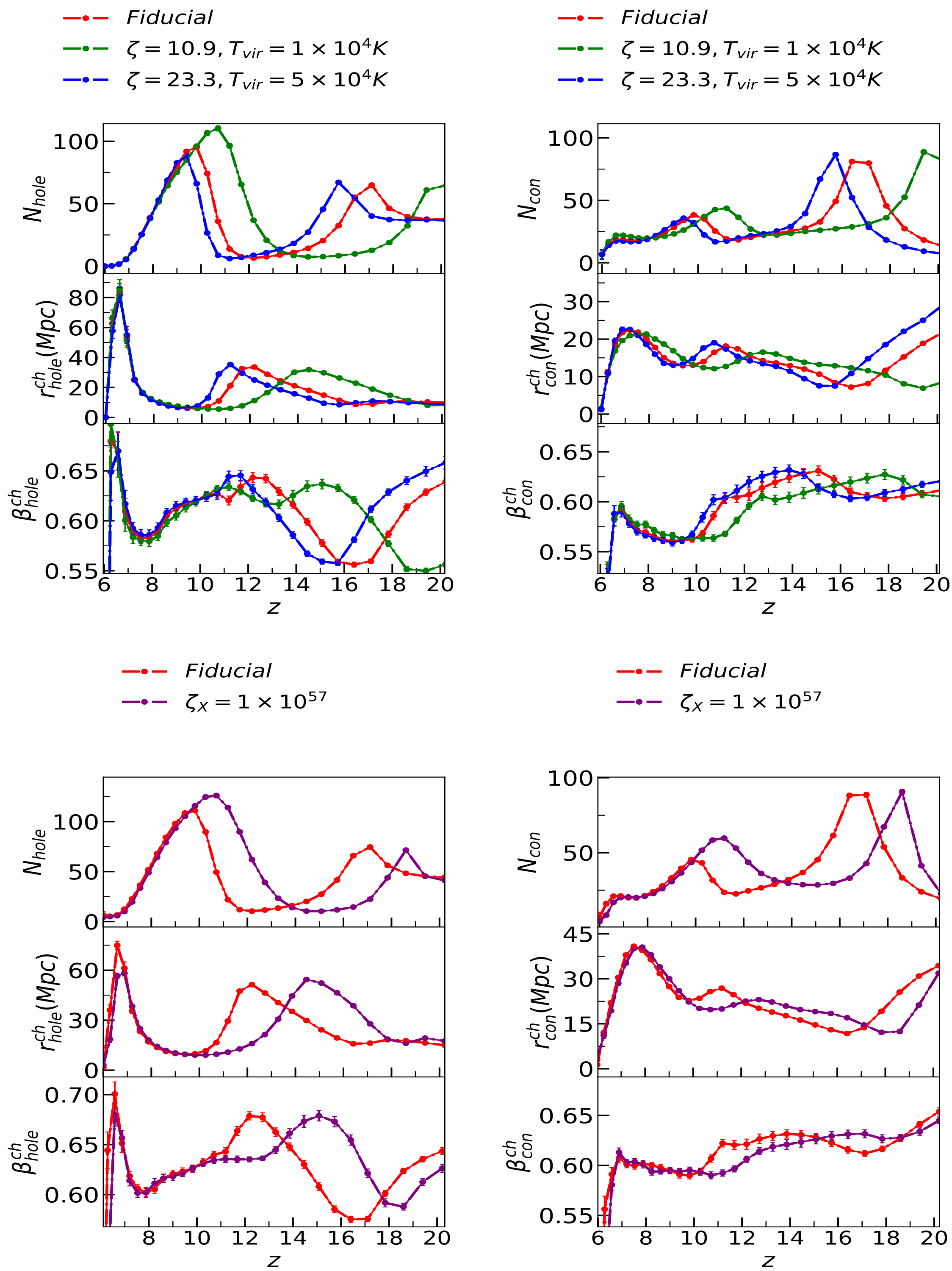

Fig. 5.14 The morphology of δT_b for models with different T_{vir} values (*upper left and right*) and model with an increased X-ray efficiency (*lower left and right*), relative to the *fiducial model*. Notice the shift for different models. For the lowest value of T_{vir} (*green* plots in upper panels) we find features similar to other values of T_{vir} at high redshifts but shifted to $z > 20.22$ which is not shown in the figure. The error bars are calculated as an error in mean over the 32 slices from our 200 Mpc box.

Model	z_{EoR}	$\bar{x}_{HI}^{EoR}$	z_{tr}
Fiducial	~ 8.7	~ 0.73	~ 17.11
$T_{vir} = 1 \times 10^4 K$	~ 9.1	~ 0.71	~ 19.4
$T_{vir} = 5 \times 10^4 K$	~ 8.6	$\sim$0.77	~ 15.7
$\zeta_X = 1 \times 10^{57}$	~ 9.12	$\sim$0.77	~ 18.6

Table 5.3 The redshift z_{EoR} below which the difference between δT_b and x_{HI} morphologies defined in terms of $\Delta r_h^{ch} < 10\%$ for different models. The last column shows the corresponding $\bar{x}_{HI}$ values at z_{EoR}.

From the table we see that the shift in z_{EoR} is a consequence of a general shift in the redshift at which EoR starts for these models and has been described in section 5.3. The shifts in z_{tr} can be traced to the differences in X-ray and Ly-α emmissivities for these models and has been described in detail in section 5.4. We observe that one model can be differentiated from another both from the morphology at a given redshift and from the shift in the transition redshifts. The transition epoch $z = z_{EoR}$ can be obtained for different models.

5.6 Conclusion and Discussion

In this chapter we have described how the Contour Minkowski Tensor and Betti numbers can be used to discriminate various models of ionization and heating history of the IGM after the first collapsed structures form. The kind of results obtained here can be used either to gain insights or compare one model from the other within reionization simulations or for discriminating models from future radio observations.

The morphological properties of the individual fields show transition at certain specific redshifts in their respective evolution. These transitions are reflected in the evolution of the morphology of the brightness temperature field. We find that the morphology of the density field does not show any marked evolution with redshift at the high redshifts probed, where it's effect on the brightness temperature fluctuations is expected to be more. Different signatures of various EoR models on the x_{HI} field are observed. Less efficient sources with lower values of T_{vir} have higher N_{hole} and smaller r_{hole}^{ch} as compared to the sources with higher T_{vir}. A shift towards higher values is observed for the various redshifts of transition for model with lower T_{vir}. The transitions points are at the redshift of fragmenation (z_{frag}), the redshift of equality of Betti numbers (which occurs at $z = z_{0.5}$, where $\bar{x}_{HI} = 0.5$) and the redshift of the end of progress of reionization (z_e). We also studied the effect of inhomogenous recombination in comparison to our *fiducial model*. We find that recombination delays the different transition redshifts and introduces more anisotropy in the growth of ionized regions. Moreover, we have observe that the size of ionized regions is smaller in the case of less efficient sources and it varies with T_{vir} in a monotonic but non linear fashion.

The evolution of the morphology of the T_S field does not show any marked transition but it exhibits a shift in the evolution to higher z values for sources with higher X-ray emissivity.

We have shown that the evolution of the brightness temperature captures the various transitions for the ionization field and spin temperature evolution. We have identified three regimes in the evolution of the morphology of δT_b. The first regime corresponding to $z > z_{tr}$ is where the morphology of the T_S field determines the evolution. This is the regime where the evolution of fluctuations in the Ly-α coupling in combination with the fluctuations in δ_{nl} dominate the evolution of the morphology of T_S. The second regime, $z_{EoR} < z < z_{tr}$ is where the morphology of δT_b is determined by an interplay between the T_S and x_{HI} morphology. We observe a transition around z_{frag} in the redshift evolution of the morphology of δT_b. In the third regime at $z < z_{EoR}$, the morphology of δT_b is similar to that of x_{HI} in terms of the morphology of holes for the respective fields. The morphology of the brightness temperature captures most of the ionization history below z_{EoR}. For our *fiducial model* the average neutral hydrogen fraction at z_{EoR} is $x_{HI} \sim 0.8$. Therefore z_e, $z_{0.5}$ and z_{frag} are captured by δT_b morphology.

The calculations show how the contour minkowski tensor and Betti numbers be used to discriminate models of EoR in an ideal scenario where there is no foreground or instrumental noise. Our results are very encouraging for application of our method to future data of the brightness temperature to constrain models of the EoR. The next step is to carry out realistic analysis by including instrumental effects in the simulations and to see if we can recover constraints on model parameters using Bayesian inference, for future radio interferometers such as the Square Kilometre Array(SKA) (Braun et al., 2015). As a corrolary to the further applications of such a study, we decribe the prospects of probing non-Gaussianity from 21cm brightness temperature maps in Appendix D.

6

Prospects of Constraining Model Parameters

6.1 Motivation

In the previous chapters we explored the redshift evolution of our statistics and compared different models qualitatively. We described how the CMT in combination with Betti numbers encapsulates the ionization history of the universe. We also studied how different physical scenarios can be discriminated using these statistics and showed that they can be used to constrain models of EoR. However, in the previous studies we did not incorporate instrumental noise and our analysis was carried out on ideal simulations.

In order to quantify the usefulness of CMT and Betti numbers as tools for extracting physical information of the EoR, we develop a pipeline for comparing theoretical models described by a two parameter model. To do so we construct mock observed 21cm signal and analyze the prospects of constraining the parameters. The pipeline consists of first obtaining the functional form of our statistics on the space of parameters and understanding their behaviour. Then the mock observed 21cm signal is prepared by adding instrumental noise field to the simulated brightness temperature field for a *mock* model. Thereafter, we perform a Bayesian analysis, comparing the theoretical statistics with their corresponding mock observed values and infer if the input models are recovered by our statistics. We choose to work with the noise characteristics of SKA I low,[1] because it would have the sensitivity for direct imaging of neutral hydrogen from scales of arc-minutes resolution to degrees, for over most of the redshift range $z \sim 6-28$ (Mellema et al., 2015) corresponding to EoR and the cosmic dawn. A detailed study of detecting ionized sources from 21cm images in the presence of system noise and foreground has been explored in (Ghara et al., 2017). In this work, we will follow a similar method for generating system noise and study a simple two parameter model of EoR described by ζ and T_{vir} (section 2.3). We also ignore the effects of foreground contamination of the images.

The chapter is organized as follow. We first describe our mock observation of the EoR in section 6.2. We then obtain the functional forms of our statistics in two dimensional parameter space and understand their smooth variation and potential degeneracies in section 6.3. We then follow up with a detailed analysis of the effect of smoothing and noise addition on our statistic in section 6.4. Next, we calculate the posterior probability and discuss the prospects of constraining our models in section 6.6.

All the important definitions and calculations pertaining to radio astronomy, used for analysis in this chapter are explained in Appendix C.

6.2 Constructing Mock 21cm data

In order to obtain mock data, we need to model 21cm maps from the EoR and system noise from the observing telescope. For our current analysis we have ignored the effects of foreground contamination and will explore it in a future work. In this section we describe the various steps involved in constructing the mock observational data.

A radio interferometeric observation measures a quantity called the visibility, $V(\vec{U}, \nu)$ which is essentially a 2 dimensional inverse Fourier transform of the sky brightness in a particular direction, $I_\nu(\vec{\theta})$:

$$\mathscr{V}(\vec{U}, \nu) = \int d^2\theta \; I_\nu(\vec{\theta}) \; e^{i2\pi\theta.\vec{U}} \tag{6.1}$$

The visibility depends upon the baseline vector, $\vec{U} = \vec{b}/\lambda$ where λ is the observed frequency and $\vec{b}$ is the vector between two antenna elements. The actual measured visibility would have a noise component, $N(\vec{U}, \nu)$ in addition to the signal component in eq. 6.1. The final observed image would then be the inverse Fourier transform of $V(\vec{U}, \nu) + N(\vec{U}, \nu)$. The inverse

[1]http://skatelescope.org

Fourier transform of $V(\vec{U},\nu)$ is $I_\nu(\vec{\theta})$, which is related to the brightness temperature δT_b as (see Appendix A):

$$I_\nu(\vec{\theta}) = \frac{2k_B\nu^2}{c^2}\,\delta T_b(\vec{\theta},\nu), \tag{6.2}$$

where δT_b is the brightness temperature. The *uv*-plane is sampled according to the baseline distribution of the antenna array and hence some information of the signal is lost while obtaining the inverse Fourier transform. The actual signal visibility is therefore the product of the baseline sampling function in the *uv*-plane and the true visibility. This is called the *dirty image*. The final image is then this *dirty image* with the system noise due to the interferometer added to it. Therefore, the two important components for modelling mock observations are the baseline distribution of the interferometer and noise sensitivity of each baseline. In this study, we consider observations from SKA I-low as it will have the required sensitivity to image the Epoch of Reionization, as mentioned earlier. In the following subsections we describe the signal and noise map used for constructing mock δT_b maps for our analysis. It is to be noted that the box size used for this analysis is bigger than what we used in earlier chapters. This is because a bigger box size mitigates errors due to cosmic variance inherent in the analysis. We would also like to point out that unlike statistical studies in the Fourier space, while performing real space analysis it is essential to smooth our field to avoid effects of shot noise. Therefore, we refer to the clean signal map as the map with a minimum smoothing scale of 4.5 Mpc.

6.2.1 Signal Map

We simulate the signal map using 21cmFAST (section 2.3). In order to construct our mock EoR model, we generated the δT_b field on a 512^3 grid of a 400 Mpc box. This gives a pixel resolution of ~ 0.78 Mpc. The initial conditions were generated on a 1024^3 grid at a redshift of $z = 300$. We choose to work with $\zeta = 17.5$ and $T_{vir} = 3 \times 10^4$ K. The mean free path, R_{mfp} or the maximum radius for ionizing radiation towards the end of EoR is set to 50 Mpc. The model yields an end of reionization at $z_e \sim 6$ and an optical depth to last scattering $\tau_{re} \sim 0.054$ consistent with PLANCK 2018 data release (Planck Collaboration et al., 2018).

The mock observation is constructed at an observed redshift of $z = 7.4$ (or observed frequency of 169 MHz) where the neutral hydrogen fraction is $x_{HI} = 0.5$ (see section 6.3 for justification). Hereafter, we refer to this model as the *mock* model. The size and resolution of the box along the line of sight fixes the bandwidth and frequency resolution of our observations respectively. The same two quantities in the tangential direction, quantify the maximum field of view and angular resolution (Appendix C.3). The bandwidth of observations corresponding to our 400 MPc box is, $\Delta\nu = 24$ MHz. The signal maps in two-dimensions are constructed by averaging δT_b along the line of sight over a thickness corresponding to frequency channel width of $\Delta\nu_c = 1$ MHz extracted from the cube. The 400 Mpc box used in this study corresponds to a maximum angular scale of $\theta_{max} \sim 2.55^o$ or a minimum baseline of $U_{min} \simeq 22.7$ at the observed wavelength of 169 MHz. The resolution of the simulation grid is 0.78 Mpc, which corresponds to an angular resolution of $\Delta\theta \simeq 0.3'$ or a maximum baseline of $U_{max} \simeq 11455$.

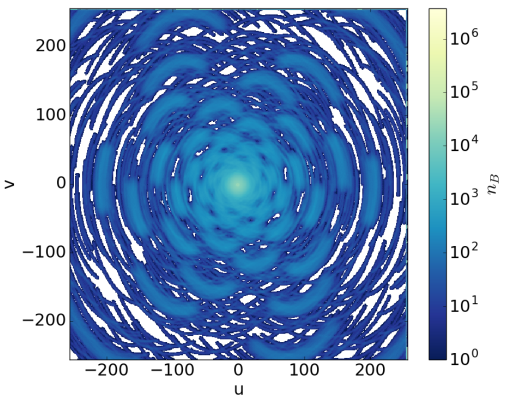

Fig. 6.1 The *uv*-coverage of the SKA-I low for 4 hours of observation per day at a declination of $\delta_{dec} = -30^o$ and integration time $\Delta t_c = 120$ seconds.

In order to obtain the *dirty image*, we generate the two-dimensional baseline distribution, $n_B^{i,j}$ in a 512× 512 grid for a 4 hours per day observation with an integration time of $\Delta t_c = 120$ seconds. The contribution of galactic nonthermal emission would add to the system noise hence the observations must be carried out at higher galactic latitudes. Therefore the southern galactic pole at around a declination of -30^0 is considered for our mock observations. In Fig.6.1 we plot the baseline distribution used for our mock observation.

SKA Parameter	Value
Redshift (z)	7.4
Central Frequency (ν_c)	169 MHz
Frequency Resolution ($\Delta\nu_c$)	1 MHz
Integration time (Δt_c)	120 sec
System Temperature (T_{sys})	$100 + 60 \times (300MHz/\nu_c)^{2.55}$ K
Number of Antenna(N_{ant})	512
Effective Collecting area (A_{eff})	962 m^2

Table 6.1 The SKA I instrument parameters used in this study for generating our mock observation at $z = 7.4$.

In table 6.1 we list the SKA parameters used for this study [2]. After generating the *uv* coverage, the following steps have been adopted for constructing the *dirty image*:

- Generate the δT_b maps from 21cmFAST using our *mock model* and take a two dimensional Fourier transform of the map.
- Incorporate the effect of empty pixels in the *uv* coverage by including a mask, such the the value at i, jth pixel is 0 where there are no baselines and 1 where $n_B^{i,j} \neq 0$.
- Multiply the mask by the Fourier tranformed map and take an inverse fourier transform of the product to obtain the *dirty image*.

We find that the *dirty image* map is visually hardly distinguishable from the signal map as the *uv* coverage is almost filled.

6.2.2 Noise maps

Since the noise from two different baselines is uncorrelated (appendix C.2) we model $N(\vec{U}, \nu)$ in the *uv*-space and take it's inverse Fourier transform to obtain the real space noise. This real space noise is then added to the *dirty image* of the signal map, in order to obtain our mock image.

The RMS brightness temperature sensitivity for each baseline for a frequency channel width $\Delta\nu_c$ and correlator integration time t_c for an observed frequency ν is given by (using eq. C.6):

$$\sigma_N = \frac{c^2\, T_{sys}}{\nu^2 A_{eff}\, \Delta\Omega\, \sqrt{2\, \Delta\nu_c \Delta t_c}}\,, \tag{6.3}$$

[2] https://www.skatelescope.org/wp-content/uploads/2012/06/84_rsm-v1.0-word-1.pdf

where A_{eff} is the effective collecting area of each antenna, $\Delta\Omega = (\Delta\theta)^2$ is the beam solid angle and T_{sys} is the system temperature. We have chosen $\Delta t_c = 120$ seconds. We carry out the following steps to generate the noise maps (Ghara et al., 2017):

- The 512×512 Fourier space grid (or uv-space) is populated with a Gaussian random field with mean zero and standard deviation σ_N given in eq. 6.3.
- Since a point on the uv-grid can correspond to multiple baselines, the noise in the (i,j) th pixel reduces by a factor of $1/\sqrt{n_B^{i,j}}$.
- When averaged over long observation hours, the noise will further reduce by a factor of $\sqrt{t_{obs}/t_{obs}^{uv}}$, where t_{obs}^{uv} is the observation time per day which is 4 hours for our analyses.
- To account for empty pixels in the uv- grid a mask is included which is 0 at the empty pixels and 1 otherwise as done before for generating the *dirty image*.
- The final real space map is obtained by taking the inverse Fourier transform of this reduced noise.

The signal to noise ratio in images is defined as:

$$SNR_{image} = \frac{\sigma_{T_S}}{\sigma_{T_N}}, \tag{6.4}$$

where σ_{T_N} is the standard deviation in the smoothed noise map obtained after performing the steps above and σ_{T_S} is the standard deviation in the smoothed signal map without masking and noise addition 6.2.1.

The noise in images can be reduced in different ways. One way to reduce the noise is to increase the time of observation t_{obs} or increase the frequency channel width $\Delta\nu_c$. Another way is to smooth the images. In Fig. 6.2 we show four maps to compare the effect of noise from SKA I low for the parameters in table 6.1. The first map on the left panel shows the signal map without masking and noise addition, smoothed at $R_s = 4.5$ Mpc. The second and third map are the mock noisy maps at $R_s = 4.5$ Mpc smoothing for $t_{obs} = 1000$ and $t_{obs} = 2000$ hours, respectively. We find that the SNR in the images increases by almost ~ 1.4 times when t_{obs} becomes twice, as expected from eq. 6.3. The right panel shows the same map smoothed at 6.5 Mpc for $t_{obs} = 1000$ hours. We find that the SNR becomes almost twice for the same t_{obs} for a 1.5 times increase in the smoothing scale. The effect of noise is to introduce small scale structures in the image. When smoothed, these small scale structures get washed out and therefore increase the SNR of the image. However, even though smoothing increases the SNR in images, it also smooths out small scale structures that are intrinsic parts of the true

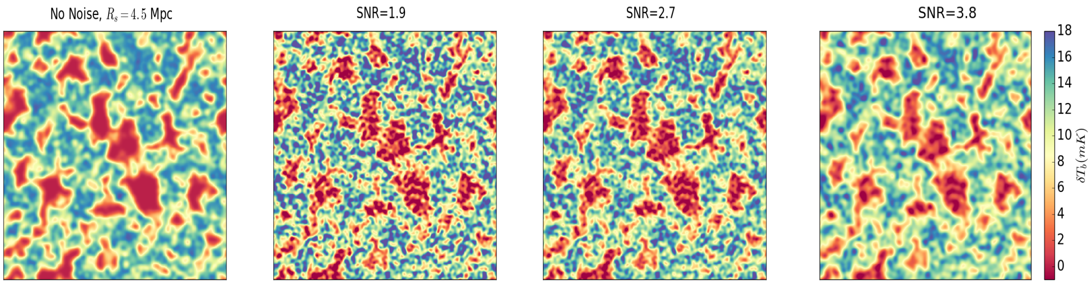

(a) **(b)** **(c)** **(d)**

Fig. 6.2 Maps showing the effect of noise on image for the field of view of $2.55^o \times 2.55^o$ corresponding to our 400 MPc box and frequency resolution of 1 MHz. Fig.(a) shows the signal map without masking and noise, smoothed at $R_s = 4.5$ Mpc. Fig.(b) shows the map with SKA noise for $t_{obs} = 1000$ hrs, $R_s = 4.5$ Mpc and SNR=1.9. Fig.(c) shows the noise image for $t_{obs} = 2000$ hrs, $R_s = 4.5$ Mpc and SNR=2.7. The map in Fig.(d) is for $t_{obs} = 1000$ hrs, $R_s = 6.5$ Mpc and SNR=3.8.

underlying signal and this leads to loss of information. This point shall be elaborated further in future sections.

6.3 Parameter Space for theoretical models

We work with theoretical models described by varying two parameters, ζ and T_{vir}. We choose to work only with the hole statistics due to it's direct physical interpretation as ionized bubbles and the associated dependence on physical parameters, as described in previous chapters. In this section we will analyze the functional form of our statistics from ideal simulations in parameter space at a fixed redshift of $z = 7.4$ with $\bar{x}_{HI} = 0.5$. In our earlier studies we focussed on the variation of our statistics with redshift. The purpose of studying the variation of our statistics in parameter space at a fixed redshift is to anticipate the behaviour of the posterior when performing Bayesian analysis as will be described in section 6.6. Moreover, using the understanding gained from analyzing the noise characteristics of SKA we choose z=7.4 because it gives a good compromise between the noise rms and the level of physical information that can be extracted from our statistics.

In order to obtain the functional form of our statistic in parameter space, we made ideal simulations for 400 models at 20×20 equally spaced points in the $\zeta - T_{vir}$ plane in the range $10^4 \leq T_{vir} \leq 8 \times 10^4$ K and $8 \leq \zeta \leq 28$. Since the redshift and R_{mfp} is fixed, we find that the maximum value of T_{vir}, that we can fix is $\simeq 8.0 \times 10^8$ K. This is because, a non-zero value of f_{coll} could not be achieved at this redshift for a higher T_{vir}, to evaluate the inequality in eq. 3.2 for $R_{mfp} = 50$ Mpc. Moreover, a wider range in parameter space can be covered for a fixed redshift if the value of R_{mfp} is also varied. Since our focus in this chapter is to build up the pipeline for Bayesian analysis to recover model parameters, we postpone the analysis for more than two parameters to our upcoming paper.

We use the same box parameters as for our mock signal simulation described in section 6.2.1. The same set of initial conditions has been used for all models. We calculate $\bar{x}_{HI}$ and the three statistics $N_{\rm hole}$, $r^{\rm ch}_{\rm hole}$ and$\beta^{\rm ch}_{\rm hole}$ for each point on parameter space. In order to be consistent with our observed maps, the statistics have been calculated as an average over 24 slices , each of which corresponds to a thickness of 16.5 MPc (corresponding to the 1 MHz frequency bandwidth of the noise map).

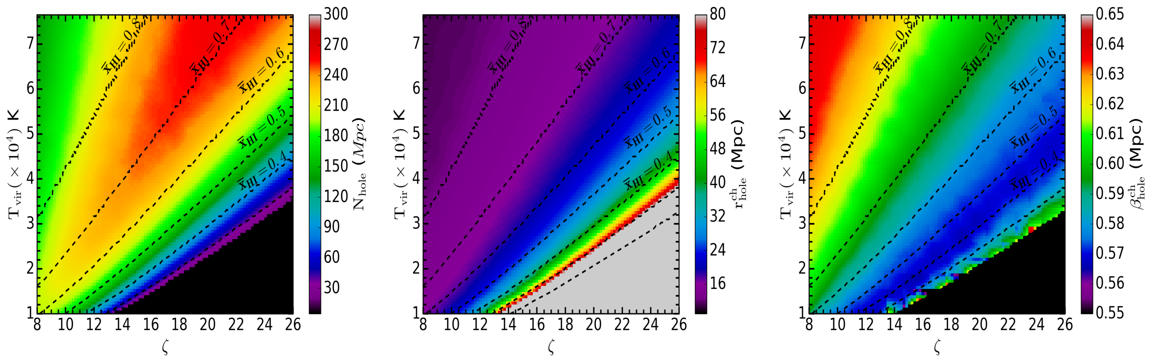

Fig. 6.3 The figure shows the behaviour of our statistics in the 2D parameter space spanned by $\zeta - T_{vir}$. The colorbar shows the values of the respective statistics and the black dotted lines are lines of constant $\bar{x}_{HI}$. The panels show N_{hole} (*left*), r^{ch}_{hole} (*middle*)and β^{ch}_{hole} (*right*). Interpolation introduces numerical artefacts below the line of $\bar{x}_{HI} = 0.3$ in the bottom right part of the panels.

For a given ζ, on decreasing T_{vir} there is a decrease in the neutral hydrogen fraction. If the field is completely ionized then the number of holes are expected to become zero, since then there is no excursion set at any threshold. A lower T_{vir} gives higher collapse fraction at a given redshift as compared to a higher T_{vir}. Therefore the inequality in Eq. 2.33 is most easily met when ζ is higher for a given T_{vir}. Therefore, regions with low T_{vir} approach complete ionization for lower values of ζ, as compared to higher T_{vir}.

The color maps in Fig. 6.3 encapsulate this dependence of the three statistics in the $\zeta - T_{vir}$ plane. These color maps show the values of N_{hole}, $r^{\rm ch}_{hole}$ and $\beta^{\rm ch}_{hole}$, obtained by interpolating the values of the respective statistics over the 20×20 models with values computed numerically using the method described in section 6.2.1. The dotted lines show the variation of $\bar{x}_{HI}$ in the parameter space. They are smoothly varying functions of the parameters. By visual inspection of the plots, we find that interpolation introduces features around very low values of $\bar{x}_{HI}$, for all statistics. These correspond to regions of the parameter space where there are almost no structures in the excursion set. Since we shall carry out our analysis for the *mock* model, which lies around $x_{HI} = 0.5$, this numerical interpolation error will not impact our results.

Since, each model is at different stages of it's ionization history at $z = 7.4$, we can interpret the color maps as a variation with $\bar{x}_{HI}$. The variation with $\bar{x}_{HI}$ is the same as studying the redshift evolution for a fixed model as described in previous chapters. The top left corner of the color maps corresponds to a high value of average neutral fraction, i.e. regions where the morphology is dominated by a big neutral (or connected regions) region dotted with numerous ionized bubbles (or holes). These bubbles increase in size and number, until $z \simeq 0.7$, shown by the red patch extending from top right to the middle of the panel for N_{hole} and the corresponding increase in size through r^{ch}_{hole}. Thereafter, there is a sharp increase in size and decrease in number, due to mergers of ionized regions. This is reflected in both N_{hole} and r^{ch}_{hole}, in going diagonally towards the bottom right region of the parameter space from the line corresponding to $\bar{x}_{HI} \simeq 0.7$. Interestingly, from the figure, we find that β^{ch}_{h} varies very mildly over the parameter space, however it captures the expected increase in anisotropy as ionization proceeds.

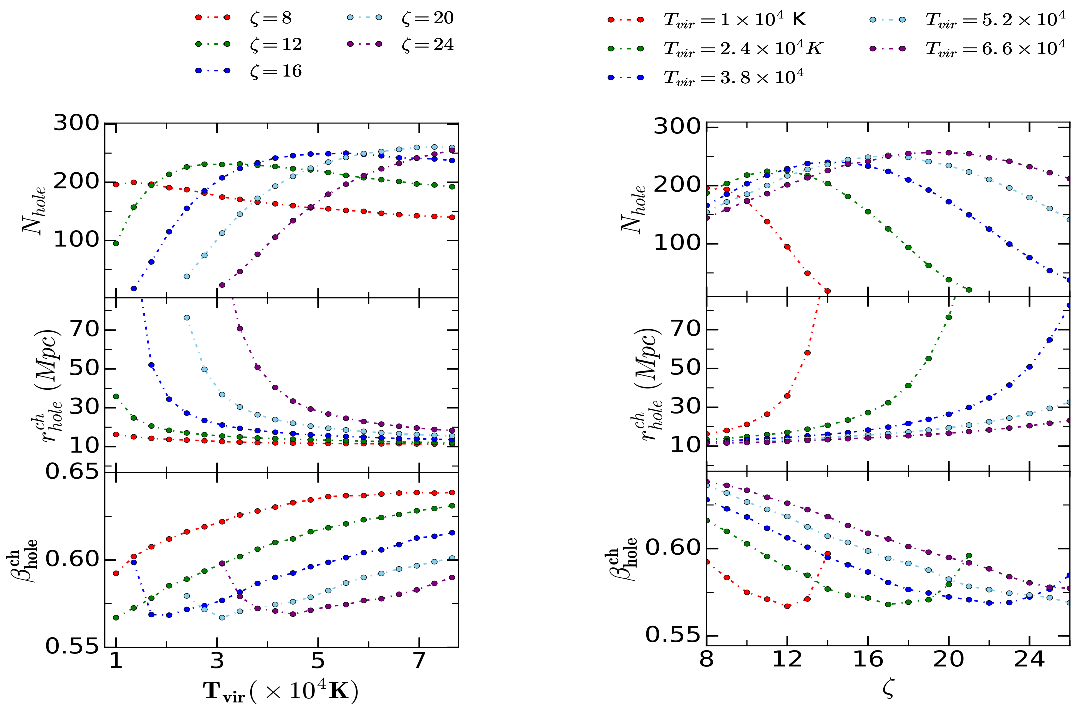

Fig. 6.4 The figure shows the variation of N_h (*top*), r^{ch}_{h} (*middle*) and β^{ch}_{h} (*bottom*) with T_{vir} for fixed ζ (*left*) and with ζ for a fixed T_{vir} (*right*).

In Fig. 6.4 we show the variation of our statistics with T_{vir} at fixed ζ on the left panel and vice versa on the right panel. The left panel shows that a high ζ value approaches complete ionization (marked by the rapid rise of r^{ch}_{hole} and β^{ch}_{hole} and corresponding decrease of N_{hole}) at a higher value of T_{vir} as compared to a lower ζ. Since a lower T_{vir} leads to higher collapse fraction, this implies that if the efficiency of the sources is less we need more number of collapsed objects (or lower T_{vir}) to attain the same value of $\bar{x}_{HI}$. We observe an opposite trend in the right panel, where a lower T_{vir} approaches complete ionization at a lower ζ value as compared to a higher T_{vir} value. This can again be understood in terms of collapse fraction. A higher collapse fraction (or lower T_{vir}) enables one to attain the same value of ionization at lower zeta values due to more frequent mergers as compared to a higher T_{vir}.

The description in this section shows that there is a systematic smooth variation of our statistic with parameters and can therefore enable us to constrain models of the EoR. We find that the statistic, N_{hole} is degenerate in its behaviour across the parameter space for models lying above and below the $\bar{x}_{HI} \simeq 0.7$ line. Therefore, in order to obtain constraints, we need to use N_{hole} in combination with r^{ch}_{hole} to break model degeneracies. We find that β^{ch}_{hole} does not vary much across the parameter space and therefore when used by itself will not provide tight constraints on model parameters, without using extra information contained in N_{hole} and r^{ch}_{hole}.

We also found that the variation of the statistics is sensitive to the value of x_{HI}, which we shall elaborate in the following subsection.

6.3.1 Dependence upon $\bar{x}_{HI}$

Before we analyse the behaviour of our statistic with $\bar{x}_{HI}$ we review the evolution of connected regions and holes as the ionization history of the universe changes. At early stages of EoR, there would be fewer number of neutral regions (or connected regions) as compared to holes (or ionized regions), since most of the neutral regions would be big connected regions. On the other hand small yet numerous ionized bubbles would begin to appear due to appearance of newer collapsed objects. This would also lead to an increase in size of holes and a corresponding decrease in the number of holes is expected as a result of bubble mergers. A corresponding increase in size of connected regions happens at intermediate $\bar{x}_{HI}$, but due to blurred distinction of connected regions and holes into neutral and ionized regions at this stage, this regime is not straightforward to interpret physically. At very small $\bar{x}_{HI}$ values where ionization is almost complete, the topology would largely consist of a single large hole dotted with numerous but small neutral regions. This behaviour described above is captured in the left panel of Fig. 6.5 for all the 400 models where each dot represents a model. Since each model is at different stages of it's ionization history, we can interpret the plots similar to the redshift evolution of a single model. The dotted line corresponds to $x_{HI} = 0.5$ and the yellow dot shows the *mock model* without noise. The errorbars are errors over 40 independent realizations of the *mock model*. The important thing to note however is that for a given $\bar{x}_{HI}$ there is more than one model, with the statistics varying over a narrow range. The narrower the spread at a given $\bar{x}_{HI}$,

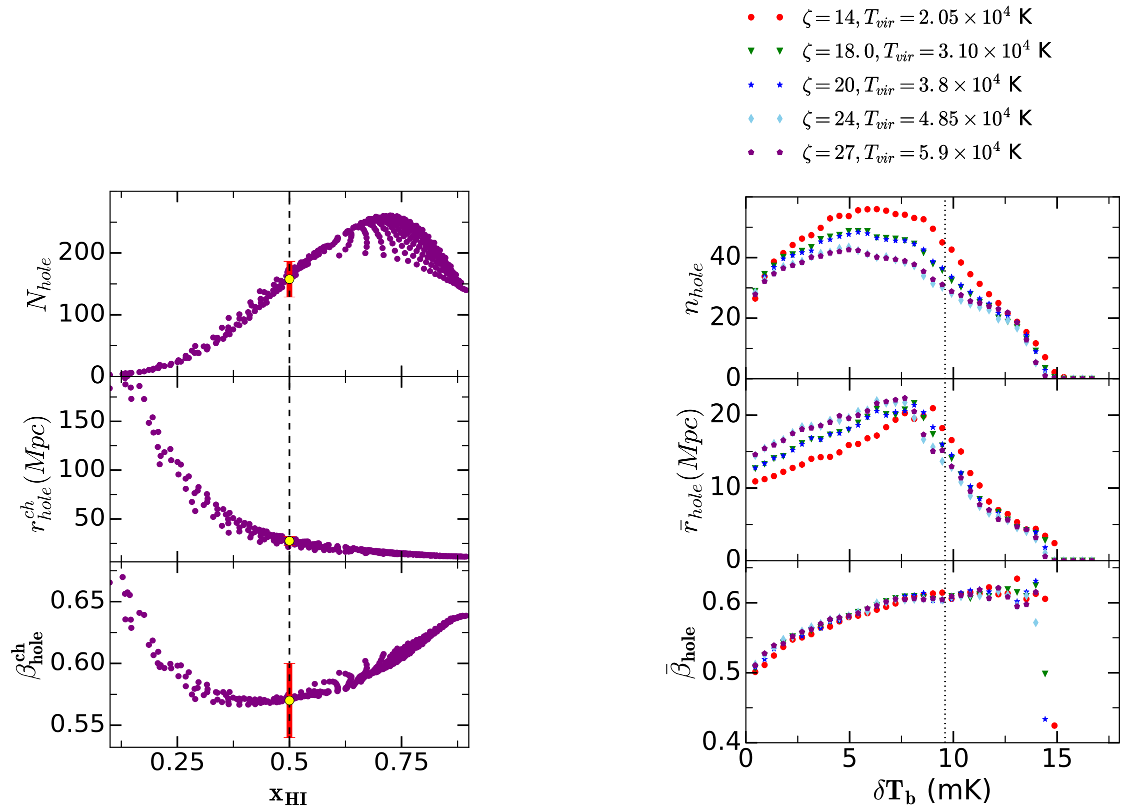

Fig. 6.5 *Left:* The figure shows the variation of our statistics with $\bar{x}_{HI}$ for the 400 known models described in text. The vertical line corresponds to the $\bar{x}_{HI}=0.5$ and the yellow dot represents the values for our *mock* model without noise addition. The red errorbars denote error due to cosmic variance. *Right:* The figure shows the variation of the statistics with δT_b field threshold, for models with $\bar{x}_{HI}=0.5$. The vertical dotted line is the mean value of δT_b. This value of $\bar{x}_{HI}$ corresponds to the value of our *mock* model.

the more degenerate the models will be. Moreover, we note that within the 1-σ errorbar, there are more than one model with $\bar{x}_{HI} = 0.5$. To elaborate this point, in the right panel of Fig. 6.5 we plot n_{hole}, $\bar{r}_{hole}$ and $\bar{\beta}_{hole}$ versus field threshold as described in eq. 3.27, for five different models having $\bar{x}_{HI} = 0.5$ at $z = 7.4$. The variation shows that n_{hole} and $\bar{r}_{hole}$ are sensitive to changes in the model, especially at threshold values less than the mean. Since the mean value of δT_b here corresponds to $\bar{x}_{HI} = 0.5$, the field values below the mean where the difference between the models is discernible would largely correspond to ionized regions (by definition in chapter 2). Higher, T_{vir} values would correspond to bigger but fewer bubbles and lower T_{vir} values would correspond to smaller but numerous bubbles.

Next, it was pointed out in the earlier subsection, the statistics are roughly constant along curves of fixed $\bar{x}_{HI}$. We show that these curves can be fitted with lines of fixed slope. We can use this behaviour to reduce the parameter space to a one-dimensional space. Thus, we can choose the lines of constant slope η, for which $\zeta \propto T_{\rm vir}/T_*$, where $T_* = 10^4$ K. As seen in the left panel of Fig. 6.6, points of constant $\bar{x}_{\rm HI}$ are linear and can be fit with straight lines with varying slope and constant y-axis intercept. For the range of x_{HI} values of interest we find that the y-intercept is ~ -2. Therefore, we change the variables $(\zeta, T_{\rm vir})$ to (η, R), where R is the radial direction along lines of constant $\bar{x}_{\rm HI}$, and η is defined by

$$\eta \equiv \frac{T_{\rm vir}/T_* + 2}{\zeta}. \tag{6.5}$$

The variation of η with $\bar{x}_{HI}$ is shown in the right panel of Fig. 6.6. We find the following two possible fits for the functional dependence of $\bar{x}_{HI}$ on η:

$$\bar{x}_{HI} = 0.78 \,\mathrm{erf}\,(4.37\eta - 0.6) \tag{6.6}$$
$$\bar{x}_{HI} = 0.8 \tanh\,(5\eta - 0.7) \tag{6.7}$$

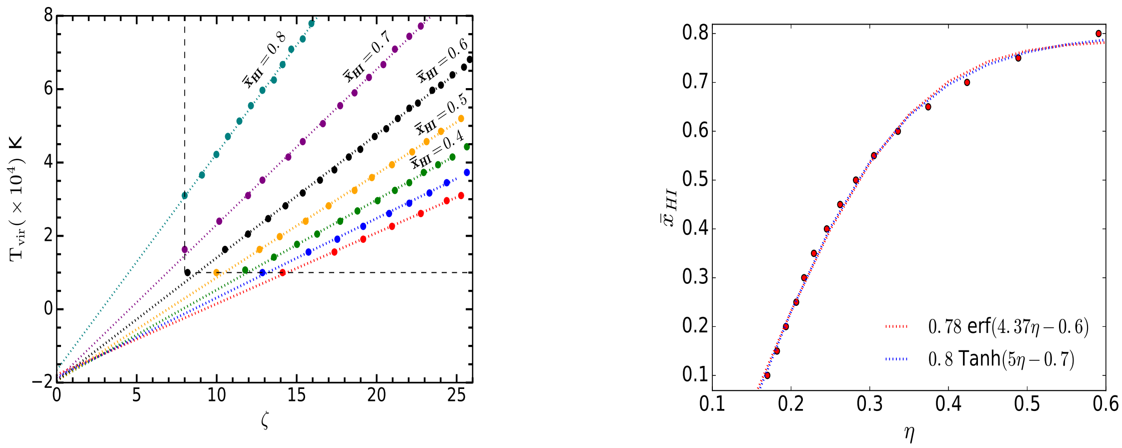

Fig. 6.6 *Left*: Lines of constant $\bar{x}_{\rm HI}$ (green). The dotted lines are lines that have the same y-axis intercept and which fit the lines of constant $\bar{x}_{\rm HI}$. The inner box marks the prior ranged used in this work. *Right*: Red dots are $\bar{x}_{\rm HI}$ versus the slope, η, defined in eq. 6.5, computed for a few selected lines. The black dotted line is obtained by fitting $\bar{x}_{\rm HI}$ to the function $a\tanh[(\eta - b)/c]$, where $a = 0.8,\ b = 0.15,\ c = 0.19$.

The analytically fitted functional form of x_{HI} depending upon η which is a parameter derived from two model parameters can serve as a very useful relation to infer the ionization history of the universe directly. So far our analysis shows that the statistics can constrain models with the same value of $\bar{x}_{HI}$, only if the models are well apart in parameter space. Therefore, by reducing the parameter space to 1D our method is expected to provide strong constraints on the ionization history.

6.4 Covariance matrix and sources of Errors

In the previous section, we studied the expected behaviour of our statistics in the parameter space under an ideal case scenario. In this section, we analyse the behaviour of our statistics for the mock observed data and compare it with the noiseless case. This will enable us to decide on an optimum observational strategy.

Error Covariance Matrix: The error covariance matrix for our statistics is given by:

$$C_{ij} = \begin{bmatrix} \left\langle (N_h - \langle N_h \rangle)^2 \right\rangle & \left\langle (N_h - \langle N_h \rangle)(r_h^{ch} - \langle r_h^{ch} \rangle) \right\rangle & \left\langle (N_h - \langle N_h \rangle)(\beta_h^{ch} - \langle \beta_h^{ch} \rangle) \right\rangle \\ \left\langle (r_h^{ch} - \langle r_h^{ch} \rangle)(N_h - \langle N_h \rangle) \right\rangle & \left\langle (r_h^{ch} - \langle r_h^{ch} \rangle)^2 \right\rangle & \left\langle (r_h^{ch} - \langle r_h^{ch} \rangle)(\beta_h^{ch} - \langle \beta_h^{ch} \rangle) \right\rangle \\ \left\langle (\beta_h^{ch} - \langle \beta_h^{ch} \rangle)(N_h - \langle N_h \rangle) \right\rangle & \left\langle (\beta_h^{ch} - \langle \beta_h^{ch} \rangle)(r_h^{ch} - \langle r_h^{ch} \rangle) \right\rangle & \left\langle (\beta_h^{ch} - \langle \beta_h^{ch} \rangle)^2 \right\rangle \end{bmatrix}, \tag{6.8}$$

where the angle brackets denote average over realizations. There will be two separate sources of errors, one due to cosmic variance and the other due to noise. Therefore the total error covariance matrix will be given by:

$$C_{ij}^{tot} = C_{ij}^{signal} + C_{ij}^{noise}, \tag{6.9}$$

where C_{ij}^{signal} is calculated by taking average over noiseless realizations by taking different initial condition seed values for the 21cmFAST simulations and C_{ij}^{noise} is calculated by taking different noise seed values for some fixed noiseless realization to which noise is added. The errorbars for each statistic, N_h, r_h^{ch} or β_h^{ch} is calculated by using the diagonal elements of the error covariance matrix. We find that the cosmic variance is much greater than variance in noise.

We also find that there are two predominant effects that interplay to affect our observed statistics:

- **Smoothing:** As mentioned earlier, the effect of smoothing is to erase small scale structures. This has a two fold effect on our statistics. Firstly, the number of structures N_h in the excursion set would decrease and there would be loss of information at smaller scales. For a fixed box size this would also translate into increased cosmic variance. Secondly, smoothing would increase the average size of structures, r_h^{ch}, in the excursion set.

- **Noise:** The effect of noise is to introduce several small scale structures in the excursion set. This increases N_h in the map and decreases the mean size of structures and hence r_h^{ch} is decreased.

Clearly, both smoothing and noise addition would shift the mean value of our statistic thereby introducing a bias in the observed measures. This is shown in Fig. 6.7. The left panel of the figure shows the variation of our statistic with the smoothing scale, for the noiseless case and for an observation time of 1000 hours and 2000 hours respectively. We find that in the presence of noise, a higher smoothing is closer to the noiseless case. The drawback of using very high smoothing is that the effect of cosmic variance becomes dominant and adds to the error. The effect of noise on n_{hole}, $\bar{r}_{hole}^{ch}$ and $\bar{\beta}_{hole}^{ch}$ is shown in the right panel of Fig. 6.7. Notice the increase in the size of errorbars due to noise addition. We find that on adding noise, n_{hole} increases at all thresholds and r_{hole}^{ch} decreases at all thresholds. The behaviour of $\bar{\beta}_{hole}$ is dependent upon threshold and does not appear to show a definitive trend with noise addition. The errorbars in the left panel of Fig. 6.7 indicate that noisy case for $t_{obs} = 2000$ hours lies within 1 σ uncertainty for the noiseless case at $R_s = 9.5$ Mpc. Therefore, we will carry out our analysis at a smoothing scale of 9.5 Mpc.

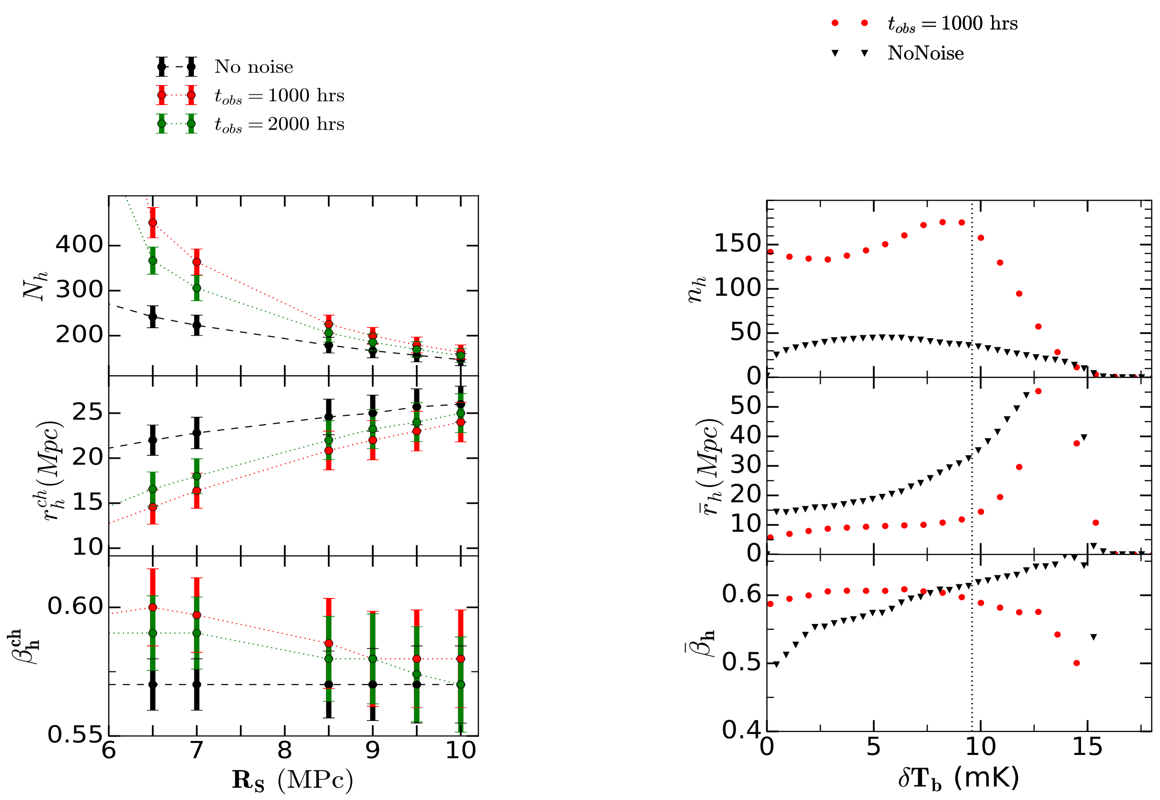

Fig. 6.7 The figure describes the effect of smoothing and noise addition on our statistics. In the left panel we plot the variation of our statistic with smoothing scale, R_s for the case of noiseless (*black*) image, and noisy image with $t_{obs} = 1000$ hrs (*red*) and $t_{obs} = 2000$ hrs (*green*). The values (and the errorbars) are obtained as a mean over 40 independent realizations. The right panel shows the variation of our statistic with δT_b field values for the case of noisy *(red)* and noiseless *(black)* image.

6.5 An estimate of error bounds on model parameters

Before we proceed towards obtaining constraints on model parameters from mock observed data, in this section we will analyse the constraining power of our statistics. In order to do so, we perform a Fisher matrix analysis to predict errors in estimated values of the model parameters .Fisher matrix quantifies the amount of information that an observable carries about an unknown parameter (Fisher, 1922). Let $\vec{\theta} = (\zeta, T_{vir})$ be the vector describing the parameters and $\vec{X} = (N_{hole}, r^{ch}_{hole}, \beta^{ch}_{hole})$ be the vector describing the observables. In Fisher matrix analysis it is assumed that the errors on model parameters are Gaussian distributed. The covariance matrix of our statistics, C_{ij} is related to the Fisher matrix F_{mn} as :

$$F_{mn} = \sum_{ij} \frac{\partial X_i}{\partial \theta_m} C^{-1}_{ij} \frac{\partial X_j}{\partial \theta_n}. \tag{6.10}$$

The Cramer Rao inequality states that the inverse of the Fisher matrix provides a lower bound on the error covariance matrix, $\tilde{C}_{mn}$ of the model paramaters (Rao, 1992; Cramér, 1999):

$$\tilde{C}_{mn} \geq F^{-1}_{mn}. \tag{6.11}$$

Since our goal is to get a rough estimate on errors in estimation of our parameters, we shall only calculate the lowest value of $\tilde{C}_{mn} \simeq F^{-1}_{mn}$. For the case of our two parameter model, the error covaraiance matrix is:

$$\tilde{C}_{mn} = \begin{bmatrix} \sigma^2_{\zeta} & \sigma_{\zeta T_{vir}} \\ & \\ \sigma_{T_{vir}\zeta} & \sigma^2_{T_{vir}} \end{bmatrix}. \tag{6.12}$$

In the above equation σ_{ζ} and $\sigma_{T_{vir}}$ are the $1-\sigma$ uncertainities in our model parameters. The correlation coefficient $\rho = \dfrac{\sigma_{\zeta T_{vir}}}{\sigma_{\zeta}\sigma_{T_{vir}}}$ describes the correlation between the two parameters. If $\rho = 1$, the the two parameters are completely correlated. In general, $-1 \leq \rho \leq 1$, where $\rho = 0$ means that the parameters are completely uncorrelated and $\rho = -1$ implies anticorrelation.

We calculated $\tilde{C}_{mn}$ for model parameters, $\zeta^* = 17.0$ and $T^*_{vir} = 3.1 \times 10^4$ K. For this purpose we first calculated the partial derivatives of our statistics with respect to the parameters at (ζ^*, T^*_{vir}). The partial derivatives have been calculated using numerical three-point-mid-point formula. Therafter, we calculate the Fisher matrix using eq. 6.10 for various combinations of our statistics using C_{ij} for the noiseless case and the noisy case with $t_{obs} = 2000$ hrs, smoothed at $R_S = 9.5$ Mpc.

We find that for the two parameters under consideration, $\det[F_{mn}] \simeq 0$ which means that the two parameters are completely correlated and hence must be related linearly as $\zeta = \eta\ T_{vir}$. Therefore, one can determine the error only in one parameter using a single element Fisher matrix obtained by setting $m = n$ in eq. 6.10, for ζ or T_{vir}. Thereafter, the error in η at (ζ^*, T^*_{vir}) is given by:

$$\Delta\eta = \sigma_\eta + \sigma_{T_{vir}}. \tag{6.13}$$

In Table 6.2 we list the errors in ζ and T_{vir} and the resultant error in η.

Parameter	N_{hole}	r^{ch}_{hole}	β^{ch}_{hole}	$N_{hole} + r^{ch}_{hole}$	$N_{hole} + r^{ch}_{hole} + \beta^{ch}_{hole}$
σ_ζ	1.342	1.436	10.05	0.68	0.496
$\sigma_{T_{vir}}(\times 10^4)$	0.470	0.772	4.22	0.288	0.206
$\Delta\eta$	1.812	2.208	14.27	0.968	0.702

Parameter	N_{hole}	r^{ch}_{hole}	β^{ch}_{hole}	$N_{hole} + r^{ch}_{hole}$	$N_{hole} + r^{ch}_{hole} + \beta^{ch}_{hole}$
σ_ζ	1.356	1.47	10.7	0.69	0.508
$\sigma_{T_{vir}}(\times 10^4)$	0.475	0.786	4.5	0.29	0.21
$\Delta\eta$	1.831	2.256	15.2	0.98	0.718

Table 6.2 The tables show the lower bounds on the errors in model parameters ζ and T_{vir} for a δT_b field smoothed at $R_S = 9.5$Mpc. The first table is for the case of no noise while the second table is for the case of SKA noise for $t_{obs} = 2000$ hrs. We find that the errors decrease on using a combination of all three statistics. We also find that for β^{ch}_{hole}, there is no increase in errors on inclusion of noise, a very mild increase for r^{ch}_{hole} and considerable increase for N^{ch}_{hole}.

From the table we find that, when used in itself, N_{hole} has the best constraining power and β^{ch}_{hole} cannot be used for constraining. As mentioned in the previous section, this is a result of the mild variation of β^{ch}_{hole} with any of the parameters. However as mentioned before, in order to break degeneracies in the variation of the statistics in N_{hole}, one needs to combine it with r^{ch}_{hole} for which the lower bounds on errors have lesser value compared to any of the individual statistic used. We find that on adding β^{ch}_{hole}, the lower bounds on errors decreases further. Therefore, on using a combination of $N_{hole} + r^{ch}_{hole} + \beta^{ch}_{hole}$ we can obtain the best constraints on our model parameters.

6.6 Bayesian analysis

In this section, we describe how we perform Bayesian analysis to recover constraints on model parameters using our statistics. Since the underlying model for our observed mock simulation is known, the analysis is aimed at showing how well the model is recovered by our statistics. The model used for constructing the mock data is the *mock* model described in section 6.2.1 with $\zeta^{mock} = 17.5$, and $T_{vir}^{mock} = 3 \times 10^4$ K.

In Bayesian analysis one calculates the posterior probability distribution of model parameters, given the observed value of the statistics. Let $\vec{\theta} = (\zeta, T_{\rm vir})$ denote the parameters vector. Let superscript 'th' refer to theoretical parameter and 'data' refer to (mock) observed data. Let $\vec{X} = (N_{hole}, r^{\rm ch}_{hole}, \beta^{\rm ch}_{hole})$ denote the vector of the 3 statistics which are functions of $\vec{\theta}$. Then, the posterior probability for the model parameters, given the data $\vec{X}^{\rm data}$ is:

$$P(\vec{\theta}^{\,\rm th}|\vec{X}^{\rm data}) = \frac{\mathscr{L}(\vec{X}^{\rm data}|\vec{\theta}^{\rm th})\,\pi(\vec{\theta}^{\rm th})}{\rm Norm}. \tag{6.14}$$

π is the prior probability which we assume to be uniform in the specified prior range. $\mathscr{L}$ is the likelihood function which we assume to be Gaussian in $\vec{X}$ and for a given covariance matrix C_{ij} it is written as:

$$\begin{aligned} \mathscr{L}(\vec{X}^{\rm data}|\vec{X}^{\rm th}) &= \frac{1}{\sqrt{(2\pi)^d \det(\mathrm{C})}} \exp\left[-\frac{1}{2}\sum_{ij}\Delta X_i C_{ij}^{-1}\Delta X_j\right] \\ &\propto e^{-\chi^2/2}, \end{aligned} \tag{6.15}$$

where $\vec{\Delta X} \equiv \vec{X}^{\rm data} - \vec{X}^{\rm th}$, $\chi^2 = \sum_{ij}\Delta X_i C_{ij}^{-1}\Delta X_j$. The normalization is given by

$$\mathrm{Norm} = \int \mathrm{d}\theta^{\rm th}\,\mathscr{L}(\vec{X}^{\rm data}|\vec{X}^{\rm th})\,\pi(\vec{\theta}^{\rm th}), \tag{6.16}$$

and $\chi^2 = \sum_{ij}\Delta X_i C_{ij}^{-1}\Delta X_j$. $\mathscr{L}$ implicitly depends on $T_{\rm vir}$ and ζ. The factor $\pi(\vec{\theta}^{\rm th})/\mathrm{Norm}$ is only a constant which can be calculated to fix the amplitude of the posterior. Therefore,

$$P(\vec{\theta}^{\,\rm th}|\vec{\theta}^{\rm data}) = \frac{1}{\mathscr{N}}\exp\left(-\frac{1}{2}\sum_{ij}\Delta X_i C_{ij}^{-1}\Delta X_j\right), \tag{6.17}$$

where

$$\mathscr{N} = \mathrm{Norm} \times \sqrt{(2\pi)^d \det(\mathrm{C})}. \tag{6.18}$$

Thus, in order to obtain the posterior, $P(\vec{\theta}^{\,\rm th}|\vec{\theta}^{\rm data})$ we need the mock observed value of our statistic, the covariance matrix and the likelihood function. We perform our analysis using

COSMOMC (Lewis & Bridle, 2002) as a generic sampler with Gaussian likelihood function. The code performs a Markov Chain Monte-Carlo sampling of the parameter space to calculate the Likelihood and subsequently the posterior. We adopt the following steps for performing the Bayesian analysis:

1. We construct 40 independent realizations of our mock data with and without noise, using the parameters and methods described in section 6.2. For noiseless case we construct realizations by varying the initial condition seed of our semi-numerical simulations and for the noisy case we fix a noiseless realization and vary the seed value for the Gaussian random noise added to it, for a given σ_N. Thereafter, we use these to calculate the error covariance matrix as described in eq. 6.9.

2. We fix our prior range between $10^4 \leq T_{vir} \leq 8 \times 10^4$ K and $8 \leq \zeta \leq 28$, due to the reasons described in section 6.3.

3. The mock observed value of our statistics is calculated as a mean over 40 realizations for a given value of t_{obs} and corresponding σ_N for our *mock model*.

4. Due to computational limitations, the Likelihood calculation is performed by interpolating values of the statistic in the parameter space by using the grid of 400 models for which the value of the statistics is calculated numerically as described in section 6.3.

For a meaningful comparison of the statistics obtained for theoretical models with the mock observed values, we should follow the *exact same procedure* to compute the theoretical statistics, for our 400 models and for the mock values. For our theory model and as mentioned before, due to limitations on computing resources, instead of averaging over independent realizations we mimic the ensemble average by carrying out the average using two dimensional slices obtained from each data cube for each model, along a fixed direction. Each slice has a thickness corresponding to 1 MHz. Therefore, we extracted 24 slices from our 400 Mpc box and thereafter smoothed the 2D slices. On the other hand, the mock observed statistics is chosen to be the mean value obtained by averaging over 40 *independent* realizations, computed for the mock model (section 6.3). The use of a single realization for the calculation of theoretical values of the statistics, will result in some statistical fluctuation when comparing with the mock observed values. However we expect (and do find) that this fluctuation is within the error bars determined by the covariance matrix.

6.6.1 One-dimensional Parameter Space

Even though we do not perform the Bayesian analysis in one dimensional space in this thesis, it is interesting to reduce the posterior probability to one dimension, keeping in mind that the degeneracy between ζ and T_{vir} can be used to reduce to one variable, namely $\bar{x}_{HI}$ using the fitting relations obtained in section 6.3.1. This can be done by transforming variables as $(\theta_1, \theta_2) \rightarrow (\varphi_1, \varphi_2)$

$$\varphi_1 = \varphi_1(\theta_1, \theta) \tag{6.19}$$

$$\varphi_2 = \varphi_2(\theta_1, \theta). \tag{6.20}$$

The variables must be made to have same dimensions first. This can be done by dividing $T_{\rm vir}$ by 10^4K.

We can rewrite χ^2 in terms of φ_i as,

$$\chi^2 = \sum_{\alpha\alpha'} \Delta\phi_\alpha \Sigma^{-1}_{\alpha\alpha'} \Delta\phi_{\alpha'}, \tag{6.21}$$

where the new covariance matrix is

$$\begin{aligned} \Sigma^{-1}_{\alpha\alpha'} = \sum_{mn} \frac{\partial\theta_m}{\partial\varphi_\alpha} \widetilde{C}^{-1}_{mn} \frac{\partial\theta_n}{\partial\varphi_{\alpha'}} &= \sum_{mn} \frac{\partial\theta_m}{\partial\varphi_\alpha} \sum_{ij} \frac{\partial X_i}{\partial\theta_m} C^{-1}_{ij} \frac{\partial X_i}{\partial\theta_n} \cdot \frac{\partial\theta_n}{\partial\varphi_{\alpha'}} \\ &= \sum_{mn} \frac{\partial X_m}{\partial\varphi_\alpha} C^{-1}_{mn} \frac{\partial X_n}{\partial\varphi_{\alpha'}}. \end{aligned} \tag{6.22}$$

Suppose X_m is independent of, say, φ_2. Then, we need only

$$\Sigma^{-1}_{11} = \sum_{mn} \frac{\partial X_m}{\partial\phi_1} C^{-1}_{mn} \frac{\partial X_n}{\partial\varphi_1}. \tag{6.23}$$

The posterior probability in terms of φ_1 is then given by

$$P(\vec{\varphi}_1{}^{\rm th} | \vec{\phi}^{\rm data}) = \frac{1}{\mathcal{N}} \exp\left(-\frac{1}{2}\Delta\varphi_1 \Sigma^{-1}_{11} \Delta\phi_1\right). \tag{6.24}$$

By, plugging in Σ^{-1}_{11} computed numerically we can obtain $P(\vec{\phi}_1{}^{\rm th}|\vec{\phi}^{\rm data})$.

The variable φ_1 in eqs. 6.24 and 6.23 is $\bar{x}_{HI}$ for our case and therefore the posterior is:

$$P(\bar{x}^{th}_{HI} | \bar{x}^{data}_{HI}) = \frac{1}{\mathcal{N}} e^{-\Delta\bar{x}^2_{HI}/2\Sigma_{11}} \tag{6.25}$$

6.7 Results: Recovering Constraints

In order to show whether the *mock* model can be recovered within admissible errors, we performed Bayesian analysis on our mock noiseless simulation. The 1 and 2-σ constraint regions and marginalized probability for each parameter for $R_s = 9.5$ Mpc are shown in Fig. 6.8 for $N_{hole} + r^{ch}_{hole}$ in the left panel and $r^{ch}_{hole} + N_{hole} + \beta^{ch}_{hole}$ on the right panel. The black dashed line corresponds to $x_{HI} = 0.5$ and the star is the input *mock* model ($T^{mock}_{vir} = 3 \times 10^4$ K and $\zeta^{mock} = 17.5$). The figure shows that within the cosmic variance limit the mock model is recovered to within 1-σ accuracy. In Fig. 6.9 we show the same plots, but for a noisy δT_b map, with $t_{obs} = 2000$ hrs smoothed at $R_S = 9.5$ Mpc. The justification for the observed time and smoothing has been explained in Section 6.6. The smoothed noise map also enables us to recover the input mock model to within 1-σ accuracy. The best fit values obtained are summarized in Table 6.3.

Parameter		$N_{hole} + r^{ch}_{hole}$	$N_{hole} + r^{ch}_{hole} + \beta^{ch}_{hole}$
ζ	No Noise, $R_S = 9.5$ MPc	$16.88^{+2.12}_{-2.92}$	$17.23^{+2.071}_{-2.915}$
	$R_s = 9.5$ Mpc, $t_{obs} = 2000$ hrs	$18.04^{+2.42}_{-3.53}$	$17.328^{2.272}_{-3.16}$
$T_{vir}(K)$	No Noise, $R_S = 9.5$ MPc	$26937.1^{+5461.2}_{-8995.6}$	$27924.5^{+5419.1}_{-9187.3}$
	$R_s = 9.5$ Mpc, $t_{obs} = 2000$ hrs	30685.7^{+6568}_{-11088}	$28645^{+5910}_{-9831.5}$

Table 6.3 The table shows values of best fit parameters and 1-σ uncertainties for ζ and T_{vir} for noiseless δT_b map and for the mock observed δT_b map with SKA noise for $t_{obs} = 2000$ hrs. Both the maps were smoothed at $R_S = 9.5$ Mpc Note that the input model for obtaining these maps was $T^{mock}_{vir} = 3 \times 10^4$ K and $\zeta^{mock} = 17.5$.

Table 6.3 shows that the constraints on $\Delta\eta$ inferred from the spread in the best-fit parameters using eq. 6.13 are tighter for $N_{hole} + r^{ch}_{hole} + \beta^{ch}_{hole}$ ($\sigma_{T_{vir}} = 7779.78$ and $\sigma_\zeta = 2.61$) as compared to $N_{hole} + r^{ch}_{hole}$ ($\sigma_{T_{vir}} = 7736.58$ and $\sigma_\zeta = 2.63$) for the case of no noise. Same behaviour is obtained in noisy case where adding β^{ch}_{hole} gives tighter constraints ($\sigma_{T_{vir}} = 8367.44$ and $\sigma_\zeta = 2.83$) as compared to the case of excluding β^{ch}_{hole} ($\sigma_{T_{vir}} = 9021.08$ and $\sigma_\zeta = 3.00$).

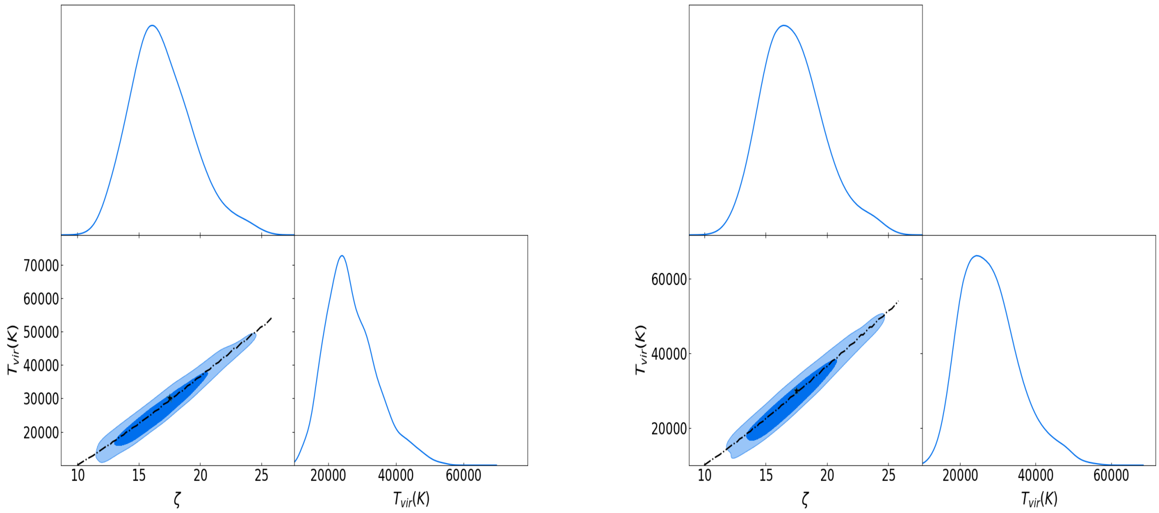

Fig. 6.8 The figure shows the the 1- and 2-σ constraints and marginalized probabilities obtained for the noiseless mock data for $R_s = 9.5$ Mpc using $N_{hole} + r^{ch}_{hole}$ (*left*) and $N_{hole} + r^{ch}_{hole} + \beta^{ch}_{hole}$ (*right*). The dark blue region is the $1-\sigma$ uncertainity and the light blue is the $2-\sigma$ region. The black dashed line is the line for which $x_{HI} = 0.5$ and the black star is the input *mock* model corresponding to $\zeta^{mock} = 17.5$ and $T^{mock}_{vir} = 3\times10^4$ K.

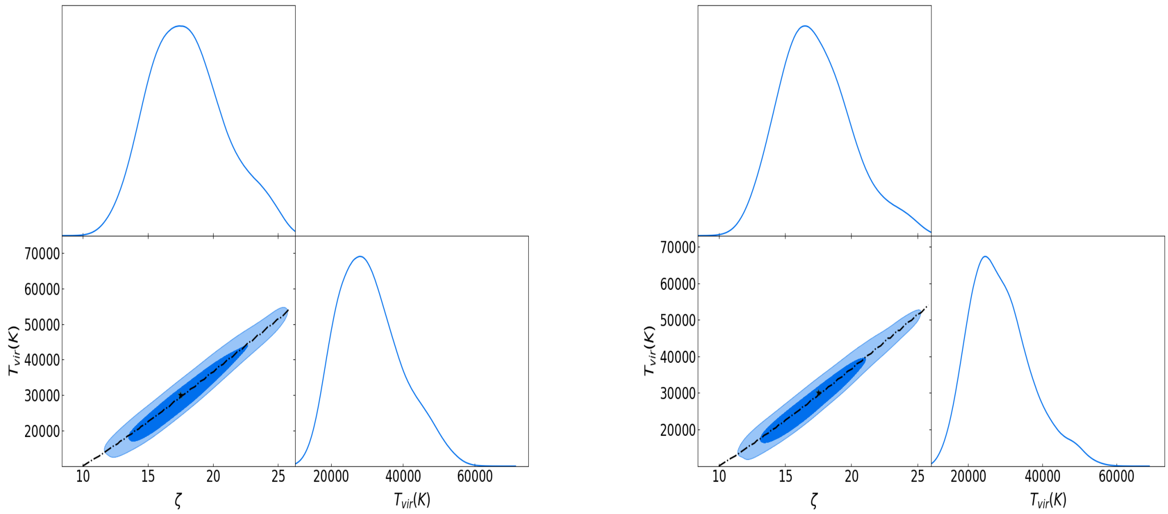

Fig. 6.9 The figure shows the the 1- and 2-σ constraints and marginalized probabilities obtained for the mock data with SKA noise, smoothed at $R_s = 9.5$ and $t_{obs} = 2000$ hrs Mpc using $N_{hole} + r^{ch}_{hole}$ (*left*) and $N_{hole} + r^{ch}_{hole} + \beta^{ch}_{hole}$ (*right*). The dark blue region is the $1-\sigma$ uncertainity and the light blue is the $2-\sigma$ region. The black dashed line is the line for which $x_{HI} = 0.5$ and the black star is the input *mock* model corresponding to $\zeta^{mock} = 17.5$ and $T^{mock}_{vir} = 3\times10^4$ K.

6.8 Conclusion and ongoing work

In this chapter, we have explored the prospects of constraining model parameters for a simple two parameter model of EoR using r^{ch}_{hole} ,N_{hole} and β^{ch}_{hole}. We first explored the behaviour of our statistics in parameter space and found that while r^{ch}_{hole} and N_{hole} are sensitive to the variation in parameters, β_{hole} shows very little variation across the parameter space. We also find that N_{hole} is degenerate in parameter space for models which have $\bar{x}_{HI}$ greater than and less than $\simeq 0.7$. Therefore, we concluded that N_{hole} and β^{ch}_{hole} cannot be individually used by themself to constrain parameters.

We then constructed a mock noisy 21-cm image at a redshift of $z = 7.4$ using SKA parameters and explored the effect of smoothing and increasing observation hours to overcome noise. We found that at a smoothing scale of $R_S = 9.5$ Mpc, the statistics of the noisy image approaches those of noiseless case for a $t_{obs} = 2000$ hrs.

Thereafter, we performed a Fisher matrix analysis and inferred that ζ and T_{vir} are strongly correlated. We found that while $N_{hole} + r^{ch}_{hole}$ gives better constraints than any of the statistics used individually, inclusion of β^{ch}_{hole} decreases the standard deviation by $\simeq 27.5\%$. Therefore, we used a combination of $r^{ch}_{hole} + N_{hole} + \beta^{ch}_{hole}$ and found that the input mock model is recovered to within $1-\sigma$ accuracy for a noiseless $\delta\ T_b$ map. On introducing SKA noise for $t_{obs} = 2000$ hrs we still recovered the mock model to within $1-\sigma$. We conclude that topology based techniques can therefore serve as complimentary to Fourier based methods to obtain constraints on EoR parameters.

A complete analysis and a comparison with power spectrum estimates would require us to include more parameters. We are currently working with a 3 parameter model of EoR described by ζ, T_{vir} and R_{mfp}, which is the base model of most semi-numerical simulations of EoR including 21cmFAST. The complete constraining power of these statistic can be exploited when we span a more complex parameter space which encompasses parameters describing galaxy properties and feedback mechanisms. In order to perform a fair comparison with observations we would need to take into account foreground subtraction, which shall be carried out in future.

7

Preliminary results for Minkowski Tensors in 3-D and future directions

7.1 Motivation

So far in the thesis, we have studied the evolution of the topology and geometry of the 21cm brightness temperature field in 2D. Actual physical processes operate in 3D and the full information may not be captured in the 2D topology of 21cm tomographic images. This is because two topologically and geometrically distinct features can appear to have the same topology in 2D. As an example of the ambiguity that 2D topology presents, consider the similarity between a prolate and an oblate shape when projected on to a 2D plane. Both would appear as ellipses in 2D while in actuality their geometry in 3D is very different. The two cases in 3D may arise due to entirely different physical processes, which would not be captured in 2D. Therefore, in order to study physical processes or test semi-analytical methods in 3D simulations of EoR, the Minkowski tensors in 3D (Schröder-Turk et al., 2013; Appleby et al., 2018b) could provide a useful tool. An example of inferring physical processes in 3D is (Bag et al., 2018, 2019), where the authors found that the largest ionized regions after percolation

[1] are found in filamentary structures. An example of testing and quantifying discrepancies between numerical simulations and analytical techniques is that of photon non-conservation in excursion set based models (Choudhury & Paranjape, 2018), where the authors find that the size of ionized regions is larger than that expected for the number of photons available to ionize. Lastly, as pointed out in chapter 4, Minkowski tensors in 3D will serve as useful descriptor of bubble sizes during EoR because they encapsulate both anisotropy and size information.

In this chapter we give an introduction to Minkowski tensors in 3D in section 7.2 . We have obtained some preliminary results for anisotropy parameter for basic reionization models, described in section 3.3. We conclude the chapter with direction of further research in section 7.4.

7.2 Definition

In 3D the boundary of an excursion set would consist of surfaces enclosing a void, tunnel or solid connected volumes, see for example (Elbers & Weygaert, 2019; Pranav et al., 2019). The rank 2 Minkowski tensors for the surfaces obtained are defined as follows:

$$W_0^{m,0}(Q) = \int \vec{r}^m dV \tag{7.1}$$

$$W_i^{m,n}(Q) = \frac{1}{2}\int \vec{r}^m \otimes \hat{n}^n G_i da, \tag{7.2}$$

for $i = 1,2,3$ where dV is the volume enclosed by the excursion set surface Q and da is the area element on these surfaces. G_i are defined below for the principal curvatures of the surface k_1 and k_2:

$$\begin{aligned} G_1 &= 1 \\ G_2 &= (k_1+k_2)/2 \\ G_3 &= k_1 k_2, \end{aligned} \tag{7.3}$$

where G_2 and G_3 are the mean curvature and the Gaussian curvature, respectively (see Appendix (E.2.0.2)). There are ten rank-2 Minkowski tensors in 3D. There are six Minkowski tensors which are linearly independent. We focus on the following two translationally invariant MTs (per unit volume):

$$W_1^{0,2} = \frac{1}{6V}\int_{\partial Q} \hat{n}^2 da \tag{7.4}$$

[1] Ionized bubbles are said to percolate when the entire ionization field is a single connected region, with scattered neutral islands. This happens when bubble mergers approach completion.

$$W_2^{0,2} = \frac{1}{3\pi V}\int_{\partial Q} G_2 \hat{n}^2 da. \tag{7.5}$$

Note that these are 3×3 matrices with the eigenvalues in eq. 7.5 having dimensions of area by volume and eigenvalues in eq. 7.5 with dimensions of length by volume. For our current purpose, we choose to work with $W_1^{0,2}$. We choose $\lambda_1 < \lambda_2 < \lambda_3$. Similar to the 2D case, the ratio of these eigenvalues encapsulate the anisotropy information of the surface. There are two ways to take the ratio as $\beta_{(1,2)} = \lambda_{1,2}/\lambda_3$. These statistics describe anisotropy information along two separate directions. Taking the example of an ellipsoid with the semi-major axes as λ_1, λ_2 and λ_3 and noting that $\beta_1 \leq \beta_2$ the following cases arise:

1. If $\beta_1 = \beta_2 = 1$ the bounding area is isotropic
2. If $\beta_1 < 1$ and $\beta_2 = 1$, i.e. $\lambda_2 = \lambda_3$ then the bounding area is oblate in shape.
3. If $(\beta_1 = \beta_2) < 1$, i.e. $\lambda_1 = \lambda_2$ then the bounding surface is prolate in shape.

Just as in the 2D case the trace of these tensors contains the information of their scalar counterparts:

$$Tr(W_1^{0,2}) = W_1 \tag{7.6}$$
$$Tr(W_2^{0,2}) = W_2, \tag{7.7}$$

where W_1 is the total surface area enclosing the excursion set and W_2 is the integral of the mean curvature of the bounding surface. W_1 and W_2 are two of the four scalar Minkowski functionals in 3D. Thus, analogous to the 2D case, in 3D we can infer ionization history using $\beta_{(1,2)}$. By an appropriate definition of the characteristic size of bubbles one can infer a size distribution using the sum of their eigenvalues. The following section describes some preliminary results obtained using $W_1^{0,2}$.

7.3 Preliminary Results: Anisotropy measures

As a first step towards our analysis in 3D, we have obtained some preliminary results by carrying out the analysis on the same set of simulations as used in Chapter 4. We analyse two different models, one with $T_{vir} = 3 \times 10^4\ K$ and the other with $T_{vir} = 1 \times 10^4\ K$ and $\zeta = 50$. The EoR ends at $z \simeq 6$ and $\simeq 7$ respectively for these two models. The fields have been smoothed at a smoothing scale of $R_s \simeq 4.5$ Mpc. The evolution of $\bar{x}_{HI}$ is described in fig.7.1.

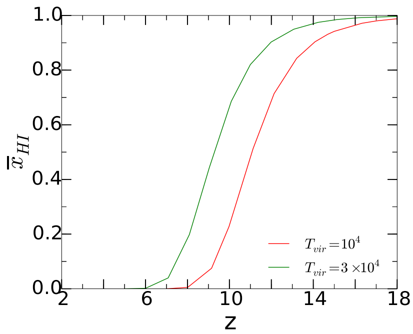

Fig. 7.1 The evolution of the mean neutral hydrogen fraction for the models with $T_{vir} = 3 \times 10^4$ K (*green*) and $T_{vir} = 10^4$ K (*red*).

We used the numerical calculation of Minkowski tensors in 3D using the marching tetrahedron algorithm (Appleby et al., 2018b). Thereafter, we find $\beta_{(c,h)1}(z)$ and $\beta_{(c,h)2}(z)$ using eq. (4.4) for holes and connected regions. We also calculate $\beta_{(1,2)}$ for all structures (i.e. both holes and connected region). Note that $\beta_{(1,2)}$ would reflect the morphology of connected region or hole depending upon which of the two have higher number count. In regions where $n_c = n_h$, it just reflects the average morphology of the two types of structures. The results are shown in figs. 7.2 and 7.3 for δ_{nl}, T_S, x_{HI} and δT_b fields for the two models under consideration. In order to understand the evolving morphology, we compare β_1 and β_2 for each type of structure for all fields using figs. 7.2 and 7.3 respectively. We summarize our interpretations for the model with $T_{vir} = 3 \times 10^4$ K:

- Shape anisotropy parameter of δ_{nl}: is described by the first column of the figures. We find that the connected (higher density) regions seem to evolve faster along the direction of the larger eigenvalue as encapsulated in β_{c1}. This is expected as a result of Zel'dovich collapse used in 21cmFAST. The inequality between β_{c1} and β_{c2} shows that the high density regions are more oblate than prolate. The same is true for $\beta_{h(1,2)}$, however there seems to be almost no evolution in the topology of holes (or voids).

- Shape anisotropy parameter of T_S: is shown in the second column of the figures. We find from the evolution of $\beta_{(1,2)}$ that for both connected regions and holes the evolution is similar. This is expected by the same reasoning as in section (5.4). We find that both connected regions and holes exhibit oblateness throughout the evolution.

- Shape anisotropy parameter of δT_b and x_{HI}: The morphology of δT_b is shown in the third column in the figures while that of x_{HI} in the fourth column. We find that connected regions show two turnovers in case of δT_b evolution for both $\beta_{1,2}$. These turnovers are similar to those found in fig. 5.14. Clearly the morphology is very different from the morphology of connected regions or holes of x_{HI} field for $z \geq 10$, where the first turnover in δT_b occurs for the model with $T_{vir} = 3 \times 10^4\ K$ for both connected region or holes. At $z < 10$ the morphology of both connected region and holes of δT_b follow that of x_{HI} field. The evolution thereafter, especially for holes for both $\beta_{h(1,2)}$is similar to that observed for the two fields in chapter 4. However the important point to note is that while throughout the evolution the morphology is oblate, in the post merger regime at a redshift of about ~ 7 for the model with $T_{vir} = 3 \times 10^4\ K$ we find that $\beta_1 \simeq \beta_2$. This implies that the morphology transitions towards prolateness. This is consistent with the results in (Bag et al., 2018, 2019).

We find that for the model with lower T_{vir} this transition to prolateness occurs at a higher redshift as expected from the evolution of it's ionized fraction. These preliminary results set the stage for an intuitive picture of 3D morphology as expected from the physical evolution explained in chapter 5.

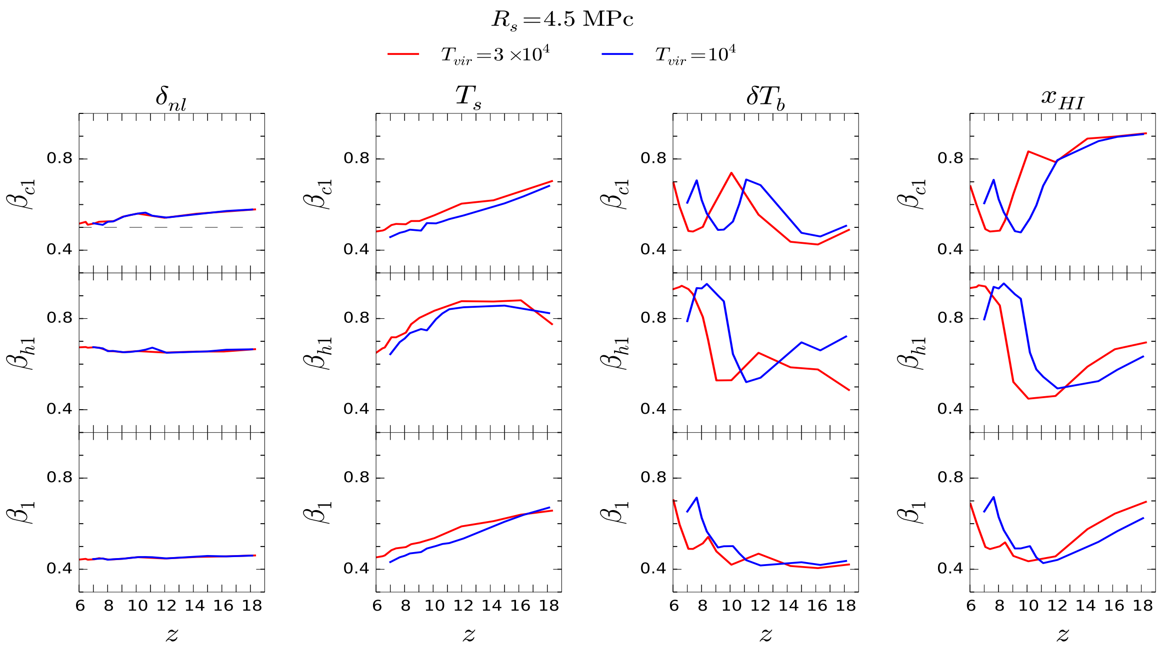

Fig. 7.2 The figure describes the evolution of β_1 for connected regions *(top panel)*, holes*(middle panel)* and all structures *(bottom panel)* with redshift for the δ_{nl}, T_S, δT_b and x_{HI} fields. The red lines describe the model with $T_{vir} = 3 \times 10^4\ K$ while the blue line is for the model with $T_{vir} = 10^4\ K$.

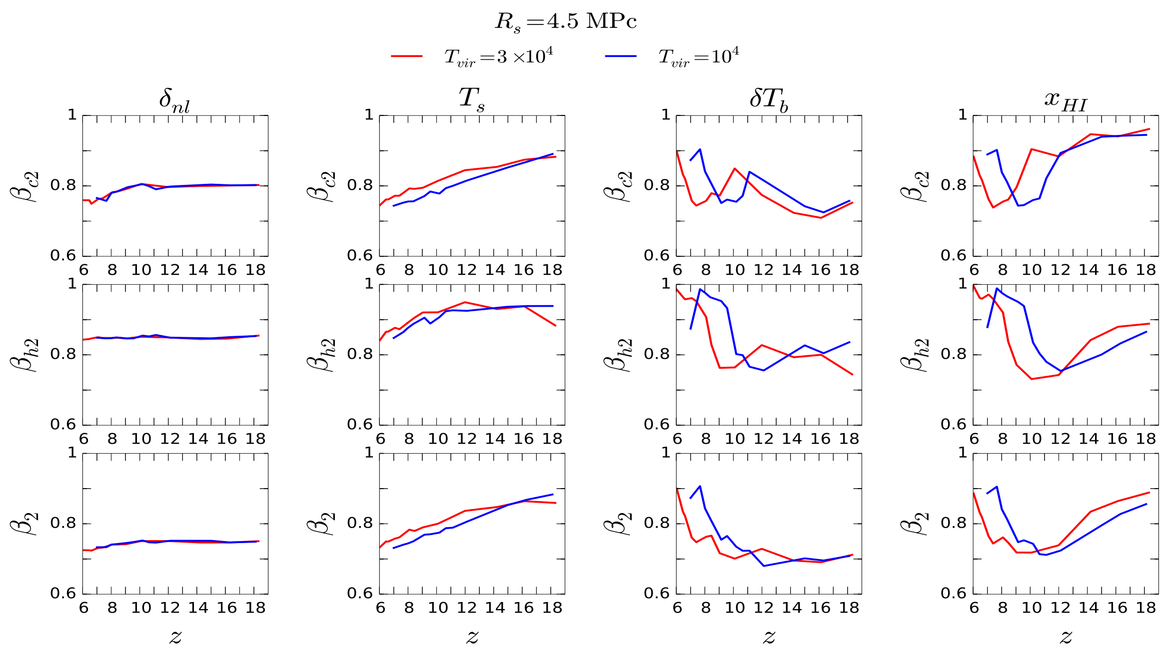

Fig. 7.3 The figure describes the evolution of β_2 for connected regions *(top panel)*, holes(middle) and all structures *(bottom panel)* with redshift for the δ_{nl}, T_S, δT_b and x_{HI} fields. The red lines describe the model with $T_{vir} = 3 \times 10^4$ K while the blue line is for the model with $T_{vir} = 10^4$ K.

We intend to carry out a detailed analysis of all morphological statistics, by using simulations with detailed models to understand the topology of the fields in 3D during the EoR.

7.4 Directions of further Research

7.4.1 Bubble Sizes:

As mentioned in chapter 4, in order to obtain a bubble size distribution of ionized regions, one would need to resort to 3D Minkowski tensors. In the previous section it was mentioned that the trace of $W_1^{0,2}$ will give a measure of the total surface area of excursion sets. The ratio of the product and the sum of the eigenvalues of this tensor will provide us with scale information. An appropriately constructed characteristic size will enable us to obtain a size distribution of ionized bubbles under different scenarios of EoR. But, it is to be noted that the observations of EoR using SKA would provide us with 2D images. Therefore, we would need ways to construct the 3D statistical information of 21cm brightness temperature using 2D images of the brightness temperature field (see (Shankar & Khatri, 2019) for such a study performed on galaxy clusters). This process is called *stereology* [2] and the statistical quantification of 2D fields in this thesis would serve as a starting point for such a study.

7.4.2 Lightcone Effect:

So far in our analysis we worked with coeval cubes i.e. we ignored the effect of expansion of the universe along our line of sight and also ignored the effect of peculiar velocities in our analysis. These effects introduce anisotropy in the 21cm signal both in real space and in power spectrum measurements. Minkowski tensors can capture any globally preferred direction in addition to anisotropy in individual structures. Minkowski tensors in 3D have been used to study the anisotropic signal produced by the redshift space distortion in low redshift matter density field (Appleby et al., 2019). Therefore, such a study could also be used for correcting any line of sight effects that leads to the distortion of the 21cm signal. In that direction, a physical effect of interest is the lightcone effect and has been studied in (Datta et al., 2012, 2014). The correlations along the line of sight differ from those which are normal to the line of sight. This causes an anisotropy in the 3-D power spectrum of the 21cm brightness temperature. The lightcone effect is a result of statistical differences in the field due to finite length of the redshift range under study because the signal along the line-of-sight direction of any observed volume would evolve with redshift. The light cone effect in real space would manifest as a distortion of ionized bubbles. The amount of anisotropy appearing due to lightcone effect depends upon the stage of reionization in the ionization history of the IGM and the bandwidth of observation. One can therefore quantify the anisotropy introduced due to the lightcone effect for different thickness (or bandwidths) along the line of sight. We expect that this quantification can help choose an appropriate bandwidth of observations for which the corrections due to lightcone effect should be made to any statistical measure.

[2] Note that stereology is different from tomography. Stereology is inferring 3D information using 2D slices while tomography is 2D slicing of 3D objects.

8

Conclusion

The detection of the 21cm signal from the cosmic dawn and the epoch of reionization will beacon a new era of cosmological exploration. Tomographic imaging of the cosmic dawn and the Epoch of Reionization will provide us with direct insights into the nature of first collapsed sources through their impact on the IGM and subsequent evolution. Theoretical modelling of the physics of the cosmic dawn and the EoR is complicated due to many different physical processes operating at different length and time scales. There are a plethora of models in literature, and we await data from observations to narrow down to the correct model. The statistical detection of the 21cm signal when complemented with imaging will provide the data that will enable us to obtain stringent constraints on the astrophysical parameters of these first sources and the evolution of the universe during this epoch. In addition, the signal will carry imprints of the origins of primordial fluctuations. By careful extraction of the primordial information from the astrophysical processes of the EoR one can infer properties of the promordial fluctuations and learn about the physics that operated at very early times. The work in this thesis has focussed on the physical questions related to the astrophysical processes of the EoR and the prospects of constraining the parameters of theoretical models.

Several observational efforts are ongoing to obtain 21cm data from the cosmic dawn and the EoR, and is expected to be available in the future. Along with theoretical modelling and experimental efforts to observe the cosmic dawn and the EoR, efficient methods for analysis of data and comparison with theoretical models forms the third crucial pillar upon which the understanding of the cosmic dawn and the EoR rests. The analysis methods are traditionally based on Fourier space observables, with a good reason since the observed data will be obtained in Fourier space and noise levels are high. The extraction of physical imformation then relies on statistics such as the power spectrum and bispectrum. However, for a majority of the physical question, such as those that are related to the large non-Gaussian nature of the fields, it is not sufficient to restrict to the first few n-point functions. Information from all orders of correlations is not only desirable but necessary for correct physical inference. Statistics that are constructed from real space variables can carry information of all orders of n-point functions. The increasing availability of cosmological data that have higher signal-to-noise ratio, and sky resolution and coverage make such statistics attractive tools to *complement or serve as alternatives* to n-point functions in Fourier space.

In this thesis we have introduced a real space morphological tool, Contour Minkowski tensor (CMT) to analyse the 21cm brightness temperature field from EoR. We showed that the size and shape information of structures encoded by the eigenvalues of CMT enable us to extract maximum information from minimum number of morphological descriptors. We devised a statistical framework which will help us answer a plethora of physical questions required to model EoR with upcoming 21cm observations. We showed that we can infer bubble size information, ionization history and astrophysical properties of first sources using CMT. We devised a pipeline for constraining model parameters by comparing theory with mock observation from future radio interferometers such as the SKA I low.

We have set a starting stage to extend to the more generalized 3 dimensional Minkowski tensors in order to obtain conclusive comparisons with other methods in literature. We also plan to combine our technique with other real space topological descriptors. The full potential of real space descriptors for 21 cm observations of EoR can be realized if the design of future interferometers allows for cleaner images from the cosmic dawn and EoR with improved foreground cleaning and data handling.

A

Fundamentals of Radiative transfer

A.1 Radiative Transfer Equation

(Based on Rybicki & Lightman (2008))

A ray of light is described in terms of the specific intensity or brightness, I_ν in units of ($ergs\ cm^{-2}s^{-1}ster^{-1}Hz^{-1}$) such that the energy through an area element dA in time dt and frequency range $d\nu$ through a solid angle $d\Omega$ is defined as:

$$dE = I_\nu dA\ dt\ d\Omega\ d\nu \tag{A.1}$$

As a monochromatic ray of light passes through a medium, it will either gain energy on account of emission or lose energy due to absorption. For a monochromatic emission, the spontaneous *emission coefficient*, j_ν (in ergs $cm^{-3}s^{-1}ster^{-1}Hz^{-1}$) is defined as the energy emitted per unit time per unit solid angle per unit volume and per unit frequency:

$$dE = j_\nu dV\ d\Omega\ dt\ d\nu \tag{A.2}$$

Therefore, the intensity added as the beam traverses a volume $dV = dA\ ds$ is given by:

$$dI_\nu = j_\nu\ ds \tag{A.3}$$

The *absorption coefficient*, α_ν (in cm^{-1}) describes the fraction of intensity absorbed per unit length ,of the total incident intensity. Therefore the loss of intensity due to absorption is given by :

$$dI_\nu = -\alpha_\nu\ I_\nu\ ds \tag{A.4}$$

If one considers a number n of randomly distributed absorbers per unit volume, each with an area of cross-section σ_ν. Then the absorption coefficient, can be expressed as, $\alpha_\nu = n\ \sigma_\nu$. The emission and absorption along a ray of light can be combined into a single equation which describes the change in its specific intensity along its path ds:

$$\frac{dI_\nu}{ds} = -\alpha_\nu\ I_\nu + j_\nu \tag{A.5}$$

The radiative transfer equation can be recast in terms of a quantity called the *optical depth* which is measured along the path of light and is defined as:

$$d\tau_\nu = \alpha_\nu\ ds \tag{A.6}$$

$$\tau_\nu(s) = \int_{s_0}^{s} \alpha_\nu ds' \tag{A.7}$$

Therefore eq. (A.5) can be written as:

$$\frac{dI_\nu}{d\tau_\nu} = -I_\nu + S_\nu, \tag{A.8}$$

where the source function $S_\nu \equiv \dfrac{j_\nu}{\alpha_\nu}$, describes the macroscopic aspects of the transfer of radiation. The solution of the transfer equation, eq. (2.10) can be obtained by multiplying with the integrating factor e^{τ_ν} and is given by:

$$I_\nu(\tau_\nu) = I_\nu(0)\ e^{-\tau_\nu} + \int_0^{\tau_\nu} e^{-(\tau_\nu - \tau'_\nu)} S_\nu(\tau'_\nu) d\tau'_\nu \tag{A.9}$$

The first term describes the absorption of the incident background radiation, while the second term describes internal absorption along the remaining path. For a constant source function the above equation becomes:

$$I_\nu(\tau_\nu) = S_\nu + e^{-\tau_\nu}(I_\nu(0) - S_\nu) \tag{A.10}$$

The three important points here are the following:

- For a black body radiation, I_ν depends only on the temperature of the black body and is given by $I_\nu = B_\nu(T)$, where $B_\nu(T)$ is the Planck's function given as:

$$B_\nu(T) = \frac{2h\nu^3/c^2}{exp(h\nu/kT) - 1} \tag{A.11}$$

- For thermal radiation, i.e. radiation from matter in thermal equilibrium at temperature T, $S_\nu = B_\nu(T)$, which is the *Kirchoff's Law*:

$$j_\nu = \alpha_\nu B_\nu(T) \tag{A.12}$$

- Therefore the transfer equation, eq. (2.10), for thermally emitting matter becomes:

$$\frac{dI_\nu}{d\tau_\nu} = -I_\nu + B_\nu(T) \tag{A.13}$$

A.2 Brightness Temperature

If we have a specific intensity I_ν, then the brightness temperature, $T_b(\nu)$ is the temperature of a black body having the same specific intensity i.e.:

$$I_\nu = B_\nu(T_b) \tag{A.14}$$

The main advantage of defining brightness in this way is in the low frequency regime of the black body spectra in eq.(A.11) called the Rayleigh Jean's regime. In this regime $h\nu \ll kT$ and hence, I_ν is linearly dependent on temperature:

$$I_\nu^{RJ}(T) = \frac{2\nu^2}{c^2} k_b T \tag{A.15}$$

Notice that the brightness temperature is also a function of frequency, unless the source is a black body in which case T_b is the same for all frequencies. This enables one to write the transfer equation, eq.(A.13) for a thermal emitter at temperature T, in this regime as:

$$\frac{dT_b}{d\tau_\nu} = -T_b + T \tag{A.16}$$

For a constant temperature, T the solution for this equation is :

$$T_b = T_b(0)e^{-\tau_\nu} + T(1 - e^{-\tau_\nu}) \tag{A.17}$$

One can write the transfer equation in this form for a thermal emitter only in the low frequency regime ($h\nu \ll kT$) because of the linearity between T_b and I_ν. This is not so in the high frequency ($h\nu \gg kt$), Wein regime of the Planck spectra.

A.3 Color Temperature

For an unresolved source, for which one can only measure the flux, the color temperature is defined as the temperature of the black body obtained by fitting the spectra of the source to that of a black body curve. In other words if we measure the slope of I_ν at an observed frequency ν_0, then color temperature is the temperature of the black body for which (Rutten et al. (1995)):

$$\left.\frac{dI_\nu}{d\nu}\right|_{\nu_0} = \left.\frac{dB_\nu(T_c)}{d\nu}\right|_{\nu_0}$$

A.4 Spin Temperature

If we have a two level system in thermodynamic equilibrium at a temperature T, then the ratio of the population between the two levels is given by the Boltzmann's law:

$$\frac{g_0 n_1}{g_1 n_0} = exp(-h\nu_{10}/k_B T) \tag{A.18}$$

Here $n_{(1,0)}$ is the population of the respective levels and $g_{(1,0)}$ is the degenracy of the states. If the system is not in equilibrium, then one can define a temperature called spin temperature T_S, which describes the relative population in the two levels. It is the temperature of the equilibrium system with the same population ratio and is defined as follows:

$$\frac{g_0 n_1}{g_1 n_0} = exp(-h\nu_{10}/k_B T_S) \tag{A.19}$$

A.5 Radiative transfer for a 2-level system

For a 2-level system lying in a radiation bath in thermodynamic equilibrium, the rate of transitions per unit volume from level 1 to level 2 and from level 2 to level 1 are balanced as:

$$n_0 B_{01} \bar{J} = n_1 A_{10} + n_1 B_{10} \bar{J}. \tag{A.20}$$

In the above equation, $B_{01}\bar{J}$ is the transition probability per unit time for absorption, A_{10} is the the transition probability for spontaneous emission per unit time and $B_{10}\bar{J}$ is the transition probability per unit time for simulated emission. The constants A_{10}, B_{10} and B_{01} are the

Einstein's coefficients. The average intensity J_ν is the brightness, I_ν integrated over total solid angle. The energy difference between two levels is described by the line profile $\phi(\nu)$ which defines $\bar{J}$ as:

$$\bar{J} = \int_0^\infty J_\nu \phi(\nu) d\nu \tag{A.21}$$

Solving for $\bar{J}$ from eq. (2.2) and substituting $n_0/n_1 = g_0/g_1\ exp(h\nu_0/kT)$ for thermodynamic equilibrium, the average intensity J becomes **?**:

$$\bar{J} = \frac{A_{10}/B_{10}}{(g_0 B_{01}/g_1 B_{10})\ exp(h\nu_0/kT) - 1} \tag{A.22}$$

As described previously, in thermodynamic equilibrium $\bar{J} = B_\nu$, which is the Planck function. Therefore the Einstein's coefficients are related as:

$$g_0 B_{01} = g_1 B_{10} \tag{A.23}$$

$$A_{10} = \frac{2h\nu^3}{c^2} B_{10} \tag{A.24}$$

The Einstein's coefficients describe the intrinsic properties of the atomic levels and the above relations hold irrespective of the system being in thermodynamic equilibrium, since there is no dependence on temperature. The radiative transfer equation can be written in terms of the Einstein's coefficients. Therefore the emission and absorption coefficient are to be written in terms of Einstein's equations. Treating stimulated emission as negative ansorption, the two quantities in terms of Einstein's equations can be written as :

$$j_\nu = \frac{h\nu_{10}}{4\pi} n_1 A_{10} \phi(\nu) \tag{A.25}$$

$$\alpha_\nu = \frac{h\nu_{01}}{4\pi} \phi(\nu)(n_0 B_{01} - n_1 B_{10}) \tag{A.26}$$

Therefore, the transfer equation , eq. (A.5) can be written as:

$$\frac{dI_\nu}{ds} = \frac{h\nu_{10}}{4\pi}(n_0 B_{01} - n_1 B_{10})\phi(\nu) I_\nu + \frac{h\nu_{10}}{4\pi} n_1 A_{10} \phi(\nu) \tag{A.27}$$

B

Some large scale structure Basics

B.1 Correlation function and Power Spectrum

The correlation function describes any deviation from a uniform distribution of a random field. For example for the case of density fluctuations, the correlation between two points at positions $\mathbf{r}'$ and $\mathbf{r}''$ is given by:

$$\xi(r', r'') = \langle \delta(r')\delta(r'') \rangle,$$

where the angle brackets denote an ensemble expectation value over independent realizations of the universe. If translation invariance holds then ξ is only a function of the distance between the two points and can be written as $\xi(\mathbf{r}' - \mathbf{r}'')$. The power spectrum of a field, $P(k)$ is the Fourier transform of the correlation function. Therefore, for a homogenous, isotropic real valued field:

$$\xi(r' - r'') = \frac{1}{2\pi} \int d^3k P(k) e^{-i\mathbf{k}.(\mathbf{r}' - \mathbf{r}'')} \tag{B.1}$$

It is essentially the variance of the field in k-space, ie. $P(\mathbf{k}) = \langle |\delta((\mathbf{k}))|^2 \rangle$, where $\delta(k)$ is the Fourier transform of $\delta(x)$. The correlation function when $\mathbf{r} = \mathbf{r}' - \mathbf{r}'' = 0$ is the variance of the field:

$$\sigma^2 = \frac{1}{2\pi^3}\int P(k)k^2 dk \tag{B.2}$$

Expressed in terms of log intervals in k, the above equation can be re-written as:

$$\sigma^2 = \frac{1}{4\pi}\int (dln\ k)\Delta^2(k), \tag{B.3}$$

where $\Delta^2(k) = \dfrac{k^3 P(k)}{2\pi^2}$, which therefore describes how much variance is contained per log interval of wave number.

For a density field with a uniform background value of ρ_0, smoothed at a scale R (or mass $M = C\rho_0 R^3$ with a window function W_R the above expression becomes:

$$\sigma_M^2 = \sigma_R^2 = \frac{1}{2\pi^2}\int_0^\infty dkk^2 P(k)\tilde{W}_R(k) = \frac{1}{4\pi}\int (dln\ k)\Delta^2(k)\tilde{W_R}^2(kR), \tag{B.4}$$

where $\tilde{W_R}$ is the Fourier transform of the smoothing filter used. The constant C depends upon the shape of the window function used.

Definition of σ_8: The variance of the density field smoothed at $8h^{-1}$ Mpc with a spherical top hat filter, linearly extrapolated to $z = 0$ is one of the cosmological parameters called σ_8.

B.2 Press-Schecter Mass function

The Press-Schecter (PS) mass function (Press & Schechter (1974)) is derived by addressing the question of what is the probability that a particle at a given position in a density field is a part of a collapsed object with mass $> M$. Their *ansatz* was that this probability is the same as the probability that a density δ_M smoothed at a scale M, is greater than the the critical overdensity for collapse i.e., $\delta_M > \delta_{crit}$:

$$P(> M) = P(\delta_M > \delta_{crit}) \tag{B.5}$$

The density smoothed at some scale, M is a Gaussian random field and therefore:

$$P(\delta_M > \delta_{crit}) = \frac{1}{\sigma_M\sqrt{2\pi}}\int_{\delta_{crit}}^\infty d\delta_M\ exp\left(-\frac{\delta_M^2}{2\sigma^2(M)}\right) = \frac{1}{2}\left[1 - erf(\frac{\delta_{crit}}{\sqrt{2}\sigma_M})\right] \tag{B.6}$$

In the $lim_{M\to 0}\sigma_M \to 0$, $erf \to 0$ the above equation tells that 1/2 of the matter is inside collapsed halos. This appears because of the Gaussian nature of the field where $P(\delta < 0) = 1/2$, i.e.

only overdense regions have been accounted for in the above formalism. Since the underdense regions would accrete over these over dense regions, a fudge factor of 2 was multiplied to the above equation [1]. Therefore,

$$P(>M) = 2 \times P(\delta_M > \delta_{crit}) \tag{B.7}$$

In order to derive the mass-function using the above formalism, one has to relate the probability $P(>M)$ for a particle to be inside an object of mass >M, to the dark matter halo mass function, $\frac{\partial n(>M)}{\partial M}dM$. One can write $\frac{\partial P}{\partial M}dM$, as the mass fraction of the universe inside collapsed halos of masses in the range, $M \pm dM/2$. On multiplying by ρ_0, one obtains the mass per unit volume inside collapsed halos. Similarly multiplying, $\frac{\partial n(>M)}{\partial M}dM$ by M gives the same quantity. Therefore (relabel $\nu = \frac{\delta_{crit}}{\sigma_M}$ and use eq. B.6 and B.7):

$$\begin{aligned}
Mn(M)dM &= \rho_0 \frac{\partial P}{\partial M} dM && \text{(B.8)}\\
\Longrightarrow \frac{\partial n(>M)}{\partial M} &= \frac{\rho_0}{M}\frac{\partial}{\partial M}\left[1 - erf\left(\frac{\nu}{\sqrt{2}}\right)\right] && \text{(B.9)}\\
&= \frac{\rho_0}{M}\frac{\partial}{\partial \nu}\left[1 - erf\left(\frac{\nu}{\sqrt{2}}\right)\right]\frac{d\nu}{dM} && \text{(B.10)}\\
&= -\frac{\rho_0}{M}\sqrt{\frac{2}{\pi}}\frac{\delta_c}{\sigma_M^2}\, exp\left(-\frac{\delta_{crit}^2}{2\sigma_M^2}\right)\frac{d\sigma_M}{dM} && \text{(B.11)}
\end{aligned}$$

where in the last step the following theorem of calculus is used:

$$\frac{d}{dx}\int_a^x f(t)dt = f(x) = -\frac{d}{dx}\int_x^a f(t)dt$$

B.3 Extended Press-Schecter Mass function

An alternate way to look at the fraction of collapsed halos is to formulate it in terms of the statistics of Markovian random walk (Bond et al. (1991b); Lacey & Cole (1993)) [2] . The

[1] This called the *cloud-in-cloud* problem. Another way to look at the problem is that the smaller underdense regions could be contained inside the larger overdense regions

[2] Markovian random walk is one in which every subsequent step depends upon the current step of the walk and not the history of the walk before the current step.

density field at a certain point x, $\delta(x)$ in the $\delta - \sigma^2(M)$ plain will exhibit a random walk as it is smoothed at subsequent smoothing scales [3]. For ease of understanding define $S = \sigma^2(M)$. It is derived by counting the number of trajectories which have their first upcrossing at $\delta_S = \delta_c$ at an $S > S_1$. Therefore, such a trajectory would have $\delta(S_1) < \delta_c$. This is same as counting mass elements inside collapsed halos with $M < M_1$ ($F(< M_1)$). The advantage of using the excursion set formulation is that it takes care of the fudge factor 2 which appears in the PS mass function [4]. The fraction of trajectories with first upcrossing (F_{FU}) above S_1 are given by (Mo et al. (2010)):

$$F_{FU}(> S_1) \equiv F(< M_1) = \int_{-\infty}^{\delta_c} [P(\delta_S, S_1) - P(2\delta_c - \delta_S, S_1)] d\delta_S \tag{B.12}$$

Therefore the mass function for the Extended Press Schecter mass function is given by):

$$F(> M_1) = 1 - F(< M_1) \tag{B.13}$$

$$\frac{\partial n(> M)}{\partial M} = \frac{\rho_0}{M} \frac{1}{\sqrt{2\pi}} \frac{\delta_c}{S^{3/2}} exp \left(\frac{-\delta_c^2}{2S} \right) \left| \frac{dS}{dM} \right|, \tag{B.14}$$

which is exactly the PS-mass function in eq. (B.11).

B.4 Conditional Press Schecter mass Function

Let a particle be a part of a spherical region of mass M_2 , with mass variance $\sigma^2(M_2)$ and overdensity $\delta_2 = \delta_c(t_2)$, which formed a collapsed structure at time t_2. Then the probability that this particle is also a part of another collapsed mass M_1 collapsed at an earlier time $t_1 < t_2$ (i.e. $M_1 < M_2$ or $S_1 > S_2$) is derived by calculating the first upcrossing for random walks whose origin is now shifted to (S_2, δ_2). Therefore the fraction of particles in halo of mass M_1 which are also a part of halo of mass M_2 is given by (Mo et al. (2010)):

$$\frac{\partial n(M_1, t_1 | M_2, t_2)}{\partial M} = \frac{M_2}{M_1} \frac{1}{\sqrt{2\pi}} \frac{\delta_1 - \delta_2}{(S_1 - S_2)^{3/2}} exp \left[-\frac{(\delta_1 - \delta_2)^2}{2(S_1 - S_2)} \right] \left| \frac{dS_1}{dM_1} \right| \tag{B.15}$$

This essentially counts all those random walks which pass through both S_1 and S_2 and the first crossing happens at (S_1, δ_1). Remember that δ_1 and δ_2 is the value of δ_c at different times.

[3] This depends upon the type of smoothing filter used. Only a sharp -space filter leads to uncorrelated steps.

[4] This is done by excluding trajectories which may have had their first upcrossing before S_1 by using their equally likely mirror trajectories.

B.5 Lagrangian Perturbation Theory(LPT) and Zel'dovich approximation

The Lagrangian coordinate system is fixed on individual particles and the displacement of the particles is described with respect to the initial positions of the particles, $\mathbf{x_1}$. The motion of the particles in the comoving Lagrangian system can be visualized as a distortion of the coordinate grid. On the other hand, the comoving Eulerian coordinate system is fixed. The particle positions, $\mathbf{x}$ are described with respect to a fixed origin on that coordinate system. The trajectory of a particle in the Lagrangian coordinate system is described by the dynamical variable $\psi(\mathbf{x_1}, \tau)$, which describes the displacement from the initial position of the particle (Bernardeau et al. (2002)):

$$x(\tau) = x_1 + \psi(x_1, \tau), \tag{B.16}$$

where τ is the conformal time given by $d\tau = dt/a(t)$. At $\tau = 0$, $\psi = 0$ and therefore x_1 is the usual comoving coordinate at this intial time. From the particle mass-conservation :

$$\begin{aligned} \overline{\rho}(\tau)d^3x_1 &= \overline{\rho}(\tau)[1+\delta(\mathbf{x},\tau)]d^3x & \text{(B.17)} \\ 1+\delta(\mathbf{x},\tau) &= 1/J(\mathbf{x_1},\tau), & \text{(B.18)} \end{aligned}$$

where $J(\mathbf{x_1}, \tau) = det(\delta_{ij} + \frac{\partial \psi_i}{\partial x_{1j}}(\mathbf{x_1}, \tau))$ is the Jacobian of transformation from the Lagrangian to Eulerian grid. Linearization of the LPT is obtained by expanding the Jacobian as:

$$\begin{aligned} J(\mathbf{x_1},\tau) &= det[\delta_{i,j} + \psi_{i,j}(\mathbf{x_1},\tau)] \approx 1 + \psi_{i,i}(\mathbf{x_1},\tau) & \text{(B.19)} \\ J^{-1}(\mathbf{x_1},\tau) &= \delta_{ij} - \psi_{i,j} & \text{(B.20)} \end{aligned}$$

The overdensity, as a result of this linearization of J and linearizing both ψ and δ in eq. (B.18) would be:

$$\nabla_{x_1}.\psi(\mathbf{x}_1, \tau) = -\delta(\mathbf{x}, \tau) \tag{B.21}$$

Zel'dovich Approximation: An extrapolation of the LPT to the non-linear regime leads to the formation of structures called *Zel'dovich Pancake*. If the jacobian in eq. (B.20) is diagonalized with eigenvalues $-\alpha$, $-\beta$ and $-\gamma$, then from eq. (B.18) one can write:

$$\delta(x, \tau) = [(1 - D(\tau)\alpha)(1 - D(\tau)\beta)(1 - D(\tau)\gamma)]^{-1} - 1 \tag{B.22}$$

If the original shape of an overdensity is ellipsoidal with $\alpha > \beta > \gamma$,being the semi-major axes then the collapse of the overdensity is fastest along the direction of the largest axis. In this case the axis with length α. This can be seen from the above equation where as $D(\tau)$ grows over time, it will reach a value of $1/\alpha$ before it reaches $1/\beta$ or $1/\gamma$ and hence δ tends to approach infinity first along that direction. This leads to the formation of flattened structures called *Zel'dovich Pancakes* (Zel'Dovich (1970)).

C

Radio Astronomy Basics

C.1 Basic definitions of radio astronomy

- **Flux Density** S_ν: In radio astronomy notation it is the same as the specific flux defined in Appendix A and expressed in units of Jansky, where 1 Jy $= 10^{-26}\ W\ m^{-2}\ Hz^{-1}$. This is the fundamental quantity measured by a radio antenna in terms of the square of the voltages. [1]

- **Effective Area** A_e: The output power P_ν from a receiver in response to a received flux density S_ν is given by $P_\nu = A_e\ S_\nu$. In ideal case $A_e = A_{tot}$, the total collecting area of an interferometer.

- **Antenna Temperature** T_A : Is the temperature of a matched resistor which has the same thermal power as the power measured by the antenna output, $T_A = S_\nu A_e / 2k_B$, where A_e is the effective collecting area of the antenna. If the source is much larger than the antenna beam then $T_A = T_b$, the source brightness temperature.

[1]For unresolved sources, the quantity of interest is S_ν, while for fully resolved or extended sources spanning the beam of the receiver as would be the case for EoR observations, the quantity of interest would be the specific intensity, I_ν in units of $Jy\ sterdian^{-1}$.

- **System Temperature** T_{sys}: Is the temperature of a matched resistor which when connected to the receiver of a noise free antenna would produce the same noise power as the noise power at the actual receiver. It has contribution from the telescope, receiver system, the sky and the atmosphere:

$$T_{sys} = T_{CMB} + T_{sky} + [1 - exp(-\tau_A)]T_{atm} + T_r, \tag{C.1}$$

where T_{sky} is the sky brightness temperature due to the galactic synchrotron and other extragalactic point sources. Usually the quiet portions of the sky have a brightness temperature, $T_{sky} \simeq \left(\frac{\nu}{180MHz}\right)^{-2.6}$. The emissions from the atmosphere contribute a T_{atm} (as a function of the zenith angle of the antenna), at higher frequencies ($\nu \gtrsim 1$ GHz). T_r is the noise due to the receiver itself which is minimized by cooling.

- **Radiometer Equation** : Describes how the uncertainity in the measurement of noise power decreases by the square root of the number of samples averaged in time. The noise voltage at a receiver is Gaussian distributed with mean zero. The variance of the noise is then the noise power, which is given by T_S defined above. Radio observations are usually bandwidth limited. Noise measurement at the receiver then proceeds in three steps:

  - To filter out the required frequency range, according to the *bandwidth* $\Delta\nu$.
  - Pass through the square law detector, which gives a high frequency fluctuating component and a DC component. Therefore the mean (or the DC component), $\langle V_0 \rangle$ is proportional to the power of the input signal (or T_{sys}). The RMS output from it is $\sqrt{2}\langle V_0 \rangle \simeq \sqrt{2}T_{sys}$.
  - The fluctuating component does not contain new information and can be suppressed by integrating the output over a time $\tau \gg (\Delta\nu)^{-1}$. By the Nyquist sampling theorem, for a bandwidth limited function there are $N = 2\Delta\nu\tau$ independent samples, spaced in time by $(2\Delta\nu)^{-1}$. Since each sample has an rms error $\sqrt{2}T_S$, for N samples the noise is reduced as:

  $$\sigma_T = \frac{\sqrt{2}T_{sys}}{\sqrt{N}} = \frac{T_{sys}}{\sqrt{\Delta\nu\tau}} \tag{C.2}$$

  The signal should be several times σ_T in order to be detectable. Hence sensitivity can be increased either by increasing the bandwidth or the integration time.

C.2 Basics of radio interferometry

An intereferometer correlates output from two (or more) radio antennas, separated by a distance $\vec{b}$, called the *baseline* vector. The signal received at the second antenna is delayed relative to the first antenna by a geometric time delay of $\tau_g = \vec{b}.\hat{s}/c$. The delay in terms of wavelength can be written as $\vec{b}.\hat{s}/\lambda$ .The output from intereferometer correlator is a quantity called the **complex visibility** for an extended source having an intensity I_ν, given by:

$$\mathscr{V}_\nu(u,v,w) = \int I_\nu(\hat{s}) exp(-i\, 2\pi\vec{b}.\hat{s}/\lambda) d\Omega \tag{C.3}$$

The vector $\hat{s}$ is the unit vector in the source direction, λ is the wavelength of observation. If u, v and w are the three components of the $\vec{b}/\lambda$ vector and l, m and n are the three components of the unit vector, $\hat{s}$ then the above equation becomes:

$$\mathscr{V}(u,v,w) = \int\int \frac{I_\nu(l,m)}{(1-l^2-m^2)^{1/2}} exp[-i2\pi(ul+vm+wn)] dl dm \tag{C.4}$$

The u is the east-west direction, v is the north-south direction and w is the up-down direction. The l, m and n are the projection of some arbitrary unit vector $\hat{s}$ in the u, v and w directions respectively.

- **Measurement equation**: If the value of $w = 0$, i.e. the baseline is confined to the $u-v$ plane, then *visibility* and sky brightness turn out to be two dimensional fourier transform pairs:

  $$\frac{I_\nu(l,m)}{(1-l^2-m^2)^{1/2}} = \int\int \mathscr{V}(u,v) exp[i2\pi(ul+vm)] du dv \tag{C.5}$$

  Every baseline vector between two elements of an interferometer would correspond to a point in the uv-plane. The more sampled the uv-plane, the cleaner is the image constructed from the interferometer.

- **Earth Rotation synthesis** : For an antenna distribution, fixed on the ground when seen from a source in the sky, the uv distribution in the uv-plane would change as the earth rotates. This increases the number of sampled points on the uv-plane and hence provides a better quality image.

- **Sensitivity of the intereferometer** : For an two element intereferometer and from the steps leading to the radiometer equation, it is straightforward to see that the result of correlating equal voltages from two elements, is the same as what square law detector would do for an individual antenna. However, in this case the noise from two different elements is uncorrelated and therefore the number of independent samples is now $2N$ instead of N. Therefore the output noise is $2^{1/2}$ times less than the case of single element interferometer.

$$\sigma_S = \frac{\sqrt{2} k_b T_{sys}}{A_e \sqrt{\Delta\nu\tau}} \tag{C.6}$$

For an N_{ant} element intereferometer, there are $N_{ant}(N_{ant}-1)/2$ independent 2-element interferometers and therefore using eq. C.2 the noise sigma in flux density becomes:

$$\sigma_S = \frac{2 k_b T_{sys}}{A_e \sqrt{[N_{ant}(N_{ant}-1)]\Delta\nu\tau}} \tag{C.7}$$

Since the beam solid angle of an interferometer ($\simeq (\lambda/b_{max})^2$) is smaller than the beam solid angle of a single dish ($\simeq (\lambda/D)^2$) of same effective area by $\eta_f = A_{tot}/b_{max}^2$, the brightness sensitivity of an interferometer is less by a factor of η_f, the ***array filling factor*** even though both have comparable effective area A_{eff}. Thus the RMS brightness temperature sensitivity σ_T is:

$$\sigma_T = \frac{\sigma_S}{\Delta\Omega}\frac{\lambda^2}{2k_B}, \tag{C.8}$$

for an image made with a beam solid angle $\Delta\Omega \simeq \Delta\theta^2$ where $\Delta\theta$ is the resolution of the interferometer (λ/b_{max}) at the observed wavelength λ.

C.3 Relating simulation box and antenna parameters

All scales associated with the simulation box are in terms of comoving distances. These are, the box size and the resolution of the box. These would correpond to the following antenna parameters along the line of sight and transverse to the line of sight for an observed redshift z:

- **Bandwidth and frequency resolution:** The radio observations for EoR would be carried out in a certain frequency bandwidth, $\Delta\nu$ centered about an observed frequency ν_o with a certain frequency resolution ν_c. This sets the size and resolution of the simulation box respectively, along the line of sight. A given frequency bandwidth $\Delta\nu$ GHz would correspond to a redshift interval $\Delta z = (1+z)^2/1.4\ \Delta\nu$. Therefore, the corresponding thickness of the box along the line of sight can be written as follows:

$$\begin{aligned} L_{thickness} &= \frac{c\,dt}{a} \simeq c\frac{\Delta z}{H(z)} \simeq \\ &= 1.8\,Mpc\,\frac{\Delta\nu}{0.1MHz}\left[\frac{1+z}{10}\right]^{1/2}, \end{aligned} \tag{C.9}$$

where in the last step we used $H \simeq H_0\sqrt{\Omega_m(1+z)^3}$, since Ω_Λ and Ω_{rad} are negligible during EoR within which the comoving interval is calculated. In order to calculate the box resolution along the line of sight, eq. C.9 is used by replacing $\Delta\nu$ by ν_c which is the frequency resolution of the interferometer.

- **Field of view and angular resolution:** The field of view of the interferometer θ_{FoV} describes the maximum angular scale that the antenna can observe for a given observed wavelength λ. It is given by λ/b_{min}, where b_{min} is the minimum baseline distance used for observation. The angular resolution of the intereferometer for an observed wavelength λ is given by λ/b_{max}, where b_{max} is the maximum baseline distance used for the observation. The resolution corresponds to the minimum transvere scale on the sky that the intereferometer can resolve. The angular field of view determines the simulation box size, while the angular resolution dtermines the resolution of the simulation box. An angular scale $\Delta\theta$ on the sky corresponds to an actual size of the object, $L = \Delta\theta\ L_{phy}$, where L_{phy} is the physical distance to the object being observed. This corresponds to a comoving transverse scale , $L_{trans} = \Delta\theta\ L_{com}$. Therefore:

$$\begin{aligned} L_{trans} &= \Delta\theta \int c\,\frac{1}{H(z)}\,dz \\ &\simeq 2.7\,\frac{\Delta\theta}{1'}\left(\frac{1+z}{10}\right)^{0.2} Mpc, \end{aligned} \tag{C.10}$$

where in the last equation, we used $H \simeq H_0\sqrt{\Omega_m(1+z)^3+\Omega_\Lambda}$ and the integral is calculated numerically. Note that the value of Ω_Λ cannot be ignored since here the integration for the comoving distance is carried over from a redshift of $z = 0$ to the redshift corresponding to the observed wavelength and effects of dark energy are non negligible at low redshifts.

D

Comments on the non-Gaussianity of δT_b field

As described in Chapter 2, the cosmological evolution of the 21cm brightness temperature field is a result of several non-linear astrophysical processes. From observations of the Cosmic Microwave Background, it is known that the initial seed fluctuations were close to Gaussian in nature ((Planck Collaboration et al., 2020)). Some models of inflation predict a relatively large amount of primordial non-Gaussianity which if tightly constrained would serve as an important probe of the fields that source inflation. Since inflation occurs at energy scales which are not accessible by direct detection through collidor experiments like the Large Hadron Collidor, these constraints serve as an important tool to understand fundamental physics at those energy scales. As cosmic structures go through non-linear evolution, these initial fluctuations start becoming non-Gaussian. This component is in addition to the primordial non-Gaussianity due to inflation and can serve as an important tool to study the evolution and growth of cosmic structures at lower redshifts. The power spectrum which is the usual statistical tool for these observed fields does not give any measurable information on non-Gaussianity, both primordial and late time. Therefore, one would need to resort to higher order correlations to extract more information. Usually bispectrum is used for extracting non-Gaussian information, however with image based real space tools we can extract even more information and hence better constraints on non-Gaussian information.

The functional variation of threshold dependence of β for a Gaussian random field was shown in Fig. 3.4 , and as calculated in (Chingangbam et al., 2017) the value of $\alpha = 1$ at all thresholds. Any change in the mean or standard deviation of the Gaussian field would lead to a change in amplitude while keeping the functional variation of β with threshold intact (if the threshold is mean subtracted and normalized). Any change in Gaussianity would lead to a change in the functional variation with field threshold. Therefore, by quantifying deviation from the functional variation with threshold one can infer the amount of non-Gaussianity. In Fig. D.1 we show the threshold dependence of β at three different epochs of ionization history, for the three fields that determine the δT_b morphology. All field thresholds have been mean subtracted and normalized in order to compare them statistically. The figure shows that the functional dependence of β with threshold for δ_{nl} does not deviate much from the variation expected for a Gaussian random field from $z = 18.32$ to $z = 9$. However, considerable deviation can be seen at $z = 7$. The T_S field is much different from Gaussian behaviour at $z = 18.32$, but approaches Gaussianity at lower redshifts. An opposite trend is seen for the neutral hydrogen fraction field and it is found that the field is highly non-Gaussian at at $z = 7$. It appears to be closest to Gaussian behaviour at intermediate redshifts, where $\bar{x}_{HI} \simeq 0.5$. The bottom row shows the varaiation for δT_b field. The variation shows that the field mimics the non-Gaussianity of the δ_{nl} field at $z = 18$. At $z = 9$, the low density regions seem to follow the non-Gaussianity of T_S, while high thresholds follow the non-Gaussianity of x_{HI}. At $z = 7$, the variation follows the x_{HI} and is highly non-Gaussian. The plots for variation of α show a similar trend. An ideal way to quantify the non-Gaussianity is to compare the variation with a Gaussian random field having the same power spectrum as the field in question.

A detailed quantification and study of different components of non-Gaussianity, both primordial and astrophysical inherent in the 21cm brightness temperature field and prospects of discerning them will be carried out in near future.

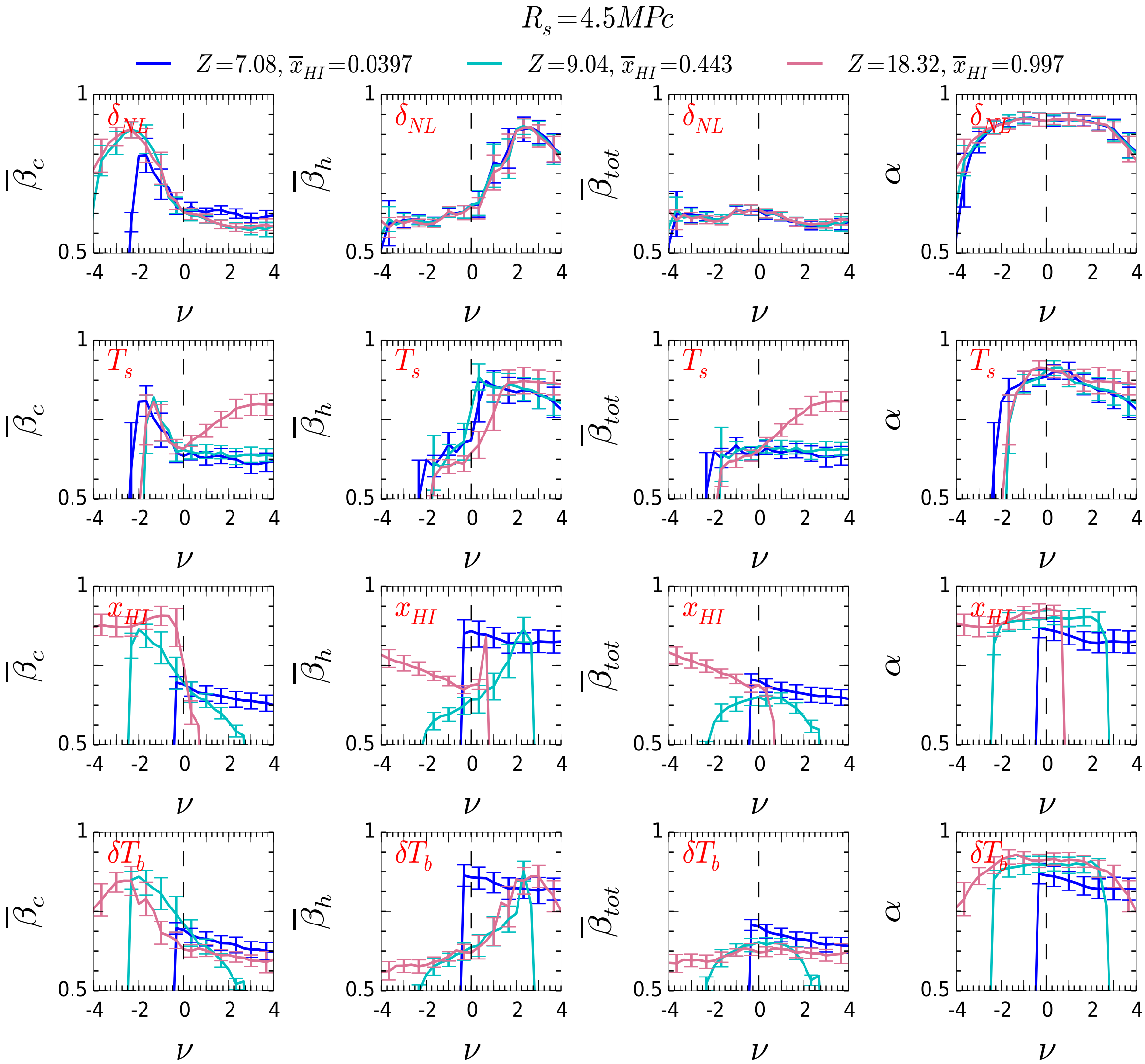

Fig. D.1 The figure shows the variation of β and α with threshold ,for the various fields of our study. For a Gaussian random field the value of $\alpha = 1$ at all thresholds. All fields have been smoothed at $R_S = 4.5$Mpc. The top row shows the variation for the non-linear density field, second row for T_S , third row for x_{HI} and the last row for δT_b. The three redshifts probed are $z = 7.08$ (*blue*), $z = 9.04$ (*teal*) and $z = 18.32$ (*pink*). The columns are the mean of β over all structures at a given threshold, for connected regions (*left*), holes (*second column*) and over both holes and connected regions (*third column*). The last column shows the variation of α for the excursion set of the field.

E

Definitions and constants

E.1 Cosmology

- Comoving coordinate system: The comoving coordinate system is the distance is the frame which is at rest with respect to the expanding universe. The r that appears in the FLRW metric in eq. (1.4) is the comoving separation between two spatial points.

- Proper distance: The proper distance is the physical distance between two spatial points in an expanding universe. It is given by:

$$d_p(t) = a(t) \int_0^r dr',$$

  where r is the comoving coordinate.

- Particle horizon: The particle horizon is defined as the maximum distance from which a light signal could reach an observer at a time t since the beginning of the universe (i.e. t=0). It is given by:

$$d_H(t) = a(t) \int_0^t \frac{cdt'}{a(t)},$$

while in comoving coordinates and introducing the *conformal time*, τ:

$$c\,d\tau = c\int_0^t \frac{cdt'}{a(t)}$$

Since, $a(t) \propto t^n$ where $0 < n < 1$ for both matter and radiation, the particle horizon always increases with time. For any physical process to be in causal contact at a given time t , it should be within the comoving particle horizon at that time.

- Hubble horizon: The rate at which a point at a distance x recedes from an observer due to the expansion of the universe is given by:

$$v = xH^{-1}(t)$$

The radius at which the recession velocity becomes equal to the speed of light, c is called the Hubble radius or Hubble horizon:

$$r_H(t) = \frac{c}{H(t)}$$

Two points which are separated by the Hubble distance at time t will not be in causal contact with each other at a later time $t_l > t$ even if they have been in causal contact before t. The comoving Hubble radius is $r_H^c = \frac{c}{aH(t)}$.

E.2 Mathematical Definitions

- Dirac Delta function:

$$\delta_D(x_1 - x_2) = \begin{cases} 1\ ,\ x_1 = x_2 \\ 0\ ,\ x_1 \neq x_2 \end{cases}$$

- Error Function:

$$erf(x) = \frac{2}{\sqrt{\pi}}\int_0^x e^{-t^2}\,dt$$

- Complementary Error function:

$$erfc(x) = 1 - erf(x) = \frac{2}{\sqrt{\pi}}\int_x^\infty e^{-t^2}dt$$

E.2.0.1 Smooth curves in 2D

- Position vector- For a 2-dimensional curve, parametrized by $'t'$, the position vector is given by:

$$\vec{r}(t) = x(t)\hat{\imath} + y(t)\hat{\jmath} \tag{E.1}$$

- Tangent vector - The tangent to the curve at any point, $t = t_0$ is given by:

$$\vec{T} = \frac{dx}{dt}(t = t_0)\hat{\imath} + \frac{dy}{dt}(t = t_0)\hat{\jmath} \tag{E.2}$$

- Arc length - The length of the parametrized curve between two points, t_1 and t_2:

$$\begin{aligned} s &= \int_{t_1}^{t_2} ds && \text{(E.3)} \\ &= \int_{t_1}^{t_2} \sqrt{\left(\frac{dx}{dt}\right)^2 + \left(\frac{dy}{dt}\right)^2}\, dt \\ &= \int_{t_1}^{t_2} |\vec{T}| dt && \text{(E.4)} \end{aligned}$$

Differentiating eq. (E.1) with respect to ds and using eq. (E.4), $\frac{dr/dt}{ds/dt}$ gives the unit tangent vector:

$$\hat{T} = \frac{d\vec{r}}{ds} \tag{E.5}$$

- Normal vector: The perpendicular to a point at the curve is called a normal vector and is given by:

$$\vec{n} = \frac{d\hat{T}}{ds} \tag{E.6}$$

and the unit normal vector:

$$\hat{n} = \frac{1}{|d\hat{T}/ds|}\frac{d\hat{T}}{ds} \tag{E.7}$$

- Local Curvature (κ): is a measure of how quickly the tangent turns with respect to the arc length:

$$\begin{aligned}
\kappa &= |\frac{d\hat{T}}{ds}| && \text{(E.8)}\\
&= \frac{1}{|\vec{T}|}|\frac{d\hat{T}}{dt}| \\
&= \frac{|\dot{x}\ddot{y}-\dot{y}\ddot{x}|}{((\dot{x})^2+(\dot{y})^2)^{3/2}} && \text{(E.9)}
\end{aligned}$$

, where the last equation is the deifinition in terms of derivatives of x and y with respect to t.

- Antisymmetric Levi-cevita Symbol ε_{ij}:

$$\begin{pmatrix} \varepsilon_{11} & \varepsilon_{12} \\ \varepsilon_{21} & \varepsilon_{22} \end{pmatrix} = \begin{pmatrix} 0 & 1 \\ -1 & 0 \end{pmatrix} \tag{E.10}$$

E.2.0.2 Concept of Curvature for 2D surfaces

For a point P on a 2D surface, one can construct a *tangent plane* passing through it. The tangent plane would consist of all such vectors, which are tangent to all curves passing through point P. Thus there are several possible tangents at a point on the surface. Also, one can draw a unique vector at point P which is normal to the plane. Any plane that passes through that normal vector is called a *normal plane*. A given normal plane would contain a corresponding unique tangent direction, which would also be a part of the normal plane. There are several possible normal planes at a point P, each containing the unique normal and a unique tangent direction. A normal plane would intersect the surface into a plane curve passing through P. There are three types of curvature for a plane:

- Principal Curvature (k_1 and k_2): The maximum and minimum curvature of the plane curves obtained by intersection of different normal planes with the surface (fig. E.1).

- Mean Curvature (G_2): The mean curvature is given by $(k_1+k_2)/2$. It is an extrinsic measure of curvature, i.e. it defines the local curvature of the surface at a point.

- Gaussian curvature (G_3): The Gaussian curvature is given by $k_1 k_2$ and is an intrinsic measure of curvature for a given surface, i.e. it is a global measure of curvature for a given surface. At every point on the surface, the Gaussian curvature is the same.

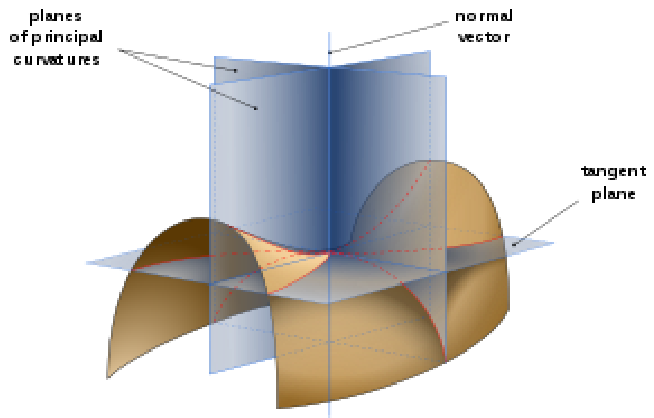

Fig. E.1 The image shows the concept of principal curvature at a saddle point. The normal planes shown in the figure are along the directions of principal curvature. The red dotted curves are the curves obtained by the intersection of the normal planes with the surface.
(*Image Credit:https://en.wikipedia.org/wiki/Curvature*)

E.3 Constants

E.3.1 Physical Constants

Constant	Definition	Value
c	*Speed of light in vaccum*	$3 \times 10^{8}\ \ m\ s^{-1}$
k_B	*Boltzmann Constant*	$1.38 \times 10^{-23}\ kg\ m^{2}\ s^{-2} K^{-1}$
h_P	*Planck's Constant*	$6.63 \times 10^{-34}\ m^{2} kg s^{-1}$
G	*Gravitational constant*	$6.67 \times 10^{-11}\ m^{-3}\ kg^{-1}\ s^{-1}$
m_e	*Mass of an electron*	$9.1 \times 10^{-31}\ kg$
e	*Charge of an electron*	$1.6 \times 10^{-19}\ Coulombs$
m_H	*Mass of neutral hydrogen atom*	$1.67 \times 10^{-27}\ kg$
σ_T	*Thomson scattering cross-section*	$6.65 \times 10^{-21}\ m^{-2}$
a_R	*Radiation constant*	$\frac{8\ \pi^{5} k_B^{4}}{15 c^{3} h_P^{3}}$
E_i^{th}	*Ionization threshold of neutral hydrogen atom*	$13.6\ eV$

E.3.2 Constants for the 21cm transition

Constant	Definition	Value
A_{21}	*Einstein's A coefficient*	$2.85 \times 10^{-15}\ s^{-1}$
ν_{21}	*Transition frequency*	1420.4057 MHz
λ_{21}	*Transition wavelength*	21.1061 cm
ΔE_{21}	*Transition energy*	$5.9 \times 10^{-6}\ eV$
T_*	*Transition temperature*	0.068 K

E.3.3 Cosmological Constants

Constant	Definition	Value (Planck Collaboration et al. (2018))
$T_{CMB,0}$	*Temperature of the CMB today*	$2.725\ K$
$\rho_c = \frac{3H_0^2}{8\pi G}$	*Critical density of the universe*	$8.62 \times 10^{-27}\ kg\ m^{-3}$
Ω_m	*Matter density parameter*	0.310
Ω_b	*Baryonic density parameter*	0.049
Ω_Λ	*Dark energy density parameter*	0.690
H_0	*Currrent value of the Hubble constant*	$67.7\ km\ s^{-1} Mpc^{-1}$
τ_{re}	*Optical depth to reionization*	0.066
h	*Hubble Parameter*	$H_0/100\ km\ s^{-1}\ Mpc^{-1}$
$\Omega_b h^2$		0.022
$\Omega_m h^2$		0.14

References

Ahn K., Mesinger A., Alvarez M. A., Chen X., 2015, arXiv preprint arXiv:1501.04141

Alesker S., 1999, Geometriae dedicata, 74, 241

Alpher R. A., Herman R., Gamow G. A., 1948, Phys. Rev., 74, 1198

Appleby S., Chingangbam P., Park C., Hong S. E., Kim J., Ganesan V., 2018a, The Astrophysical Journal, 858, 87

Appleby S., Chingangbam P., Park C., Yogendran K. P., Joby P. K., 2018b, *ApJ*, 863, 200

Appleby S., Kochappan J. P., Chingangbam P., Park C., 2019, *ApJ*, 887, 128

Arons J., Wingert D. W., 1972, The Astrophysical Journal, 177, 1

Bag S., Mondal R., Sarkar P., Bharadwaj S., Sahni V., 2018, Monthly Notices of the Royal Astronomical Society, 477, 1984

Bag S., Mondal R., Sarkar P., Bharadwaj S., Choudhury T. R., Sahni V., 2019, Monthly Notices of the Royal Astronomical Society, 485, 2235

Bandyopadhyay B., Choudhury T. R., Seshadri T., 2017, Monthly Notices of the Royal Astronomical Society, 466, 2302

Bardeen J. M., Bond J., Kaiser N., Szalay A., 1986, The Astrophysical Journal, 304, 15

Barkana R., Loeb A., 2001, In the beginning: The First sources of light and the reionization of the Universe, Phys

Barr S., 1989, Experiments in Topology

Becker R. H., et al., 2001, The Astronomical Journal, 122, 2850

Bernardeau F., Colombi S., Gaztanaga E., Scoccimarro R., 2002, Physics reports, 367, 1

Bharadwaj S., Ali S. S., 2004, Monthly Notices of the Royal Astronomical Society, 352, 142

Bharadwaj S., Pandey S. K., 2005, Monthly Notices of the Royal Astronomical Society, 358, 968

Birkinshaw M., 1999, Physics Reports, 310, 97

Bond J., Cole S., Efstathiou G., Kaiser N., 1991a, The Astrophysical Journal, 379, 440

Bond J., Cole S., Efstathiou G., Kaiser N., 1991b, The Astrophysical Journal, 379, 440

Bowman J. D., Morales M. F., Hewitt J. N., 2009, The Astrophysical Journal, 695, 183

Bowman J. D., Rogers A. E. E., Monsalve R. A., Mozdzen T. J., Mahesh N., 2018, *Nature*, 555, 67

Bradt H., 2008, Astrophysics Processes

Braun R., Keane E., Bourke T., Green J. A., Wagg J., 2015, PoS, p. 174

Bromm V., Coppi P. S., Larson R. B., 2002, The Astrophysical Journal, 564, 23

Buchert T., France M. J., Steiner F., 2017, Classical and Quantum Gravity, 34, 094002

Chen Z., Xu Y., Wang Y., Chen X., 2019, *ApJ*, 885, 23

Chingangbam P., Yogendran K. P., Joby P. K., Ganesan V., Appleby S., Park C., 2017, jcap, 2017, 023

Choudhury T. R., 2009, Current Science, pp 841–857

Choudhury T. R., Paranjape A., 2018, Monthly Notices of the Royal Astronomical Society, 481, 3821

Choudhury T. R., Haehnelt M. G., Regan J., 2009, Monthly Notices of the Royal Astronomical Society, 394, 960

Ciardi B., Ferrara A., 2005, Space Science Reviews, 116, 625

Cooray A., 2005, Monthly Notices of the Royal Astronomical Society, 363, 1049

Cooray A., Li C., Melchiorri A., 2008, prd, 77, 103506

Cramér H., 1999, Mathematical methods of statistics. Vol. 43, Princeton university press

Datta K. K., Mellema G., Mao Y., Iliev I. T., Shapiro P. R., Ahn K., 2012, MNRAS, 424, 1877

Datta K. K., Jensen H., Majumdar S., Mellema G., Iliev I. T., Mao Y., Shapiro P. R., Ahn K., 2014, MNRAS, 442, 1491

DeBoer D. R., et al., 2017, Publications of the Astronomical Society of the Pacific, 129, 045001

Dicke R. H., Peebles P. J. E., Roll P. G., Wilkinson D. T., 1965, *ApJ*, 142, 414

Dodelson S., 2003, Modern cosmology

Dyson J. E., Williams D. A., 1997, The physics of the interstellar medium. CRC Press

Elbers W., Weygaert R. v. d., 2019, Monthly Notices of the Royal Astronomical Society, 486, 1523

Ewen H. I., Purcell E. M., 1951, in , Classics in Radio Astronomy. Springer, pp 328–330

Fan X., et al., 2003, The Astronomical Journal, 125, 1649

Fan X., et al., 2006, The Astronomical Journal, 132, 117

Fialkov A., Barkana R., Visbal E., 2014, *Nature*, 506, 197

Field G. B., 1958, Proceedings of the IRE, 46, 240

Field G. B., 1959, *ApJ*, 129, 551

Field G. B., 1962, The Astrophysical Journal, 135, 684

Fisher R. A., 1922, Philosophical Transactions of the Royal Society of London, 222, 594

Fixsen D. J., 2009, *ApJ*, 707, 916

Flegg H., 1974, From Geometry to Topology

Friedmann A., 1924, Zeitschrift fur Physik, 21, 326

Friedrich M. M., Mellema G., Alvarez M. A., Shapiro P. R., Iliev I. T., 2011, Monthly Notices of the Royal Astronomical Society, 413, 1353

Furlanetto S. R., 2006, Monthly Notices of the Royal Astronomical Society, 371, 867

Furlanetto S. R., Furlanetto M. R., 2006, Monthly Notices of the Royal Astronomical Society, 374, 547

Furlanetto S. R., Oh S. P., 2016, Monthly Notices of the Royal Astronomical Society, 457, 1813

Furlanetto S. R., Stoever S. J., 2010, Monthly Notices of the Royal Astronomical Society, 404, 1869

Furlanetto S. R., Zaldarriaga M., Hernquist L., 2004a, The Astrophysical Journal, 613, 1

Furlanetto S. R., Zaldarriaga M., Hernquist L., 2004b, The Astrophysical Journal, 613, 16

Furlanetto S. R., Oh S. P., Briggs F. H., 2006, Physics reports, 433, 181

G E Schröder-Turk G. E., Kapfer S., Breidenbach B., Beisbart C., Mecke K., 2010, Journal of microscopy, 238, 57

Gamow G., 1946, Phys. Rev., 70, 572

Ganesan V., Chingangbam P., 2017, jcap, 2017, 023

Ganesan V., Chingangbam P., Yogendran K., Park C., 2015, Journal of Cosmology and Astroparticle Physics, 2015, 028

Ghara R., Choudhury T. R., Datta K. K., 2015, Monthly Notices of the Royal Astronomical Society, 447, 1806

Ghara R., Choudhury T. R., Datta K. K., Choudhuri S., 2017, Monthly Notices of the Royal Astronomical Society, 464, 2234

Giri S. K., Mellema G., Dixon K. L., Iliev I. T., 2018, Mon. Not. Roy. Astron. Soc., 473, 2949

Gleser L., Nusser A., Ciardi B., Desjacques V., 2006, Monthly Notices of the Royal Astronomical Society, 370, 1329

Glover S., 2005, Space Science Reviews, 117, 445

Gnedin N. Y., 2000, The Astrophysical Journal, 535, 530

Gorce A., Pritchard J. R., 2019, Monthly Notices of the Royal Astronomical Society, 489, 1321

Gott III J. R., Park C., Juszkiewicz R., Bies W. E., Bennett D. P., Bouchet F. R., Stebbins A., 1990, The Astrophysical Journal, 352, 1

Goyal P., Chingangbam P., Appleby S., 2020, jcap, 2020, 020

Greig B., 2019, arXiv e-prints, p. arXiv:1909.13860

Gunn J. E., Peterson B. A., 1965, The Astrophysical Journal, 142, 1633

Guth A. H., 1981, Physical Review D, 23, 347

Harker G. J., et al., 2009, Monthly Notices of the Royal Astronomical Society, 393, 1449

Hogan C., Rees M., 1979, Monthly Notices of the Royal Astronomical Society, 188, 791

Hong S. E., Ahn K., Park C., Kim J., Iliev I. T., Mellema G., 2010, arXiv preprint arXiv:1008.3914

Hu W., White M., 1997, arXiv preprint astro-ph/9706147

Huang Y., Wu X.-P., Zheng Q., Gu J.-H., Xu H., 2016, Research in Astronomy and Astrophysics, 16, 036

Hubble E., 1934, *ApJ*, 79, 8

Hug D., Schneider R., Schuster R., 2008, St. Petersburg Mathematical Journal, 19, 137

Hutter A., Watkinson C. A., Seiler J., Dayal P., Sinha M., Croton D. J., 2020, Monthly Notices of the Royal Astronomical Society, 492, 653

Iliev I. T., Mellema G., Pen U. L., Merz H., Shapiro P. R., Alvarez M. A., 2006, *MNRAS*, 369, 1625

Jensen H., Laursen P., Mellema G., Iliev I. T., Sommer-Larsen J., Shapiro P. R., 2013, Monthly Notices of the Royal Astronomical Society, 428, 1366

Joby P. K., Chingangbam P., Ghosh T., Ganesan V., Ravikumar C. D., 2019, jcap, 2019, 009

Kakiichi K., et al., 2017, Monthly Notices of the Royal Astronomical Society, 471, 1936

Knox L., Scoccimarro R., Dodelson S., 1998, Physical Review Letters, 81, 2004

Kolb E. W., Turner M. S., 1990, Front. Phys., 69, 1

Koopmans L., et al., 2014, in Proceedings of Advancing Astrophysics with the Square Kilometre Array (AASKA14). 9-13 June, 2014. Giardini Naxos, Italy. Online at http://pos. sissa. it/cgi-bin/reader/conf. cgi? confid= 215, id. 1. p. 1

Kulkarni G., Keating L. C., Haehnelt M. G., Bosman S. E., Puchwein E., Chardin J., Aubert D., 2019, Monthly Notices of the Royal Astronomical Society: Letters, 485, L24

Lacey C. G., Cole S., 1993, Mon. Not. Roy. Astron. Soc., 262, 627

Lee K.-G., Cen R., Gott III J. R., Trac H., 2008, The Astrophysical Journal, 675, 8

Lemaître A. G., 1931, Monthly Notices of the Royal Astronomical Society, 91, 483

Lewis A., Bridle S., 2002, *Phys. Rev. D*, 66, 103511

Lin Y., Oh S. P., Furlanetto S. R., Sutter P., 2016, Monthly Notices of the Royal Astronomical Society, 461, 3361

Linde A. D., 1982, Physics Letters B, 108, 389

Liu A., Parsons A. R., Trott C. M., 2014, Physical Review D, 90, 023018

Loeb A., Furlanetto S. R., 2013, The First Galaxies in the Universe

Madau P., Haardt F., 2015, The Astrophysical Journal Letters, 813, L8

Madau P., Meiksin A., Rees M. J., 1997, The Astrophysical Journal, 475, 429

Majumdar S., Pritchard J. R., Mondal R., Watkinson C. A., Bharadwaj S., Mellema G., 2018, *MNRAS*, 476, 4007

Malhotra S., Rhoads J. E., 2004, The Astrophysical Journal Letters, 617, L5

Mantz H., Jacobs K., Mecke K., 2008, Journal of Statistical Mechanics: Theory and Experiment, 2008, P12015

Matsubara T., 2007, The Astrophysical Journal Supplement Series, 170, 1

McMullen P., 1997, Supplemento Ai Rendiconti Circ Mat Palermo, 50, 259

Mecke K., Arns C., 2005, Journal of Physics: Condensed Matter, 17, S503

Mecke K. R., Buchert T., Wagner H., 1993, arXiv preprint astro-ph/9312028

Mellema G., Koopmans L., Shukla H., Datta K. K., Mesinger A., Majumdar S., 2015, arXiv preprint arXiv:1501.04203

Mesinger A., Furlanetto S., 2007, The Astrophysical Journal, 669, 663

Mesinger A., Furlanetto S., Cen R., 2011, *MNRAS*, 411, 955

Mesinger A., Greig B., Sobacchi E., 2016, Monthly Notices of the Royal Astronomical Society, 459, 2342

Miralda-Escudé J., Haehnelt M., Rees M. J., 2000, The Astrophysical Journal, 530, 1

Mo H., Van den Bosch F., White S., 2010, Galaxy formation and evolution. Cambridge University Press

Morales M. F., Hewitt J., 2004, *ApJ*, 615, 7

Paciga G., et al., 2013, Monthly Notices of the Royal Astronomical Society, 433, 639

Padmanabhan T., 1993, Structure formation in the universe. Cambridge university press

Paranjape A., Choudhury T. R., 2014, Monthly Notices of the Royal Astronomical Society, 442, 1470

Park C., et al., 2013, J. Korean Astron. Soc., 46, 125

Parsons A. R., et al., 2010, The Astronomical Journal, 139, 1468

Peebles P., 1968, The Astrophysical Journal, 153, 1

Peebles P. J. E., 1980, The large-scale structure of the universe

Peebles P. J. E., 1993, Principles of Physical Cosmology

Peng Oh S., Mack K. J., 2003, Monthly Notices of the Royal Astronomical Society, 346, 871

Penzias A. A., Wilson R. W., 1965, *ApJ*, 142, 419

Phillips P. R., 1995, The Astrophysical Journal, 455, 419

Planck Collaboration et al., 2018, arXiv e-prints, p. arXiv:1807.06209

Planck Collaboration et al., 2020, Planck 2018 results. IX. Constraints on primordial non-Gaussianity (`arXiv:1905.05697`), doi:10.1051/0004-6361/201935891

Pranav P., et al., 2019, Monthly Notices of the Royal Astronomical Society, 485, 4167

Press W. H., Schechter P., 1974, Astrophys. J., 187, 425

Price D., et al., 2018, Monthly Notices of the Royal Astronomical Society, 478, 4193

Pritchard J. R., Furlanetto S. R., 2006, *MNRAS*, 367, 1057

Pritchard J. R., Loeb A., 2010, Physical Review D, 82, 023006

Pritchard J. R., Loeb A., 2012, Reports on Progress in Physics, 75, 086901

Rahman N., Shandarin S. F., 2003, Monthly Notices of the Royal Astronomical Society, 343, 933

Rao C. R., 1992, in , Breakthroughs in statistics. Springer, pp 235–247

Raste J., Sethi S., 2018, The Astrophysical Journal, 860, 55

Rees M., 1968, The Astrophysical Journal, 153, L1

Reichardt C. L., 2016, in , Understanding the Epoch of Cosmic Reionization. Springer, pp 227–245

Robertson H. P., 1935, *ApJ*, 82, 284

Rutten R. J., et al., 1995, Radiative transfer in stellar atmospheres. Sterrekundig Instituut Utrecht

Rybicki G. B., Lightman A. P., 2008, Radiative processes in astrophysics. John Wiley & Sons

Sahni V., Sathyaprakash B. S., Shandarin S. F., 1998, The Astrophysical Journal Letters, 495, L5

Scheuer P., 1965, Nature, 207, 963

Schmalzing J., Buchert T., 1997, The Astrophysical Journal Letters, 482, L1

Schmalzing J., Górski K. M., 1998, Monthly Notices of the Royal Astronomical Society, 297, 355

Schröder-Turk G. E., Mickel W., Kapfer S. C., Schaller F. M., Breidenbach B., Hug D., Mecke K., 2013, New Journal of Physics, 15, 083028

Scott D., Rees M., 1990, Monthly Notices of the Royal Astronomical Society, 247, 510

Seager S., Sasselov D. D., Scott D., 1999, The Astrophysical Journal, 523, L1

Shankar S., Khatri R., 2019, arXiv e-prints, p. arXiv:1908.04454

Shapiro P. R., Giroux M. L., 1987, The Astrophysical Journal, 321, L107

Shaver P., Windhorst R., Madau P., De Bruyn A., 1999, arXiv preprint astro-ph/9901320

Shull J., 1979, The Astrophysical Journal, 234, 761

Singh S., et al., 2017, The Astrophysical Journal Letters, 845, L12

Singh S., et al., 2018, The Astrophysical Journal, 858, 54

Sobacchi E., Mesinger A., 2014, Mon. Not. Roy. Astron. Soc., 440, 1662

Sokolowski M., et al., 2015, Publications of the Astronomical Society of Australia, 32

Starobinsky A., 1980, Physics Letters B, 91, 99

Strömgren B., 1939, *ApJ*, 89, 526

Sunyaev R., Zeldovich Y. B., 1972, Comments on Astrophysics and Space Physics, 4, 173

Tegmark M., Silk J., Rees M. J., Blanchard A., Abel T., Palla F., 1997, The Astrophysical Journal, 474, 1

Thompson A. R., Moran J. M., Swenson G. W., et al., 1986, Interferometry and synthesis in radio astronomy. Wiley New York et al.

Tingay S. J., et al., 2013, Publications of the Astronomical Society of Australia, 30, e007

Tomita H., 1986, Progress of Theoretical Physics, 76, 952

Trac H., Gnedin N. Y., 2011, Advanced Science Letters, 4, 228

Van de Hulst H., 1982, in , Classics in Radio Astronomy. Springer, pp 302–316

Venkatesan A., Giroux M. L., Shull J. M., 2001, The Astrophysical Journal, 563, 1

Volonteri M., Gnedin N. Y., 2009, The Astrophysical Journal, 703, 2113

Walker A. G., 1937, Proceedings of the London Mathematical Society, s2-42, 90

Wang X., Tegmark M., Santos M. G., Knox L., 2006, The Astrophysical Journal, 650, 529

Wang Y., Park C., Xu Y., Chen X., Kim J., 2015, The Astrophysical Journal, 814, 6

Watkinson C. A., Pritchard J. R., 2014, *MNRAS*, 443, 3090

Watkinson C. A., Majumdar S., Pritchard J. R., Mondal R., 2017, Monthly Notices of the Royal Astronomical Society, 472, 2436–2446

Watts P., Coles P., Melott A., 2003, The Astrophysical Journal Letters, 589, L61

Weinberg S., 1972, Gravitation and Cosmology: Principles and Applications of the General Theory of Relativity

Wouthuysen S. A., 1952, *AJ*, 57, 31

Wyithe J. S. B., Morales M. F., 2007, Monthly Notices of the Royal Astronomical Society, 379, 1647

Yadav J. K., Bagla J. S., Khandai N., 2010, *MNRAS*, 405, 2009

Yoshiura S., Shimabukuro H., Takahashi K., Matsubara T., 2017, Monthly Notices of the Royal Astronomical Society, 465, 394

Zahn O., Lidz A., McQuinn M., Dutta S., Hernquist L., Zaldarriaga M., Furlanetto S. R., 2007, The Astrophysical Journal, 654, 12

Zahn O., Mesinger A., McQuinn M., Trac H., Cen R., Hernquist L. E., 2011, Monthly Notices of the Royal Astronomical Society, 414, 727

Zaldarriaga M., Furlanetto S. R., Hernquist L., 2004, The Astrophysical Journal, 608, 622

Zaroubi S., 2012, Astrophysics and Space Science Library, p. 45–101

Zel'Dovich Y. B., 1970, Astronomy and astrophysics, 5, 84

Zeldovich Y. B., Kurt V. G., Syunyaev R., 1968, Zhurnal Eksperimentalnoi i Teoreticheskoi Fiziki, 55, 278

Zygelman B., 2005, The Astrophysical Journal, 622, 1356

van Haarlem M. P., et al., 2013, Astronomy & astrophysics, 556, A2